

University of California  
Santa Barbara

**Design and Characterization of High-strength  
Bond Coats for Improved  
Thermal Barrier Coating Durability**

A dissertation submitted in partial satisfaction  
of the requirements for the degree

Doctor of Philosophy  
in  
Materials

by

David John Jorgensen

Committee in charge:

Professor Tresa M. Pollock, Chair  
Professor Carlos G. Levi  
Professor Matthew R. Begley  
Professor Ted D. Bennet

September 2016

The Dissertation of David John Jorgensen is approved.

---

Professor Carlos G. Levi

---

Professor Matthew R. Begley

---

Professor Ted D. Bennet

---

Professor Tresa M. Pollock, Committee Chair

July 2016

Design and Characterization of High-strength  
Bond Coats for Improved  
Thermal Barrier Coating Durability

Copyright © 2016

by

David John Jorgensen

For the trees.

## Acknowledgements

The research for this dissertation and the personal development gained along the way was not performed in isolation. There are many people to whom I am gratefully indebted for their time, assistance, expertise, and kindness. First and foremost, I want to thank my advisors Tresa Pollock and Carlos Levi for taking me in five years ago. They accepted a huge risk by agreeing to advise me sight unseen. I showed up to Santa Barbara with a large hole in my leg and no background in materials but they were confident that I would figure it out. My transition from chemical engineering to materials could not have gone more smoothly than it has under their guidance. Both Tresa and Carlos have been great mentors over the years, culling my scientific skills; I am forever grateful.

I would also like to thank Professor Matt Begley for his enthusiastic mechanics tutelage. From thin films to finite elements, Matt has instilled in me an appreciation for the power of a fundamental mechanics knowledge and collaboration applied to materials research. He has been an inspiration and a pleasure to work with for the past five years. Furthermore, Matt and his family kindly gave me a place to live for a number of months during my time in Santa Barbara, giving me the opportunity to care for their golden retrievers and live beyond my means.

I want to thank the fourth member on my committee, Professor Ted Bennett, for his support and offering his laser-material interaction expertise. He pushed me to ensure that the results and claims from the fs laser test were not overstepping feasibility. His skepticism inspired a significantly better understanding of the underlying mechanics, the inherent applications, and limitations of the test.

Throughout all of my work, Chris Torbet has continually been there to support my science. Chris has done everything from ensuring a clean and safe working and laboratory environment, to maintaining the group computer server, to helping with experimental

fixturing, and diagnosing circuit breaker failures. Chris is the lifeblood of the Pollock lab and I am supremely thankful for his kindness, wisdom, and patience over the years.

I must acknowledge my colleagues from GE who have guided and assisted with my dissertation project and who helped to focus the research towards industrially relative areas. Akane Suzuki, Don Lipkin, and Julie Chapman have all graciously helped with composition selection and fabrication of the bond coats used herein. Furthermore, Akane and Don were excellent mentors during my summer internship at GE Global Research. Akane never ceases to amaze me with her ability to get things done quickly and cleverly. In addition, while at GE GRC, Earnie Hearn's assistance and patience got me going on my first cyclic oxidation tests. Of course, I cannot neglect to thank Scot Weaver, who made all the IPD coatings for this dissertation, a campaign requiring an enormity of diligence and attention to detail. They all gave me a glimpse of industrial life after graduation and have inspired me to continue working in the aerospace industry.

Back at UCSB, I want to acknowledge the mentoring that Wesley Jackson gave me when I first arrived. His expertise and insight in oxidation and high temperature coatings set me off on the right foot to a successful dissertation. Similarly, I am indebted to McLean Echlin's kindness for much of my fs laser expertise, not to mention inheriting a host of useful LabView programs I was able to meld into my own grand automation schemes. Both of these Post Docs did a great job encouraging and helping me get up to speed in the beginning of my graduate career. McLean, along with Tom Nizolek, had the fortune of sharing an office with me for three years. I spent many enjoyable hours discussing science, life, and motorcycles with both of them. Before I switched offices, I also had the fantastic experience of sharing a corner of an office with Alan Liu and Andrew Pebley for my first 18 months of grad school. We spent many late nights working on our homework in the office: great times of learning and building lasting friendships. Alan

was able to convince me to join him for some California-essential surfing while out here. I'll never forget watching the sunsets while floating on the waves of Devereux.

Throughout this dissertation I have spent countless sessions on the scanning electron microscopes in the MRL facilities, for which I must acknowledge Mark Cornish's excellent care. He did a fantastic job training and teaching me about SEMs and has helped to keep my research moving smoothly throughout the duration. Similarly, every few months I would run into Valdimir Tolpygo while in the microscopy facility. Vladimir taught me a lot about microscopy for materials and how to push the limits of microscopes. His inquisitiveness and prodding inspired the identification of chemical segregation during the fs ablation of NiAl. Furthermore, Vladimir was kind enough to donate the FeCrAlY samples used in the development of the fs laser test. His willingness to teach and mentor has been sincerely appreciated.

In addition to all the scientists, professors, and engineers mentioned above, I also want to thank the entire Pollock and Levi groups for their continued help, clarification, and interactions over the years. The people in these two groups were instrumental in catching me up to speed with metallographic sample preparation, understanding the difference between stress and strain, and crystallography in the early years. Specifically, Luke Rettberg was very helpful with an introduction to techniques and best practices for polishing René N5 samples. He also taught me a lot about mechanical testing and SPLCF tests while also being a great partner and opponent in countless boardgames. Everyone in both the groups were all a pleasure to work alongside and bounce ideas off. Learning about their individual projects and challenges helped to round out my materials education and broaden my scope of understanding. At the very least, I was given plenty of opportunities for crocheting during group meetings.

I also want to thank the administrative staff in the Materials Department for being so helpful over the years. They keep everything moving smoothly. Aubriana, Gabrielle, Ali, Stefani, Tawny, Jocelyn, and Budd – you’ve been a pleasure to work with.

Last but not least, I’d like to thank my parents and family for supporting me throughout this entire journey. For everything, from my father flying to Alabama to help me rush to CA after I was in a motorcycle crash and then blew out my pickup’s transmission a week later, to lending me their timeshare in Rosarito, Mexico to relax for a week after my qualifying exam, my parents could always be counted on for anything I needed. They did an outstanding job instilling in me the confidence that I can take on and achieve anything I set my mind to. Further, I want to acknowledge all the support that my girlfriend Grace has given me over the past years. It has been a push to the finish filled with lots of long weekends, but she has always been understanding and willing to accommodate my difficult schedule and needs. She has always been there to cheer me up and help me unwind after mind-numbing 6-hour sessions on the SEM and never complained when I would wake up in the middle of the night to check on experiments. I am supremely thankful for her. Without the help and loving support of all of these people, I would not have been able to successfully complete this dissertation. It has been a great journey that I am happy to have shared with so many wonderful people.

# Curriculum Vitæ

## David John Jorgensen

### Education

<b>Ph.D. in Materials</b>	University of California, Santa Barbara	2011-2016
<b>B.S. in Chemical Engineering</b>	University of Colorado, Boulder	2007-2011
National Merit Scholar, Summa Cum Laude, with Honors		

### Publications

1. D.J. Jorgensen, T.M. Pollock, M.R. Begley. “Dynamic Response of Thin Films on Substrates Subjected to Femtosecond Laser Pulses.” *Acta Materialia* (**84**) 2015, pp136-144.
2. D.J. Jorgensen, M.S. Titus, T.M. Pollock. “Femtosecond Laser Ablation and Nanoparticle Formation in Intermetallic NiAl” *Applied Surface Science* (**353**) 2015, pp700-707.
3. D.J. Jorgensen, A. Suzuki, D.M. Lipkin, T.M. Pollock. “Sulfur and Minor Element Effects in the Oxidation of Bilayer  $\gamma'+\beta$  Bond Coats for Thermal Barrier Coatings on René N5.” *Superalloys* 2016.
4. D.J. Jorgensen, A. Suzuki, D.M. Lipkin, T.M. Pollock. “Bond coatings with high rumpling resistance: Design and characterization.” *Surface and Coatings Technology* (**300**) 2016, pp25-34.
5. D.J. Jorgensen, R.W. Jackson, T.M. Pollock. “A Robust Technique To Characterize Rumpling in Next-generation High-strength Bond Coats.” *Surface and Coatings Technology*. Submitted 2016.

## Experience

**GE Global Research Intern**                      Niskayuna, NY                      Jun-Sep 2013  
Manufacturing & Materials Technology High Temperature Alloy Processing Laboratory  
Pioneered improvements in durability and life for future generation turbine blades and coatings while working with a multinational team. Built understanding of complex systems through experimentation.

**3M Corporate Research Intern**                      St. Paul, MN                      May-Jul 2009  
Process Laboratory Laser Processing Group  
Demonstrated proof-of-concept for optically pumped distributed feedback polymer lasers by coordinating and performing material design and selection, process development, and device fabrication.

**Senior Honors Thesis**                      CU-Boulder                      Aug 2010-May 2011  
“Development and Characterization of a Chemical-inhibited Photopolymer System in Order to Achieve Sub-diffraction Index Resolution”  
Advisors: Chris Bowman, Bob McLeod  
Enabled sub-diffraction refractive index feature resolution in a holographic photopolymer by using chemical polymerization inhibitors. Understood the polymerization scheme with a diffusion-based photo-excitation model.

**Senior Design Project**                      CU-Boulder/NREL                      Jan-May 2011  
“Techno-Economic Analysis of Algae-Based Biofuel Production”  
Collaborated with a small team and industrial liaison to design and simulate a large-scale process converting algal syngas into gasoline. Brainstormed creative solutions and performed economic and sensitivity analyses on the operation, supply, and product streams to verify scheme feasibility as part of projects deliverables.

**CU Discovery Learning Apprentice**                      CU-Boulder                      Aug 2008-May 2009  
“High Quality Polymer Optics Development and Characterization”  
Optimized polymer matrix for use in optics research. Evaluated the feasibility of an imbedded polymer laser by characterizing a dye-doped optical polymer.

## Leadership

**Mentor - CISEI Program** UCSB Jun-Aug 2014  
Lead an international undergraduate student through a summer research project to investigate the failure mechanisms of a variety of Ni-based bond coats.

**Mentor/Project Sponsor ME125CH** UCSB Oct-Dec 2011  
Oversaw the development and production of an automated laser focusing system by guiding an undergraduate team on a semester-long project.

**Officer** Tau Beta Pi Jan 2010-May 2011  
National Engineering Honors Society - Colorado Beta Chapter  
Work with other officers to lead and direct chapter. Increase member participation and campus community awareness of engineers impact on society

## Technical Presentations

1. "Bilayer  $\gamma'+\beta$  bond coats for improved thermal cycling performance." D.J. Jorgensen, A. Suzuki, D.M. Lipkin, C.G. Levi, T.M. Pollock. Indo-US Bilateral Workshop on Ceramic Films and Multilayers, Coorg, India. February 25-28, 2016
2. " $\gamma'$  Ni<sub>3</sub>Al bond coats for high-efficiency gas turbine engines." D.J. Jorgensen, A. Suzuki, D.M. Lipkin, T.M. Pollock. The Fourth International Education Forum on Environment and Energy Science, Maui, HI. December 6-10, 2015. **Best Presentation Award**
3. "Design tools for next-generation bond coat development for TBCs." D.J. Jorgensen, J.W. Pro, M.R. Begley, T.M. Pollock. UCSB Structural Materials Seminar, Santa Barbara, CA. October 2, 2015
4. "Measuring TGO-bond coat interface toughness with a dynamic fs laser impulse." D.J. Jorgensen, M.R. Begley, T.M. Pollock. GOALI-SYDES annual meeting, Evendale, OH. August 11-13, 2015
5. "Dynamic interface toughness characterization via a new femtosecond laser ablation technique." D.J. Jorgensen, J.W. Pro, M.R. Begley, T.M. Pollock. ICMCTF 42, San Diego, CA. April 23, 2015
6. "Design, synthesis, and performance of  $\gamma'$  Ni<sub>3</sub>Al bond coats." D.J. Jorgensen, R.W. Jackson, A. Suzuki, D.M. Lipkin, T.M. Pollock. TMS 2015, Orlando, Florida. March 18, 2015
7. "Dynamic interface characterization via a low-fluence femtosecond laser ablation technique." D.J. Jorgensen. UCSB Structural Materials Seminar, Santa Barbara, CA. November 14, 2014

8. "Furnace cycling behavior of rumpling-resistant  $\gamma'$  coatings." D.J. Jorgensen, R.W. Jackson, V.S. Dheeradhada, B.P. Bewlay, A. Suzuki, D.M. Lipkin, T.M. Pollock. GOALI-SYDES annual meeting, Niskayuna, NY. September 22, 2014
9. "fs laser-based coating adhesion investigations: experiments and static vs. dynamic analysis." D.J. Jorgensen, J.W. Pro, M.R. Begley, T.M. Pollock. GOALI-SYDES annual meeting, Niskayuna, NY. September 22, 2014
10. " $\gamma'$  and  $\gamma'+\beta$  overlay bond coats for SPLCF resistance: cyclic oxidation behavior." D.J. Jorgensen, D.M. Lipkin, A. Suzuki, V.S. Dheeradhada, B.P. Bewlay, P.R. Subramanian, T.M. Pollock. Ceramic & Metallurgy Technology Seminar. GE Global Research, Niskayuna, NY, USA. September 20, 2013
11. "TGO-bond coat interface characterization via fs laser-induced buckling." D.J. Jorgensen, R.W. Jackson, M.R. Begley, T.M. Pollock. GOALI-SYDES annual meeting. GE Global Research, Niskayuna, NY, USA. June 17-18, 2013
12. "TGO-bond coat interface characterization via fs laser-induced buckling." D.J. Jorgensen, T.M. Pollock. UCSB Structural Materials Seminar. Santa Barbara, CA, USA. May 24, 2013
13. "Assessing the toughness of the TGO-bond coat interface in TBCs through a laser-induced buckle mechanism." D.J. Jorgensen, R.W. Jackson, M.R. Begley, C.G. Levi, T.M. Pollock. UCSB Structural Materials Seminar. Santa Barbara, CA, USA. June 1, 2012
14. "Phase equilibria in the B2-L1<sub>2</sub> Ni-Al system: Development of an oxidation resistant, high creep strength bond coat." D.J. Jorgensen, R.W. Jackson, T.M. Pollock. GOALI-SYDES annual meeting, Niskayuna, NY, USA. August 3, 2012
15. "Interfacial Toughness Studies (NiAl-TGO): ultrafast laser-induced oxide buckling and mechanistic analysis." D.J. Jorgensen, R.W. Jackson, M.R. Begley, T.M. Pollock. GOALI-SYDES annual meeting. Niskayuna, NY, USA. August 3, 2012
16. "Assessing TGO interfacial toughness of TBCs using ultra-fast laser pulses." D.J. Jorgensen, R.W. Jackson, M.P. Echlin, T.M. Pollock. DYNES Workshop. Santa Barbara, CA, USA. January 9, 2012

## Poster Presentations

1. "Design and characterization of high-strength bond coats for increased TBC life." D.J. Jorgensen, A. Suzuki, D.M. Lipkin, T.M. Pollock. Winter Study Group on High Temperature Materials, Santa Barbara, CA. January 13-15, 2016
2. " $\gamma'$  bond coat development and fs laser assessment for next-generation turbine engine thermal barrier coatings." D.J. Jorgensen, J.W. Pro, A. Suzuki, M.R. Begley, D.M. Lipkin, T.M. Pollock. Gordon Research Conference Physical Metallurgy. Biddeford, ME. July 19-24, 2015

3. "Furnace cycling behavior of rumpling-resistant  $\gamma'$  bond coats." D.J. Jorgensen, R.W. Jackson, A. Suzuki, D.M. Lipkin, T.M. Pollock. ICMCTF 42. San Diego, CA. April 20-24, 2015
4. "A new technique for measuring TGO interface toughness." D.J. Jorgensen, R.W. Jackson, M.R. Begley, T.M. Pollock. ECI Thermal Barrier Coatings IV, Irsee, Germany. June 22-27, 2014
5. "SPLCF and rumple-resistant and  $\gamma'$  bond coatings cyclic oxidation behavior." D.J. Jorgensen, A. Suzuki, D.M. Lipkin, R.W. Jackson, V.S. Dheeradhada, B.P. Bewlay, T.M. Pollock. UCSB Winter Study Group on High Temperature Coatings. Santa Barbara, CA, USA. January 7-8, 2014
6. "Interfacial toughness of thermally grown oxides via fs laser buckling technique." D.J. Jorgensen, R.W. Jackson, T.M. Pollock. UCSB Winter Study Group on High Temperature Coatings. Santa Barbara, CA, USA. January 7-8, 2014
7. "Probing oxide-metal interface properties using ultra-fast laser pulses." D.J. Jorgensen, R.W. Jackson, M.P. Echlin, T.M. Pollock. TMS Superalloys 12 Conference. Champion, PA, USA. September 9-13, 2012
8. "Assessing TGO Interfacial Toughness of TBCs using Ultra-fast Laser Pulses." D.J. Jorgensen, R.W. Jackson, M.P. Echlin, T.M. Pollock. UCSB Materials 25th Anniversary Reunion. Santa Barbara, CA, USA. July 12-14, 2012
9. "Assessing TGO Interfacial Toughness of TBCs using Ultra-fast Laser Pulses." D.J. Jorgensen, R.W. Jackson, M.P. Echlin, T.M. Pollock. UCSB Winter High Temperature Coatings Conference, Santa Barbara, CA, USA. January 10-11, 2012

## Abstract

Design and Characterization of High-strength  
Bond Coats for Improved  
Thermal Barrier Coating Durability

by

David John Jorgensen

High pressure turbine blades in gas turbine engines rely on thermal barrier coating (TBC) systems for protection from the harsh combustion environment. These coating systems consist of a ceramic topcoat for thermal protection, a thermally grown oxide (TGO) for oxidation passivation, and an intermetallic bond coat to provide compatibility between the substrate and ceramic over-layers while supplying aluminum to sustain  $\text{Al}_2\text{O}_3$  scale growth. As turbine engines are pushed to higher operating temperatures in pursuit of better thermal efficiency, the strength of industry-standard bond coats limits the lifetime of these coating systems. Bond coat creep deformation during thermal cycling leads to a failure mechanism termed rumpling. The interlayer thermal expansion differences, combined with TGO-imposed growth stresses, lead to the development of periodic undulations in the bond coat. The ceramic topcoat has low out-of-plane compliance and thus detaches and spalls from the substrate, resulting in a loss of thermal protection and subsequent degradation of mechanical properties. New creep resistant  $\text{Ni}_3\text{Al}$  bond coats were designed with improved high-temperature strength to inhibit this type of premature failure at elevated temperatures. These coatings resist rumpling deformation while maintaining compatibility with the other layers in the system. Characterization methods are developed to quantify rumpling and assess the TGO-bond coat interface toughness of experimental systems.

Cyclic oxidation experiments at 1163 °C show that the Ni<sub>3</sub>Al bond coats do not experience rumpling but have faster oxide growth rates and are quicker to spall TGO than the (Pt,Ni)Al benchmark. However, the Ni<sub>3</sub>Al coatings outperformed the benchmark by over threefold in TBC system life due to a higher resistance to rumpling (mechanical degradation) while maintaining adequate oxidation passivation. The Ni<sub>3</sub>Al coatings eventually grow spinel NiAl<sub>2</sub>O<sub>4</sub> on top of the protective Al<sub>2</sub>O<sub>3</sub> layer, which leads to the detachment of the ceramic topcoat. Furthermore, bilayer Ni<sub>3</sub>Al+NiAl architectures have been investigated to improve the oxidation performance of the monolithic Ni<sub>3</sub>Al coatings while maintaining their high strength. These bilayer architectures are shown to improve the cyclic oxidation performance of the monolithic layers and increase the TBC system life. The design, characterization, and experimentation of these coatings is discussed and related to the development of high-strength coatings.

# Contents

<b>Curriculum Vitae</b>	<b>ix</b>
<b>Abstract</b>	<b>xiv</b>
<b>List of Figures</b>	<b>xviii</b>
<b>List of Tables</b>	<b>xxi</b>
<b>1 Introduction</b>	<b>1</b>
1.1 Thermal barrier coating properties and failure mechanisms . . . . .	5
1.2 Rumpling-induced TBC failure . . . . .	9
1.3 Experimental observations of rumpling . . . . .	11
1.4 Theoretical analyses of rumpling . . . . .	12
1.5 NiAl alloying . . . . .	19
<b>2 Design of Rumpling-resistant Bond Coats</b>	<b>22</b>
2.1 Modeling high-strength coatings . . . . .	25
2.2 Advantages and challenges of Ni <sub>3</sub> Al . . . . .	32
2.3 An integrated computational materials engineering approach to bond coats	35
2.4 Experimental overlay coatings . . . . .	38
2.5 Chapter summary . . . . .	48
<b>3 Oxidation of Monolithic <math>\gamma'</math> Coatings</b>	<b>49</b>
3.1 Isothermal oxidation experiments . . . . .	50
3.2 Thermal expansion measurements . . . . .	58
3.3 Rumpling quantification . . . . .	59
3.4 Cyclic oxidation at 1204 °C . . . . .	85
3.5 Cyclic oxidation and TBC testing at 1163 °C . . . . .	103
3.6 Chapter summary . . . . .	134

<b>4</b>	<b>Bilayer <math>\gamma' + \beta</math> Bond Coats</b>	<b>136</b>
4.1	Experimental sample preparation . . . . .	138
4.2	Isothermal oxidation of bilayer bond coats . . . . .	140
4.3	Cyclic oxidation of bilayer coatings at 1163 °C . . . . .	142
4.4	$\gamma' + \beta$ bilayers in TBC systems . . . . .	150
4.5	Sulfur and Hf effects in monolayer and bilayer architected bond coats . . . . .	153
4.6	TBC system failure in bilayer systems . . . . .	167
4.7	Chapter summary . . . . .	169
<b>5</b>	<b>Interface Toughness Measurement Using Dynamic fs Laser Ablation</b>	<b>171</b>
5.1	Impulse-based dynamic mechanics . . . . .	173
5.2	Interface toughness of $\text{Al}_2\text{O}_3\text{-FeCrAl(Y)}$ . . . . .	201
5.3	Chapter summary . . . . .	216
<b>6</b>	<b>Conclusions and Future Outlook</b>	<b>218</b>
6.1	Sustained peak low cycle fatigue testing . . . . .	222
6.2	Hot corrosion and water vapor testing . . . . .	223
6.3	High-strength coatings enabling advanced TBCs . . . . .	224
6.4	Alloying for improved oxidation of $\gamma'$ phase . . . . .	224
6.5	Tailor-made bond coats for TBC systems . . . . .	225
<b>A</b>	<b>FT Algorithm for Rumpling Quantification</b>	<b>227</b>
A.1	2D mean surface roughness $S_a$ . . . . .	227
A.2	2D root-mean-square surface roughness $S_q$ . . . . .	227
A.3	2D surface tortuosity . . . . .	228
A.4	Mathematica code . . . . .	228
<b>B</b>	<b>Balint and Hutchinson Rumpling Model</b>	<b>252</b>
B.1	Mathematica code for B&H model . . . . .	252

# List of Figures

1.1	Jet engine efficiency (Perepezko) . . . . .	3
1.2	Thermal barrier coating schematic . . . . .	3
1.3	Gas turbine engine temperature capability (Clarke et al) . . . . .	4
1.4	Thermal barrier coating failure mechanisms (Levi et al) . . . . .	5
1.5	(Pt,Ni)Al bond coat thermal biaxial stresses from CTE mismatch . . . . .	15
1.6	(Pt,Ni)Al bond coat & René N5 CTE . . . . .	15
1.7	(Pt,Ni)Al bond coat stress state during rumpling . . . . .	16
1.8	TGO stress state during rumpling . . . . .	17
1.9	Rumpling amplitude growth during thermal cycling . . . . .	18
2.1	Bond coat property design triad . . . . .	22
2.2	Rumpling simulation of 3 h cycles at 1150 °C . . . . .	26
2.3	B&H model applied to T&C experiments . . . . .	28
2.4	B&H model applied high-strength coatings . . . . .	31
2.5	Ni-Al phase diagram . . . . .	33
2.6	Ni-Al oxidation diagram . . . . .	35
2.7	Ni-Al-Cr oxidation diagram at 1000 °C . . . . .	36
2.8	Calculated Ni-Al-Cr isopleths for DJ1 and DJb compositions . . . . .	42
2.9	As-heat treated microstructure of monolithic coatings . . . . .	44
2.10	GDMS of major elements in coatings . . . . .	45
2.11	GDMS of minor elements in coatings . . . . .	46
2.12	As-heat treated microstructure of bilayer coatings . . . . .	47
3.1	Isothermal oxidation at 1093 °C (monolayers) . . . . .	51
3.2	Isothermal oxidation at 1163 °C (monolayers) . . . . .	53
3.3	Isothermal oxidation at 1163 °C – TGO (monolayers) . . . . .	53
3.4	Isothermal oxidation of DJb at 1204 °C . . . . .	55
3.5	Isothermal oxidation rate fits for parabolic kinetics . . . . .	57
3.6	CTE of $\gamma'$ DJ1 coating compared to René N5 . . . . .	60
3.7	Surface roughness of $\gamma'$ and (Pt,Ni)Al coatings during cyclic oxidation . . . . .	62
3.8	Rumpled (Pt,Ni)Al and non-rumpled $\gamma'$ coatings after cyclic oxidation . . . . .	63

3.9	Synthetic rumpling matrices . . . . .	65
3.10	Synthetic asperity matrices . . . . .	66
3.11	Synthetic grit blasting matrix . . . . .	66
3.12	FT of RumpMix synthetic dataset . . . . .	70
3.13	FT of asperity synthetic datasets . . . . .	71
3.14	Variation of synthetic rumpling profile examples . . . . .	73
3.15	Comparison of $S_q$ and FT during synthetic rumpling . . . . .	74
3.16	Variation of synthetic asperity profile examples . . . . .	75
3.17	Comparison of $S_q$ and FT during synthetic asperity growth . . . . .	76
3.18	Comparison of FT and $S_q$ during rumpling w/ asperities . . . . .	78
3.19	FT algorithm applied to rumpling of 5Pt coating (from Jackson et al) . .	80
3.20	Surface roughness and mass change of 5Pt (Jackson et al) . . . . .	80
3.21	5Pt coating cross section (Jackson et al) . . . . .	81
3.22	FT algorithm example - (Pt,Ni)Al 120 cycles, 1204 °C . . . . .	88
3.23	Spalled oxide after 120, 1204 °C thermal cycles . . . . .	90
3.24	TGO scalloping after isothermal DJ1 oxidation . . . . .	90
3.25	Half-life cross sections at 1204 °C . . . . .	91
3.26	End-of-life cross sections at 1204 °C . . . . .	92
3.27	Mass gain & integrated spalling, 1204 °C cyclic oxidation . . . . .	93
3.28	Surface roughness and tortuosity 1204 °C cyclic oxidation . . . . .	94
3.29	Optical images of TGO at 120 cycles, 1204 °C . . . . .	95
3.30	Rumpling maximum amplitude and wavelength - 1204 °C cyclic oxidation	96
3.31	XRD analysis of coatings at 1204 °C . . . . .	97
3.32	Furnace cycle test 1163 °C TBC lifetime . . . . .	107
3.33	Furnace cycle test 1163 °C DJ1 cross sections . . . . .	108
3.34	Furnace cycle test 1163 °C DJ2 cross sections . . . . .	110
3.35	Furnace cycle test 1163 °C DJb cross sections . . . . .	111
3.36	Furnace cycle test 1163 °C PtAl cross sections . . . . .	113
3.37	Cyclic oxidation 1163 °C mass change (monolayers) . . . . .	114
3.38	Cyclic oxidation 1163 °C rumpling amplitude (monolayers) . . . . .	115
3.39	FT radial averages of coatings - cyclic oxidation 1163 °C (monolayers) . .	117
3.40	Cyclic oxidation 1163 °C surface roughness, $S_q$ (monolayers) . . . . .	118
3.41	Cyclic oxidation 1163 °C TGO spalling (monolayers) . . . . .	119
3.42	Cyclic oxidation 1163 °C cross sections (monolayers) . . . . .	120
3.43	Development of $NiAl_2O_4$ – DJ1 TGO at 1163 °C . . . . .	122
3.44	Chemical segregation in DJ1 coating at 1163 °C . . . . .	123
3.45	Semiquantitative model for (Pt,Ni)Al TBC system lifetime . . . . .	127
3.46	TBC failure map - (Pt,Ni)Al coating . . . . .	129
3.47	TBC failure map - $\gamma'$ coating . . . . .	131
4.1	As-heat treat cross sections – (DJ1 and DJb mono/bilayers) . . . . .	139
4.2	Isothermal oxidation parabolic kinetics fits (bilayers) . . . . .	141

4.3	Isothermal oxidation DJ1+DJb bilayer - 250 h 1163 °C . . . . .	142
4.4	Cyclic oxidation 1163 °C Mass (bilayers) . . . . .	143
4.5	Cyclic oxidation 1163 °C TGO spalling (bilayers) . . . . .	144
4.6	Cyclic oxidation 1163 °C Rumpling amplitude (bilayers) . . . . .	145
4.7	Cyclic oxidation 1163 °C Roughness (bilayers) . . . . .	146
4.8	DJ1+DJb oxidation cross section 1163 °C . . . . .	147
4.9	DJ2+DJb oxidation cross section 1163 °C . . . . .	148
4.10	Furnace Cycle Test 1163 °C TBC lifetime (DJ1, DJ1+b(low-S)) . . . . .	151
4.11	Furnace Cycle Test 1163 °C DJ1+DJb bilayer cross sections . . . . .	152
4.12	End-of-life cross sections – high/low-S . . . . .	155
4.13	TGO after thermal cycling at 1163 °C – high/low-S . . . . .	156
4.14	Cyclic oxidation mass change at 1163 °C – high/low-S . . . . .	157
4.15	Cumulative TGO spalling at 1163 °C – high/low-S . . . . .	159
4.16	Rumpling amplitude at 1163 °C – high/low-S . . . . .	160
4.17	Pegging formation in bilayer DJ1+DJb . . . . .	162
4.18	Sulfur segregation schematic . . . . .	166
4.19	TBC failure map - $\gamma'+\beta$ coating . . . . .	168
5.1	Fs laser impulse buckling schematic . . . . .	175
5.2	Relative timing of fs laser-material interactions . . . . .	176
5.3	Example responses of films subjected to fs laser impulse . . . . .	186
5.4	SiO <sub>2</sub> film initial velocity theory & experiment . . . . .	190
5.5	FIB cross section of SiO <sub>2</sub> buckle on Si . . . . .	191
5.6	Axisymmetric buckle debond and film fracture regime map . . . . .	193
5.7	fs laser test of SiO <sub>2</sub> film on Si . . . . .	195
5.8	SiO <sub>2</sub> -Si detachment threshold fitting . . . . .	196
5.9	Comparison of theory and model of SiO <sub>2</sub> film cracking . . . . .	197
5.10	Laser setup schematic for fs laser interface test . . . . .	203
5.11	Laser setup photograph - sample stage side . . . . .	203
5.12	Laser setup photograph - laser side . . . . .	204
5.13	FeCrAl fs laser experiment . . . . .	207
5.14	FeCrAlY fs laser experiment . . . . .	208
5.15	Detail of fs laser irradiated TGO-FeCrAl interface . . . . .	209
5.16	Detail of fs laser irradiated TGO-FeCrAlY buckles . . . . .	210
5.17	Detail of FeCrAl(Y) TGOs . . . . .	210
5.18	TGO initial velocity for fs laser ablation of Al <sub>2</sub> O <sub>3</sub> on FeCrAl . . . . .	211
5.19	DJb low-S and high-S surface profiles and FT - 1150 °C . . . . .	215

# List of Tables

1.1	Properties of TBC layers . . . . .	6
2.1	Nominal experimental coating compositions . . . . .	38
2.2	Coatings and René N5 activity at 1150 °C . . . . .	38
2.3	Experimental coating compositions, measured . . . . .	41
3.1	Parabolic oxidation kinetics fit values . . . . .	58
3.2	Rumpling wavelength for the 5Pt coating (Jackson et al) . . . . .	82
3.3	Staggered FCT button roation for TBC tests . . . . .	106
3.4	FCT results summary - 1163 °C . . . . .	124
4.1	Parabolic oxidation kinetic fit values (bilayers) . . . . .	141
4.2	$\beta$ -phase disappearance at 1163 °C . . . . .	160
4.3	Oxidation and TBC life summary - 1163 °C . . . . .	163
5.1	Physical constants for Al <sub>2</sub> O <sub>3</sub> and FeCrAl . . . . .	205

# Chapter 1

## Introduction

The global demand for energy is projected to monotonically increase for at least the next thirty years [1]. In 2013 alone, electrical and combined cycle (heat + power) plants consumed 1200 Gm<sup>3</sup> of natural gas, which resulted in the release of over 4.8 billion metric tonnes of CO<sub>2</sub> into the atmosphere (calculation from data in [1]). Natural gas accounts for about 20% of the global CO<sub>2</sub> emissions, which is a strong contributor to climate change [2]. However burning coal produces about 22% more carbon dioxide for the same amount of energy produced from natural gas and therefore coal accounts for about 46% of the global CO<sub>2</sub> emissions [1]. The primary means of using natural gas to create electrical energy is by fueling land-based gas turbine engines to run electrical generators. Similarly, commercial aviation jet engines also rely on gas turbine engines to generate thrust by powering a turbofan. The primary difference between the two is that gas turbines in airplanes are often smaller, lighter, and have traditionally operated at higher temperatures than land-based gas turbines. For both of these applications, increased fuel efficiency results in decreased greenhouse gas emissions and decreased operation cost, which leads to a lower cost for passengers and users.

The efficiency of these engines, which burn fuel using the Brayton cycle, is controlled by the compression ratio and therefore the firing temperature of the high-pressure turbine section. Improving the efficiency of these engines leads to a decrease in CO<sub>2</sub> emissions because less fuel is burned for the same amount of energy produced for a given distance traveled. As shown in Figure 1.1, the specific power of aviation gas turbine engines (power per fuel intake rate) increases proportionally with turbine inlet temperature. The current development trend is 1% improvement in efficiency for every 10 °C increase in gas temperature. The deviation from ideal efficiency in these engines is primarily due to bleeding air from the compressor to cool the engine components.

The U.S. Department of Energy has established efficiency and operating temperature goals for power generation turbines, overlaid on Figure 1.1, that are above the present rate of capability improvement even for aircraft turbines [3]. Improved materials systems will be needed in order to meet these goals; higher temperature capability with less cooling air may mean that engine components are operating at higher temperatures than previous generations. Engine designers must be able to take full advantage of new materials to push the efficiency of gas turbines to these higher goals. As an example, an increase of 10 °C in firing temperature of a single land-based engine would save about 8 Mt of CO<sub>2</sub> emissions over the life of a two-engine combined cycle power plant [4].

One of the primary enabling technologies for high-temperature operation of these engines is the thermal barrier coating (TBC) system (Figure 1.2). This system consists of three layers applied to high pressure turbine (HPT) blades and other parts in the hot section of turbine engines. The first layer is an intermetallic bond coat that serves as a mechanical compatibility layer between the metallic substrate and the ceramic over-layers. The bond coat serves as an aluminum source from which to grow a dense and passivating thermally grown oxide, and is usually made from NiCoCrAlY or (Pt,Ni)Al [7–9]. The thermally grown oxide, or TGO, is a thin layer of  $\alpha$ -Al<sub>2</sub>O<sub>3</sub> (1-10  $\mu$ m

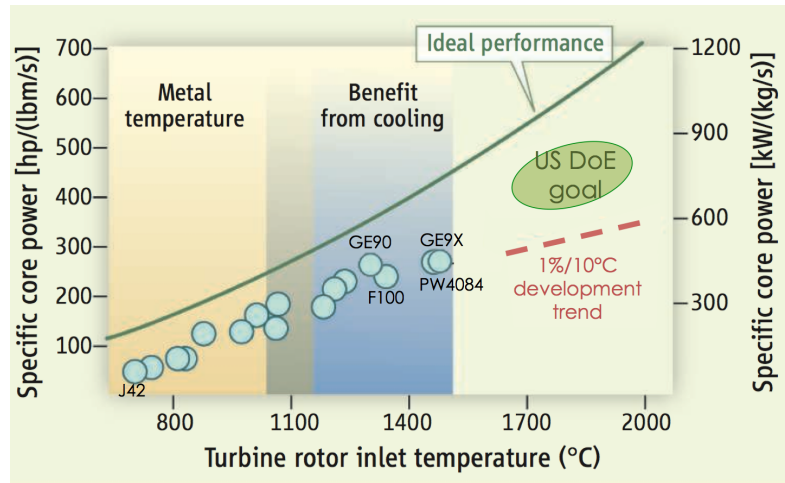


Figure 1.1: Gas turbine specific power (an analogue of efficiency) as function of turbine inlet temperature. Figure adapted from [5].

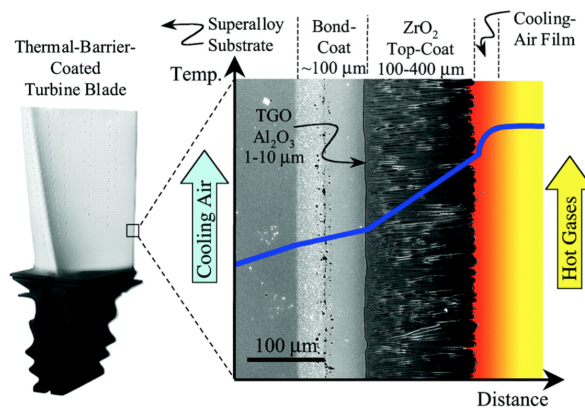


Figure 1.2: Thermal barrier coating on a high pressure turbine blade [6]. The TBC protects the substrate from the heat and oxidative atmosphere of the hot gas path.

thick) that protects the underlying bond coat and substrate from oxidation in the harsh combustion environment. The top coat, a ceramic layer with low thermal conductivity, has historically consisted of 7-8 wt% yttria stabilized zirconia (YSZ) and protects the underlying layers by sustaining a large through-thickness thermal gradient. Top coats can be applied with a number of techniques, but the most common method for high pressure turbine blades in jet engines is electron beam physical vapor deposition (EB PVD). This method produces a porous coating with a feathery microstructure that provides a high degree of in-plane compliance, which improves the ability of the topcoat to maintain adhesion during thermal cycling of the engine.

Thermal barrier coating systems have dramatically improved the temperature capability of gas turbine engines, as shown in Figure 1.3. The advent of TBCs allowed for an immediate increase in engine hot gas path temperatures of about 150 °C [7]. Additional improvements in TBC microstructure, processing, and advanced film cooling techniques has allowed another 300-400 °C increase in gas temperatures. The gas path temperatures now exceed the incipient melting temperatures of most superalloy substrates, making the thermal protection systems essential to engine life.

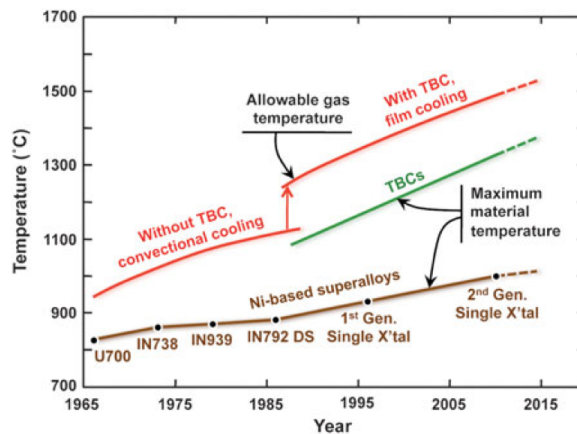


Figure 1.3: Maximum temperature capability of gas turbine engines [7].

## 1.1 Thermal barrier coating properties and failure mechanisms

Thermal barrier coatings are composed of a system of materials with drastically disparate thermal expansion coefficients (CTE) and elastic properties, as shown in Table 1.1 for some common coating materials. TBCs must be carefully designed to account for compatibility between layers with such a wide variety of properties. Furthermore, TBC systems are evolving dynamically throughout service: the topcoat is sintering and becoming more dense and stiff, the bond coat chemistry is changing due to interdiffusion with the substrate and oxidation, and the TGO is growing thicker [10–12]. As a result, the layers of TBC systems must be designed not only in conjunction, but also in anticipation of evolving properties to maximize coating longevity and durability.

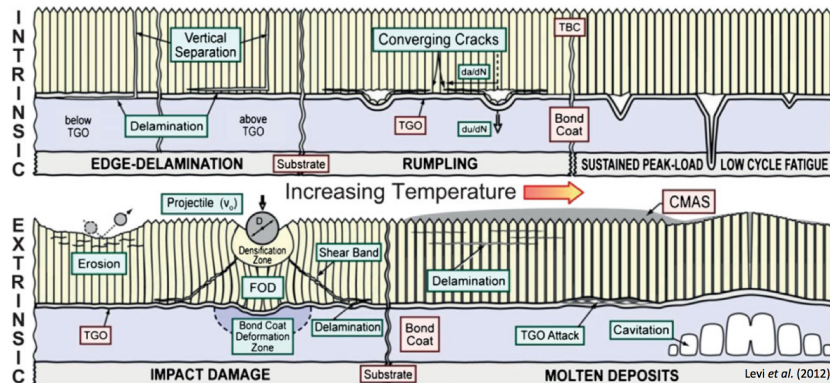


Figure 1.4: Bond coats are directly related to all of the intrinsic TBC failure mechanisms. Figure from [13].

Figure 1.4 shows the menu of failure mechanisms that TBC systems must withstand in order to protect the HPT components [13]. These failure mechanisms range from damage caused by foreign objects impacting the TBC and fracturing the topcoat to thermomechanical deformation and degradation as a result of continuous thermo-mechanical cycling. One key hurdle to increasing the firing temperature of modern engines is the

Table 1.1: Properties of TBC layers

	CTE (ppm/K)	Young's modulus E (GPa)	$\nu$
TGO ( $\alpha$ -Al <sub>2</sub> O <sub>3</sub> ) [10]	8-9	375	0.21
(Ni,Pt)Al as-fab [11]	15.5	118 – 0.024T (°C)	
aged <400°C [17]	14.6		
aged >600°C [17, 18]	12.4	200	
aged (effective) 0-1200°C [19]	19.2		
ZrO <sub>2</sub> topcoat [10]	11-13	0-100	
René N5 0-1100°C [18, 20]	12-16	160 (800°C)	

presence of low-melting eutectic compositions of sand, dust, and volcanic ash that are ingested by jet engines during service [14, 15]. Calcium-magnesium aluminosilicates (CMAS) form glassy melts in the hot gas path at temperatures as low as 1200 °C, deposit on the top coat of the TBC, and penetrate or chemically react with the topcoat [13]. These forms of attack primarily result in stiffening of the topcoat, resulting in a loss of compliance, and also dissolution of the TBC, which results in decreased thermal protection [15]. The commonly pursued methods of creating CMAS-resistant topcoats rely on doping the zirconia with rare-earth elements such as Gd that react with the melts and quickly precipitate a stable crystalline phase to prevent further penetration of, or reaction with, the topcoat [13]. However, one significant problem with most of these advanced CMAS-resistant topcoat compositions is that they have a low fracture toughness and are, therefore, more susceptible to fracture near the TGO-top coat interface [6, 16]. This problem is exacerbated by a type of bond coat deformation, termed rumpling, as explained in the following sections. Rumpling is detrimental because it leads to detachment and/or fracture of the topcoat, depending on the competition between the respective fracture toughnesses of the layers and interfaces and fracture driving forces. A topcoat with low fracture toughness is more likely to fracture on a bond coat that is rumpling due to the out-of-plane displacements the bond coat imposes.

### 1.1.1 Intrinsic failure mechanisms related to bond coats

The top row of Figure 1.4 shows the variety of intrinsic failure mechanisms related to TBC systems with standard bond coats and topcoats. Of these three mechanisms, all are related to inadequacies of the bond coat and are becoming more prevalent as systems are pushed to higher temperatures [13, 18]. Edge delamination at the TGO-bond coat interface can occur due to impurity contamination in the bond coat or substrate (such as sulfur), or due to a large TGO delamination driving force. The TGO driving force for delamination scales with the strain energy stored in the TGO:

$$G_0 = \frac{\varepsilon^2 h \bar{E}}{2} = \frac{\sigma^2 h}{2\bar{E}} \quad (1.1)$$

where  $\varepsilon$  is the TGO strain after cooling,  $h$  is the TGO thickness,  $\bar{E} = E/(1 - \nu^2)$  is the biaxial elastic modulus of the TGO, and  $\sigma$  is the TGO residual biaxial stress, and  $\nu$  is the Poisson's ratio of the coating layer [21]. The residual strain of the TGO is related to the residual stress as  $\varepsilon = \sigma/\bar{E}$ . The delamination driving force, or energy release rate, is directly proportional to the strain energy stored in the film,  $G_0$ .

There is a large driving force for cracking and delamination of the TGO because of the large compressive stress state of the TGO at room temperature, which is a result of the thermal expansion mismatch between the TGO and the substrate during temperature excursions [22]. The substrate, which is usually an order of magnitude thicker than the TBC layers, controls the total strain in the coating during thermal expansion. The resulting biaxial stresses in the bond coat and TGO, assuming elastic deformation and

neglecting the TGO growth stress, are calculated as:

$$\sigma_{\text{BC}} = \frac{E_{\text{BC}}}{1 - \nu_{\text{BC}}}(\alpha_{\text{BC}} - \alpha_{\text{sub}}) \quad (1.2)$$

$$\sigma_{\text{TGO}} = \frac{E_{\text{TGO}}}{1 - \nu_{\text{TGO}}}(\alpha_{\text{TGO}} - \alpha_{\text{sub}}) \quad (1.3)$$

where  $E$  is the elastic modulus, and  $\alpha$  is the CTE of the bond coat (BC), thermally grown oxide (TGO), or the substrate (sub). The larger the CTE mismatch  $\Delta\alpha = (\alpha_{\text{BC}} - \alpha_{\text{sub}})$ , the larger the stresses in the coating layers will be. After a moderate length soak at maximum temperature, the bond coat is nearly stress free due to creep relaxation [23]. The TGO maintains a growth stress at temperature due to a balance between creep and growth of new oxide at the transverse grain boundaries [24]. Upon cooling to room temperature from 1000 °C, with CTEs given in Table 1.1, the TGO is under compression in the range of 3-5 GPa and the bond coat is under about 1 GPa of compression. This significant compressive stress at room temperature results in a large delamination driving force as per Equation 1.1.

The second intrinsic failure mechanism, rumpling, is of primary interest in this dissertation and is described in detail in the following sections. The third intrinsic failure mechanism, oxidation-assisted fatigue, also known as sustained peak-load low cycle fatigue (SPLCF), is caused by large through-thickness thermal gradients that develop on internally cooled turbine blades during takeoff and landing cycles that put the outer surface into a state of compression at high temperature. Creep relaxation during this compressive hold results in a tensile stress upon decrease of the thermal gradient, which opens surface cracks and promotes crack face oxidization. The oxidized crack tips push into the bond coat and substrate upon subsequent compression cycles as has been shown in SPLCF experiments [25, 26]. Crack growth in this scenario is dependent on the superalloy and coating properties [26]. Modeling of SPLCF experiments shows that increasing

the creep strength of the bond coat will decrease the crack extension rate [27] even after the crack has penetrated completely into the substrate [28].

Finally, bond coat cavitation induced by locally tri-axial stress states is the final failure mechanism directly related to bond coats (bottom right of Figure 1.4). This mechanism has appeared more recently as TBC systems are operated at higher temperatures. Its presence is related to both the penetration of CMAS into the topcoat [13] and the  $\beta \rightarrow \gamma'$  transformation [29]. While the exact mechanism and properties related to this type of deformation are not yet well-understood, it is clearly related to the interaction of the bond coat with the rest of the system.

The collective properties and complementary behavior of all three layers of a thermal barrier coating systems are essential to the long life of HPT components. These systems are dynamically evolving throughout service with continuously cycling stress states. Oftentimes, designing a TBC to withstand a single failure mechanism without careful consideration of the impact the design has on other failure types will not lead to an improvement in overall performance. Therefore, these systems must be carefully balanced to withstand a multitude of factors resulting from their harsh environment. One of the prevalent failure mechanisms of TBCs is rumpling as these coatings are pushed to higher temperatures. This thesis will focus on methods to mitigate bond coat rumpling deformation without significantly compromising other essential properties, so as to improve TBC durability.

## 1.2 Rumpling-induced TBC failure

As the combustion temperature and the resultant TBC temperatures are increased in pursuit of higher operating efficiency and lower emissions, bond coat rumpling is accelerated, leading to premature TBC failure [30]. In this type of failure, the bond coat

forms undulations of a characteristic wavelength due to a ratcheting creep mechanism during thermal cycling [31, 32]. The ceramic topcoat, which has a low out-of-plane compliance, cannot deform with the bond coat and therefore detaches from coating, buckles, and subsequently spalls, resulting in loss of thermal protection. While the exact causes and mechanisms of rumpling are still debated in the literature, it is agreed that bond coat deformation is the result of complex stress hysteresis caused by thermal expansion mismatch stresses and TGO growth stresses [32–39].

Rumpling manifests itself differently with and without a ceramic topcoat. Because the topcoat is relatively thick (ca. 130  $\mu\text{m}$ ) compared to the amplitude of bond coat undulations (ca. 1–10  $\mu\text{m}$ ), the topcoat provides physical constraint to the out-of-plane deformation of the bond coat during thermal cycling. The bond coat and TGO form invaginations toward the substrate when a topcoat is present instead of rumpling both toward and away from the substrate sinusoidally without a topcoat; this will be described further in the following chapters. These invaginations result in the bond surface moving downward, away from the topcoat interface, and can serve as crack nuclei when the system is under mechanical load. These cracks at the topcoat-TGO interface can link up during subsequent cycles and lead to topcoat detachment, buckling, and spalling as mentioned earlier. Without a topcoat, rumpling is characterized by a dominant wavelength that is a function of the system properties (elastic moduli, thickness, and thermal expansion coefficients) [31] and has been quantified on Pt-modified aluminide and MCrAlY coatings by monitoring the evolution of the surface roughness with thermal cycling [38]; typical wavelengths are in the range of 60–150  $\mu\text{m}$ . It is known that the presence and magnitude of rumpling is highly sensitive to superalloy and bond coat composition [40], requiring caution when comparing experimental results from separate studies. A number of experiments and models have been studied in attempt to separate out the root causes or driving forces of rumpling, as described in the following sections.

### 1.3 Experimental observations of rumpling

Numerous investigators have conducted experiments to determine the driving forces and mechanisms of rumpling. Panat and coworkers conducted a series of experiments including isothermal exposures of bond coats in air and vacuum, oxidation of substrates alone (no bond coat), and cyclic exposures [41–45]. To paraphrase their conclusions, some degree of rumpling is possible for both NiAl coatings and (Pt,Ni)Al coatings at high temperature (1200 °C) isothermal conditions without a thermally grown oxide layer [43]. The rumpling pattern in the NiAl systems is not correlated with the bond coat grain structure or microstructure, however it was correlated with grain size for the (Pt,Ni)Al. Their experiments indicated that the equi-biaxial stress resulting from thermal mismatch with the substrate is a primary driver of some degree of surface roughening, and that this stress is relaxed via both volume and surface diffusion at the low stress levels typically seen in bond coats at high temperature (tens of MPa). However, at a slightly lower temperature, 1150 °C, Panat witnessed no rumpling of the NiAl coating during isothermal exposures [45].

Around the same time, Tolpygo and Clarke conducted a parallel series of experiments to understand the thermal cycle dependence of rumpling [12, 32, 37–40, 46]. To summarize their findings, cyclic oxidation of a (Pt,Ni)Al coating in vacuum with a thin TGO (0.4  $\mu\text{m}$ ) for 100 cycles at 1150 °C gives a rumpling amplitude that is 70% the height of the rumples when the cycling is conducted in air [32]. Changing the length of the high-temperature hold in air from 6 min to 3 h increases the total rumpling magnitude after 100 cycles to 1150 °C, indicating that more time for bond coat creep relaxation or more time for TGO lateral growth is a significant driver for rumpling [32]. However, it was also shown that short cycles give a large rumpling amplitude for the same total amount of time at 1150 °C due to the increased number of thermal excursions causing

increased ratcheting deformation [12]. Tolpygo and Clarke also conducted thermal cycles in air fully above the martensitic transformation (750-1150 °C) and found that there is an equivalent rumpling amplitude to the standard 25-1150 °C cycle, indicating that the martensitic transformation may not be a significant factor in rumpling. Further experiments found that the dominant rumpling wavelength increases with bond coat thickness in NiAl [39] and that decreasing the cycle temperature decreases the rumpling amplitude to the point where rumpling of a (Pt,Ni)Al coating is very slow at 1100 °C [12].

It has been well-established in the papers mentioned above that there is a strong temperature and time dependence to rumpling behavior. Pan and coworkers measured the strain-rate dependence and creep properties of a (Pt,Ni)Al coating using microtensile tests and found that the creep strength diminishes to 25 MPa at 1150 °C [11]. They also note that there is a strong rate dependence to the creep properties of (Pt,Ni)Al, and that there is significant extensive creep during both loading and unloading of samples. It was observed that the thermal cycling/aging of (Pt,Ni)Al bond coats improves the intermediate temperature strength (600-800 °C) of the bond coat due to the presence of the L1<sub>0</sub> martensite phase. The B2→L1<sub>0</sub> phase transformation on cooling results in a volumetric decrease, which results in a large bond coat tensile stress, as described later.

## 1.4 Theoretical analyses of rumpling

As found in the previously mentioned experimental observations, rumpling is a complex phenomenon that is the result of the interactions between several material properties and processes such as CTE mismatches, heating/cooling rates, diffusion/creep, TGO growth/growth strain, and bond coat strength. The Balint and Hutchinson (B&H) rumpling model is the most comprehensive attempt to resolve these competing interactions and can be used to draw insight from the coating rumpling behavior exhibited in the

present experiments [31, 33]. In short, the B&H model accounts for rumpling rate,  $\dot{\delta}$ , via the nonlinear interaction between the equi-biaxial stress state of the bond coat imposed by the bond coat-substrate CTE mismatch and the normal traction imposed by the presence of the TGO:

$$\dot{\delta} = L\dot{\varepsilon}_0 \exp\left(\frac{-T_{ref}}{T}\right) \times \frac{p}{\sigma_0} \left[ a \left(\frac{\sigma_{BC}}{\sigma_0}\right)^{n-1} + b \left|\frac{p}{\sigma_0}\right|^{n-1} \right] \quad (1.4)$$

where  $L$  is the rumpling wavelength,  $\dot{\varepsilon}_0$  is the reference bond coat creep rate,  $T_{ref}$  is the reference temperature for bond coat creep,  $\sigma_0$  is the reference bond coat creep strength,  $n$  is the creep exponent,  $p$  is the magnitude of the sinusoidal normal traction  $t = p \cos(\pi x/L)$ , and  $\sigma_{BC}$  is the magnitude of the bond coat equi-biaxial stress. The coefficients,  $a$  and  $b$  are functions of the creep exponent,  $n$ , and represent the nonlinear interaction between the equi-biaxial stress,  $\sigma_{BC}$ , and the normal traction,  $p$ . In the B&H simulations  $n = 4$ , which results in  $a = 0.72$  and  $b = 0.15$ .

The B&H model incorporates the bond coat stress state as a balance between the strain imposed by the substrate from the CTE mismatch and power law creep relaxation.

$$\dot{\sigma}_{BC} = \frac{E_{BC}}{1 - \nu_{BC}} \left[ -\frac{\dot{\varepsilon}_0}{2} \left(\frac{\sigma_{BC}}{\sigma_0}\right)^n \exp\left(\frac{-T_{ref}}{T}\right) + (\alpha_{sub} - \alpha_{BC})\dot{T} \right] \quad (1.5)$$

where  $\dot{\sigma}$  is the stress rate-of-change,  $\nu_{BC}$  is the Poisson's ratio of the bond coat,  $\alpha$  is the CTE of the substrate (sub) and bond coat (BC),  $\dot{T}$  is temperature rate-of-change, and the other variables are the same as Eq. 1.4. The TGO behaves elastically in the model, except at the maximum temperature, wherein a yield strength  $\sigma_y = 300$  MPa is imposed. The TGO has a constant growth strain rate at 1150 °C that is set so that the TGO grows a total of 5% laterally in 100 h (growth strain rate  $\approx 10^{-7}$  s<sup>-1</sup>).

The equi-biaxial stress in the bond coat is driven by the CTE mismatch between the bond coat and the substrate, as mentioned above. Again, the thermal expansion of the superalloy substrate controls the strain in all layers of the TBC because the substrate is substantially thicker than the bond coat, TGO, or topcoat [47]. Therefore, the thermal expansion mismatch between the bond coat and the superalloy provides a temperature-dependent bond coat stress state. This biaxial stress state is altered by the presence of the TGO and TBC, which have much lower thermal expansion coefficients and cause surface normal tractions due to initial non-planar flaws. The temperature-dependent stress state varies throughout the temperature excursion and provides a driving force for bond coat rumpling near the maximum cycle temperature, when the bond coat has low strength [11]. The bond coat experiences creep relaxation of the thermal stresses while the system is held at maximum temperature. Repeated heating and cooling causes the progressive amplitude increase of rumple peaks. This is caused by the asymmetry in the stress-temperature relationship where stresses can relax and deform the bond coat at high temperature, but creep relaxation is not active at low temperatures.

The B&H model can be used to explain the nature of creep ratcheting as being due to relaxation of the bond coat thermal stresses during the high temperature hold and the asymmetry in the thermal stress state [31, 33]. The calculated thermal stresses in a (Pt,Ni)Al bond coat on René N5 are shown in Figure 1.5 for a 10 min heating cycle and 1 min cooling. These stresses result from the thermal expansion coefficient (CTE) difference between the layers (Figure 1.6). At the beginning of each heating cycle, at room temperature, the system is fully elastic and the bond coat is under almost 1 GPa of tension. Above 300 °C the bond coat begins to relax from a combination of creep and a decrease in CTE mismatch with the substrate. At 600-700 °C the bond coat undergoes the reversible martensitic transformation  $L1_0 \rightarrow B2$  and experiences a 0.7% volumetric expansion [17, 48]. Immediately after the transition, the bond coat is in compression and at

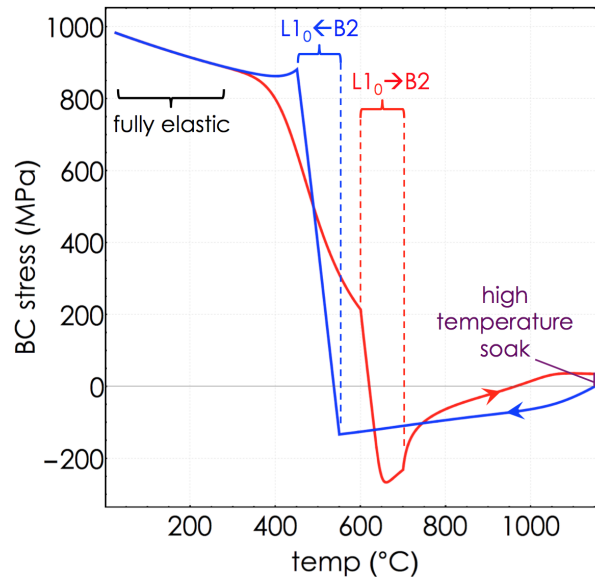


Figure 1.5: Equi-biaxial stress in a (Pt,Ni)Al bond coat [17, 48] on René N5 [18] during a 10-min heating cycle (red) and a 1-min cooling cycle (blue) between 25 and 1150 °C.

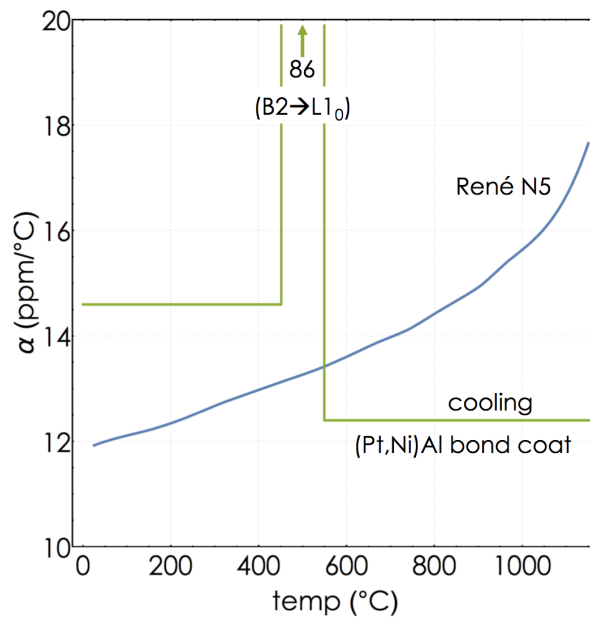


Figure 1.6: Thermal expansion coefficients (CTEs) of a (Pt,Ni)Al bond coat [17, 48] and René N5 [18]. The martensitic transformation causes a large effective CTE on heating and cooling over a small temperature range. The transformation temperature shifts to higher temperatures on heating, and is also a function of alloy composition.

a temperature where creep proceeds rapidly. The CTE of the substrate is now above the CTE of the bond coat and the bond coat is pulled into tension with increasing temperature. The tensile stresses decay rapidly once the system reaches maximum temperature. At the beginning of each cooling cycle, after a long hold period at high temperature, the bond coat is essentially stress free. Upon cooling the bond coat has a larger CTE than the substrate and also undergoes a volumetric decrease from the  $B2 \rightarrow L1_0$  martensitic transformation and is under elastic biaxial residual tension at room temperature.

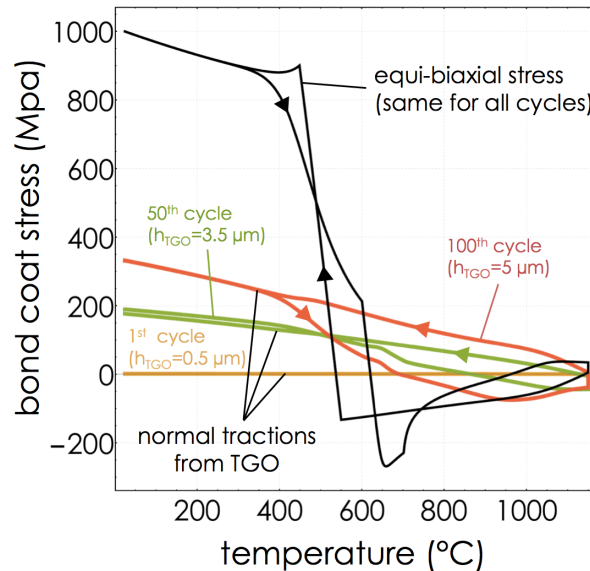


Figure 1.7: Stress state of the bond coat consists of an equi-biaxial stress and normal traction from the TGO. Simulations conducted with 10 min heating, 1 min cooling, and 1 h soak at 1150 °C using the B&H model.

The experimental work of Panat and coworkers has demonstrated that this equi-biaxial stress alone is sufficient to cause a small degree of surface roughness [41, 44]. However, the presence of a non-planar TGO provides a significantly increased driving force for rumpling by the addition of an out-of-plane normal traction on the bond coat. The magnitude of the normal traction relative to the equi-biaxial stress is shown in Figure 1.7. The biaxial stress stays the same each cycle, but the TGO normal traction changes as the TGO increases thickness and rumpling deforms the topology of the bond

coat. The hysteresis in the normal traction is negligible at the beginning of the cycle, when the rumpling amplitude is small, and increases as the bond coat thickens and the corresponding ratcheting grows the rumples.

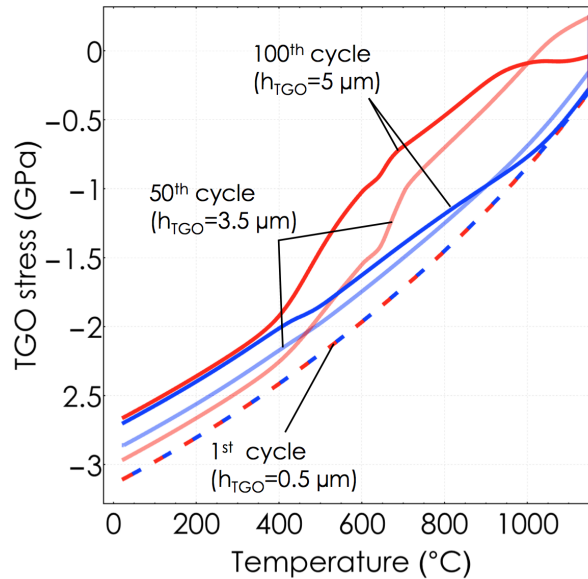


Figure 1.8: Calculated biaxial stress state of a TGO for three select cycles from a 100-cycle simulation of a cyclic oxidation test. Simulations conducted with 10 min heating, 1 min cooling, and 1 h soak at 1150 °C using the B&H model.

In the Balint and Hutchinson model, the bond coat experiences a dramatic increase in rumpling amplitude during the heating portion of the cycle. The peak height is relaxed during the high-temperature soak as the TGO and bond coat both experience creep.. This model incorporates a large portion of the total rumpling amplitude growth to the martensitic transformation (biaxial stress) and the stress transients during temperature changes. Calculations with the Balint and Hutchinson model are performed using Euler time stepping wherein the system of equations are simultaneously solved and then progressively perturbed by a small amount for subsequent steps through time. A full 100-cycle calculation of the rumpling amplitude using the B&H model is shown in Figure 1.9. This calculation was conducted for  $L = 25 \mu\text{m}$ , and uses the same material parameters and heating cycle as in Figures 1.6-1.8. Creep relaxation of the bond coat at

the maximum temperature of each cycle causes a decrease in rumpling amplitude after an initial peak value. This sharp peak and decay is an artifact of the model that arises because the TGO only relaxes at the maximum temperature. The hysteresis in each cycle increases as the TGO grows in thickness and the bond coat rumpling amplitude grows.

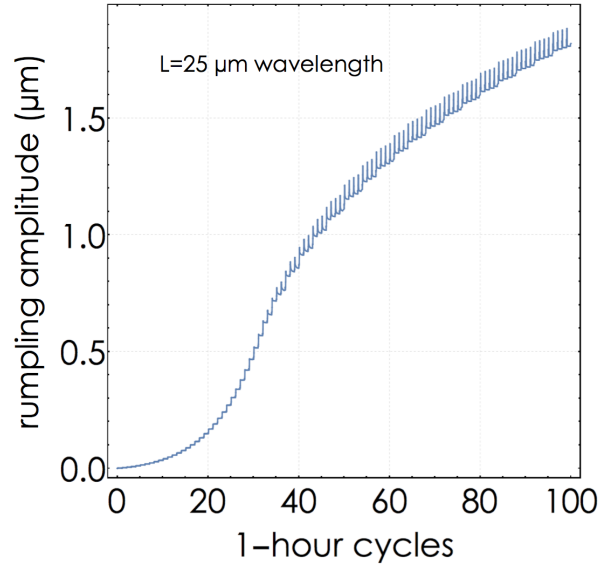


Figure 1.9: Calculated rumpling amplitude for the dominant rumpling wavelength  $L = 25 \mu\text{m}$  for a thermal cycle consisting of 10 min heating, 1 h soak, and 1 min cooling. Material properties taken from [18, 48].

As will be discussed in Section 2.1, the Balint and Hutchinson model suggests that the important material properties that affect rumpling are the bond coat creep strength, TGO growth stress and growth rate, and the CTE mismatch between the coating layers. This model can be used to explore various materials and design strategies to inhibit rumpling deformation.

## 1.5 NiAl alloying

### 1.5.1 Ru-modified aluminides

A number of experimental investigations have been conducted to explore the possibility of moderating rumpling by alloying the  $\beta$  NiAl phase. It has already been shown that the modification of a nickel aluminide with Pt decreases the yield strength [11, 49], which tends to exacerbate rumpling as will be shown in the next chapter. In an attempt to strengthen NiAl bond coats, Tryon and coworkers designed a series of Ru-modified NiAl and (Pt,Ni)Al alloys [50–55]. They showed that the RuAl alloys had excellent creep properties compared to the NiAl. Ruthenium, although acting as a strengthener, forms a volatile oxide at high temperatures, which results in catastrophic oxide and topcoat spallation [53]. Therefore, Ru can only be practically alloyed into bond coats at very low concentrations ( $\lesssim 3$  at%) without being extremely detrimental to the oxidation behavior; this is not a high enough concentration to significantly reduce rumpling behavior [54]. One of the primary lessons from these studies is that an alloy must remain both chemically and structurally compatible with the superalloy and topcoat in order to be a candidate material for bond coats. Oxidation properties are equally important as interlayer compatibility and strength for bond coats.

### 1.5.2 $\beta$ -phase combinatorial studies

In search of  $\beta$ -NiAl coatings that resist rumpling while maintaining good oxidation, Adharapurapu and coworkers conducted a combinatorial search of Ni-Al-Cr-Hf alloys with Pd or Pt using the ion plasma discharge overlay coating technique [18, 56]. They systematically modified the concentrations of alloying elements to create  $\beta$ -phase coatings with between 1 and 9 at% Pd or Pt. The cyclic oxidation behavior of all of these coatings

at 1100 °C was relatively similar, although the Pd-modified coatings had a slightly higher spallation density than the Pt-modified coatings [56]. The best performing coatings in this study were chosen for in-depth analysis. Coatings with a baseline composition of 60 Ni, 34 Al, 6 Cr, 0.3 Hf (atomic %) were created with additions of +5Pd, +5Pt, and a +6Cr/+5Pd combination where the Pt and Pd are substituted for Ni and the Cr is substituted for Al [57]. Thorough examination of the cyclic oxidation testing of this array of  $\beta$ -phase coatings led to the conclusion that all  $\beta$  NiAl coatings rumple at high temperatures [58].

The most intriguing observation of this series of experiments is the comparison between cyclic oxidation life and thermal barrier coating system life. While the cyclic oxidation lifetime at 1150 °C for these coatings varied drastically, 850 cycles for the high Cr alloy (possibly due to S contamination) and 1780 cycles for the +5Pt coating, the TBC lifetime at 1163 °C<sup>1</sup> was essentially equal for all coatings at  $300 \pm 50$  cycles [57, 58]. The TBC lifetime in furnace cycle experiments is usually measured as the cycle at which  $\geq 20\%$  of the ceramic topcoat detaches from the substrate; this is the most important lab test for bond coats as it evaluates the synergy of the whole TBC system. Despite a huge variation in cyclic oxidation lifetime, all of the  $\beta$  coatings had the same TBC lifetime, including an industry standard (Pt,Ni)Al coating. Practically speaking, this discrepancy between oxidation lifetime and TBC lifetime indicates that the properties of  $\beta$  coatings are imbalanced. The oxidation properties of these coatings have been over-engineered at the expense of high-temperature mechanical properties.

The wisdom gained from the RuAl and combinatorial  $\beta$  bond coat experiments is that it is unlikely that a  $\beta$ -phase bond coat can be designed that simultaneously maintains interlayer compatibility with the rest of the TBC and high-temperature strength as

---

<sup>1</sup>1163 °C is 2125 °F, and is the most aggressive standard temperature commonly used in industry to assess topcoats and bond coats during laboratory-scale evaluation.

these coatings are pushed to higher temperatures. Rather than trying to incrementally alloy and improve this well-studied class of coating, a new material system exhibiting a balance of properties is needed to improve TBC life as jet engine temperatures continue to increase.

This dissertation will focus on the principles and properties necessary for bond coat development. The approach is to employ material models to understand how potential material properties are expected to affect rumpling behavior. Further, this dissertation addresses the design of candidate coating materials and characterizes their behavior and ultimate mechanisms of TBC failure. As newer coatings are developed with longer lifetimes and changes in the primary failure modes, new methods to evaluate and assess coatings will be needed; the interface strength between the TGO and bond coat will become a key parameter of bond coat design. In regards to this concern, work performed developing the analytical and experimental tools necessary to measure the interface strength between a thin ceramic film and a metallic substrate will be discussed. Finally, the implications for future coating design will be discussed.

## Chapter 2

# Design of Rumpling-resistant Bond Coats

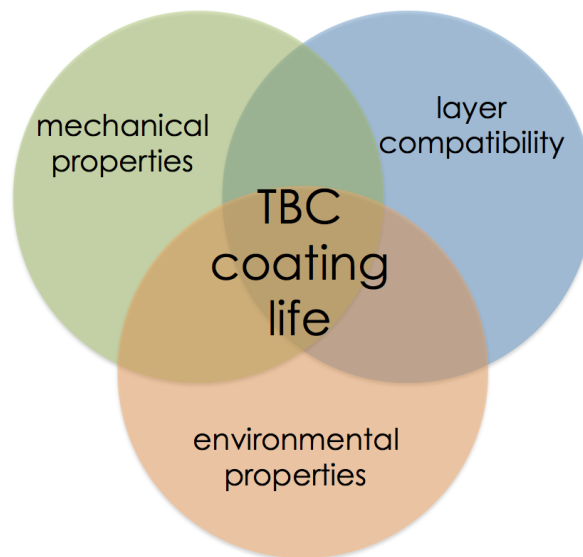


Figure 2.1: The bond coat property triad must be balanced and improved concurrently to increase thermal barrier coating life.

Future bond coat design must consider three main categories, shown in Figure 2.1, in order to optimize thermal barrier coating system performance. First and foremost is layer compatibility; the bond coat must serve as an intermediately compliant layer to maintain

topcoat adhesion to the metallic substrate. This is generally achieved with bond coat properties (modulus, thermal expansion, strength, conductivity) that are intermediate to the substrate and ceramic topcoat. If the topcoat is lost, the rest of the system sustains a 200-300 °C temperature increase and mechanical properties degrade rapidly [59]. Creep and oxidation rates of the bond coat and superalloy substrate are accelerated and lead to expeditious degradation of the substrate. Second, the bond coat must have adequate environmental and oxidation properties in order to serve as an aluminum reservoir from which to form and maintain a scale that provides oxidation passivation. For the high pressure turbine (HPT) in general, this requires the growth of an  $\alpha$ -Al<sub>2</sub>O<sub>3</sub> (corundum) scale. Of the passivating oxide scales, Al<sub>2</sub>O<sub>3</sub> is preferred because it is slow growing, resistant to water vapor attack, exhibits excellent stability, and is insoluble with the traditional topcoat, yttria stabilized zirconia (YSZ). Third, the mechanical properties of the bond coat must be considered. An ideal coating has adequate high-temperature strength to resist rumpling deformation and is also ductile at low temperatures to be damage tolerant and resist crack growth. The ideal combination of these three categories is not straight forward because the interactions of the TBC system are complex. In the past, Edisonian trial-and-error procedures have been used by testing various bond coat compositions in the same TBC system to optimize coating behavior.

The present state-of-the-art bond coat is a Pt-modified nickel aluminide (Pt,Ni)Al. This coating has exceptional oxidation properties in that it forms an exclusively Al<sub>2</sub>O<sub>3</sub> scale and is able to maintain it for thousands of thermal cycles during service. Pt is a noble metal and substitutes for Ni in the NiAl B2 crystal structure [60]; this results in a lower concentration of Ni at the surface, which tends to enhance the oxidation of Al over Ni. The thermally grown oxides on a (Pt,Ni)Al coating are dense with columnar, inward growing Al<sub>2</sub>O<sub>3</sub> grains. Further, Pt alloying lowers the Al activity near the bond coat surface, which promotes diffusion of Al against the concentration gradient from the

bulk alloy and coating outward, to ensure that the supply flux of Al to the growing TGO scale matches the transport of oxygen anions through the TGO. This prevents internal oxidation of the coating or superalloy because there is ample supply of Al cations to meet the O anions at the TGO-bond coat interface. Unfortunately, the (Pt,Ni)Al coating interdiffuses with the substrate during heat treatment to create an interdiffusion zone (IDZ) containing Pt and Al-enriched topologically close-packed phases that drop out of  $\gamma$  solution [61] and can also cause the formation of a secondary reaction zone (SRZ) on some Ru-containing substrates such as René N6 [62]. Despite this non-advantageous behavior, the (Pt,Ni)Al coating is commonly used because of its predictable lifetimes [63], and adequate behavior at current operating temperatures. However, the strength of a (Pt,Ni)Al bond coat is below 25 MPa at service temperatures above 1000 °C [11]. This leads to rapid rumpling as described previously; therefore (Pt,Ni)Al will not be a suitable solution for future turbine engines. To make a broad generalization, MCrAlY coatings, where M usually stands for Ni+Co, have relatively similar behavior to the Pt aluminides [64]. They have excellent oxidation properties but also have strength below 25 MPa at temperatures above 1000 °C [18].

As engines are pushed to higher temperatures, rumpling and oxidation-assisted fatigue failure mechanisms can limit the life of HPT components as a result of an imbalance in the bond coat design triad. The strength of these coatings needs to be increased without a large debit in the oxidation properties in order to improve TBC life, as will be described in the next section. Previous attempts at making high-strength bond coats, such as the Ru-modified aluminides, were unsuccessful because the strengthening element, Ru, proved catastrophic to the oxidation behavior.

## 2.1 Modeling high-strength coatings

The rumpling model developed by Balint and Hutchinson (B&H) can be used to gain insight on the benefits and implications of high-strength coatings [19, 31, 33]. This rumpling model is the most comprehensive attempt to resolve the interactions between CTE mismatches, heating/cooling rates, diffusion/creep, TGO growth and growth strain, and bond coat strength. It can be used to understand how changing specific bond coat properties is expected to alter rumpling behavior. However, a critical comparison of theory and experiment must first be made to validate the analytical model.

### 2.1.1 B&H rumpling model validation

To date, the most complete set of experiments elucidating the rumpling behavior of (Pt,Ni)Al bond coats was conducted by Tolpygo and Clarke (T&C) [32]. This series of experiments included thermal cycling with various high-temperature holds, cycling above the martensitic transition temperature, and cycling under vacuum. These sets of experiments provide an excellent opportunity to evaluate the B&H model. Recall that the B&H model accounts for rumpling rate,  $\dot{\delta}$  (Eq. 1.4), via the nonlinear interaction between the equi-biaxial stress state of the bond coat that is imposed by the bond coat-substrate CTE mismatch and the surface-normal traction imposed by the presence of the TGO. The TGO behaves elastically in the model, except at the maximum temperature, wherein a yield strength  $\sigma_y = 300$  MPa is imposed. The bond coat experiences an increase in rumpling amplitude upon heating and then relaxation during the high-temperature hold, resulting in an abatement of the rumpled magnitude. Cyclic ratcheting plasticity from the stress hysteresis results in a progressive growth of the rumpling amplitude with

---

<sup>1</sup>A substantial amount of material in Section 2.1.1 is reproduced from *Bond coatings with high rumpling resistant: design and characterization* D.J. Jorgensen, A. Suzuki, D.M. Lipkin, T.M. Pollock, Surface and Coatings Technology 2016 [65]

continuous cycling. The B&H model has the assumption that TGO growth and creep only occur at maximum temperature and bestows a large importance of the martensite transition to rumpling growth, as will be demonstrated.

Model comparisons to the T&C experiments were made using the Euler time-stepping algorithm described by B&H, but using a temperature-dependent CTE for the René N5 substrate [18] and temperature-dependent CTE and modulus for the bond coat [11, 17]. An example of the Mathematica code written for the simulations is in Appendix B. The martensitic transformation is modeled to occur between 550 and 450 °C during cooling and 600 and 700 °C during heating as in the original model [31]. The TGO growth is such that the thickness increases from 0.5 to 3  $\mu\text{m}$  and the lateral growth strain is a total of 5% after 100 hours at 1150 °C. Rumpling at a range of wavelengths,  $L$ , was simulated for every virtual experiment.

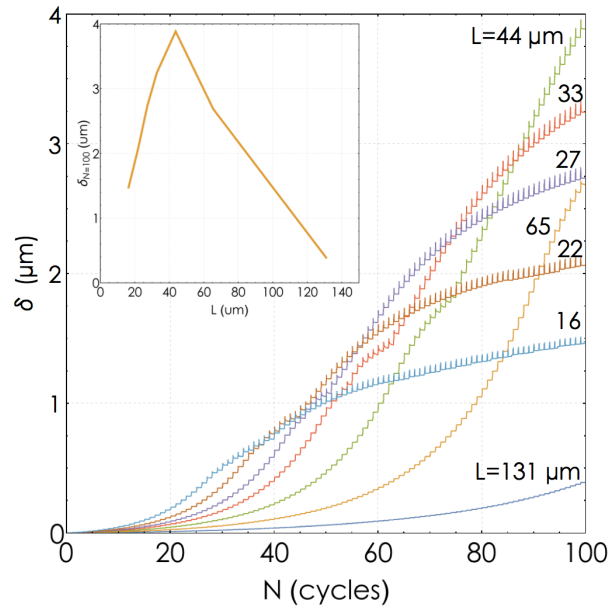


Figure 2.2: Simulated rumpling behavior of the T&C 3-hour thermal cycle. Early on in the simulation, when the TGO is thin, the shorter wavelengths experienced the fastest rumpling; the initial primary rumpling wavelength is approximately 16  $\mu\text{m}$ . The inset shows the maximum rumpling amplitude after 100 cycles as a function of TGO wavelength.

Tolpygo and Clarke had a base experimental cycle that ramped from room temperature to 1150 °C in 5.6 min, soaked for 1 h, and ramped back to room temperature in 5.6 min. They characterized the rumpling amplitude of the coating after 100 cycles by measuring the root-mean square (RMS) surface roughness, which does not include any direct information on wavelength. The first observation made by T&C is that increasing the hold time at 1150 °C from 6 minutes to 1 hour to 3 hours, while maintaining the same 200 °C/min heating and cooling rates, increases the RMS roughness at the end of 100 cycles from 1 to 3.4 to 4.1  $\mu\text{m}$ , respectively. Simulating this series of experiments reported by T&C with the B&H model gives a peak rumpling amplitude of about 1.1 to 3.2 to 3.9  $\mu\text{m}$  (a ratio of 1 : 2.9 : 3.5). An example calculation is shown in Figure 2.2 for the 3-hour hold cycle, where the rumpling displacement is shown as a function of cycles for a variety of wavelengths. The inset shows the total rumpling displacement after 100 cycles. The nonlinear interaction between the surface-normal and biaxial bond coat stresses results in complex rumpling behavior for different wavelengths. Longer rumpling wavelengths begin to grow faster as the TGO grows in thickness while the growth rate of shorter wavelengths tapers off. The predictions for the rumpling amplitude after 100 cycles of all three of the cycles as a function of wavelength are shown in Figure 2.3 (blue line = 6 min hold, black line = 1 h, orange line = 3 h). It should be noted that the comparison between peak rumpling amplitude and RMS roughness is not direct because the RMS roughness is a simplified parameter; the trends should be consistent, however. Therefore, to a good approximation, the B&H model does a good job predicting the impact of longer cycle times to rumpling behavior, meaning that the effect of bond coat creep and/or TGO growth strain is well captured.

The second observation from the T&C experiments is that thermal cycling above the martensite transformation temperature (750-1150 °C) causes the same change in RMS roughness as the full temperature range cycle (25-1150 °C) with the same 1-hour soak at

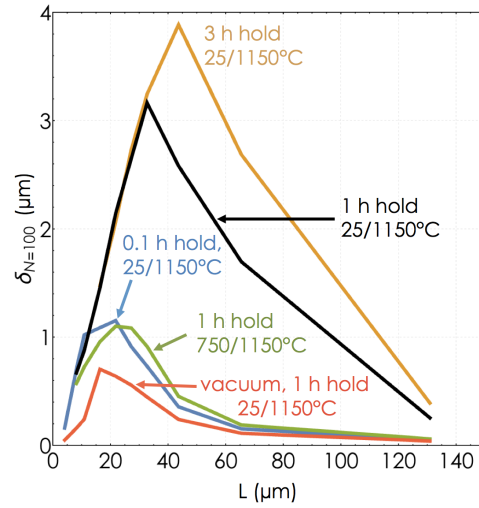


Figure 2.3: Rumpling amplitude after one hundred cycles calculated using the B&H model modified to represent the experiments conducted by T&C [32].

temperature. T&C conducted this cycles using the same 200 °C/min heating and cooling rates, but added a 10 min soak at 750 °C between cycles. Appreciable creep relaxation of the bond coat can still occur during this lower-temperature hold, which can create more stress hysteresis. Simulations of this 750/1150 °C cycle (green line in Figure 2.3), changing only the temperature profile from the previous simulation, give a maximum rumpling amplitude of about 1.1 μm compared to 3.2 μm for the 25/1150 °C cycle. This discrepancy indicates that the B&H model relies too heavily on the biaxial stress caused by the volumetric expansion/contraction of the bond coat upon heating/cooling for rumpling deformation. Increasing the TGO growth rate so that the TGO grows to 4 μm and 9% total growth strain after 100 hours gives a final undulation amplitude of 1.6 μm, which still does not achieve the proper magnitude.

The third observation made by T&C is that the RMS roughness of the bond coat is about 30% lower when thermal cycling is performed in vacuum (sealed in quartz tube) compared to cycling in air. In this experiment, the sample was pre-oxidized in air to form a thin TGO before cycling to limit bond coat vaporization during annealing in vacuum.

This vacuum cycle was modeled by decreasing the TGO growth rate so that the thickness only increases from 0.5 to 0.8  $\mu\text{m}$  and the growth strain was a total of 0.1% after 100 hours at temperature, in close agreement with the experimental observations. As shown by the red line in Figure 2.3, the results of this virtual cycle indicate that the maximum rumpling amplitude is only about 0.7  $\mu\text{m}$  when cycled in vacuum, which is almost an 80% decrease in rumpling amplitude compared to the 3.2  $\mu\text{m}$  amplitude when cycled in air. This discrepancy again indicates that the B&H model does not sufficiently incorporate the impact of the TGO traction for bond coat deformation.

The two discrepancies between the T&C experiments and the B&H model are complementary in that they both underestimate the increase in rumpling amplitude resulting from the presence of the TGO. This can be partly rectified in the B&H model by modifying the  $a$  and  $b$  coefficients of Equation 1.4 to make the system more creep-rate sensitive to normal stresses and less sensitive to biaxial stress. As an example, if  $a = 0.14$  and  $b = 34.5$ , then the rumpling amplitude of the 750/1150  $^{\circ}\text{C}$  virtual cycle conducted above the martensite transition is increased to 80% the amplitude of the normal 25/1150  $^{\circ}\text{C}$  cycle (whereas it was only 34% with the original values of  $a = 0.72$  and  $b = 0.15$ ). Another means to increase the hysteresis of the TGO traction is by increasing the high-temperature yield stress of the TGO. Increasing this value from 300 MPa to 1.9 GPa while also using  $b = 7.5$  gives a final rumpling amplitude in the simulation of 8.22  $\mu\text{m}$  for the 750/1150  $^{\circ}\text{C}$  cycle, which is 89% of the 9.23  $\mu\text{m}$  amplitude simulated for the base cycle with these values. However, these types of changes, by themselves or in combination, cannot bring the B&H model to consistently agree with all three of the T&C experiments at once. It is possible that the absence of TGO growth and creep at intermediate temperatures is too great a simplification. After all, the experiments by T&C show that a thin TGO cycled in vacuum provides enough traction or restraint on the bond coat to enable a rumpling amplitude after 100 cycles that is only 30% smaller than when

cycled in air. In summary, the B&H model is under-predicting the impact of the TGO on the ratcheting plasticity of the bond coat while overcompensating for the effect of the equi-biaxial stresses imposed by the martensitic transformation and bond coat-substrate CTE mismatch. Nevertheless, the model is useful for assessing general trends of changing the bond coat strength and TGO thickness, as will be justified in the following sections.

### 2.1.2 B&H model applied to high-strength bond coats

The effect on rumpling behavior of a high-strength coating can be analyzed using the B&H model (with the original  $a$  and  $b$  coefficients). Furthermore, other related effects such as increasing the TGO growth rate, as might be expected if the oxidation properties are slightly compromised compared to a (Pt,Ni)Al coating, can also be assessed. This is easily accomplished by changing the creep strength of the bond coat,  $\sigma_0$ , and the growth rate of the TGO in the B&H model. Figure 2.4 shows a comparison of the final rumpling amplitude after 100 virtual cycles for systems where the TGO grows from 0.5 to 8  $\mu\text{m}$  and/or  $\sigma_0 = 100$  MPa in comparison with a bond coat with the properties described above. The black line, representing the calculation with bond coat yield strength  $\sigma_0 = 25$  MPa and a final TGO thickness  $h_{100} = 3$   $\mu\text{m}$ , is the same properties as the base-case for the T&C experiments explained in the previous section. The martensitic transformation was not removed from the simulations of the high-strength coatings because the B&H model relies on the martensitic transition rather than the normal traction of the TGO for most of the creep hysteresis, as explained in previously. In addition, a 10-minute heating and 2-minute cooling period was used for these simulations to more closely represent the experiments conducted in a box furnace described later. The B&H model indicates that increasing the growth rate of the TGO without changing the bond coat strength (green line in Figure 2.4) increases the rumpling amplitude. This occurs

because the thicker TGO imposes a larger traction on the bond coat, in accordance with unpublished experiments by Tolpygo and Clarke referenced in Figure 10 of [31]. As explained in Section 3.3.4, rumpling with a thicker TGO is more pronounced at longer wavelengths. The blue line in Figure 2.4 indicates that increasing the bond coat creep strength drastically inhibits rumpling at all wavelengths. Even with the fast-growing TGO (yellow line in Figure 2.4), the strong bond coat resists rumpling, with only a slight increase in total amplitude over the thin TGO.

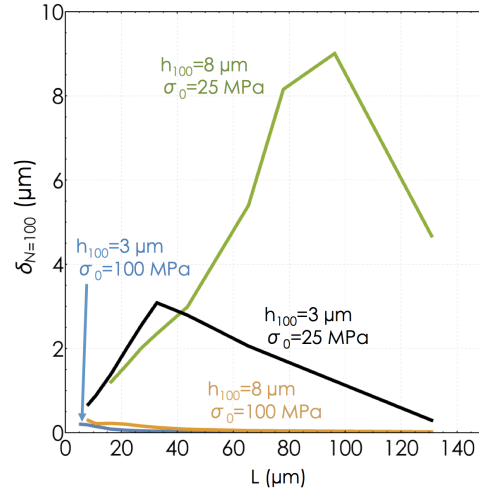


Figure 2.4: Rumpling amplitude after 100 cycles, calculated using the modified B&H model to examine the effect of increasing the TGO growth rate and bond coat creep strength,  $\sigma_0$ . The parameter  $h_{100}$  is the final TGO thickness after 100 cycles. All virtual cycles have a 1 hour hold at temperature and are conducted between 25-1150 °C.

These simulations demonstrate that strong coatings are expected to resist rumpling to a large degree, even if increasing the strength coincides with an increase in the oxidation rate of the coating; other modeling by Karlsson et al corroborates this conclusion [34–36, 66]. It is worth noting that the B&H model can also be used to simulate the effect of adding a thick ceramic thermal barrier coating on rumpling behavior. The model predicts that the TBC drastically inhibits rumpling due to the thick ceramic layer constraining out-of-plane motion, which is generally observed experimentally. The

primary differences between a topcoat and a TGO are that a TGO has much higher in-plane stiffness and has a growth strain at temperature, which leads to increased rumpling with thicker TGO and reduced rumpling under a topcoat. Notwithstanding the difference in behavior from a topcoat, the presence of a topcoat does not solve the problem of rumpling. Rather, the stiffness of the adherent topcoat causes the bond coat creep relaxation associated with rumpling to manifest itself in a different manner. With a topcoat, the bond coat forms invaginations and moves downward, instead of deforming the bond coat out of plane during cyclic oxidation without a topcoat present (shown later in Figure 3.36). The TGO rumples uninhibited after the topcoat detaches from the TGO. The B&H rumpling model does not describe the formation of TGO invaginations with a topcoat present and so is more appropriately suited to model the rumpling behavior of bond coats without a topcoat. This still leads to topcoat detachment from the bond coat and results in topcoat spalling and TBC system failure. The advantages of high-strength coatings with respect to rumpling behavior are clear: they decrease rumpling amplitude during thermal cycling even if the driving forces for rumpling, such as a thicker TGO, are enhanced.

## 2.2 Advantages and challenges of $\text{Ni}_3\text{Al}$

In the search for a high-strength bond coat to satisfy the mechanical property requirements in next-generation TBCs, the rest of the design triad in Figure 2.1 must also be considered. A strong candidate coating material that can satisfy all these requirements is the  $\gamma'$  phase,  $\text{Ni}_3\text{Al}$ , in the Ni-Al binary shown in Figure 2.5. This phase has the  $L1_2$  crystal structure, which is an ordered face-centered cubic (FCC) phase. In contrast, (Pt,Ni)Al coatings have the B2 crystal structure at high temperatures, which is an ordered body-centered cubic (BCC) phase. The atom packing of  $\text{Ni}_3\text{Al}$  is more dense

than the open BCC crystal structure, as shown in Figure 2.5. This is one of the primary reasons that  $\text{Ni}_3\text{Al}$  has a self-diffusivity that is orders of magnitude slower than  $\text{NiAl}$  [67]. Hancock and coworkers also found that the self-diffusivity of the  $\gamma'$  phase is not a strong function of composition as it is with the  $\beta$  phase [68, 69]. The diffusion rate of the  $\beta$  phase increases as coatings lose Al due to inter-diffusion with the substrate or oxidation and become Ni-rich whereas the diffusion rate for  $\gamma'$  coatings is affected to a smaller degree by Ni-enrichment. The activation energy for the  $\beta$ -phase decreases with Ni-enrichment due to a decrease in Ni-site vacancies and increase in Ni antisite defects, which facilitates the anti-site bridge transport mechanism elucidated by Xu and Van Der Ven [69–71]. At high homologous temperatures and low stresses, such as during thermal cycling, diffusional flow can dominate the creep behavior of coatings. Studies of  $\text{Ni}_3\text{Al}$  have shown that the creep properties are superior to  $\text{NiAl}$ , partly for this reason [23, 72, 73]. Therefore, it is expected that the  $\gamma'$  phase should provide more rumpling-resistance than  $\beta$  phase bond coats, satisfying the mechanical strength requirement of the design triad.

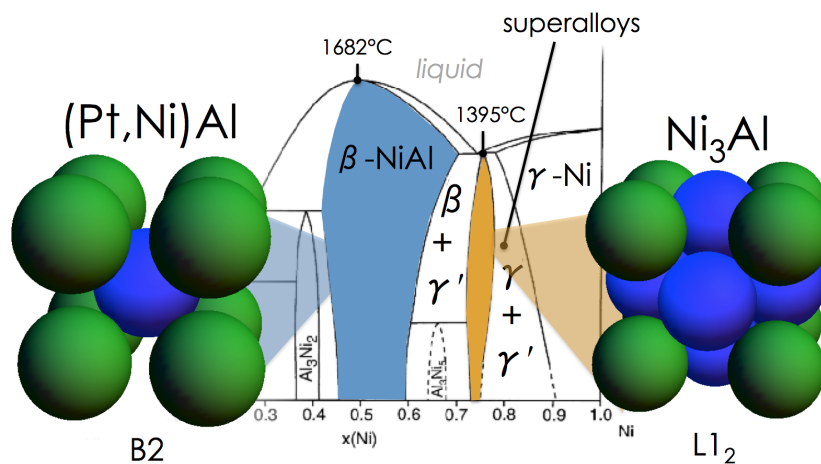


Figure 2.5: Ni-Al binary phase diagram, modified from [74]. Superimposed is the  $L1_2$  crystal structure of  $\text{Ni}_3\text{Al}$   $\gamma'$  phase and the B2 crystal structure of the  $\text{NiAl}$   $\beta$  phase. Most superalloys compositions for high pressure turbine blades are located in the  $\gamma + \gamma'$  two-phase field as indicated.

A second advantage of  $\text{Ni}_3\text{Al}$  is that the composition is in closer equilibrium with  $\gamma+\gamma'$  superalloy substrates, as a heavily-alloyed version of  $\gamma'$  forms the strengthening precipitates in these alloys. As indicated in Figure 2.5,  $\beta$  coatings are not in an adjacent phase field to superalloys in the Ni-Al binary as is the  $\gamma'$  phase. This indicates that there is likely to be less diffusion between a  $\gamma'$  coating on a superalloy substrate than there is with a  $\beta$  coating. Improved phase stability leads to more predictable coating behavior as well as decreases in the likelihood of the formation of a secondary reaction zone or topologically close-packed phases that can occur with current  $\beta$ -phase coatings [61, 62]. In addition, this means that there should be a lower driving force for coating alloying elements to diffuse into the substrate and vice versa because the activities of the alloying elements can be designed to be similar.

With all the advantages of the  $\gamma'$  phase, there is also a key challenge that must be addressed when designing a bond coat. The oxidation properties of  $\text{Ni}_3\text{Al}$  are nowhere as ideal as those of NiAl. This is due to the formation of NiO, and spinel  $\text{NiAl}_2\text{O}_4$  during oxidation at temperatures of interest ( $< 1200$  °C) [75, 76], as illustrated by the oxidation diagram in Figure 2.6. The Al-rich end of this diagram forms the desired oxidation product at even modest temperatures (below 1000 °C), as indicated by the green highlighting. However, at the  $\gamma'$  phase nominal composition indicated in the diagram, 25 at% Al-75 at% Ni, the ideal oxidation behavior is only exhibited at temperatures above 1200 °C, which is beyond the temperature capability of the substrate. While a binary  $\gamma'$ -phase coating would be expected to form a passivating oxide scale initially, further thermal cycling in an oxidizing environment will lead to the growth of non-protective oxide phases.

Fortunately, work by Pettit, Giggins, Gleeson, and coworkers has shown that ternary alloying with chromium or platinum has dramatic effects on the oxidation behavior of the  $\gamma'$  phase [77, 78]. Figure 2.7 shows the impact of a ternary Cr addition to Ni-Al at

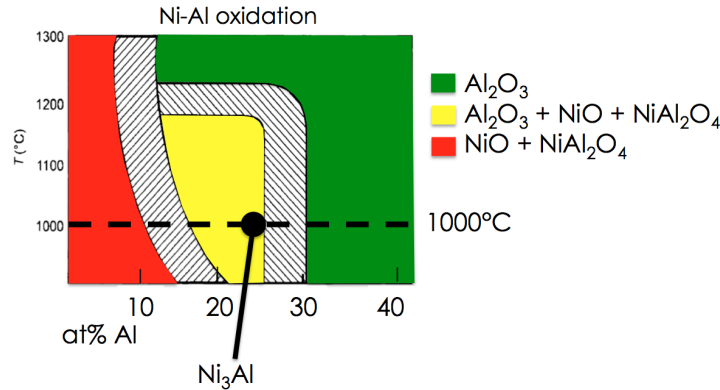


Figure 2.6: Ni-Al binary oxidation diagram, modified from [77]. The green area highlights the composition-temperature relationship leading to ideal oxidation behavior: Al<sub>2</sub>O<sub>3</sub> formation only. In the yellow region, the alloy initially forms an Al<sub>2</sub>O<sub>3</sub> scale, but it is overtaken by NiAl<sub>2</sub>O<sub>4</sub> and NiO phases with further cyclic oxidation exposure. Only non-protective oxides grow in the red region.

1000 °C. The same color-scheme is used as the legend in Figure 2.6 to show the desired oxidation areas. This figure shows that a small addition of Cr can be added to the  $\gamma'$  phase to encourage Al<sub>2</sub>O<sub>3</sub> formation, imparting the ability to maintain the scale at 1000 °C. This strategy can be used to balance out the oxidation properties of the high-strength  $\gamma'$  phase. Therefore, alloyed Ni<sub>3</sub>Al is a strong candidate bond coat alloy that may be able to unite the design triad by providing a coating with high strength, compatibility with the substrate, and adequate oxidation properties. The challenge remains to define an optimal Ni<sub>3</sub>Al composition; this is discussed in the following section.

## 2.3 An integrated computational materials engineering approach to bond coats

Thermo-Calc software with the TCNI5 Ni-based superalloys database [79] was used with a CalPhaD-based approach to explore  $\gamma'$  composition space and identify candidate coating compositions with a high likelihood of success at mitigating the rumpling

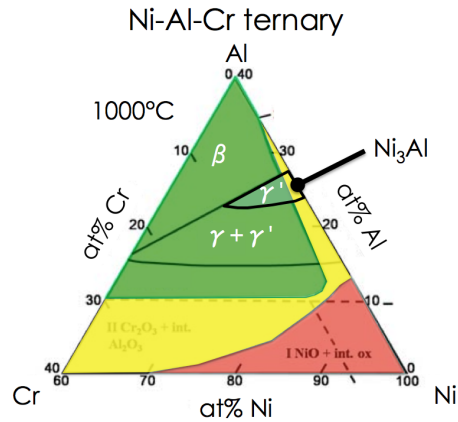


Figure 2.7: Ni-Al-Cr ternary oxidation diagram at 1000 °C, modified from [77]. The green area highlights the compositions that lead to the ideal oxidation behavior:  $\text{Al}_2\text{O}_3$  formation only. In the yellow region, the alloy initially forms an  $\text{Al}_2\text{O}_3$  scale, but it is overtaken by  $\text{NiAl}_2\text{O}_4$  and  $\text{NiO}$  phases with further cyclic oxidation exposure. A few atomic percent Cr alloyed into the  $\gamma'$  phase leads to an alloy that grows and maintains a passivating oxide scale. Coloring is the same as the legend in 2.6.

mechanism outlined in Section 1.2, while maintaining good environmental properties and compatibility with the layers. Pt and Pd were not considered for this investigation to demonstrate the feasibility of improving overall coating performance without the use of precious metals, although it is possible that they could be alloyed to great effect at improving oxidation properties. The outline of the design process is as follows. First, elements known to stabilize the  $\gamma'$  phase (Ta, Mo, W, Ti, Hf), strengthen the  $\gamma'$  phase (Si, Hf, Ta, Ti, Nb) [80, 81], or have beneficial effects on the cyclic oxidation behavior of NiAl or  $\text{Ni}_3\text{Al}$  (Cr, Si, Zr, Hf, Y) [82–85] were considered as potential alloying additions. Second, because bond coats are continuously depleted of Al during service by oxidation and inter-diffusion with the substrate, the candidate alloying elements were evaluated for their relative  $\gamma'$  stabilization efficacy as measured by the maximum width of the  $\gamma'$  field as a function of Al, in a Ni-Al isopleth. All concentrations of alloying elements that were soluble in the  $\gamma$ ,  $\gamma'$ , or  $\beta$  phases at high temperature were considered. Stabilizing the  $\gamma'$  phase ensures the coatings maintain the desired high strength for a greater fraction

of service life. Finally, the change in the solidus temperature as a function of alloying composition was evaluated to avoid incipient melting during post-coating annealing heat treatments or service.

The work of Rawling and Staton-Bevan [81] and Thornton et al [86] demonstrated the temperature dependence of the yield strength of ternary  $\gamma'$  alloys. Collectively, they found that Nb, Si, Ti, and small amounts of Ta and Hf are the best strengtheners for  $\text{Ni}_3\text{Al}$ . Nb is generally detrimental for oxidation due to rapid formation of  $\text{Nb}_2\text{O}_5$  and  $\text{NbAlO}_4$  [87], and was therefore eliminated from alloying element consideration. Thermo-Calc databases suggested that Ta and Hf were the most potent  $\gamma'$  stabilizers at 1150 °C, giving a maximum field width of 10 and 9.4 at% Al at concentrations of 7.4 Ta and 9 at% Hf, respectively.

Analyses with Thermo-Calc indicated that Si and Cr tended to decrease the width of the  $\gamma'$  field slightly while Ti had little effect. Only Ta was predicted to increase the solidus temperature. In all, thousands of compositions were screened for inter-diffusion compatibility with the superalloy René N5, maximum  $\gamma'$ -phase stability at 1150 °C, and solidus temperature. The coatings were designed to be nearly in equilibrium with René N5 at 1150 °C in that the activity of many of the alloying elements was set to be close to that of the substrate. This limits the amount of inter-diffusion between the substrate and the coating. Ultimately, a base  $\gamma'$  alloy, DJ1, with Ni-Al-Ta-Cr-Hf and a second  $\gamma'$  alloy, DJ2, with additional solid-solution strengtheners Si and Ti were selected. A  $\beta$ -phase composition, DJb, was also designed to be activity-matched to DJ1; this coating provides a control for comparison of cyclic oxidation and rumpling behavior. The nominal compositions of these coatings are listed in Table 2.1 and their associated activity values in Table 2.2. The amount of each alloying element selected was an attempt to optimize a multi-parameter space - solidus, high-temperature strengthening, oxidation, and substrate inter-diffusion (via matching the chemical activity at 1150 °C). The DJ1 coating

was designed to test the hypothesis that a  $\gamma'$ -phase coating will be rumpling resistant compared to a  $\beta$ -phase coating and therefore improve TBC lifetime. A small number and concentration of alloying elements were used in order to minimize confounding variables during testing. DJ1 is designed as a  $\gamma'$  alloy with Ta added to stabilize the  $\gamma'$ -phase, Cr to improve selective Al oxidation, and Hf as an impurity getterer. DJ2 is based on the DJ1 composition, but with additional solid solution strengtheners to evaluate whether a stronger coating will be even more resistant to rumpling deformation. DJb is designed as a control composition, having the same elemental activity as the alloying additions in DJ1, it should be a fair comparison between the rumpling behavior of  $\beta$  and  $\gamma'$  coatings.

Table 2.1: Target composition (in atomic %) of the three experimental coatings and the substrate used in these experiments. René N5 composition from [20].

(at%)	Ni	Al	Cr	Ta	Si	Ti	Hf	Co	Mo	W	Re
DJ1	70.5	23.2	3.0	2.50	-	-	0.8	-	-	-	-
DJ2	70.4	22.1	3.0	2.49	0.5	0.8	0.8	-	-	-	-
DJb	61.63	33.7	4.30	0.35	-	-	0.02	-	-	-	-
René N5	63.5	13.9	8.1	2.3	-	-	2.3	8.2	3.0	1.6	1.0

Table 2.2: Target coating element and substrate activity at 1150 °C as calculated by Thermo-Calc TCNI5.

(1150 °C)	Ni ( $\times 10^{-4}$ )	Al ( $\times 10^{-7}$ )	Cr ( $\times 10^{-3}$ )	Ta ( $\times 10^{-8}$ )	Si ( $\times 10^{-9}$ )	Ti ( $\times 10^{-8}$ )	Hf ( $\times 10^{-10}$ )
DJ1	5.03	5.08	1.10	1.20	-	-	4.3
DJ2	4.47	5.97	1.20	2.62	2.46	6.51	9.34
DJb	4.95	4.98	1.74	1.33	-	-	5.50
René N5	6.16	2.00	1.14	2.62	-	-	.506

## 2.4 Experimental overlay coatings

The experimental coatings were fabricated using an ion plasma discharge (IPD), also known as cathodic arc method, at GE Global Research in Niskayuna, NY [18]. This

technique creates overlay coatings by striking an electric arc between an electrode and an ingot under high vacuum. The arc erodes the ingot, creating plasma and particle droplets that are accelerated with a bias voltage into the part to be coated. Deposition rates, chemistry, and thicknesses are extremely flexible with this technique. Ingot compositions were calculated to give the target coating compositions after coating. Ingots were cast by Sophisticated Alloys in Butler, PA. The chemistry transfer functions used to determine the source ingot composition and the IPD coating parameters have been established by GE. The coatings were deposited onto (001) single crystal René N5 disk substrates ( $\varnothing = 19.1$  mm  $h = 2.1$  mm, or  $\varnothing = 25.4$  mm  $h = 3.2$  mm). The disk substrates were created from ingots grown by PCC Airfoils in Minerva, OH. The ingots were centerless ground to one of the above specified diameters  $\pm 0.008$  mm by Bitec div Sample Machining Inc. in Dayton, OH. The disks were cut using wire electrical discharge machining (WEDM) to the desired thickness, and then low-stress ground on both sides. The disks were then put in a vibra-dyne with course-grit stones for 3-4 hours. Before IPD coating, the disks were grit blast using a standard procedure with 220 grit  $\text{Al}_2\text{O}_3$  particles, and then ultrasonically cleaned in methanol.

The IPD coating of the buttons was performed by lying the substrates on the bottom of the coater and mounting two source ingots above the substrates. A single face of each sample was coated at a time: 45  $\mu\text{m}$  of the coating was deposited, followed by a light sputter etch and the final 5  $\mu\text{m}$  of coating. The samples were flipped over and the procedure was repeated on the second face of the substrate for the cyclic oxidation specimens. The TBC samples were removed before the second round because they were only coated on a single face and the sides. The arrangement of the samples and the ingot was set to that the samples would be evenly coated on the sides and faces. Total deposition time for a single face of a set of buttons was approximately one hour.

After IPD coating, the samples were annealed for 4 h at 1080 °C in vacuum to allow for homogenization of the coating and inter-diffusion/bonding with the substrate. The samples were grit blast and then ultrasonically cleaned in de-ionized water, acetone, isopropanol, and methanol before further testing. Experimentally measured compositions of the coatings in both the as-coated and as-heat treated state are in Table 2.3. Ni-Al-Cr phase diagrams calculated at 1163 °C with ThermoCalc for the DJ1 and DJb compositions are shown in Figure 2.8. Two versions of the DJb compositions were fabricated, one with a high sulfur concentration (DJb high-S) and one with a low sulfur concentration (DJb low-S); these allow exploration of the effects of sulfur contamination on bond coat behavior as explained in the following chapters. The X-ray fluorescence (XRF) and electron probe microanalysis (EPMA) measurements were made at GE Global Research and the Glow Discharge Mass Spectroscopy (GDMS) measurements were made by Evans Analytical Group in Liverpool, NY. The XRF and EPMA measurements were made on coatings in the as-coated condition. The GDMS measurements were made on the as-heat treated specimens, allowing for inter-diffusion with the substrate, Co was present in all the samples although it was not in the source ingots.

Table 2.3: Composition (in atomic %) of the four experimental coatings. EPMA and XRF compositions are in the as-coated state. GDMS is measured in the as-heated treated state and is an integral average of the composition through the coating thickness.

	(at%)	Ni	Al	Cr	Ta	Hf	Ti	Si	Co	C (wt.ppm)	S(wt.ppm)
DJ1	EPMA	69.4	24.0	3.3	2.0	0.63	-	-	-		
	XRF	70.8	24.1	1.8	2.6	0.73	-	-	-		
	GDMS	69	22	2.5	1.5	0.46	-	-	1.8	720	2.1
DJ2	EPMA	67.9	24.0	3.3	2.4	0.67	0.90	0.60	-		
	XRF	68.9	24.9	1.8	2.6	0.75	0.80	0.40	-		
	GDMS	68	22	2.3	1.5	0.45	0.76	0.38	1.2	1060	4.1
DJb high-S	EPMA	57.5	36.9	5.3	0.34	-	-	-	-		
	XRF	57.9	37.0	4.6	0.44	0.02	-	-	-		
	GDMS	61	31	3.6	0.18	0.011	-	-	1.5	860	15
DJb low-S	EPMA	58.7	35.6	5.3	0.3	0.12	-	-	-		
	GDMS	55	37	4.1	0.19	0.035	-	-	1.7	1100	3.7

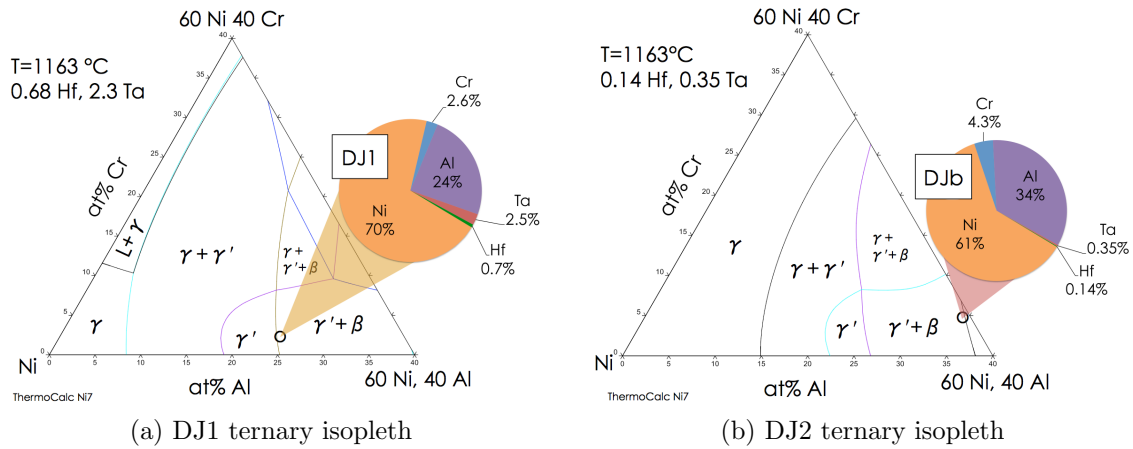


Figure 2.8: Phase diagram for the DJ1 and DJb as-coated compositions at 1163 °C. Diagrams shown the Ni-Al-Cr isopleth, which are the dominant diffusing species in the system. The DJ1 coating is positioned at the Al-rich end of the  $\gamma'$ -phase field and the DJb coating is positioned at the Al-lean end of the  $\beta$ -phase field.

Microstructures of the four as-heat treated experimental coatings are in Figure 2.9. These cross sections are from the same samples used for the GDMS measurements in Table 2.3 and Figures 2.10 and 2.11, which show the depth profiles of major and minor elements. The deposited compositions for the nominally monolithic  $\gamma'$  DJ1 and DJ2 coatings were slightly Al rich and were therefore deposited in the  $\gamma'+\beta$  two-phase space. The annealing treatment caused some of the excess Al in the coatings to diffuse into the substrate to create a diffusion zone with precipitated refractory element phases. Above the diffusion zone is a  $\gamma'$  layer, where the excess Al diffused away. Near the top of the coatings is a  $\gamma'+\beta$  layer where there is still excess Al. Thermo-Calc predicts that the coatings were deposited with 8% and 16%  $\beta$ -phase for the DJ1 and DJ2 coatings and this qualitatively agrees with the microstructures. The DJb coatings exhibited precipitation of the  $\gamma'$  phase at the grain boundaries during furnace cooling but are fully single-phase  $\beta$  field at higher temperatures. The bright contrast phase at the intersection between the DJ2 coating and substrate is a Hf-rich carbide. This inhibited diffusion, as evidenced by the much thinner diffusion zone below the DJ2 coating compared to the other three

coatings. The Hf activity of the DJ2 coating, Table 2.2, is twice that of the other coatings and significantly higher than the René N5 substrate. Therefore, there is a driving force for Hf in the DJ2 coating to diffuse towards and into the substrate during annealing. The Hf reacts with C when it reaches the substrate surface; evidence of this reaction is seen in the GDMS scan Figure 2.10b, where there is a concentration of Hf and C at the substrate-coating interface. All other coatings, which had Hf approximately equal to the substrate, do not exhibit this characteristic Hf peak at the interface nor the presence of HfC at the bond coat-substrate interface.

A comparison of the concentration profiles in Figure 2.10 with the activity values calculated with Thermocalc (Table 2.2) shows good qualitative agreement. None of the concentration gradients within the coating are very steep, indicating that the coating is in close activity with the substrate. The Ni and Al gradients are the steepest, increasing and decreasing in concentration, respectively, moving deeper into the coating. These two elements also have the largest difference in activity with the substrate.

All of the coatings exhibited sulfur and impurity segregation to the surface and bond coat-substrate interface, as shown in Figure 2.11. The high sulfur DJb coating had almost 100 wt.ppm of S at the surface, which is likely detrimental to oxidation behavior because S has been shown to decrease the TGO-bond coat interface strength [88–92].

### 2.4.1 Bilayer coatings

It has been discussed that  $\beta$ -phase coatings, although forming a passivating and dense  $\text{Al}_2\text{O}_3$  TGO, cause TBC failure due to rumpling deformation at elevated temperatures as a result of low strength. It has also been established that the mechanical strength and creep properties of the  $\gamma'$  phase is superior to the  $\beta$  phase, although the oxidation properties are somewhat compromised as described in Section 2.2. The ideal balance

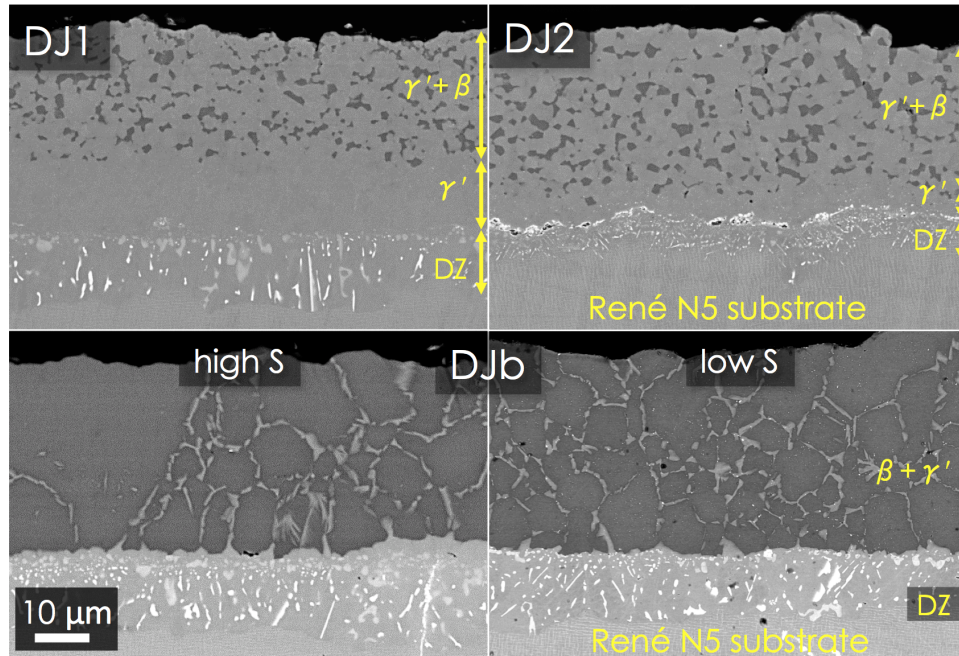


Figure 2.9: Cross sections of the experimental coatings in the as-heat treated state (4 h, 1080 °C in vacuum). Scale bar applies to all images.

of properties for a bond coat would marry the high-strength of the  $\gamma'$  phase with the oxidation behavior of the  $\beta$  phase. A bilayer coating architecture offers the potential to combine both the high-strength of the  $\gamma'$  phase with the superior oxidation behavior of the  $\beta$  phase. To this end, a series of bilayer coatings were fabricated, consisting of a thick  $\gamma'$  layer (DJ1 or DJ2) topped by a thin  $\beta$  layer (DJb). The design concept is that the DJb top-layer will grow an initially dense and passivating  $\text{Al}_2\text{O}_3$  scale and transform to the  $\gamma'$  phase through loss of Al. The thick  $\gamma'$  layer beneath will maintain the slow-growing TGO without rumpling for the rest of the coating life. Bilayer architected coatings were manufactured with the IPD method described above. DJ1+DJb and DJ2+DJb samples with both the high-S and low-S DJb compositions were made. First, 45  $\mu\text{m}$  of the  $\gamma'$  phase was deposited on both sides of the button. Next, the coatings were lightly sputter etched to clean the coating surface before deposition of 5  $\mu\text{m}$  of DJb. Because the DJb composition is activity-matched with the DJ1 coating, it is expected that the behavior

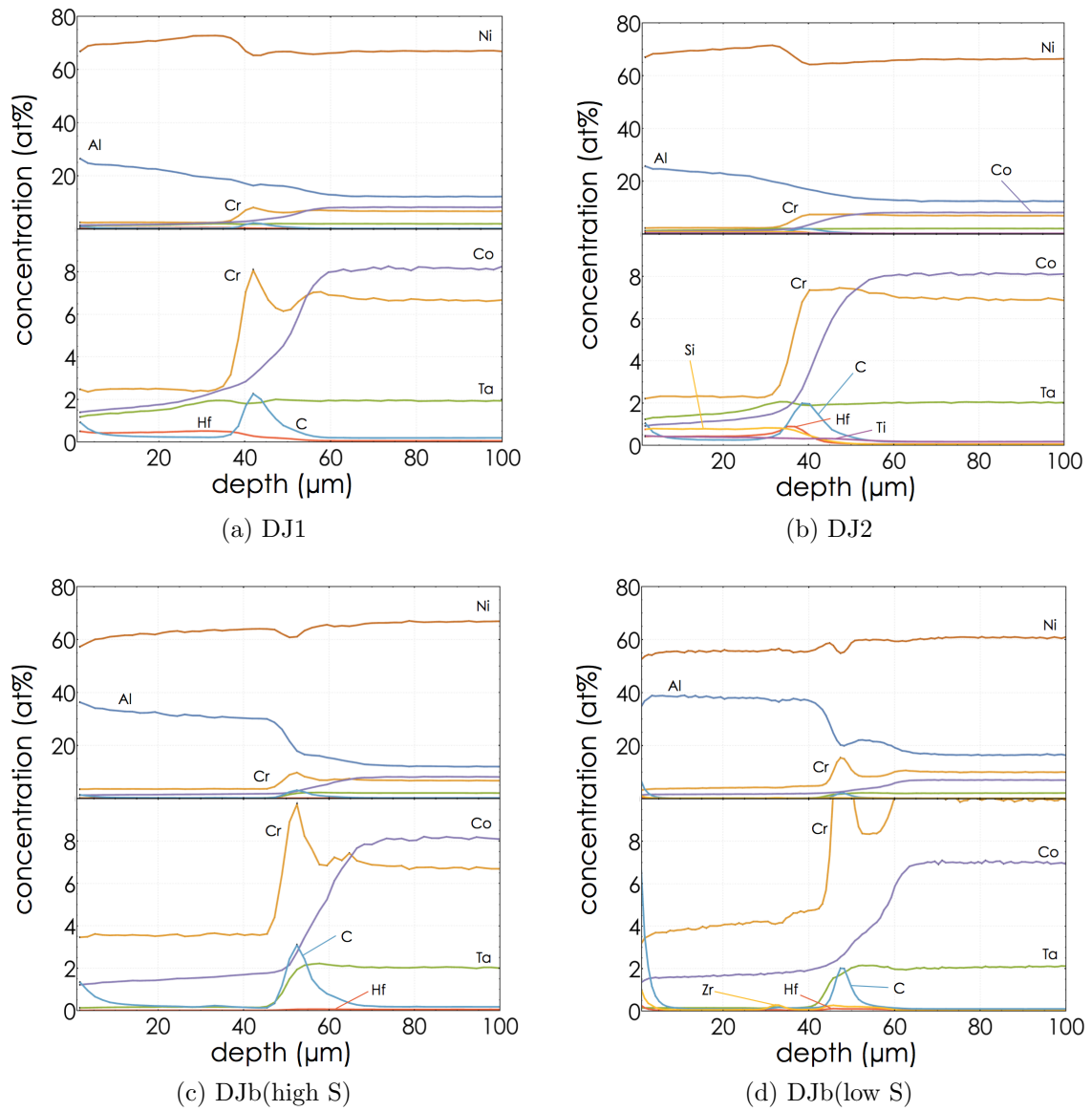


Figure 2.10: GDMS scans of the major elements in four experimental coatings in the as-heat treated state. Zr and C are impurities.

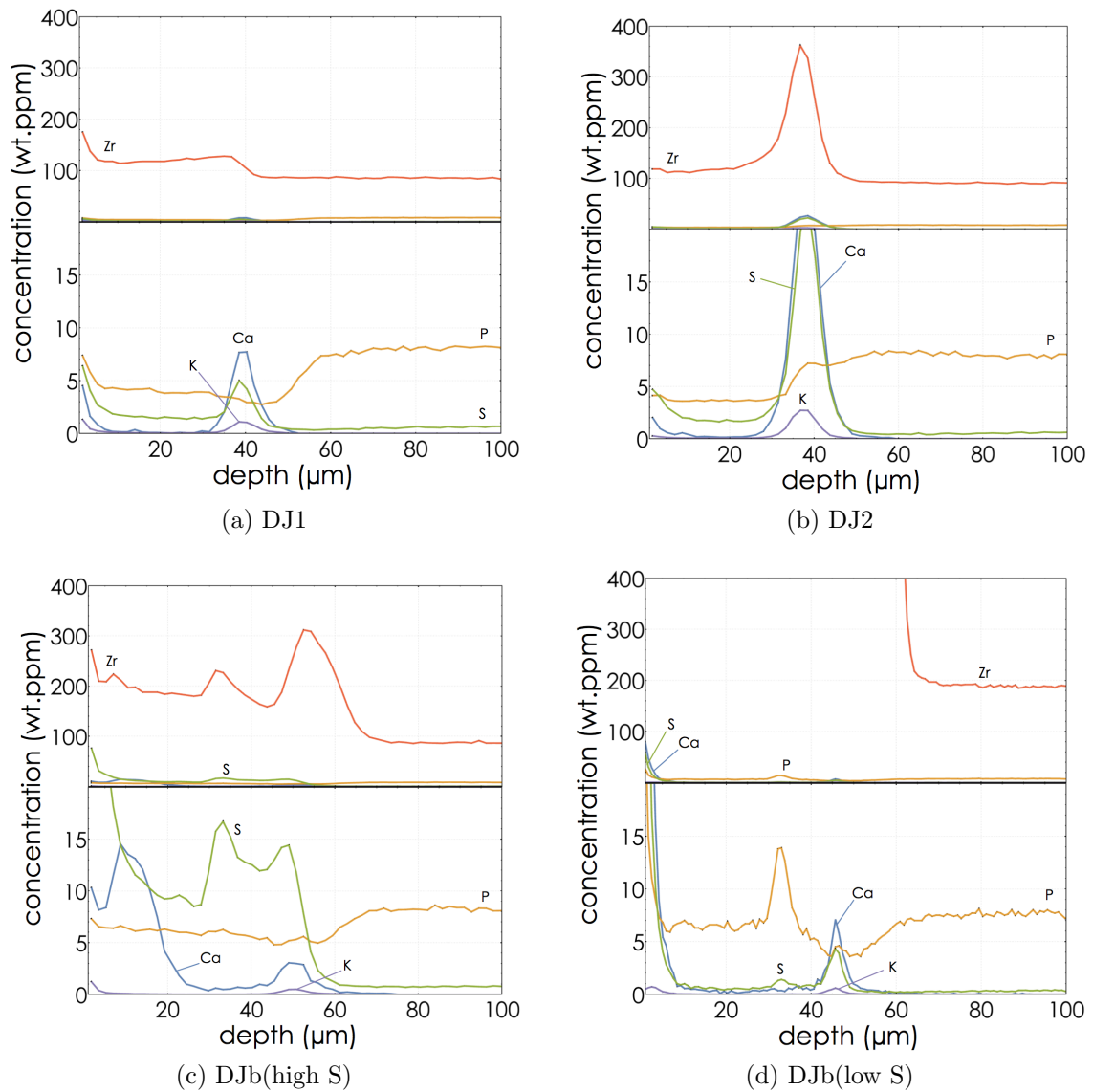


Figure 2.11: GDMS scans of the impurity elements in four experimental coatings in the as-heat treated state.

of this combination will exhibit the most synergy. However, it is still useful to test the generality of the  $\beta$  over-layer concept using the DJ2+DJb architecture. Microstructures of these coatings are in Figure 2.12. The high and low sulfur variants of DJ1+DJb architecture are identical in appearance; only the low-S version is shown. Again, the  $\gamma'$  layer initially shows some two-phase character because it was slightly Al-rich. It is interesting to note that the HfC diffusion layer that is present in the monolithic DJ2 coating (Figure 2.9) does not exist in the DJ2+DJb(low-S) bilayer (Figure 2.12). While this is not completely understood, it is possible that the lower Hf activity in the DJb top-layer reduces the driving force for Hf diffusion into the substrate. Note that the inter-diffusion zone size is approximately the same size in both of the bilayer coatings in Figure 2.12. The bright contrast specs in the DJ2 coating are HfC that formed during annealing. ThermoCalc TCNI7 calculates these carbides to be thermodynamically stable in the as-coated composition. Carbon is an impurity that can originate in either the source ingot or as a contaminate due to poor cleaning of the IPD coater.

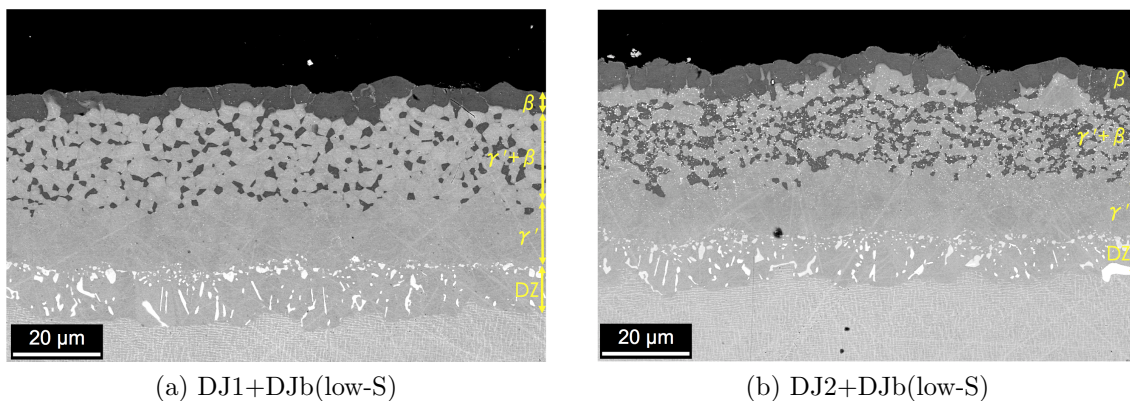


Figure 2.12: Bilayer architecture bond coats in the as-heat treated state: 4 h 1080 °C in vacuum. Overlay coatings were made at GE Global Research in NY using the IPD method [18].

## 2.5 Chapter summary

The design of advanced bond coats for thermal barrier coating systems requires a delicate balance of mechanical and environmental properties with compatibility with the rest of the system. Current state-of-the-art bond coats become unbalanced as turbine engines are pushed to higher temperatures; their high-temperature strength quickly decays. As a result, these coatings are susceptible to high-temperature rumpling deformation during thermo-mechanical cycling, which ultimately leads to premature topcoat detachment TBC system failure. The Balint and Hutchinson model is used to understand how changes in bond coat strength and TGO growth rate are expected to impact the rumpling behavior of these coatings. It is shown that an increase in the bond coat strength should inhibit rumpling at all wavelengths, even if the driving forces for rumpling are increased. The  $\gamma'$ -Ni<sub>3</sub>Al phase is proposed as a candidate material that can re-unify the properties of the bond coat design triad at high temperatures with proper alloying. Two experimental  $\gamma'$ -phase overlay coatings, DJ1 and DJ2, have been developed to test the behavior and properties of the  $\gamma'$  coatings during cyclic oxidation tests. These coatings contain Cr and Hf for oxidation resistance and Ta to stabilize the  $\gamma'$  phase; the DJ2 variant contains additional high-temperature strengtheners Ti and Si. In addition, a series of bilayer  $\gamma'+\beta$  coatings have been developed to marry the exceptional oxidation behavior of NiAl with the high strength of Ni<sub>3</sub>Al. The following chapters will examine the behavior and performance of these coatings in a variety of thermal and oxidation tests.

# Chapter 3

## Oxidation of Monolithic $\gamma'$ Coatings

It is essential to design experiments that scrutinize each property of the bond coat trinity (Figure 2.1) to evaluate bond coat performance. Isolating each of these key material parameters would be ideal because it allows an understanding of how properties may be balanced to maximize TBC life. Unfortunately, experiments that readily evaluate all the properties in the design space individually do not exist. As will be discussed in Chapter 5, there is no straightforward means to measure the interface toughness between a thermally grown oxide and bond coat. To date, the most straightforward and reliable combination of experiments used to evaluate bond coat performance and screen their potential performance in an engine is a combination of isothermal oxidation, cyclic oxidation, and furnace cycling with a top coat. Burner rig testing is a typical industry standard to assess ceramic topcoat quality and was is not considered in this dissertation. This combination assesses the oxidation properties directly, but indirectly assesses the mechanical properties and inter-layer compatibility. Oxidation behavior is highly dependent on kinetics and therefor difficult to predict from first principles. This chapter will discuss methods of characterization and performance of the monolithic

experimental coatings in the aforementioned tests. Furthermore, the benefits of the bilayer coatings has been investigated and will be discussed in the following chapter.

### 3.1 Isothermal oxidation experiments

Isothermal oxidation tests were conducted at 1093, 1163, and 1204 °C (2000, 2125, and 2200 °F) to complement other planned cyclic oxidation, furnace cycle TBC, and fatigue tests, as explained later. These temperatures were selected because they are industry standards for accelerated bond coat tests. These samples were made by coating one side of an approximately 5 × 5 mm piece of René N5 along with the rest of the samples described in Section 2.4. Weight change measurements of these samples during oxidation would not be informative because the the oxide scales will have different constitution on the coated and bare sides of the substrate. Only the DJ1, DJ2, and high-S DJb monolithic samples were isothermally oxidized. It is not expected that the  $\text{Al}_2\text{O}_3$  growth rates will change drastically between the high and low S versions of DJb, although the oxide scale morphology may differ as found previously [93]. Cross sections of the coatings after 250 h at 1093 °C are in Figure 3.1, and after 250 h at 1163 °C in Figure 3.2. Both the DJ1 and DJ2  $\gamma'$  coatings have transformed to the  $\gamma+\gamma'$  phase primarily due to diffusion of Co and Cr from the substrate. EDS measurements of these coatings show that the  $\gamma'$  phase contains more nickel than the  $\gamma$  phase, which contains significantly more Cr and Co. As a result, the  $\gamma$  phase in these backscattered electron micrographs is darker in contrast than the  $\gamma'$  phase. The DJb coating still contains a layer of  $\beta$  phase at 1093 °C after 250 h, but has fully transformed to  $\gamma'$  at 1163 °C.

The TGOs on the two  $\gamma'$  coatings are slightly thicker and more porous than the  $\beta$  coating although all three TGOs are predominantly  $\text{Al}_2\text{O}_3$ . The porosity in the TGOs on the DJ1 and DJ2 coatings, visible in Figure 3.3, is likely due to the TGO volume

contraction during from the conversion of metastable  $\theta$ - $\text{Al}_2\text{O}_3$  to the thermodynamically stable  $\alpha$ - $\text{Al}_2\text{O}_3$  [94]. It is important to know the modulus because the energy release rate for TGO spalling depends linearly on the TGO elastic modulus (Equation 1.1). The effect of the porosity on the TGO modulus can be estimated by using the model fit by Phani and Niyogi [95]:

$$E = E_0(1 - P)^{2.143} \quad (3.1)$$

where  $P$  is the porosity volume fraction and  $E_0$  is the fully dense modulus. Image analysis of the TGO scale on the DJ1 coating gives a porosity of around 2.4%. This gives an  $\text{Al}_2\text{O}_3$  matrix modulus of 360 GPa.

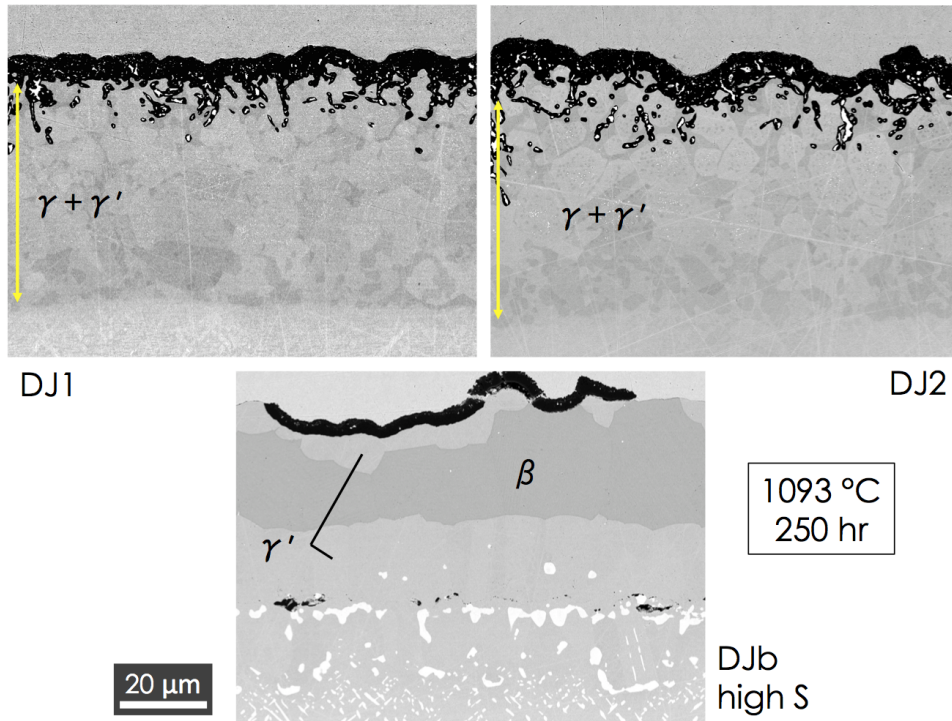


Figure 3.1: Cross sections of the experimental coatings after isothermal oxidation for 250 h at 1093 °C.

Both the DJ1 and DJ2 coatings exhibited significant growth of  $\text{HfO}_2$  particles both within and below the alumina scale. The volume fraction of  $\text{HfO}_2$  particles in the DJ1 TGO after 250 h at 1163 °C was estimated to be about 7% using image analysis methods

of 20  $\mu\text{m}$  of scale length in metallographic cross sections. The room temperature elastic modulus of  $\text{HfO}_2$  is around 200 GPa [96], which is approximately half the modulus for  $\alpha$ - $\text{Al}_2\text{O}_3$ . A Reuss model can be used to calculate the effect the embedded  $\text{HfO}_2$  particles have on the composite TGO modulus.

$$\frac{1}{E_c} = \frac{(1 - V_p)}{E_m} + \frac{V_p}{E_p} \quad (3.2)$$

where  $E_c$  is the composite modulus,  $V_p$  is the particle volume fraction,  $E_m$  is the matrix modulus, and  $E_p$  is the particle modulus. With 7% volume fraction of  $\text{HfO}_2$  particles in an  $\text{Al}_2\text{O}_3$  matrix, this gives a room temperature composite modulus of about 350 GPa down from 375 GPa for a pure  $\text{Al}_2\text{O}_3$  TGO. Combining both the effects of  $\text{Al}_2\text{O}_3$  porosity and  $\text{HfO}_2$  particles gives a porous TGO composite modulus estimate of 340 GPa, which is about 10% lower than a pure, dense  $\text{Al}_2\text{O}_3$ . The implication is that the TGO strain energy release rate will be about 10% lower for these  $\gamma'$  coatings than for the  $\beta$  coating with the same TGO thickness as per Equation 1.1.

Selective internal oxidation of elements with a very high oxygen affinity, such as Hf, is common in these types of alloys [97–99]. There is evidence that increasing the concentration of Cr or adding Pt to the coating may help to eliminate this presumably detrimental behavior. Regardless, these  $\text{HfO}_2$  particles that oxidize near the bottom of the TGO and protrude into the bond coat are known as pegs or stringers; it is still somewhat ambiguous as to whether or not these stringers are helpful or harmful [100]. On one hand, the oxide stringers provide physical interlocking between the TGO and the bond coat, potentially improving the adhesive strength of the TGO [101]. On the other hand, the protrusions can act as stress concentrators from which to nucleate cracks in the TGO during heating and cooling. The net effect has not been systematically studied to date.

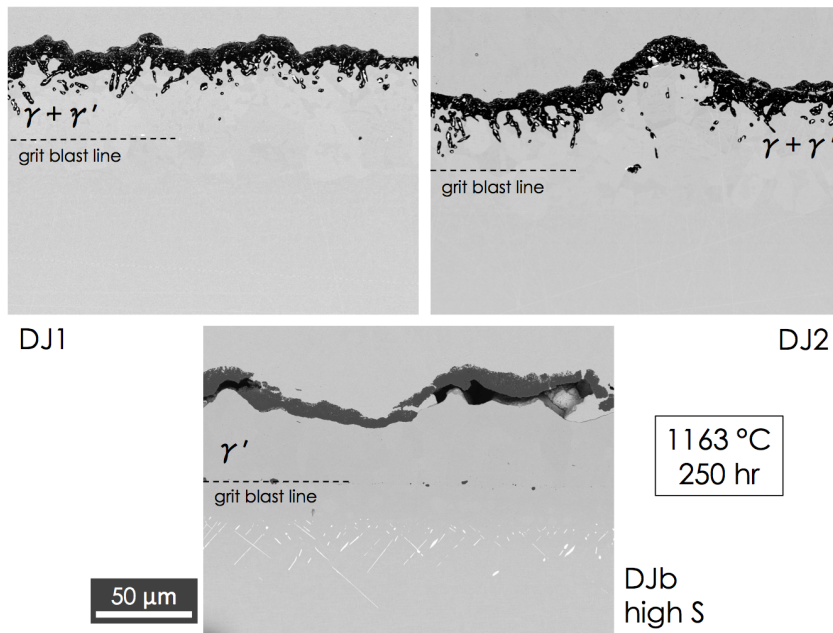


Figure 3.2: Cross sections of the experimental coatings after isothermal oxidation for 250 h at 1163 °C.

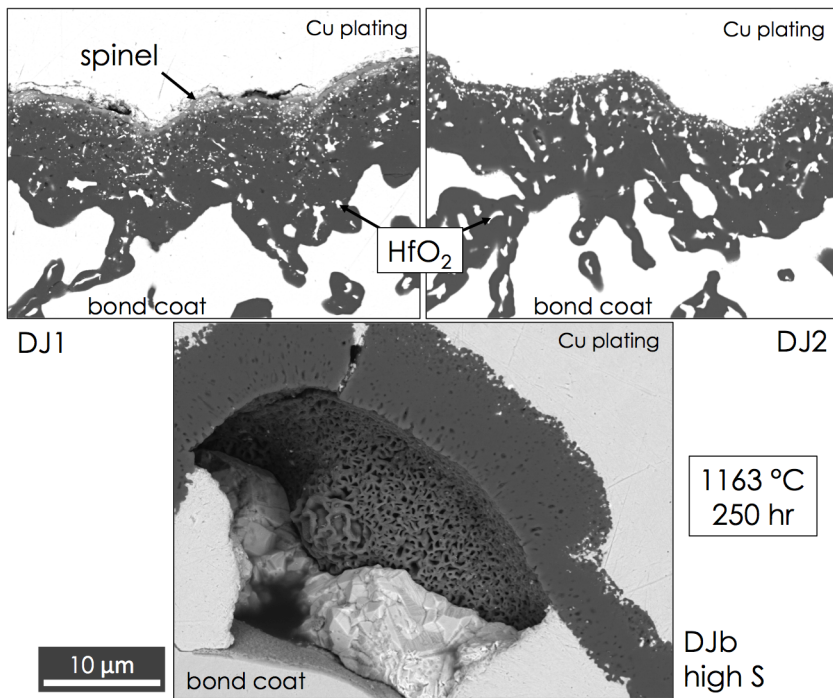


Figure 3.3: Enlarged views of the thermally grown oxides from the cross sections of the experimental coatings after isothermal oxidation for 250 h at 1163 °C.

Figures 3.2 and 3.3 show cross sections of the monolithic coatings after 250 h of isothermal oxidation at 1163 °C. This is same temperature at which the furnace cycle tests with a YSZ topcoat, described later in the chapter, were conducted. Again, the behavior of the  $\gamma'$  coatings, DJ1 and DJ2, is similar to that observed at 1093 °C. The thermally grown oxide on the  $\beta$  coating undergoes a phenomenon known as wrinkling at this temperature [93]. Wrinkling occurs when the compressive strain energy in the TGO due to the lateral growth exceeds the bending stiffness of the TGO at temperature and causes out-of-plane buckling of the TGO. The TGO-bond coat interface toughness must be low, such as in this case with the high-S  $\beta$  coating. As a result, there is a significant amount of TGO detachment and out-of-plane growth with a 10-20  $\mu\text{m}$  wavelength. This type of behavior is distinguished from rumpling because the TGO deformation is not associated with large-scale bond coat deformation as it is in rumpling. The enlarged view of the TGO in Figure 3.3 shows that the TGO is thicker and more porous over the wrinkle detachments in the DJb coating where growth via vapor phase transport of Al has occurred, compared to the right side of this figure where the TGO remained attached. Otherwise, the TGO on the DJb coating is generally thinner than the TGO on the two  $\gamma'$  coatings.

The behavior of TGO on the DJb(high-S) coating is an interesting example of the relationship between wrinkling and rumpling. Figure 3.4 shows the thermally grown oxide after 50 and 150 h at 1204 °C. The upper micrograph, at 50 h, still exhibits the  $\beta$ -phase with small pockets of  $\gamma'$  whereas the entire coating has converted to  $\gamma'$  by 150 h in the lower micrograph. The top image shows a degree of long-wavelength rumpling where the growth of the TGO has caused plastic deformation of the bond coat compared to the as-coated condition shown in Figure 2.9, in accordance with observations reported previously [42]. Both the bond coat and TGO have low creep strength at this temperature [11, 24]. There are small pockets of  $\gamma'$  in the bond coat near the surface of

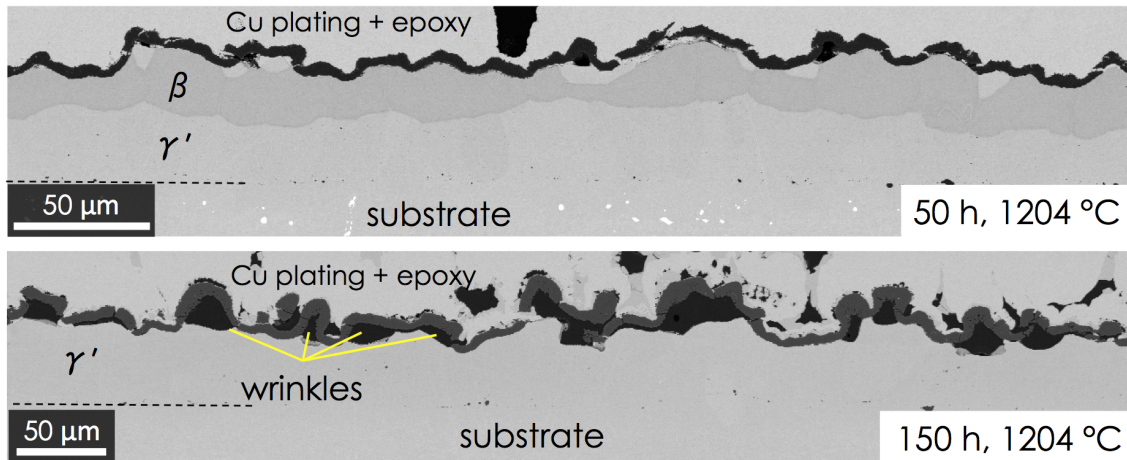


Figure 3.4: Cross sections of the DJb (high-S) coating after isothermal oxidation for 50 and 150 h at 1204 °C.

the TGO that are accompanied by some small detachments/wrinkles in the TGO. The bottom micrograph is in stark contrast to the first in that the majority of the bond coat has detached from the bond coat and wrinkled out of plane. This appears to have occurred once the entire bond coat has converted to the higher-strength  $\gamma'$  phase. The TGO buckles out of plane once the bond coat will not accommodate the extensive lateral TGO growth. Once the TGO detaches from the coating, it continues to grow through vapor-phase transport of cations from the coating, hence the thicker and more stringy appearance of the detached scale. This gives the TGO the thicker and more porous/stringy appearance, such as seen on the underside of the enlarged image in Figure 3.3. It is also possible that wrinkling is caused by a difference in the TGO lateral growth strains when growing on the  $\beta$  compared to the  $\gamma'$  phase. If the lateral growth rate is much higher once the coating has converted to  $\gamma'$ , then this would provide an adequate driving force for wrinkling. It is possible that the decrease in Al-activity during the  $\beta \rightarrow \gamma'$  transformation causes TGO growth to be dominated on the lateral grain boundaries and bottom of the scale, which could increase the growth stress. However, a decrease in high-temperature creep strength

as the coating transforms from NiAl to Ni<sub>3</sub>Al is the most satisfactory explanation for the TGO out-of-plane wrinkling on top of the  $\gamma'$ -phase coating.

### 3.1.1 Oxidation rate

A direct means of comparing the oxidation rates of the experimental coatings is use of a temperature-dependent parabolic fit to the the oxide thickness as a function of time. This relationship works well for passivating scales because the oxidation rate, hence the oxide growth rate  $dh/dt$ , is a linear function of the oxide thickness,  $h$  [94].

$$\frac{dh}{dt} = k'h \Rightarrow h^2 = \frac{k't}{2} \quad (3.3)$$

where  $t$  is the time and  $k'$  is a parabolic oxidation rate constant. The temperature,  $T$ , dependence to the oxidation rate constant can be expressed with an Arrhenius relationship as:

$$\frac{k'}{2} = k \exp\left(\frac{-Q}{RT}\right) \quad (3.4)$$

where  $k$  is the pre-exponential factor,  $R$  is the ideal gas constant, and  $Q$  is the apparent activation energy for oxidation [94]. This gives a final function in traditional form for the oxidation rate of the three coatings as

$$h^2 = k \exp\left(\frac{-Q}{RT}\right)t \quad (3.5)$$

In Equation 3.5, there are two fitting parameters:  $Q$  and  $k$ . The thickness measurements of the three coatings taken from the four combinations of time and temperature result in experimental fits shown in Figure 3.5. The results of the least squares fit to Equation 3.5 is shown in Table 3.1. The best fit to this limited set of data indicates that the oxidation rate of DJb is significantly lower and less sensitive to temperature than both of the

$\gamma'$  coatings, DJ1 and DJ2. Experimentally, this is validated because the average TGO thickness on the DJb coating was the smallest for all four experiments. The two  $\gamma'$  coatings have an oxidation rate that is similar, although the DJ1 is more temperature sensitive.

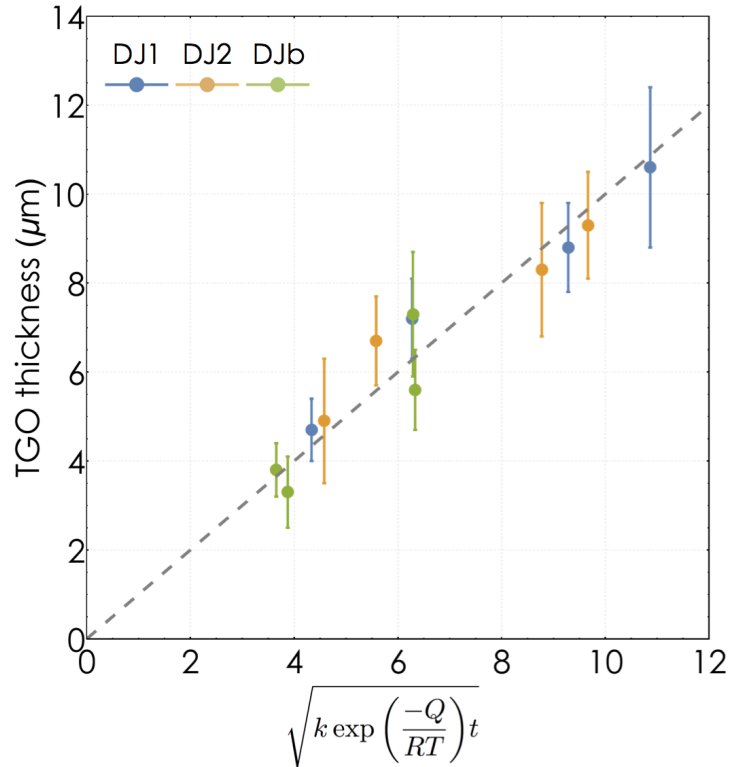


Figure 3.5: TGO thickness as a function of oxidation time for four experiments: 1093 °C (250 h), 1163 °C (250 h), 1204 °C (50 h), and 1204 °C (150 h). Error bars represent the standard deviation of all the measurements of the TGO thickness made from each sample. The data were fit simultaneously to Equation 3.5 and the results are shown in Table 3.1.

In summary, it has been shown that the isothermal oxidation rate of the two  $\gamma'$  coatings is higher than the  $\beta$  coating. The DJ1 and DJ2 coatings grow thicker scales that are predominantly  $\text{Al}_2\text{O}_3$  with embedded  $\text{HfO}_2$  particles and some finite porosity that is likely due to the  $\theta \rightarrow \alpha\text{-Al}_2\text{O}_3$  transition, which results in a volume contraction. The thinner oxide scale on the  $\beta$  coatings grows more slowly, but is also susceptible to rumpling and wrinkling due to the low strength of the NiAl layer and stiffness of the

Table 3.1: Fitting parameters for the temperature-dependent parabolic oxidation rate Equation 3.5 for the three monolithic experimental coatings.

	k (cm <sup>2</sup> /s)	Q (kJ/mol)
DJ1	7.8	355
DJ2	$8.9 \times 10^{-2}$	303
DJb	$7.1 \times 10^{-5}$	226

TGO film. This scale rumples the  $\beta$  bond coat under isothermal conditions and then the TGO wrinkles once the coating transforms to the  $\gamma'$  phase. The  $\gamma'$  coatings do not exhibit rumpling or wrinkling, but the DJ1 coating has a thin layer of spinel  $\text{NiAl}_2\text{O}_4$  on top of the  $\text{Al}_2\text{O}_3$  at all temperatures. Isothermal oxidation tests alone are not enough to determine which coating will perform best in a TBC system. It is not straightforward to assess whether the spinel growth or rumpling and wrinkling is more deleterious. Cyclic oxidation tests provide additional insight into the behavior of these coatings as explained in the following sections

## 3.2 Thermal expansion measurements

The coefficient of thermal expansion (CTE) mismatch with the substrate is an important parameter to consider when evaluating the rumpling behavior of a coating, as explained in Chapters 1 and 2. For this reason, CTE measurements of a bulk ingot with composition similar to DJ1 were made on two separate specimens. The ingot was cast and then heat treated in air for 250 h at 1100 °C to homogenize the microstructure. The sample was furnace cooled after annealing. Cross section micrographs indicated that the as-annealed microstructure contained about 10% residual  $\beta$ -phase after the slow cooling. Cylindrical specimens were cut from the ingot with an electro discharge machine (EDM) with  $\varnothing \approx 9.5$  mm and 25.4 mm in length. The samples were then ground and polished to

a 1200 grit finish with SiC paper to remove any EDM-affected material. Measurements of the CTE were made using an Orton 2016HU dilatometer with a sealed quartz tube. A reducing gas mixture of Ar+5% H<sub>2</sub> was used to limit oxidation during the measurements. Heating and cooling rates were 3 °C/min from 25-1150 °C. Each sample was measured at least three times, and the measurements are shown in Figure 3.6 in comparison to the René N5 CTE from [102].

The CTE has a constant slope for the DJ1 composition because these samples are monolithic  $\gamma'$ -phase, whereas the CTE of René N5 increases rapidly above 900 °C as the  $\gamma'$ -phase dissolves into solution of the  $\gamma$  matrix. Because the CTE of the  $\gamma'$  coating is very similar to the substrate in these experiments, it is expected that the stress in the coating will be very low except at temperatures above 900 °C, where the CTE mismatch will put the bond coat into tension as the substrate expands more quickly. The average CTE of the DJ1 coating at 1150 °C is about 15.8 ppm/°C, compared to 17.5 for the René N5 substrate.

### 3.3 Rumpling quantification

The primary motivation for bond coat cyclic oxidation testing without the ceramic topcoat is to clearly assess the rumpling and oxidation behavior of the bond coat. Again, TBC failure from rumpling results from the displacement of the bond coat away from the TBC; therefore, characterization of the evolution of the bond coat surface topography is of interest. Optical profilometry has been employed to nondestructively measure the bond coat surface as rumpling progresses with continued thermal cycling. Unfortunately, many of the recently-developed creep-resistant bond coats have oxidation performance

---

<sup>1</sup>A substantial portion of the material in this section is reproduced from reference [103] *A Robust Technique to Characterize Rumpling in Next-generation High-strength Bond Coats* by Jorgensen, Jackson, and Pollock submitted to Surface and Coatings Technology in 2016

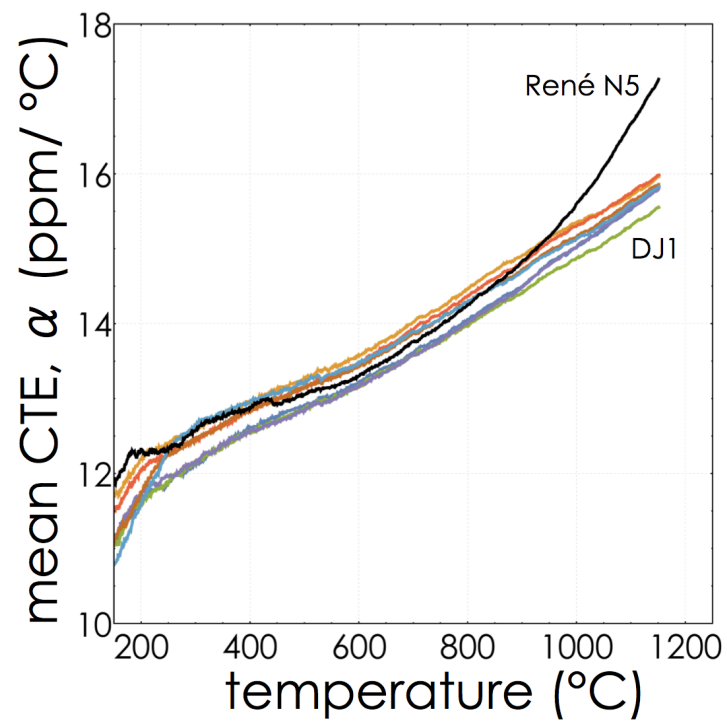


Figure 3.6: Coefficient of thermal expansion measurements of two separate samples of polycrystalline specimens with the DJ1 composition in comparison with a René N5 measurement from [102].

that is less optimal than the present industry standards, MCrAlY and platinum-modified aluminide (Pt,Ni)Al [51, 53, 65, 90, 97–99]. Poor oxidation behavior is often manifested as the growth of mixed oxide TGOs, with HfO<sub>2</sub> pegs and spinel NiAl<sub>2</sub>O<sub>4</sub> oxides forming in combination with the preferred Al<sub>2</sub>O<sub>3</sub> scale.

The majority of studies investigating rumpling have been performed on bond coats that exclusively form an Al<sub>2</sub>O<sub>3</sub> TGO. In these systems, measurements of the TGO surface directly indicates the displacement of the bond coat surface because the TGO surface follows the bond coat topography. The difficulty herein lies in characterizing the extent of bond coat displacement (rumpling) a particular coating exhibits during cyclic oxidation when the TGO is not of uniform thickness or structure. Common methods of measuring bond coat rumpling nondestructively, including measurements of the change in surface roughness or surface tortuosity [38], tend to fail when the scale of the structural inhomogeneities in the coating are of the same magnitude as the rumpling deformation being characterized, as will be demonstrated. That is to say, surface roughness and tortuosity measurements can be misleading because a plan view (top down) measurement of the surface roughness will be as sensitive to non-uniform oxide growth as it is to the systematic and periodic deformation of the bond coat. Accurate measurements of bond coat rumpling are critical for coating design, which requires a balance between strength and oxidation behavior to maximize TBC life. Experimental measurements such as surface roughness that indicate an increased surface roughness (and therefore increase in apparent rumpling) due to *both* bond coat deformation and non-uniform oxidation serve only to obfuscate the behavior of the coating. Further, a method that allows for rapid verification of rumpling nondestructively is of interest for high-throughput assessments of bond coats during development.

An example of the inefficacy of traditional surface descriptors, such as root-mean-square (RMS) roughness ( $S_q$ ), to indicate rumpling during thermal cycling tests is shown

in Figure 3.7. This figure shows the change in RMS roughness of high-strength  $\gamma'$  coating (DJ1) is similar to (Pt,Ni)Al for the first 200-300 cycles. The cross sections of the coatings, Figure 3.8, clearly show that the  $\gamma'$  coating did not rumple while the (Pt,Ni)Al is subject to significant rumpling. The surface roughness change for the  $\gamma'$  coating is primarily from inhomogeneous oxide features, such as shown in the inset of Figure 3.7. A technique to isolate the surface roughness contributions of periodic bond coat rumpling from effects such as non-uniform TGOs and missing data is needed in order to quantitatively measure the rumpling behavior of a bond coats.

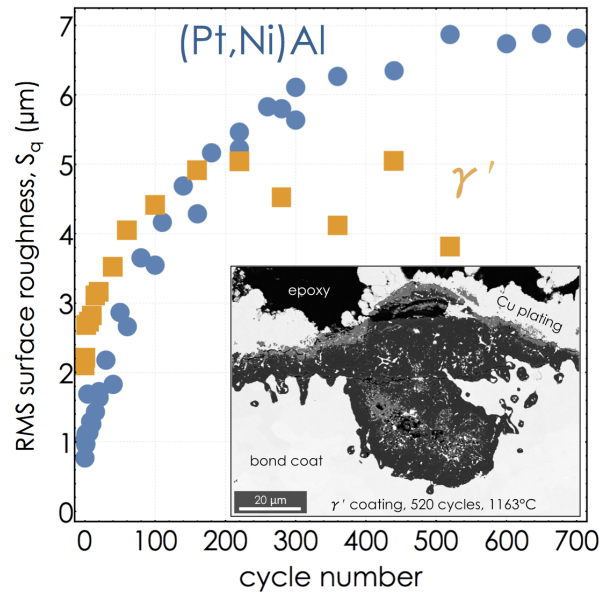


Figure 3.7: Comparison of the measured surface roughness of DJ1, a high-strength experimental coating and (Pt,Ni)Al coating. Inset shows an example of inhomogeneous oxide features that increases the surface roughness of the  $\gamma'$  coating. Cross sections of these coatings are shown in Figure 3.8.

To these ends, a nondestructive method of analyzing and quantifying rumpling from 2D optical profilometer data has been developed. The method described employs a Fourier transform (FT) as a means of filtering out the “noise” from other phenomena that influence the surface roughness in an oxide scale, caused by actual measurement noise, missing data, or non-homogeneous oxidation. This method is benchmarked, using

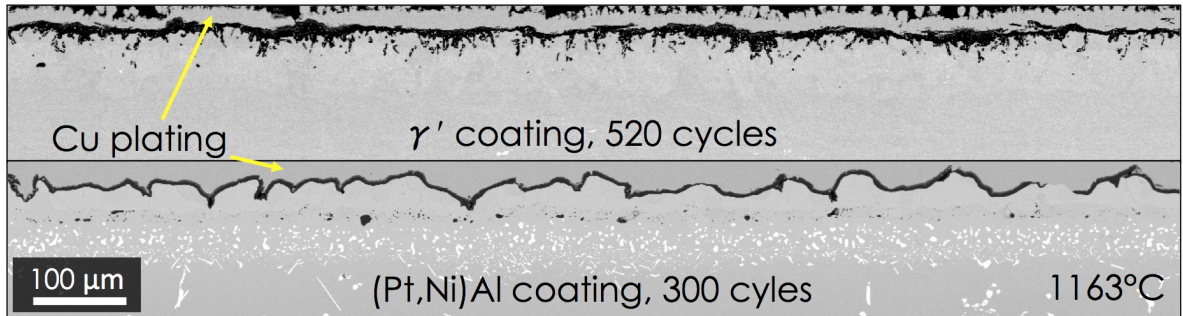


Figure 3.8: Cross sections of a high-strength experimental coating and (Pt,Ni)Al coating discussed in [90]. The (Pt,Ni)Al coating exhibits clear rumpling whereas the  $\gamma'$  DJ1 coating does not, although they have a similar RMS surface roughness of about 4-5  $\mu\text{m}$  (Figure 3.7).

synthetic datasets, against typical surface roughness variables average roughness  $S_a$  and tortuosity, which are commonly used to quantify rumpling. The FT algorithm is found to be equally useful as  $S_a$  at characterizing rumpling in coatings that have good oxidation properties and a uniformly deforming scale. However, when the coatings have complex oxidation behavior, the FT method far outperforms the benchmark descriptors in differentiating between surface features resulting from oxide inhomogeneities and bond coat deformation (rumpling).

### 3.3.1 Synthetic datasets for benchmarking

Synthetic surface profile datasets were employed to approximate the topologies that oxidizing bond coats exhibit and to test the FT approach. These datasets are kept mathematically simple so that trends are straightforward, yet complex enough to capture the important characteristics of rumpling and the inhomogeneous aspects of irregularly oxidizing surfaces. The synthetic profile datasets consist of 2D sinusoidal components to represent systematic bond coat undulations and collections of randomly located Gaussian profiles to represent the “asperities” resulting from  $\text{HfO}_2$  pegs and spinel oxides forming on the surface of the alumina scale as well as an initial grit-blasting surface treatment.

All synthetic datasets are square matrices with 2000 elements (pixels) on each side. This dataset is representative of a surface scan that is  $2 \times 2$  mm using an optical profilometer with a lateral resolution of  $1 \mu\text{m}$ . Two different sinusoidal rumpling matrices were used – the first matrix, [*RumpMix*], was composed of fifteen each of 2D sinusoids with periods of 25, 50, and 100 pixels randomly rotated and averaged together. Each individual sinusoid was calculated as

$$z(x, y) = \sin \left[ \frac{2\pi}{P} (x \cos \theta + y \sin \theta) \right]$$

where  $P$  is the period,  $x$  and  $y$  are the pixel coordinates, and  $\theta$  is an angle randomly selected between 0 and  $2\pi$ . The second rumpling matrix, [*Rump100*], was calculated as above, but with 45 sinusoids all having a period  $P = 100$  pixels. The amplitude of these matrices is then modified linearly, as explained later; the amplitude is relative to multiples of the instrument vertical resolution in a measurement and therefore dimensionless. A visual representation of the rumpling matrices is shown in Figure 3.9 in comparison with a cyclically oxidized (Pt,Ni)Al coating. The reason for two rumpling matrices is to demonstrate that while the method works well in analyzing a realistic bond coat system that is expected to rumple with a single primary wavelength (determined by the TGO thickness and elastic properties [31]), the method also works well to identify specific individual contributions from other periodic and systematic effects that have the same spatial separation as random asperities. In the case of higher-order rumpling (shorter wavelengths and higher frequencies), the surfaces begin to look to the human eye similar to a surface that is spontaneously rough from oxidation. However, the power of the Fourier transform clearly distinguishes these two effects, as will be demonstrated.

The surface asperity matrices were generated using a multitude of 2D Gaussian profiles:

$$z(x, y) = A \exp \left[ \frac{-x^2}{2\sigma^2} - \frac{y^2}{2\sigma^2} \right]$$

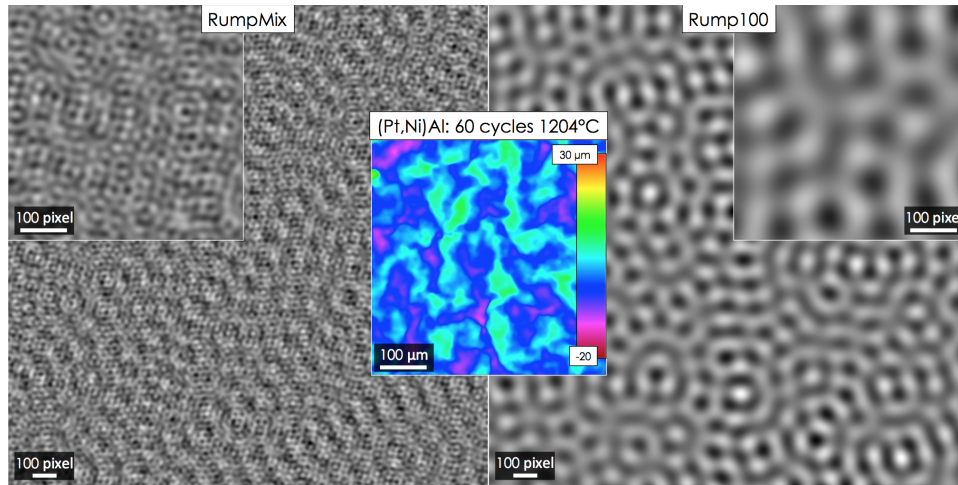


Figure 3.9: Images of matrices representing the rumpling profiles. Images have been scaled to the range 0-255 for visualization. Upper insets show the details of the the upper left  $500 \times 500$  pixel region of each matrix. Central inset is an optical profilometer measurement example of a (Pt,Ni)Al coating after 60x 45-minute cycles at 1204 °C.

where  $\sigma$  is a width parameter randomly selected between 0 and 7, and  $A$  is the height of the asperity randomly selected between 0 and 15. For the first asperity matrix,  $[Asper1]$ , individual Gaussian functions were randomly generated within a  $25 \times 25$  pixel subset and then ten thousand of these were randomly placed into a  $2000 \times 2000$  element matrix. The  $25 \times 25$  matrix was used for computational efficiency to cut off the infinitesimal Gaussian tails at a finite distance. The second asperity matrix,  $[Asper3]$ , was a manipulation of  $[Asper1]$  such that  $[Asper3] = [Asper1] + (0.67)\text{Flip}([Asper1]) + (0.33)\text{Shift}([Asper1])$ , where  $\text{Flip}(X)$  reverses the order of the matrix rows and  $\text{Shift}(X)$  swaps diagonally the four quadrants of the matrix. A visual representation of the asperity matrices is shown in Figure 3.10 in comparison with a cyclically oxidized  $\gamma'$  bond coat.

A similar generation procedure to  $[Asper1]$  was used to approximate a surface that was initially grit blasted before oxidation, as is commonly performed before experiments. (Grit blasting is used before TBC deposition to ensure mechanical bonding with the ceramic topcoat and promote  $\alpha\text{-Al}_2\text{O}_3$  formation during service [104].) The sole difference is that one hundred thousand random Gaussian distributions were used. A  $500^2$  pixel

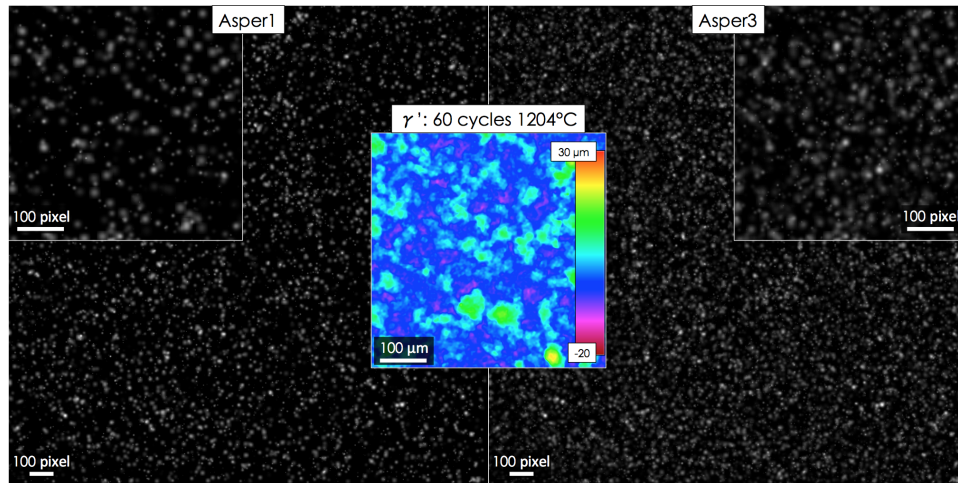


Figure 3.10: Images of matrices representing the asperity matrices [*Asper1*] and [*Asper3*]. Images have been scaled in range 0-255 for visualization and are therefore dark where the amplitude is very low. Upper insets show the details of the the upper left  $500 \times 500$  pixel region of each matrix. Central inset is an optical profilometer measurement example of an experimental  $\gamma'$  coating after 60x 45-minute cycles at 1204 °C.

portion of this matrix, [*GritBlast*], is visually represented in Figure 3.11. Increasing the density of simulated asperities by an order of magnitude has the effect of creating a more consistently rough surface finish due to overlapping Gaussian distributions rather than a collection of disperse asperities.

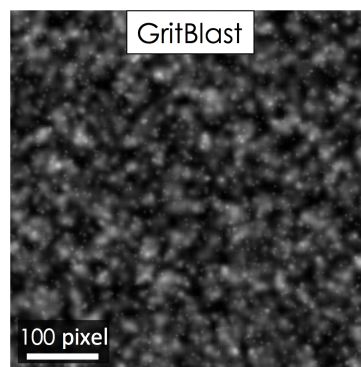


Figure 3.11: Visual representation 1/16th of the matrix used to represent grit blasting. Image dimensions correspond to the insets in Figures 3.9 and 3.10.

Linear combinations of the matrices described above are used to simulate the behavior of rumpling and oxidation observed in cyclic oxidation experiments of bond coats. As

an example, an initially grit-blasted and oxidized surface is mathematically represented as  $[GritBlast] + [Asper1]$ . A highly-rumpled surface is represented as  $[GritBlast] + [Asper1] + (20)[RumpMix]$ , and a surface with a high density of surface asperities from oxides and a small amount of rumpling could be described as  $[GritBlast] + (10)[Asper3] + (2)[RumpMix]$ .

### 3.3.2 Fourier transform algorithm for quantifying rumpling

Characterization of rumpling of surface profiles is performed with a custom-coded *Mathematica* program to calculate and analyze Fourier transforms (FTs) of the surface profiles. An example of this algorithm is in Appendix A.4. The FT represents the spectrum of sinusoidal components needed to represent the surface topology. The data from an optical profilometer scan of any size is directly converted to a 2D matrix of height values with a known lateral resolution. The algorithm to analyze a single matrix representing a surface profile during cyclic oxidation follows these steps:

1. Pad the outside of the matrix with zeros to be any desired even-dimension that is square (e.g.  $2000 \times 2000$  pixels)
  - (a) The final interpolation density (pixel resolution) of the points in frequency-space is limited by the number of points in the padded matrix such that:  $df = \frac{1}{N\delta x}$  where  $df$  is the frequency resolution,  $N$  is the number of points along an edge of the padded square matrix, and  $\delta x$  is the real-space lateral resolution of the data from the profilometer.
  - (b) Zero-padding is mathematically equivalent to heterodyning, which is another means of increasing interpolation density of discrete FTs by incorporating small frequency shifts to the raw data [105]. Padding is used because it is

straight-forward to understand and conceptualize at the expense of being only slightly more computationally intensive.

2. The 2D non-normalized Fourier transform is calculated from the padded matrix. If the matrix dimensions are of the form  $N = 2^n$  where  $n$  is any positive integer, then the Fast Fourier Transform (FFT) algorithm may be used, resulting in a small increase in computation speed.
3. The quadrants of the resulting matrix are diagonally swapped so that the low-frequency information that was originally in the four corners is now centered in the matrix.
  - (a) This process moves the direct current (DC) element of the matrix to position  $(x_{DC}, y_{DC}) = (N/2 + 1, N/2 + 1)$ . The DC value is the mean height of the profile, a global up/down shift of the data.
4. The radial average, centered about the DC element, is calculated. Each pixel is located  $r = \sqrt{(x_k - x_{DC})^2 + (y_i - y_{DC})^2}$  away from the center, where  $x_k$  and  $y_i$  are the coordinates of the  $k^{\text{th}}$  and  $i^{\text{th}}$  elements along the rows and columns.
  - (a) Radii that are fractions of a pixel are rounded to the nearest tenth pixel.
  - (b) Calculating the mean value of all the pixels that are equidistant from the center is a computationally expensive calculation for large matrices. A list of equidistant pixels and their associated radii is pre-calculated for efficiency and loaded into RAM when needed.
  - (c) Symmetry/periodicity of the FT allows for only one half of the matrix to be radially averaged.

5. The lists of radially averaged values and their distance from the DC center are exported for further processing and visualization. The distance of the  $k^{\text{th}}$  pixel from the DC center is used to compute its frequency as  $f_k = r_k/(N\delta x)$
6. For a cyclic oxidation experiment where it is desired to measure the progression of rumpling, the radially averaged FT of cycle  $j$  can be normalized by the radially averaged FT before oxidation as  $FT_j/FT_0$ . This allows the evolution of the surface profile to be quantified, resulting in a relationship of the increase in periodic surface amplitude as a function of frequency/wavelength.
7. For heavily padded matrices, there can be a lot of noise in the normalized profiles due to rounding of pixel fractions pixel-pixel measurement variations. This is simply addressed with a weighted moving average of the profile.

### **Applying the FT algorithm to base matrices**

The FT algorithm is applied to the [*RumpMix*] and its individual component datasets described in Section 3.3.1 and the results are shown in Figure 3.12. The inset shows the central  $200^2$  pixels of the FT before radially averaging, where the rings belonging to the individual periods are visible. The three peaks of the component sinusoids, corresponding to wavelengths of 25, 50, and 100 pixels, are clearly visible in the radial average of [*RumpMix*], shown in black, which has a lower amplitude than the three component matrices because it is composed of an average of the three components. The sharpness of the peaks, generally only three or four points wide, occurs because the synthetic datasets are made up of 2D sinusoids with exactly the same periods periods. The peak width in an actual rumpling bond coat would be more broad due to the presence of a distribution of active wavelengths centered about a primary rumpling wavelength [31].

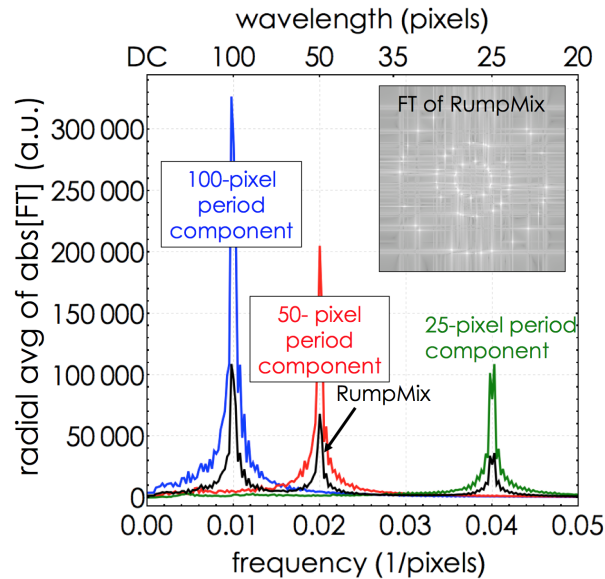


Figure 3.12: The results of the FT algorithm applied to the three individual components of the  $[RumpMix]$  matrix, having periods of 25, 50, and 100 pixels and FT algorithm applied to  $[RumpMix]$  itself showing features from the periodic signals.

Applying the FT algorithm to the  $[Asper1]$ ,  $[Asper3]$ , and  $[GritBlast]$  synthetic matrices, it is seen that there are no clear peaks in the radial averages shown in Figure 3.13. There is no definition or features visible in the FT in the inset. In general, increasing the amplitude and quantity of random asperities does not produce a peak in the FT at any specific wavelength. Instead, there is a global increase in FT amplitude due to the increased magnitude of sine waves needed to represent a surface with an overall larger amplitude.  $[Asper3]$ , with about three times the number of asperities as  $[Asper1]$ , has a slightly larger amplitude, while  $[GritBlast]$ , with an order of magnitude more asperities, has the highest amplitude throughout the spectrum. The small peaks that appear in the line graphs are only single points and are representative of noise, not a systematic stabilization of a specific frequency. In general, a high amplitude at low frequencies (long wavelengths) that is monotonically decreasing toward higher frequencies is a typical characteristic of a random surface finish [106].

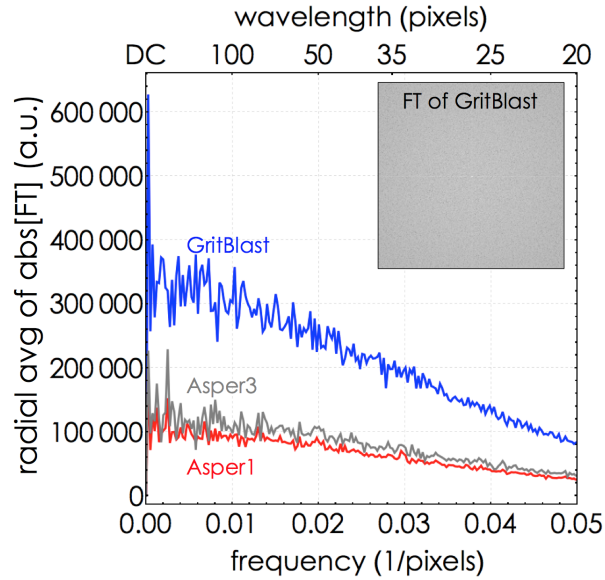


Figure 3.13: The results of the FT algorithm applied to the  $[Asper1]$ ,  $[Asper3]$ , and  $[GritBlast]$  matrices. Inset shows the characterless nature of the central  $200^2$  pixels in the FT of  $[GritBlast]$  before radially averaging.

### 3.3.3 Benchmarking FT algorithm against standard parameters

#### Detection of rumped bond coats

The efficacy of the FT algorithm at identifying and quantifying rumpling is compared against the standard surface profile measures commonly used for rumpling:  $S_a$  (Eq. A.1),  $S_q$  (Eq. A.2), and the surface tortuosity (Eq. A.3) using two experiments with the synthetic datasets. The first experiment represents a grit-blasted surface that develops small oxidation asperities and rumples continuously. This is mathematically represented as  $z(x, y) = [GritBlast] + [Asper1] + (Amp)[RumpMix]$  where the value of  $Amp$  is continuously increased. Another assessment is also conducted, substituting in  $[Rump100]$  and  $[Asper3]$  respectively. The simplest metric used to quantify the development of rumpling with the FT algorithm is the value of the maximum peak height minus the noise floor at high frequencies. In a real experiment, this peak would be compared to either the initially grit-blasted surface or the surface after a single cycle once the base

TGO has developed. It is easier for all rumpling descriptors to quantify changes in rumpling when the reference scan includes the oxide asperities because this minimizes the amount the surface changes between the reference state and subsequent measurements. For demonstrative purposes, this method is used for calculating the surface roughness, while the FT algorithm is normalized by only the [*GritBlast*] matrix in step 6 of the algorithm (using the less-advantageous reference state before the asperities have developed). This choice means that the traditional surface roughness descriptors have a decided advantage because the FT algorithm must also filter out the effect of the asperities. That is to say, the normalization in the FT algorithm is taken as  $FT([GritBlast])$  and then the evolution of this parameter is represented as:

$$\Delta FT^{peak} = FT_i^{peak} - FT_0^{peak} \quad (3.6)$$

$$FT_i^{peak} = Max(FT_i) - [Mean(FT_i)]_{\lambda=8}^{20 \text{ pixels}} \quad (3.7)$$

where  $FT_0^{peak}$  is calculated when  $Amp = 0$ , and  $i$  represents successive values of  $Amp$ . The value of  $FT^{peak}$  is taken from a peak with at least 2 pixels in width. The noise floor is taken as the average of all data in the FT with a wavelength,  $\lambda$ , between 8 and 20 pixels. The max peak in the present synthetic datasets always corresponds to a 100-pixel wavelength due to the way the datasets were generated. The benchmark values of  $S_a$  (Eq. A.1) and  $S_q$  (Eq. A.2) are closely related and follow the same trends for these experiments. For clarity, only the change in  $S_a$  will be plotted as  $\Delta S_a = S_{a,i} - S_{a,0}$ .

An example of the effect this simulation has on the surface topology for three values of  $Amp$  is shown in Figure 3.14. The initial value of the surface roughness is  $S_a = 8.27$ . This example shows the total roughness of the sample is increasing and there are more pixels with a high Z-value as the value of  $Amp$  increases. However, even by  $Amp = 50$ , the surface is not obviously rumpled to the naked eye as in the central inset of Figure 3.9.

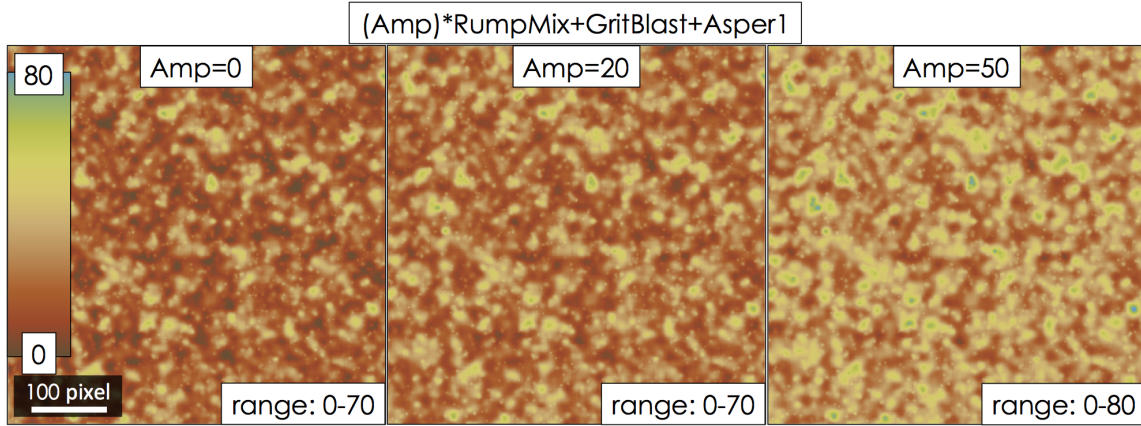


Figure 3.14: Top left corner of the  $500 \times 500$  pixels of the  $[GritBlast] + [Asper1] + (Amp)[RumpMix]$  for  $Amp = 0, 20, 50$ . All images use the same topological color scaling for  $Z$ -value.

A comparison of the FT algorithm and  $S_a$  is shown in Figure 3.15 as a function of  $Amp$  for the two different rumpling matrices. This plot shows that the FT algorithm is, at the very least, as effective as  $S_a$  at measuring rumpling. For the  $[RumpMix]$  matrix, both of the descriptors are about equal, showing a marked increase from their initial value around  $Amp = 10 - 15$ . For the  $[Rump100]$  matrix, the FT algorithm detects rumpling earlier and is more sensitive to changes in the rumpled amplitude because all of the rumpled signal is concentrated at a single wavelength in  $[Rump100]$ . The amplitude of the real surface height is directly proportional to the peak height of an individual wavelength in the Fourier transform. When  $Amp = 100$ , the increase in  $S_a$  is about 3.5-fold for both rumpling matrices. This is an increase in “rumpling signal” of about 40%. On the other hand, the value of the FT algorithm is 3.1 and 8.5, indicating an increase in “rumpling signal” of about 1400 and 3800% because the initial  $FT_0^{\text{peak}}$  value is only 0.22. The surface tortuosity for these profiles (Eq. A.3) starts at 3.3 at  $Amp = 0$  and only increases to 4.4 and 3.5 for the  $[RumpMix]$  and  $[Rump100]$  matrices by  $Amp = 100$ . These small increases in tortuosity make this a poor indicator for rumpling of grit-blasted surfaces.

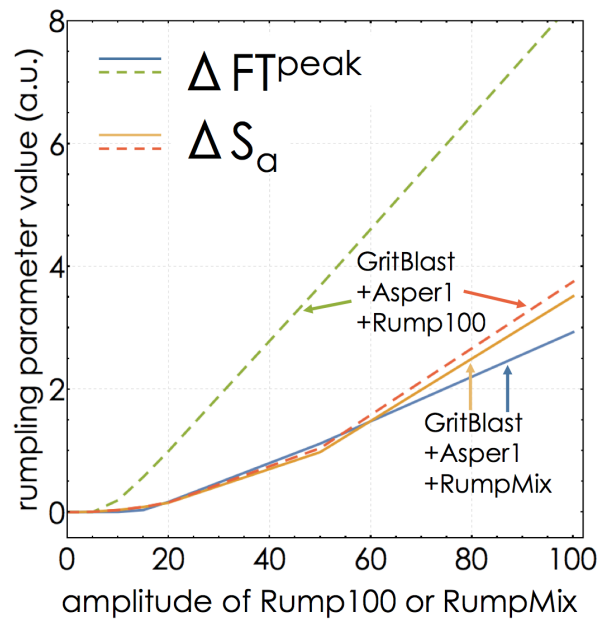


Figure 3.15: The change in “rumpling” parameters as a function of the amplitude of the rumpling matrices in the synthetic surface profiles  $[GritBlast] + [Asper1] + (Amp)[RumpMix]$  and  $[GritBlast] + [Asper1] + (Amp)[Rump100]$ .  $\Delta S_a$  is plotted as  $S_{a,i} - S_{a,0}$ , where  $S_{a,0} = 8.27$  when  $Amp = 0$ . And the FT algorithm is plotted as  $FT_i^{peak} - FT_0^{peak}$ , where  $FT_0^{peak} = 0.22$ .

### Avoiding false-positive indications of rumpling

It will now be shown that when there is no rumpling, but instead an increase in surface roughness only due to the formation of oxide asperities, the FT algorithm filters out the additional roughness whereas  $S_a$  calculations would indicate a false positive for rumpling. The matrix representations for this regime are  $[GritBlast] + (Amp)[Asper1]$  and  $[GritBlast] + (Amp)[Asper3]$ .

Figure 3.16 shows the effect of increasing the amplitude of the  $[Asper3]$  matrix. The initial surface roughness of  $[GritBlast]$  is  $S_a = 7.90$ . In contrast to Figure 3.14, only the amplitude of individual asperities is drastically increasing while the majority of the surface stays at the same level. When  $Amp = 50$ , the surface topology is reminiscent of the central inset of Figure 3.10.

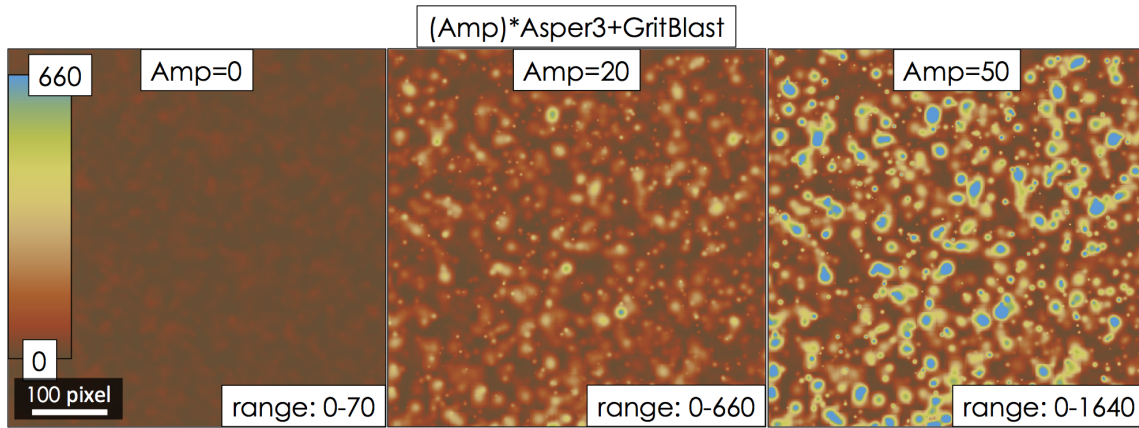


Figure 3.16: Top left corner of the  $500 \times 500$  pixels of the  $[GritBlast] + (Amp)[Asper3]$  for  $Amp = 0, 20, 50$ . All images use the same topological color scaling for Z-value. The scale for  $Amp = 50$  image is saturated at large values, where all values larger than 660 appear the same color.

A plot comparing the values of the rumpling indicators is shown in Figure 3.17, with  $\Delta S_a$  and  $\Delta FT^{peak}$  calculated as described above. The FT algorithm, which only measures an increase in the *periodic* surface amplitudes, is completely unaffected by aperiodic components of the surface for all amplitudes of  $[Asper1]$  or  $[Asper3]$ . On the other hand,

$S_a$  is a strong function of the amplitude of the asperity matrices. When  $Amp = 100$ ,  $S_a$  shows a false increase in rumpling of over 200, which is an increase of about 2500%. The value of  $S_a$  increases faster for the [Asper3] matrix because there are more total asperities. Comparing the surface tortuosity, the initial value is 3.1 at  $Amp = 0$  and the values of the tortuosity rapidly increase to over 70 at  $Amp = 20$  and reach over 1600 at  $Amp = 100$  for both matrices. Again, this indicates that surface tortuosity is too sensitive to random surface roughness stemming from oxide asperities, making it a poor rumpling indicator for coatings without a thin and homogeneous oxide scale.

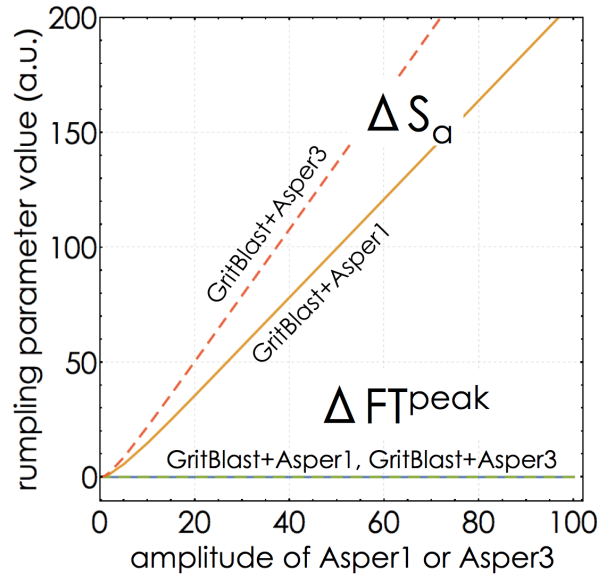


Figure 3.17: The change in “rumpling” parameters as a function of the amplitude of the Asperity matrices in the synthetic surface profiles [GritBlast] + (Amp)[Asper1] and [GritBlast] + (Amp)[Asper3].  $S_a$  is plotted as  $S_{a,i} - S_{a,0}$ , where  $S_{a,0} = 7.90$  when  $Amp = 0$ . The FT algorithm is plotted as  $FT_i^{peak} - FT_0^{peak}$ , where  $FT_0^{peak} = 0.00$ .

### Combinations of rumpling and oxide asperities

A comparison of rumpling quantification sensitivity will now be made for surfaces that are *both* covered in asperities and are rumpling during testing. The comparison is done with two combinations of matrices: [GritBlast] + (50)[Asper1] + (Amp)[RumpMix]

and  $[GritBlast] + (50)[Asper3] + (Amp)[Rump100]$ , where  $Amp$  is increased as before. The initial surface roughness is  $S_a = 108$  and  $145$  for the  $[GritBlast] + (50)[Asper1]$  and  $[GritBlast] + (50)[Asper3]$  matrices. Figure 3.18 shows a comparison of the FT algorithm with  $S_a$ . Because the initial surface roughness at  $Amp = 0$  is large, the data are presented as fractional increases from their initial value to give an indication of confidence each indicator conveys. When  $Amp = 200$ , the increase in  $S_a$  is less than 1% for both matrices and is still below 100% for  $Amp = 2000$ . In contrast, the FT parameter, which is plotted as the fractional increase in peak height, shows a much stronger indication of rumpling. The noise level is high and diminishes the relative values of peak signal-to-noise ratios with such large-amplitude asperities in this example. The fractional increase at  $Amp = 200$  would be multiple orders of magnitude larger if the FT radial average normalization in step 6 of the algorithm included the  $[Asper]$  matrices. As discussed above, the FT algorithm is much more sensitive to a single rumpling wavelength ( $[Rump100]$ ) than it is when multiple wavelengths are simultaneously active. In general, it is found that the FT algorithm gives a better indication of rumpling because it can filter out the surface profile contributions from asperities. Tracking values of  $S_a$  to indicate an increase in rumpling would be useless in this extreme case because the change in measurement value would be insignificant compared to the starting value.

### 3.3.4 Application to experimental bond coat systems

To show the utility of the FT algorithm, it is applied to optical profilometry data collected for a separate study [57]. The experimental  $\beta$ -phase coatings rumbled extensively during 1150 °C cyclic oxidation, regardless of composition. More information on the rumpling behavior can be obtained using the FT algorithm profile datasets collected to calculate the surface roughness,  $S_q$ . For simplicity, only the “5Pt” coating will be

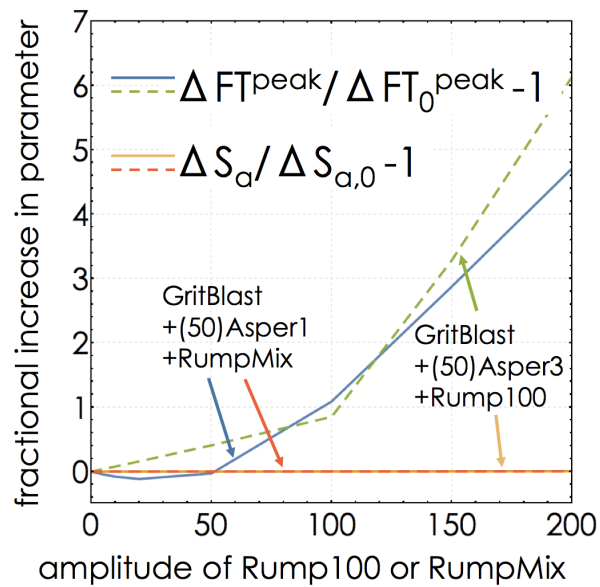


Figure 3.18: Comparison of the FT algorithm and  $S_a$  rumpling indicators for synthetic surface profiles  $[GritBlast] + (50)[Asper1] + (Amp)[RumpMix]$  and  $[GritBlast] + (50)[Asper3] + (Amp)[Rump100]$  for increasing values of  $Amp$  to simulate increased rumpling with significant oxide asperities.  $S_a$  is presented as the fractional increase from  $Amp = 0$  and the FT algorithm is presented as the fractional increase in peak height from  $Amp = 0$ .

discussed here. This sample was an overlay ion plasma discharge coating with a nominal composition of  $\text{Ni}_{55}\text{Al}_{34}\text{Cr}_6\text{Pt}_5\text{Hf}_{0.3}$  (in atomic %) [57]. The initial roughness of the sample after grit-blasting was approximately  $S_q = 2 \mu\text{m}$ . The sample was furnace cycled at  $1150 \text{ }^\circ\text{C}$  with a 45-minute dwell and  $200 \text{ }^\circ\text{C}/\text{min}$  heating and cooling rates. The lifetime of this coating, defined as the cycle at which net mass loss occurred, was about 1800 cycles. The primary rumpling wavelength peak height from the FT algorithm applied to profilometry measurements from this experiment is shown in Figure 3.19. Comparing this FT-based rumpling analysis with the mass change and surface roughness values shown in Figure 3.20, maximum rumpling occurs at the same point, 400-500 cycles, where the mass reaches a peak and the rate-of-change of the surface roughness approaches a minimum. After this point, the FT algorithm indicates that the rumpling amplitude begins to decrease as TGO spalling dominates the mass change, suggesting that preferential spallation of TGO from the peaks of the undulating surface flattens out the profiles.

Confirmation that the amplitude of rumpling decreases with repeated oxide spallation is apparent from the cross sections of the 5Pt samples in Figure 3.21. The rumpling amplitude is significantly lower at 1750 cycles, compared to 500 cycles. In contrast to the  $S_q$  measurement shown in 3.20, which is continuously increasing, the FT algorithm correctly measures a decrease in height of the rumpled peaks near the coating end-of-life.  $S_q$ , and equivalently  $S_a$ , measure an increase in surface roughness because the spalling of a thick TGO near the end of life creates a significant amount of random additional surface area. By 1800 cycles, the rumpling amplitude has dropped to about three times the initial value. The insets of Figure 3.19 show examples of the optical profilometer data that was used for the FT algorithm. The scan dimensions are small and, therefore, there was some noise in the amplitude of the primary wavelength. Five of the profile scans for each cycle were analyzed together and the results averaged to mitigate this noise. Further, the insets show missing data from the scans as white pixels. The quantity of

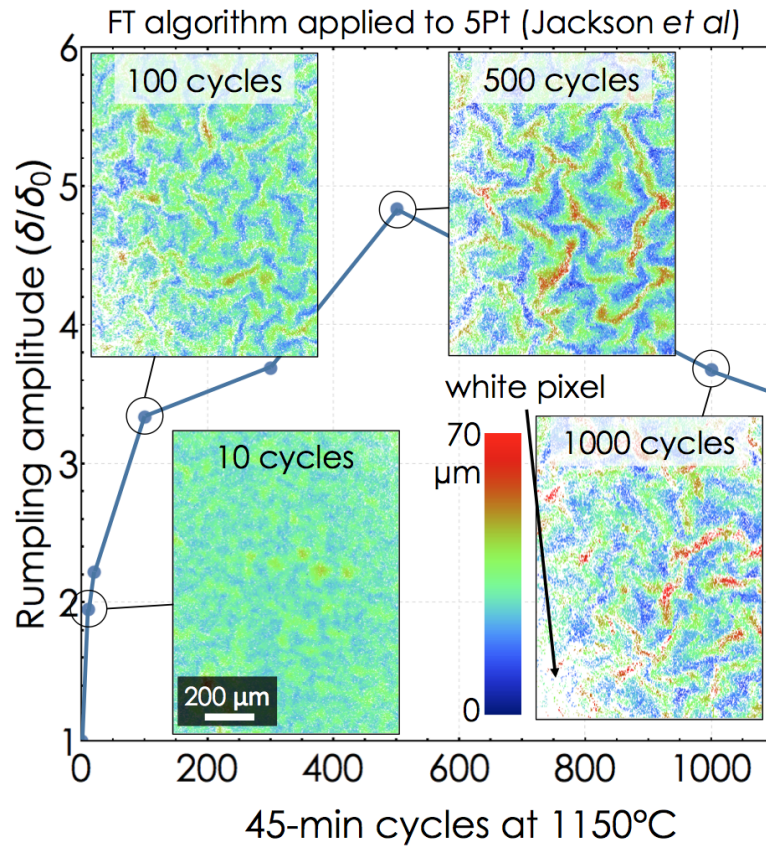


Figure 3.19: Application of the FT algorithm to real profilometer data from a  $\beta$ -phase bond coat shown to undergo rumpling. All surface profiles are at the same lateral and  $z$ -resolution. White pixels indicate missing data.

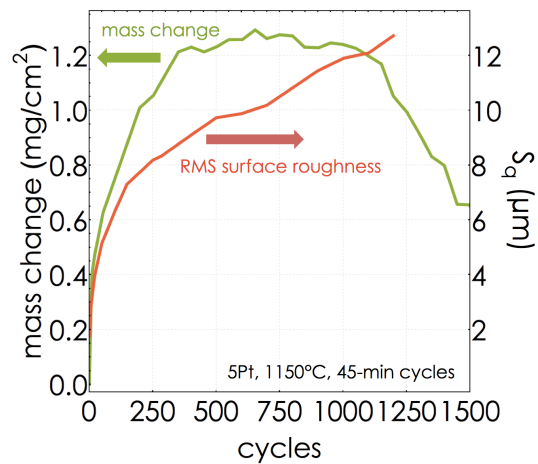


Figure 3.20: Root-mean-square surface roughness and mass change of the 5Pt coating. Data are reproduced from [57].

missing data increases dramatically as the surface roughness of the sample increases and there is significant spalling. The missing and noisy data do not result in erroneous results when the FT algorithm is used, since it has the same effect as random asperities in the profile, which do not influence the FT algorithm.

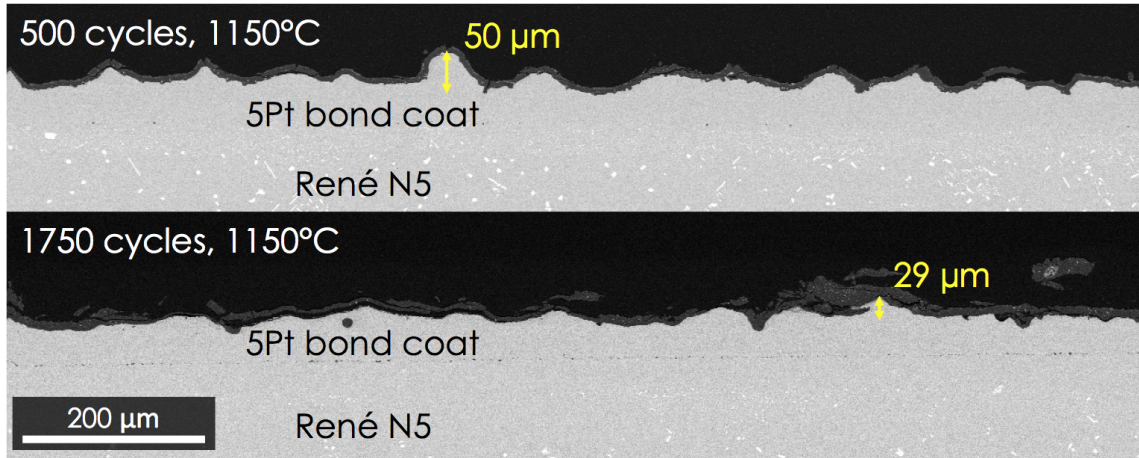


Figure 3.21: Cross sections of the 5Pt coating taken after 500 and 1750 thermal cycles at 1150 °C. The amplitude of the rumples decreases by 1750 cycles. Scale bar applies to both micrographs.

The evolution of the primary rumpling wavelength is of interest for this coating. Balint and Hutchinson developed an analytical rumpling model and determined that the primary rumpling wavelength should scale with the thickness of the TGO, indicating that for thicker oxides, longer rumpling wavelengths,  $L^*$ , should exhibit dominant amplitude increases [31]:

$$L^* = h \sqrt{\frac{\pi^2 \bar{E}}{12\sigma}} \quad (3.8)$$

where  $h$  is the TGO thickness,  $\sigma$  is the growth stress in the TGO, and  $\bar{E}$  is the biaxial modulus of the TGO. This represents a balance between the elastic energy stored in the compressed film and the bending resistance due to stiffness. Balint and Hutchinson also note that when the oxide is thinner (after a few thermal cycles) the oxide has less bending

stiffness and it is easier to change the dominant wavelength than at later times when the oxide is thicker and resists significant changes in the rumpling wavelength. Taking typical values for the TGO properties:  $E = 375$  GPa,  $\sigma = 300$  MPa, and  $\nu = 0.2$ , gives a critical rumpling wavelength  $L^* = 49$   $\mu\text{m}$  when  $h = 1.5$   $\mu\text{m}$  and  $L^* = 131$   $\mu\text{m}$  with  $h = 4$   $\mu\text{m}$ .

Because the FT gives the amplitude as a function of frequency (equivalently wavelength), the wavelength at which peak rumpling is occurring is directly evaluated. Table 3.2 shows the peak rumpling wavelength as a function of cycle number. The dominant rumpling wavelength is slowly increasing from 50 to 130  $\mu\text{m}$  while the TGO is still thin and growing quickly. The wavelength stabilized at 130  $\mu\text{m}$  by 500 cycles.

Table 3.2: Primary rumpling wavelength as a function of cycles for 5Pt  $\beta$ -phase coating thermally cycled at 1150  $^\circ\text{C}$ . FT algorithm was applied to data collected previously [57].

cycle no.	wavelength ( $\mu\text{m}$ )
10	50
20	55
100	81
300	117
500	130
1000	130
1500	130

### 3.3.5 Discussion

The purpose of collecting rumpling metrics during cyclic oxidation testing of candidate bond coat compositions is to quantify the degree of ratcheting plastic deformation in the bond coat as a function of cycling. Bond coat deformation drives the non-compliant thermal barrier coating to separate from the bond coat, buckle, and spall from the airfoil. Quantitative information will permit a more rigorous evaluation of the bond coat compositions that mitigate this type of deformation and enable improvement in TBC

system lifetimes in the combustion environment. Surface roughness measurements from profilometry directly measure the deformation in the bond coat only if the thermally grown oxide is uniform in thickness, which is the case for TGOs grown on (Pt,Ni)Al and MCrAlY coatings early in thermal cycling. On the other hand, the topology in the oxide is different than that of the bond coat surface when there is the growth of local oxide asperities or frequent TGO spallation, both of which occur near the end of life. In this case, surface roughness measurements do not provide a good measure of bond coat deformation, but rather represent a convolution of bond coat deformation and oxide non-uniformity. Conversely, a creeping bond coat deforms in a more continuous fashion forming wave-like undulations to accommodate the strain. The Fourier transform algorithm is thus a good way to identify these periodic features, as it is insensitive to other forms of surface inhomogeneity.

### **Limitations of the FT algorithm**

There are some limitations of the FT algorithm that must be discussed. First, the algorithm is only useful for extracting sinusoidal information from surface profiles. For bond coat rumpling, the intended application, this is acceptable because bond coats are expected to rumple with a distribution about a primary wavelength that resembles a complex 2D sinusoidal surface; this will be substantiated in the following sections. The wavelength of the sinusoid depends on the TGO thickness and the elastic properties of the system [19, 31]. The FT algorithm is not amenable to the characterization of the increase in amplitude of random oxide asperities. Second, there is a tendency for rumpling bond coats to preferentially spall TGO from the peaks of rumples. This type of spalling will preferentially flatten out the measured profile of a bond coat and TGO system. If the oxide thickness is comparable to the magnitude of rumpling undulations, then care must be used when analyzing the top surface as measured by an optical profilometer after

prevalent oxide spalling beings. It is possible that spalling from the rumple peaks will flatten out the surface enough to avoid detection with the FT algorithm if the inter-cycle characterization frequency is not frequent enough. Third, the resolution and size of the profilometer data limits the resolution at which primary rumpling wavelength can be determined. This is likely not an issue for experimental bond coat systems because there will be a distribution of rumpling wavelengths centered about some mean value of the “rumpling wavelength.” Fourth, the minimum area of an optical profilometer scan necessary to produce consistent and representative results must be determined early on in an experiment. Typical metrology suggests that the length of the scan should be at least ten times longer than the longest wavelength being characterized. For a bond coat with a primary rumpling wavelength of around  $130\ \mu\text{m}$  this means the scan must be at least  $1.3 \times 1.3\ \text{mm}$ , but still have a satisfactory sampling resolution. The Fourier transforms conducted on the data of Jackson *et al* [57] only had  $640 \times 480$  pixels with a lateral resolution of  $1.93\ \mu\text{m}/\text{pixel}$ , which resulted in noisy values for rumpling amplitude because the scan dimensions were only  $1.2 \times 0.9\ \text{mm}$ . Increasing the size of the scan can drastically cut down this noise because a more representative amount of the surface is being sampled. However, despite these limitations, the FT algorithm was able to extract the desired information, including the subtlety that the rumple amplitude decreases with prevalent oxide spallation. This type of analysis would be more difficult with standard surface roughness descriptors.

### 3.3.6 Summary of FT algorithm for rumpling quantification

A Fourier transform-based algorithm to quantify rumpling of bond coatings has been presented. The algorithm has been benchmarked with synthetic datasets against the  $S_a$  and surface tortuosity indicators commonly used for rumpling to explore the strengths

and limitations of the algorithm. Finally, the FT algorithm has been used to characterize the observed rumpling of a thermally cycled  $\beta$ -phase coating. The following conclusions can be made.

1. The FT algorithm is at least as sensitive as common surface descriptors to the detection of rumpling in a bond coat that grows a uniform and thin  $\alpha$ - $\text{Al}_2\text{O}_3$  scale.
2. The FT algorithm provides a more accurate measure of the rumpling amplitude compared to the surface roughness and tortuosity descriptors and the algorithm also avoids false-positive indications of “rumpling” when the bond coat grows a nonuniform and thick  $\text{Al}_2\text{O}_3$  scale with inclusions and asperities such as  $\text{HfO}_2$  pegs and spinel oxides.
3. The FT algorithm detects an increase in rumpling wavelength on Pt-containing bond coatings that is in agreement with analytical rumpling models.
4. The FT algorithm correctly measures a decrease in the amplitude of rumped peaks once prevalent oxide spalling begins, whereas the traditional surface roughness metrics are deceiving.

### 3.4 Cyclic oxidation at 1204 °C

The previous section developed a quantitative means to assess the rumpling behavior of all kinds of bond coats. This technique will be used to assess the rumpling deformation of the coatings at 1204 °C. Cyclic oxidation testing at 1204 °C is an extremely harsh laboratory test for a bond coat or superalloy. None of these metallic materials are designed to withstand such extreme temperatures in service, which is currently closer to 1000 °C. However, accelerated tests are useful because they require far less testing time

than the thousands of hours required in the field, which enables faster development, and because they give an indication of the behavior in future generation engines as designers push these systems to higher temperatures. An ideal cyclic oxidation test (without a topcoat) is assessed in such a way as to give an indication of what the behavior of a full TBC system would be. In this regard, measuring the rumpling is useful because it can be correlated with TBC lifetimes.

### 3.4.1 Experimental

The coatings were deposited onto (001) single crystal René N5 disk substrates ( $\varnothing = 19.1$  mm,  $h = 2.1$  mm) using ion plasma deposition [18] and heat treated as described in Section 2.4. A benchmark (Pt,Ni)Al coating ( $\varnothing = 25.4$  mm,  $h = 3.2$  mm) made by electroplating Pt onto René N5 followed by vapor phase aluminization at GE Aviation in Cincinnati, OH was used as a standard for comparison. All coatings were grit blasted with a standard grit blasting procedure using 220 grit alumina particles prior to testing. The specimens were ultrasonically cleaned for twenty minutes in methanol before being thermally cycled 120 times at 1204 °C in an air atmosphere. The hour-long thermal cycle consisted of a ten-minute ramp from room temperature to 1204 °C followed by a forty-four minute hold and six minutes of cooling by forced ambient air, reaching a minimum inter-cycle temperature of 70 °C. Cyclic oxidation testing was carried out in a bottom-loading Rapid Temp furnace (CM Furnaces) in Nisakayuna, NY. An interrupted test was conducted to 60 cycles and showed good repeatability.

The samples were periodically removed for analysis and the mass, surface profile, oxide coverage, and surface phase constitution were measured using a balance, Alicona

---

<sup>2</sup>A substantial portion of the material in this section is reproduced from reference [65] *Bond Coatings with High Rumpling Resistance: Design and Characterization* by Jorgensen, Suzuki, Lipkin, and Pollock published by Surface and Coatings Technology in 2016.

InfiniteFocus optical profilometer, SEM, and XRD. The profilometer has a vertical resolution of tens of nanometers and a lateral resolution of hundreds of nanometers.

Cross section micrographs showing the microstructures of the three experimental coatings in the as-heat treated condition are in Figure 2.9. Both of the nominally  $\gamma'$  coatings (DJ1 and DJ2) were slightly Al-rich and therefore contain a small amount of secondary  $\beta$ -phase. Some of the surplus Al in these coatings diffused into the substrate during the heat treatment and no  $\beta$  phase was detected by the end of the first thermal cycle.

### Characterization of surface topology

Characterization of the progressive rumpling was investigated using a custom-coded *Mathematica* program to calculate Fourier transforms (FTs) of the surface profiles as described in detail in Section 3.3 [103]. An area of approximately  $5 \times 1$  mm near the center of each sample was measured with the optical profilometer and converted to a 2D matrix of height values having dimension  $5893 \times 1238$ . Figure 3.22a is an example surface profile from the (Pt,Ni)Al coating taken after 120 cycles. The matrix of height values was zero-padded around the perimeter to dimensions of  $6000 \times 6000$  points to increase the frequency resolution upon transformation and ensure that the frequency sampling was the same in all directions after the FT. A discrete Fourier transform of each matrix was computed, shifted to DC-center the data (Figure 3.22b), and then radially averaged to collect the information from all directions along the surface (Figure 3.22c). The radially averaged FTs of the surface profiles of subsequent cycles were normalized by the radially averaged FT at the 0th cycle ( $FT_{120c}/FT_{0c-1}$ ) to quantify the evolution of surface topology during the test (Figure 3.22d). A 500-point moving average was drawn through the resulting values in frequency space to eliminate noise associated with the uneven padding of the initial matrices and the normalization of the transforms. The

Fourier transform represents the spectrum of sinusoidal components needed to represent the surface topology. The peak value of these curves,  $\delta_{max}/\delta_0$ , which corresponds to the frequencies/wavelengths that experienced the largest amplitude increase during the test, is measured to give the primary rumpling wavelength and the extent to which rumpling has proceeded throughout the test.

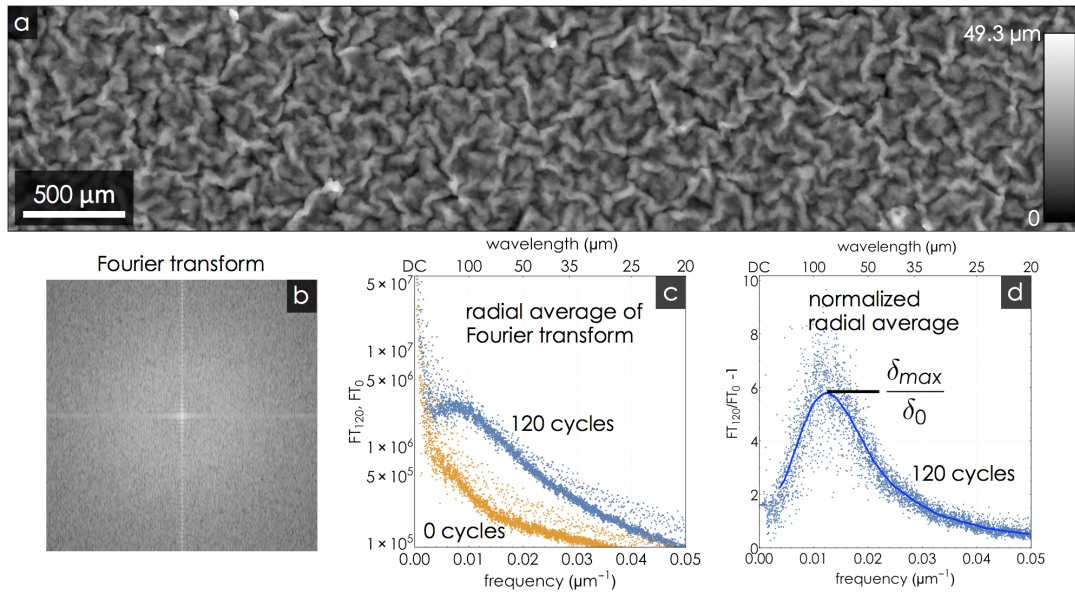


Figure 3.22: (Pt,Ni)Al coating surface after 120 cycles at 1204 °C as an example of the Fourier transform surface analysis. (a) Optical profilometer scan of the surface oxide. (b) Low-frequency center of the 2D Fourier transform of the surface profile measurement. The logarithm of the individual matrix values has been taken and the total range has been scaled between 0 and 244. A diffuse donut-shaped peak is visible that correlates to the peaks seen in c and d. (c) Radial average of the transformed profile at 0 cycles and 120 cycles. Individual pixel values were grouped together in 0.1 pixel radii bins and averaged. (d) The 120-cycle radial average normalized by the 0-cycle radial average. The normalization is  $(FT_{120c}/FT_{0c}-1)$  so that the relative increase is shown. The solid line is a 500-point moving average showing an increase in primary wavelength of approximately 95 μm with an amplitude that has grown about six-fold versus the original value. This indicates significant rumpling of the bond coat. The curve is analogous to the analytical analysis presented in Figure 9 of Balint and Hutchinson [31].

### Characterization of oxide spalling

The amount of spalled surface oxide was measured using a backscattered electron (BSE) SEM. The freshly exposed metallic surface appears bright in comparison to the oxide scales, as shown after 120 cycles in low magnification images in Figure 3.23. These images were segmented into binary images of oxide and exposed alloy using basic image processing. The area fraction of exposed-coating pixels was calculated, which is the area fraction of alloy freshly exposed during that cycle due to cracking and spalling of the oxide scale upon cooling. The total amount of bond coat that was exposed throughout the test (or total amount of failed TGO-bond coat interface) was quantified by integrating these values using first-order interpolation between measurements. This is a measure of the cumulative total fraction of the bond coat-TGO interface that has failed throughout the test. There was some indication in the isothermal oxidation test, detailed in Section 3.1, that thick TGOs on the  $\gamma'$  coatings could fracture midway through the TGO. This results in a loss in mass for the sample, but would not be detected by BSE contrast since the metallic bond coat is not exposed. An example of this scalloping fracture behavior from an isothermal oxidation sample is shown in Figure 3.24.

### 3.4.2 Results

In terms of TGO adherence, as detailed in the following sections, the results of cyclic oxidation testing indicate that the DJ1  $\gamma'$  coating without Si and Ti additions formed the most protective TGO. Cross section micrographs of the coatings in the interrupted test (60 cycles) and at the end of the test (120 cycles) are given in Figures 3.25 and 3.26. While the  $\gamma'$  coatings oxidized more rapidly than the (Pt,Ni)Al and DJb coating, the  $\gamma'$  coatings exhibited less rumpling.

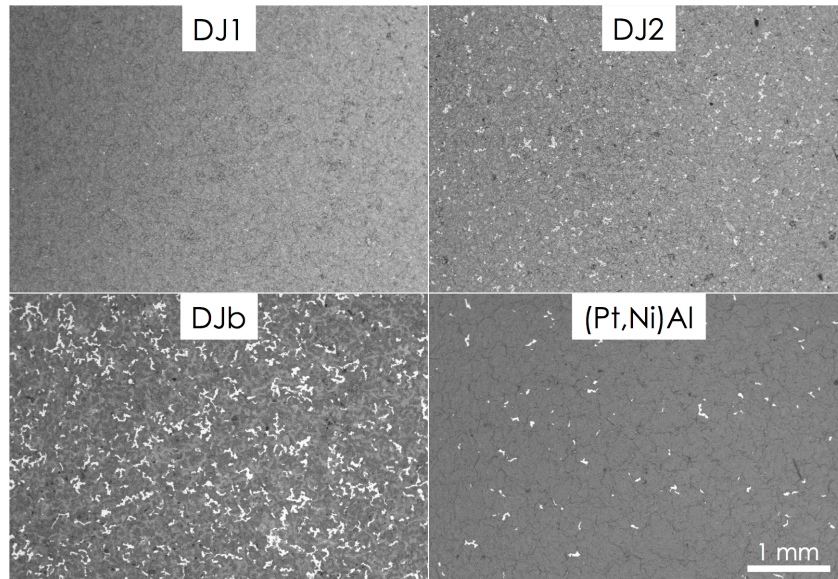


Figure 3.23: Backscattered electron images showing the plan view of the samples after 120 cycles at 1204 °C. The lighter contrast in each image is the exposed bond coat surface due to spalling of the TGO. After 120 cycles, the DJ1 coating shows the least amount of freshly exposed bond coat, followed by (Pt,Ni)Al, and DJ2, and DJb(high-S).

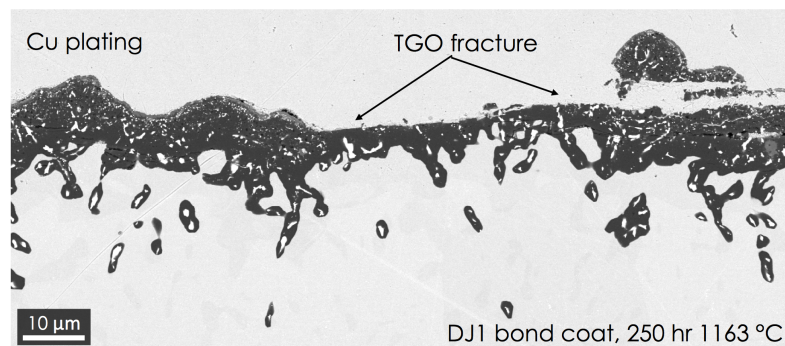


Figure 3.24: Cross section of DJ1 coating after isothermal oxidation for 250 h at 1163 °C. The TGO fractured midway through its thickness, resulting in a partial spalling of the TGO. This type of behavior, if occurring during a cyclic oxidation test, would not be detected by the BSE images taken to quantify the spalling behavior.

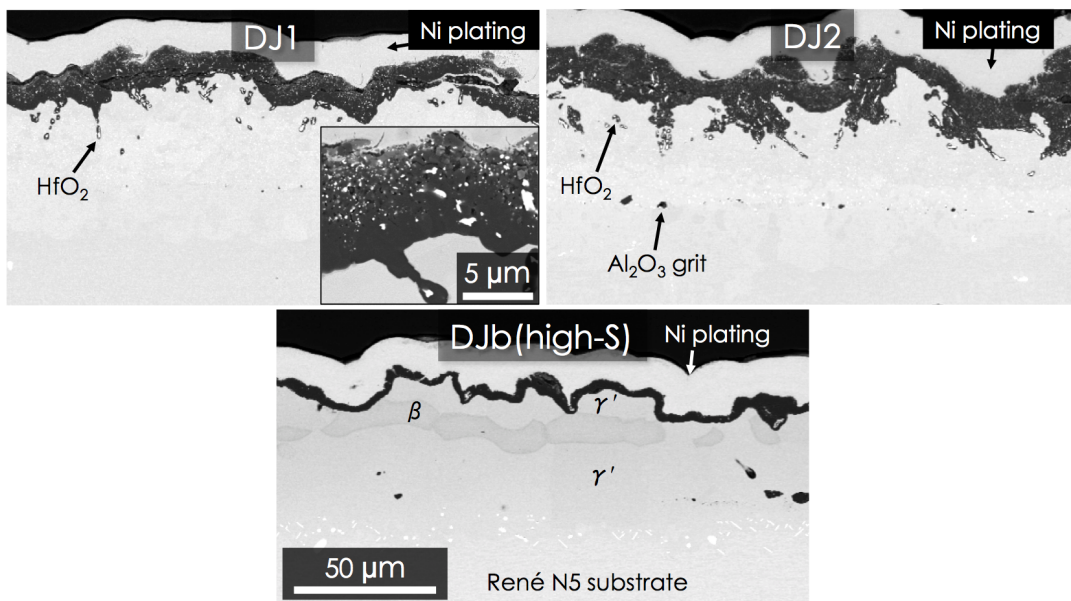


Figure 3.25: Cross sections of the coatings after 60 cycles at 1204 °C. The  $\gamma'$  coatings DJ1 and DJ2 have selective oxidation of Hf beneath the oxide scale to form HfO<sub>2</sub> pegs. Both of these coatings exhibit oxidation that is non uniform, creating TGOs that have significant variations in thickness. The inset in the upper image shows the porosity gradient in the TGO from the DJ1 sample in detail. The bottom of the TGO is more dense than the top, where there are more intermixed hafnia particles. DJb coating exhibits extensive rumpling with a thin and dense Al<sub>2</sub>O<sub>3</sub> scale.

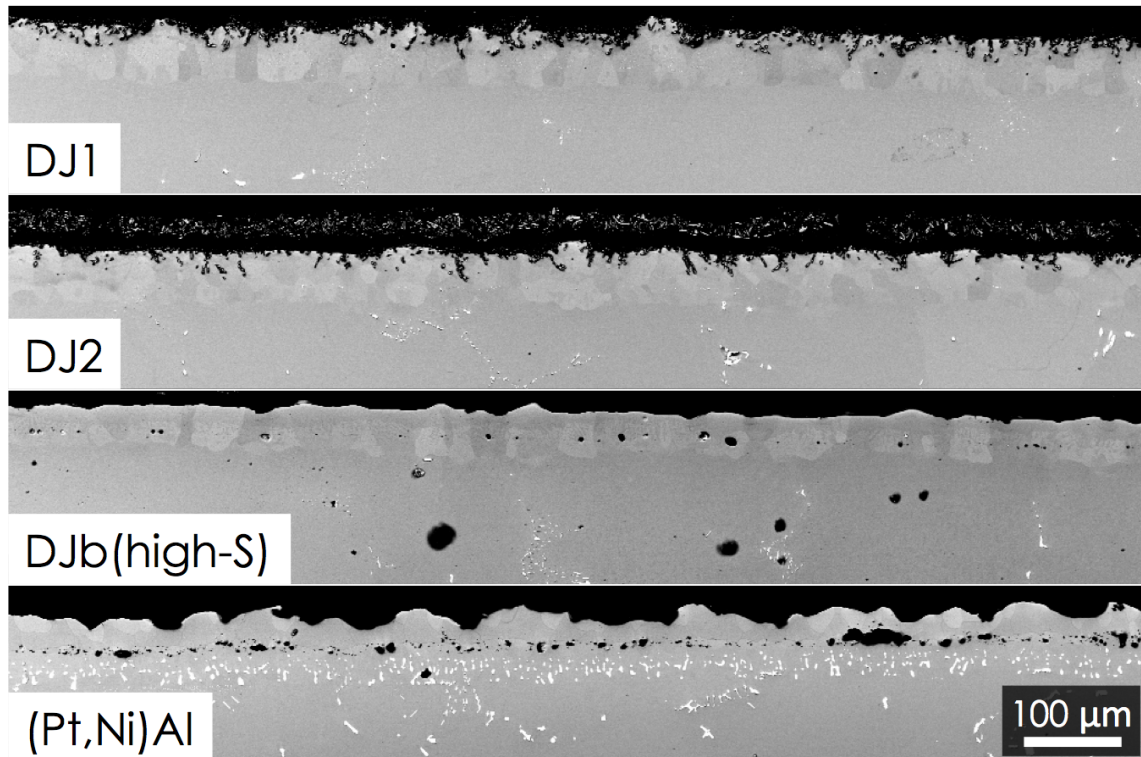


Figure 3.26: Cross sections of the coatings after 120 cycles at 1204 °C. The (Pt,Ni)Al standard coating experienced significant rumpling while the DJ1 and DJ2 coatings did not. The DJb(high-S) coating initially experienced rumpling, but then the surface flattened out due to breakaway oxidation. Both the DJ1 and DJ2 coatings had internal oxidation of Hf near the surface, but the  $\beta$  coatings did not. While none of the experimental coatings exhibit an interdiffusion zone or formation of TCP phases at 120 cycles, the (Pt,Ni)Al coating did. There is the presence of grain growth into the substrate from the experimental coating-substrate interfaces.

## Mass gain

The mass of each sample changes due to the formation and local spallation of TGO. The surface area-normalized mass change of the four coatings is shown in Figure 3.27a. Both of the  $\gamma'$  coatings gained mass faster than the (Pt,Ni)Al coating. The (Pt,Ni)Al sample gained mass continually throughout the test, despite clear evidence of oxide spalling, Figure 3.27; this is discussed in more detail in Section 3.4.3.

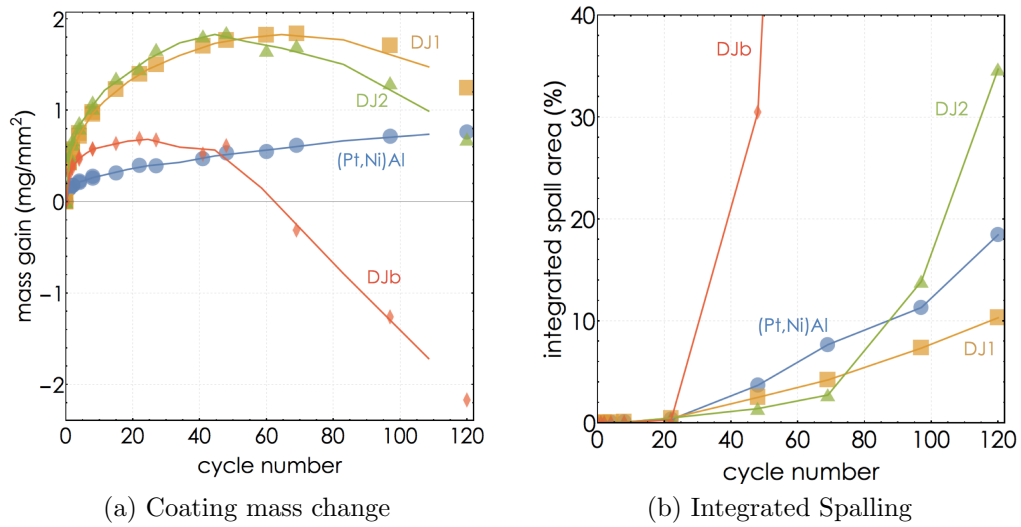


Figure 3.27: (a) The mass gain of the three experimental coatings and the (Pt,Ni)Al standard as a function of thermal cycles. The solid lines are 2-point moving averages. (b) Plot of the spalled oxide area fraction measurements integrated over all cycles at 1204 °C.

## Surface topology

The root-mean-square (RMS) surface roughness  $S_q$  is shown in Figure 3.28a as a function of cycles, where

$$S_q = \sqrt{\frac{1}{MN} \sum_{k=0}^{M-1} \sum_{i=0}^{N-1} z(x_k, y_i)^2} \quad (3.9)$$

$z(x_k, y_i)$  is the height of each pixel,  $M$  is the number of pixels in the  $k$  direction, and  $N$  is the number of pixels in the  $i$  direction. Previous characterization of the rumpling of MCrAlY and (Pt,Ni)Al bond coats has successfully used the RMS surface roughness of the TGO as an indicator of bond coat rumpling (explained in Section 3.3) [32, 40, 57]. In this case, the roughness of the top surface of the TGO is dominated by the local topology of the oxide scale rather than by deformation of the bond coat and so the FT algorithm explained previously is used to quantify rumpling. It is compared to the RMS roughness and 2D tortuosity ( $A/A_0$ ) in Figure 3.28 for reference. When the TGO is nonuniform, such as is the case with these experimental coatings, the tortuosity values are noisy and inconsistent because the surface area of the TGO does not accurately represent the surface area of the bond coat. Figure 3.29 is a plan-view optical image of the coatings where the TGO inhomogeneities are clearly visible, indicating that a means to separate the TGO inhomogeneities from the systematic deformation of the bond coat is needed.

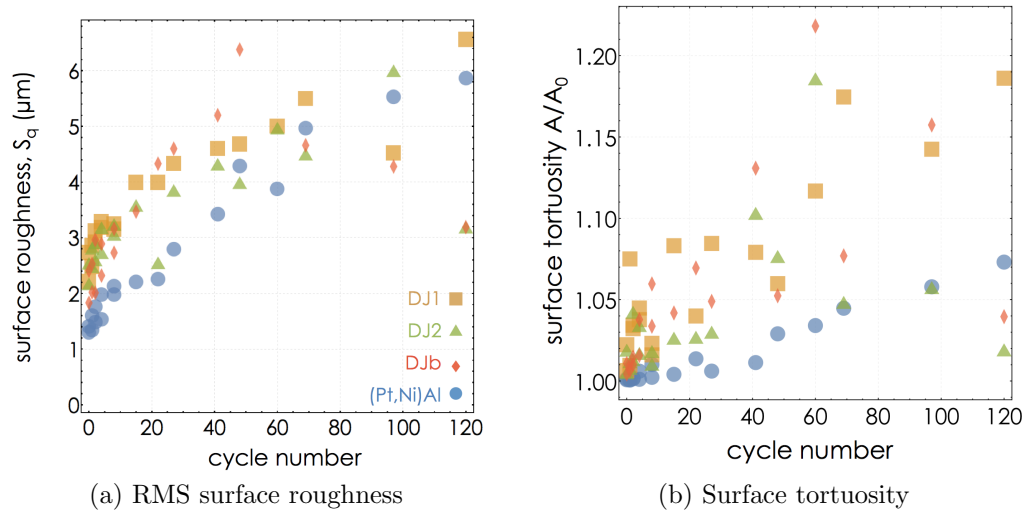


Figure 3.28: (a) The RMS surface roughness,  $S_q$  and (b) 2D surface tortuosity as a function of one-hour cycles at 1204 °C for the four bond coats tested. All coatings show similar  $S_q$  behavior while only the (Pt,Ni)Al coating shows a surface tortuosity trend. The absence of a trend for the three experimental coatings is due to the large amount of scatter from the formation of locally thick regions (mounds) in the TGO as seen in Figure 3.29 and local spalling of the oxide as seen in Figure 3.23.

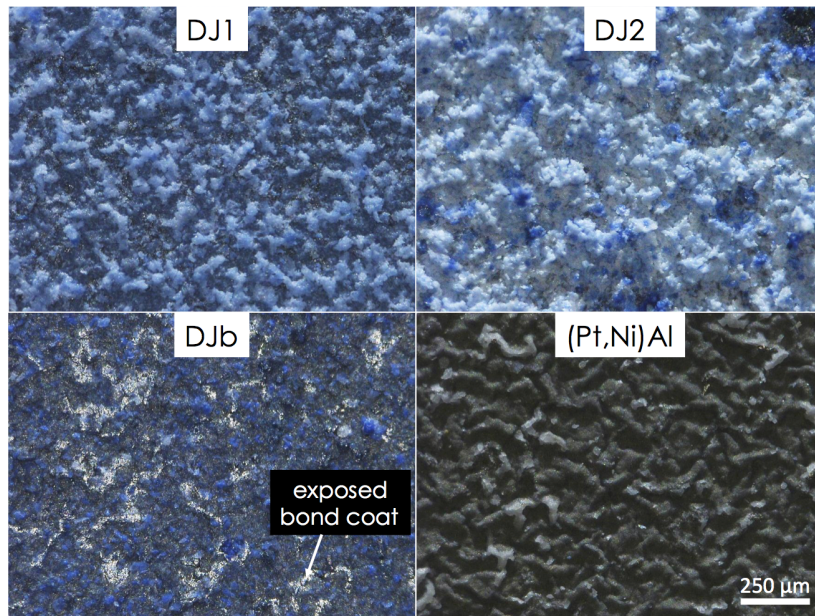


Figure 3.29: Light optical images of the external oxide scales of the bond coated samples after 120 cycles at 1204 °C.  $\text{NiAl}_2\text{O}_4$  appears as dark blue,  $\text{Al}_2\text{O}_3$  appears as grey, and  $\text{TiO}_2$  rutile is pale blue. The large-amplitude undulations in the rumpled (Pt,Ni)Al bond coat are clearly visible with a primary wavelength of 80  $\mu\text{m}$ .

As described in Section 3.4.1, the radially averaged FTs of the coatings were normalized by the 0-cycle curves so that the change in surface topology is quantified. Taking the value of the peak gives a measure of the amount that the dominant surface wavelength increases in amplitude throughout the test. These measurements are presented in Figure 3.30a and the primary rumpling wavelength is presented in Figure 3.30b. The baseline (Pt,Ni)Al coating experienced significant rumpling at a relatively constant wavelength while the two experimental  $\gamma'$  coatings DJ1 and DJ2 showed substantially less rumpling at increasing wavelengths. The  $\beta$ -phase DJb coating initially shows rumpling that was comparable to the (Pt,Ni)Al coating but was abated as it transformed to  $\gamma'$ -phase and experienced breakaway oxidation.

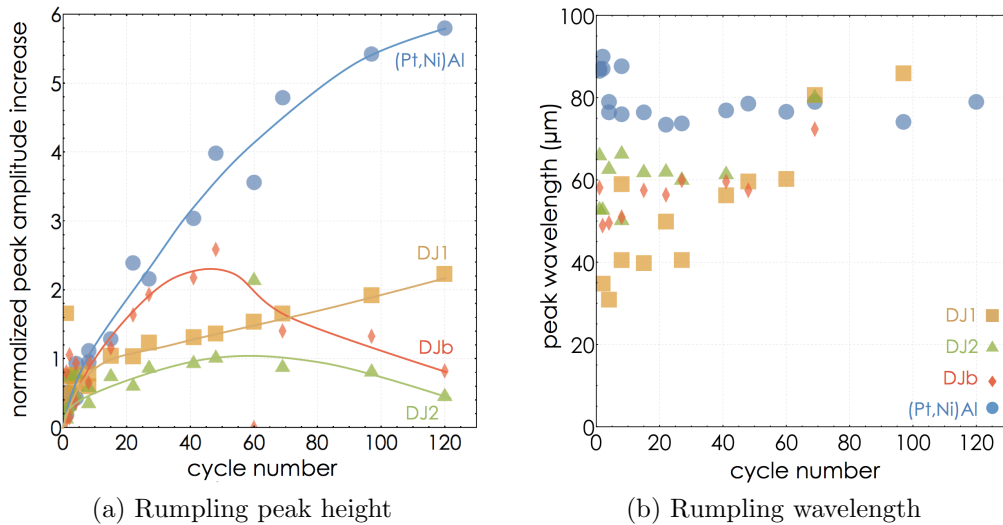


Figure 3.30: (a) The amplitude of the peak value from the FT-analyzed surfaces ( $\delta_{max}/\delta_0$ ). This measure of bond coat rumpling is insensitive to surface roughness effects, such as may be due to poor oxidation behavior. The curves are drawn to guide the eye for trends of the four coatings. (b) Evolution of the wavelength of the FT peak as a function of cycles. The (Pt,Ni)Al coating, with a slow-growing scale, experienced rumpling at a relatively constant wavelength of about 75-80  $\mu\text{m}$  that continuously increased in amplitude. In contrast, the DJ1 and DJ2 coatings, which had fast-growing TGOs, had a significantly smaller surface undulation amplitude that continuously increased in wavelength. The peak location for the DJ2 sample was longer than 200  $\mu\text{m}$  after 80 cycles and is not shown because it was too close to the DC shift of the transform to be differentiated. This is characteristic of a mostly flat bond coat surface, consistent with Figure 3.26. Lines are drawn to guide the eye.

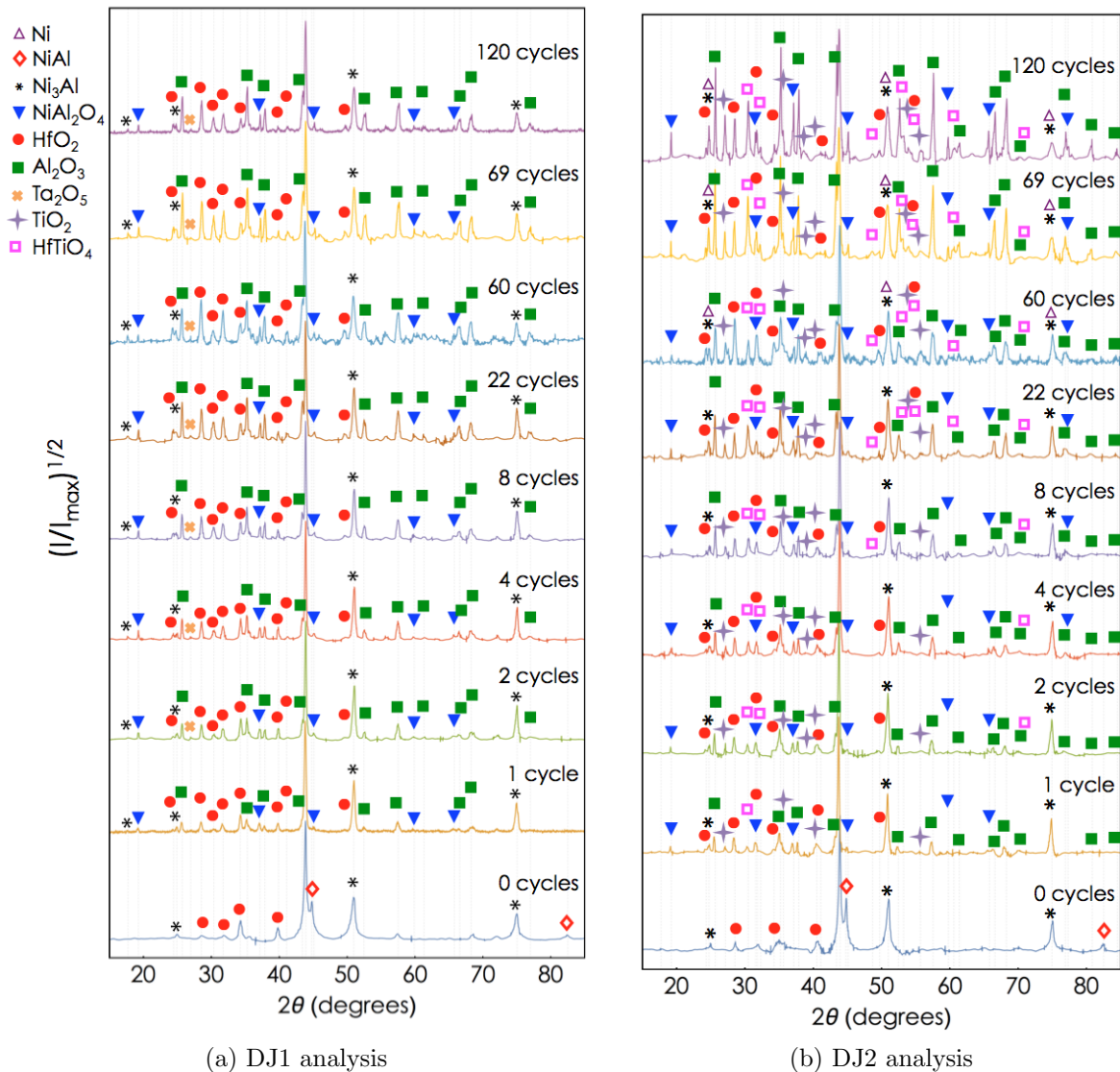


Figure 3.31: X-ray diffraction (XRD) normalized intensity as a function of  $2\theta$  for the (a) DJ1 and (b) DJ2 coatings at selected cycles. Both of the  $\gamma'$  coatings were slightly Al-rich after deposition and heat treatment, which resulted in the presence of NiAl until after the first cycle. The spinel ( $\text{NiAl}_2\text{O}_4$ ) in the DJ1 coating became increasingly enriched in Co in the last 50 cycles of the test as measured by the peak shifts.

### Evolution of coatings and thermally grown oxides

Results of the XRD phase analysis of the two  $\gamma'$  coatings DJ1 and DJ2 are shown in Figure 3.31. The DJ1 and DJ2 coatings began with  $\gamma'+\beta$  phases and  $\text{HfO}_2$  particles after deposition and heat treatment and lost Al during thermal cycling due to interdiffusion with the substrate and formation of the TGO. Analysis indicated that the DJ1 coating contained monoclinic  $\text{HfO}_2$  and the DJ2 coating had monoclinic and what was best described by the metastable orthorhombic  $\text{HfO}_2$ . The DJ1 coating maintained some  $\gamma'$ - $\text{Ni}_3\text{Al}$  phase throughout the test whereas the DJ2 coating transitioned to a solid solution of  $\gamma$ -Ni at around 60 cycles. Both the DJ1 and DJ2 coatings produced thermally grown oxide scales that were predominately  $\alpha$ - $\text{Al}_2\text{O}_3$  with an intermixing of other oxides. The DJ1 coating contained trace amounts of  $\text{Ta}_2\text{O}_5$  throughout the test but showed a continuous increase in the intensity of the  $\text{NiAl}_2\text{O}_4$  peaks.  $\text{HfO}_2$  pegs formed underneath the oxide scales and at the surfaces of both  $\gamma'$  coatings due to the selective oxidation of Hf. In addition, both of the  $\gamma'$  coatings formed a discontinuous layer of nickel aluminate spinel ( $\text{NiAl}_2\text{O}_4$ ) on top of the corundum layer. Based on the shift in diffraction peaks, the Ni spinel evolved to an intermixed layer of Ni and Co spinel on the  $\gamma'$  coating near the end of life by diffusion of Co from the superalloy substrate through the coating and  $\text{Al}_2\text{O}_3$  layers. The DJ2 coating formed rutile  $\text{TiO}_2$  immediately upon cycling and a small amount of  $\text{HfTiO}_4$  within the first 10-30 cycles. The rutile dominated the top of the coating at the end of life, as seen by the pale blue color in Figure 3.29. These layers of oxides are porous and have lower elastic moduli than  $\text{Al}_2\text{O}_3$  and therefore may be beneficial in decreasing TGO spalling due to decreased energy release rate upon cooling. However, rutile would likely be detrimental to TBC adhesion because the mutual solubility of  $\text{TiO}_2$  and  $\text{ZrO}_2$  would lead to a degradation of the TBC/TGO interface toughness [107]. The

DJb coating formed exclusively  $\alpha$ -Al<sub>2</sub>O<sub>3</sub> until it transformed to Ni<sub>3</sub>Al and then began to grow NiO and NiAl<sub>2</sub>O<sub>4</sub> during breakaway oxidation.

### Thermally grown oxide spallation

The area fraction of TGO that spalled from the surface of the bond coat upon cooling was analyzed periodically throughout the test, as explained in Section 3.4.1. The results of these measurements were integrated with linear interpolation as a function of cycles and are plotted in Figure 3.27b. This type of analysis gives a cumulative measure of the quantity of TGO that has spalled from the metallic surface and has regrown during the test. However, this measurement does not include any loss of oxide that may have occurred due to fracturing within the oxide scale itself. By the end of the 120 cycles, the DJ1 coating experienced the lowest cumulative spalling, followed by the (Pt,Ni)Al coating, DJ2 coating, and the DJb(high-S) coating. Plan view images of the four coatings at 120 cycles are shown in Figure 3.23; these images give a sense of the simplicity with which this technique can be used to segment out the exposed bond coat from the oxide layer as well as the relative performance of the coatings with regards with maintaining the oxide scale.

## 3.4.3 Discussion

### Oxidation behavior

In comparison with the (Pt,Ni)Al coating, which grew predominately  $\alpha$ -Al<sub>2</sub>O<sub>3</sub> throughout the test, the oxide scales grown on the  $\gamma'$  coatings consisted primarily of  $\alpha$ -Al<sub>2</sub>O<sub>3</sub> with HfO<sub>2</sub> pegs that were selectively oxidized below the surface and eventually overtaken and enveloped by the scale. Ni and Co-rich spinels formed on top of the alumina scale throughout the test, likely due to enhanced diffusion through the TGO at

high-angle grain boundaries. These oxides created a thin layer across the top surface of the samples and formed small clumps of oxide randomly distributed across the surface (see Figure 3.29).

### **Bond coat rumpling**

As seen in Figure 3.30a, the (Pt,Ni)Al coating experienced a significantly higher degree of rumpling compared to the two  $\gamma'$ -based coatings. While the presence of rumpling in a Pt-modified NiAl coating is expected at these temperatures (1204 °C), the mechanism(s) responsible for the absence of rumpling in the  $\gamma'$  coatings are worth consideration. The analytical rumpling model of Balint and Hutchinson [31] has shown that bond coats with thicker TGOs tend to rumple at a faster rate and with a longer wavelength [19, 39]. However, the present experiments demonstrate that the  $\gamma'$  coatings have a significantly lower rumpling amplitude increase notwithstanding a larger oxide thickness (based on mass change measurements and micrographs). The rumpling simulations described in Section 2.1.2 suggest that the  $\gamma'$  coatings resist rumpling due an increased creep strength. A second consideration is the thermal expansion mismatch between the bond coat and the superalloy. René N5 has a CTE around 16-17 ppm/°C at 1200 °C due to the dissolution of the  $\gamma'$  precipitates into the Ni matrix [18, 50, 108]. The CTE of the  $\gamma'$  phase is closely matched to René N5 below 900 °C, but then lags below due to the dissolution of the  $\gamma'$  precipitates into the Ni matrix of René N5 (Figure 3.6) [18, 50, 108]. This means that the rumpling driving force due to CTE mismatch in a  $\gamma'$  coating slightly lower than a  $\beta$  coating. However, the comparison of the Balint and Hutchison model with Tolpygo and Clarke's experiments suggests that the equibiaxial stress state due to bond coat CTE is less important than the TGO-imposed stresses.

By comparing DJ1 to the DJ2 coating, it is evident that the addition of the high temperature strengtheners, Si and Ti, leads to a smaller increase in rumpling amplitude

during the first 60 cycles (see Figure 3.30a), in accordance with the calculations performed in Section 2.1.2. The decrease in the rumpling amplitude after 60 cycles for the DJ2 coating is due to the prevalent oxide spalling that occurs in this coating, as indicated by the increase in TGO spalling rate in Figure 3.27b. Therefore, it is likely that bond coatings with the  $\gamma'$  phase experience less rumpling than  $\beta$ -phase coatings by increasing the high-temperature strength. It is also possible that the creep properties (and therefore the growth stress) of the TGO are modified by the presence of  $\text{HfO}_2$  particles and voids in the TGO. Although not demonstrated in this work, the B&H model indicates that decreasing the TGO growth stress leads to a decrease in rumpling amplitude. It is also expected that an increase in the TGO bending stiffness with no change in TGO growth stress would inhibit rumpling.

Balint and Hutchinson determined that the primary rumpling wavelength should scale with the properties of the TGO [31]:

$$L^* \propto h \sqrt{\frac{\pi^2 \bar{E}}{12\sigma_y}} \quad (3.8 \text{ revisited})$$

where  $h$  is the TGO thickness,  $\bar{E}$  is the biaxial elastic modulus of the TGO, and  $\sigma_y$  is the high temperature yield strength (growth stress) of the TGO. This represents a balance between the elastic energy stored in the compressed film and the bending resistance due to stiffness. A plot of the wavelength as a function of cycles for the coatings is in Figure 3.30b. This plot shows the primary wavelength  $L^*$  of the surface topology as a function of cycles at 1204 °C. Figure 3.30a shows the relative amplitude of this peak. Clearly, the wavelength of the DJ1 and DJ2 coatings continuously increased as a function of cycles while maintaining a relatively stable amplitude. (It should be emphasized that there was very little rumpling measured in the  $\gamma'$  coatings so the determination of the “peak” wavelength is subject to a large uncertainty). The (Pt,Ni)Al coating, however, has

a consistent wavelength of about 80  $\mu\text{m}$  but an amplitude that is continuously increasing. This contrast can be explained by the rate at which the respective TGO scales grew on the coatings. According to Balint and Hutchinson, once a primary rumpling wavelength has been established it is difficult to suppress it. This is seen in the (Pt,Ni)Al sample where the slow-growing oxide scale has ample time to establish and settle on a primary wavelength before the oxide thickness increases so significantly as to change the preferred wavelength,  $L^*$ . That is to say that the rumpling “inertia” in a slow growing scale is difficult to overcome because the plastic deformation cannot be undone. On the other hand, the  $\gamma'$  coatings have much faster growing scales and have a larger impact on rumpling wavelength stability during thermal cycling; this results in a small rumpling amplitude with a continuously increasing wavelength, per Equation 3.8.

### Comparison to Pt-modified $\gamma+\gamma'$ coatings

Recent research on the oxidation and rumpling properties of Pt-containing  $\gamma+\gamma'$  bond coats has shown that this phase combination is also resistant to rumpling deformation at the expense of slightly faster oxidation rate than the  $\beta$ -phase (Ni,Pt)Al coatings [109–111]. These experiments were performed at 1150 °C on two-phase coatings that were in the Al-rich side of the  $\gamma+\gamma'$  phase field. There is a delicate balance between the Pt and Hf concentrations that causes the growth of  $\text{NiAl}_2\text{O}_4$  formation over the  $\text{Al}_2\text{O}_3$  scale and  $\text{HfO}_2$  pegs beneath the scale [109]. The presence of hafnia pegs was associated with Ni-spinel growth in these experiments [109].

The behavior of the nominally single-phase  $\gamma'$  coatings examined here is similar to the Pt-modified two-phase  $\gamma+\gamma'$  with respect to rumpling resistance and the development of a corundum scale with Ni-spinel above it. Pt modification would likely improve the oxidation and corrosion properties by enhancing a slow-growing, dense alumina scale. It is, therefore, possible that Pt-modification to the single-phase  $\gamma'$  coatings would also

have a beneficial effect on the oxidation behavior, perhaps at a lower Pt concentration due to the higher initial concentration of Al. A direct comparison of topcoat retention for both optimized single- and two-phase coatings is of interest for future work.

### 3.4.4 Conclusions

The 1204 °C oxidation behavior of two experimental  $\gamma'$  coatings has been analyzed. The changes in mass, oxidation spalling, surface roughness, and rumpling have been quantified and compared to a standard (Pt,Ni)Al. The  $\gamma'$  phase was found to be more resistant to rumpling than unmodified and Pt-modified  $\beta$  phase coatings. The resistance to rumpling is best understood as arising from improved creep properties. The DJ1 coating was more resistant to TGO spalling from the surface of the bond coat than the (Pt,Ni)Al coating throughout the test, despite the formation of a thicker oxide. While the  $\gamma'$ -phase coatings oxidize faster than the (Pt,Ni)Al coating under the conditions examined, it will be shown in the following section that the  $\gamma'$  coating can be more resistant to TBC failure at elevated temperatures.

## 3.5 Cyclic oxidation and TBC testing at 1163 °C

The accelerated testing of cyclic oxidation behavior in the previous section suggests that, based on oxidation life and TGO spalling, the (Pt,Ni)Al coating should outperform the DJ1 and DJ2 coatings. However, if rumpling rate and amplitude is a dominant failure mechanism for these TBC systems, the DJ1 and DJ2 coatings should have a longer lifetime than the (Pt,Ni)Al coating. A direct comparison of cyclic oxidation lifetime with the full TBC system lifetime is the best way to assess the predictive power of a cyclic oxidation test. To this end, a pair of cyclic oxidation and furnace cycle tests with the full TBC system have been conducted using the same thermal cycle at 1163 °C. This

temperature is the most severe test used by GE Aviation in its assessment of bond coats and topcoats (Julie M. Chapman, personal communication, September 2015). Bond coat oxidation heuristics suggest that the cyclic oxidation lifetime should double for every drop in 25 °C (Don M. Lipkin, personal communication, July 2013), meaning that the  $\gamma'$  coatings are expected to have cyclic oxidations lifetimes in the range of 500-600 cycles. It will be shown that rumpling is effectively abated by both of the  $\gamma'$  DJ1 and DJ2 coatings in contrast to both the  $\beta$  coatings DJb and (Pt,Ni)Al. Resistance to rumpling is accompanied by a drastically increased TBC lifetime.

### 3.5.1 Experimental

The samples were prepared as described in the previous chapter. The cyclic oxidation samples consisted of  $\varnothing = 19.1$  mm,  $h = 2.1$  mm René N5 disks that were coated on both sides while the TBC samples were  $\varnothing = 25.4$  mm,  $h = 3.2$  mm René N5 disks coated on one side only. The TBC samples were sent to Surface Technologies in Indianapolis, IN for a coating with 130  $\mu\text{m}$  of a standard 7 wt.% YSZ EB-PVD topcoat. All samples were thermally cycled in a bottom-loading Rapid Temp furnace (CM Furnaces) in Santa Barbara, CA. The TBC samples were cycled until  $\geq 20\%$  of the topcoat detached from the substrate (delamination or spall); this was characterized using low-angle incident light and image analysis methods to measure the area detached. Two samples of each coating were cycled until TBC failure along with interrupted samples at approximately 25, 50, and 75% of the average TBC lifetime. These interrupted samples were simultaneously cycled along with the other buttons using a 4-stage staggered button rotation originally used by Curt Johnson of GE Global Research as shown in Table 3.3. This series of interrupted specimens enables an assessment of the evolution of the coating and thermally grown oxide. The 50 and 75% life buttons were created by cutting a single sample in half with

a cubic boron nitride slow-speed saw. Previous tests have indicated that this practice does not impact the TBC system behavior far away from the cut surface (Don M. Lipkin, personal communication, July 2013) The thermal cycle consisted of a nominal 15-min ramp from 93 °C to test temperature (1163 °C), a 45-min hold, followed by 12 min of forced air cooling to below 93 °C. The TBC samples were examined every 20 cycles for topcoat detachment. The samples were rotated in a quasi-random star pattern after each inspection interval. Pieces of uncoated CMSX-4 were used as furnace ballast when a partial-life TBC sample was removed during the rotation; this maintained similar heating and cooling rates in the furnace throughout the test. The cyclic oxidation samples were either cycled until their counterpart TBC system failed or until the samples were losing mass at a predictable rate. Samples were periodically removed for mass, X-ray diffraction (XRD), surface topology (3D profile), and oxide coverage analyses. Surface topology of the cyclic oxidation samples was measured with a Veeco white light interferometer (WYKO NT1100) using the vertical scanning interferometry (VSI) mode with a sub-micron lateral resolution and approximately nanometer vertical resolution. The DJ1, DJ2, DJb (high-S), and (Pt,Ni)Al samples were tested in both the cyclic oxidation (bond coat on both sides) and TBC (bond coat + topcoat on one side) geometries. DJb(low-S) was tested in cyclic oxidation, but not with the topcoat.

It has already been established that the as-coated microstructure of ceramic topcoats has a large impact on overall TBC system life [112–114]. In furnace cycle testing, this is predominantly due to changes in the topcoat density affecting the in-plane compliance of the ceramic. A more porous and feathery microstructure has a lower modulus and a lower residual stress, which is correlated with a longer TBC system life during furnace cycle testing [115]. The dominant processing variables that influence an EP-PVD topcoat microstructure are the coating homologous temperature and the rotation speed [116]. Most industrial coaters passively heat their substrates by the vapor cloud of the evaporated

ceramic, which means that the location of a part within an EB-PVD coater will affect the TBC system performance. To control for these variables, each set of sample buttons (e.g. 100% life, 25 % life) for all of the different bond coat combinations were coated at the same time while mounted next to each other in the EB-PVD coater. This ensures that the measurements of TBC system lifetimes are direct comparisons and only measuring the influence of the bond coat and not on the initial topcoat microstructure.

Table 3.3: A staggered 4-day button rotation schedule for the TBC samples allows for simultaneous testing of interrupted and end-of-life samples. All buttons of the same bond coat are removed from rotation once both 100% samples have experienced  $\geq 20\%$  topcoat detachment.

	day 1	day 2	day 3	day 4
100% life A	×	×	×	×
100% life B	×	×	×	×
75% life	×	×	×	
50% life	×	×		
25% life	×			

### 3.5.2 Results

#### Furnace cycle testing with TBC at 1163 °C

As mentioned earlier, the most important quality of a bond coat is how long it can hold the topcoat onto the substrate. The creep and oxidation rate of the bond coat and superalloy dramatically increase once the topcoat has spalled from the substrate. With this in mind, the TBC lifetimes of the two sets of experimental coatings are shown in Figure 3.32. The values listed in this figure show the average lifetime and half the difference between the two individual samples. The DJ1 coating has a lifetime that is on average more than three times longer than the (Pt,Ni)Al coating at these elevated

temperatures. The DJ2 coating had a lifetime that was about half that of the DJ1 coating, and the DJb(high-S) coating lasted about half as long as (Pt,Ni)Al.

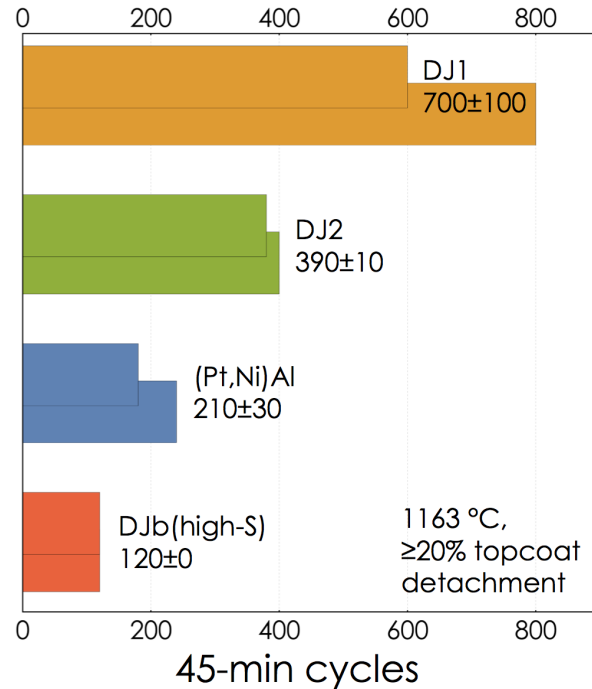


Figure 3.32: Cycle lifetime of experimental coatings during 45 min furnace cycling at 1163 °C. End-of-life is measured as  $\geq 20\%$  topcoat detachment.

Figure 3.33 shows cross sections of the DJ1 coating progressing through its furnace cycle life at 1163 °C. Very quickly, the  $\gamma'$ -phase coating formed a  $\gamma$  layer near the TGO. The formation of this layer was correlated with the development and growth of the  $\text{NiAl}_2\text{O}_4$  spinel layer on top of the TGO (lighter phase in the micrographs between the topcoat and TGO). Ultimately, the DJ1 coating failed at the TBC-TGO interface due to the presence of this spinel layer, which has negligible fracture toughness compared to the YSZ topcoat [117, 118]. The spinel layer can fracture and create small detachments that link up and allow the topcoat to buckle and spall from the sample. It is noteworthy that the majority of the TGO maintained adhesion to the bond coat even though the TGO was quite thick, in the range of 10  $\mu\text{m}$  at end of life. It is possible that the  $\text{HfO}_2$  stringers

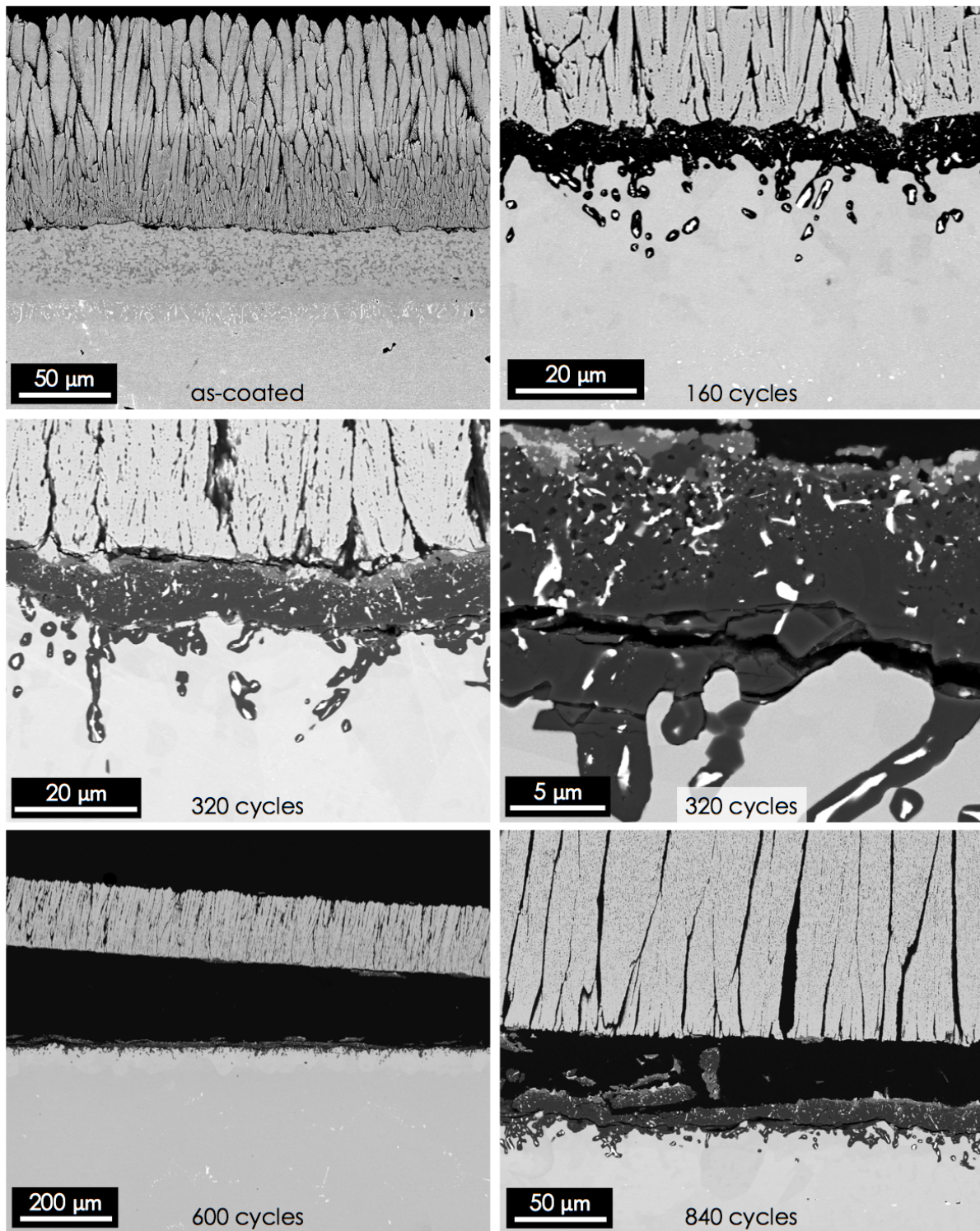


Figure 3.33: Cross sections of the DJ1 coating during furnace cycle testing of the TBC system at 1163 °C.

that formed below the TGO layer formed mechanical interlocking with the bond coat and therefore improved the TGO adhesive strength as has been suggested by others [119]. A previous mechanics analysis has indicated that the  $\text{HfO}_2$  stringers are unlikely to cause significant crack initiation [100] and would instead serve as a tortuous path for crack advance.

The DJ2  $\gamma'$  coating behaved relatively similarly to the DJ1  $\gamma'$  coating. The primary difference is that the TBC failed much earlier (390 versus 700 cycles for DJ1), and therefore the growth of the spinel  $\text{NiAl}_2\text{O}_4$  was not as thick at failure. The TBC system failed at a combination of TGO-topcoat and TGO-bond coat interfaces, such as seen in the 400-cycle image in the bottom left of Figure 3.34. The TGO was more porous and friable and therefore had a greater tendency to fracture within itself. Cracks in the brittle TGO layer can easily deviate into either of the topcoat-TGO or TGO-bond coat interfaces, link up, and cause large scale topcoat delamination. Comparing the DJ2 TGO growth in the TBC system to that in the 1204 °C oxidation (Figure 3.25), it is clear that the oxidation is more uniform for this bond-coated sample.

Turning now to the behavior of the  $\beta$  coatings, Figure 3.35 shows the furnace cycle life of DJb(high-S). Again, this TBC system had lifetime of only 120 cycles. The primary failure location was at the TGO-bond coat interface, likely due to the high concentration of sulfur in the bond coat. The TGO is much more dense and thin than the TGO grown on the  $\gamma'$  coatings. Isothermal oxidation measurements in Figure 3.5 indicate that the TGO on the DJb coating grows more slowly than the DJ1 and DJ2 coatings. It should be noted at this point that the separation between the TGO and the DJb bond coat seen in the cross section micrographs taken at 40/80/100 cycles occurred during sample preparation. The large residual stress of the TGO caused the TGO to delaminate from the bond coat once the free surface from the cross-section cut was created and released the constraint on the TGO. Evidence of the martensitic transformation occurring within

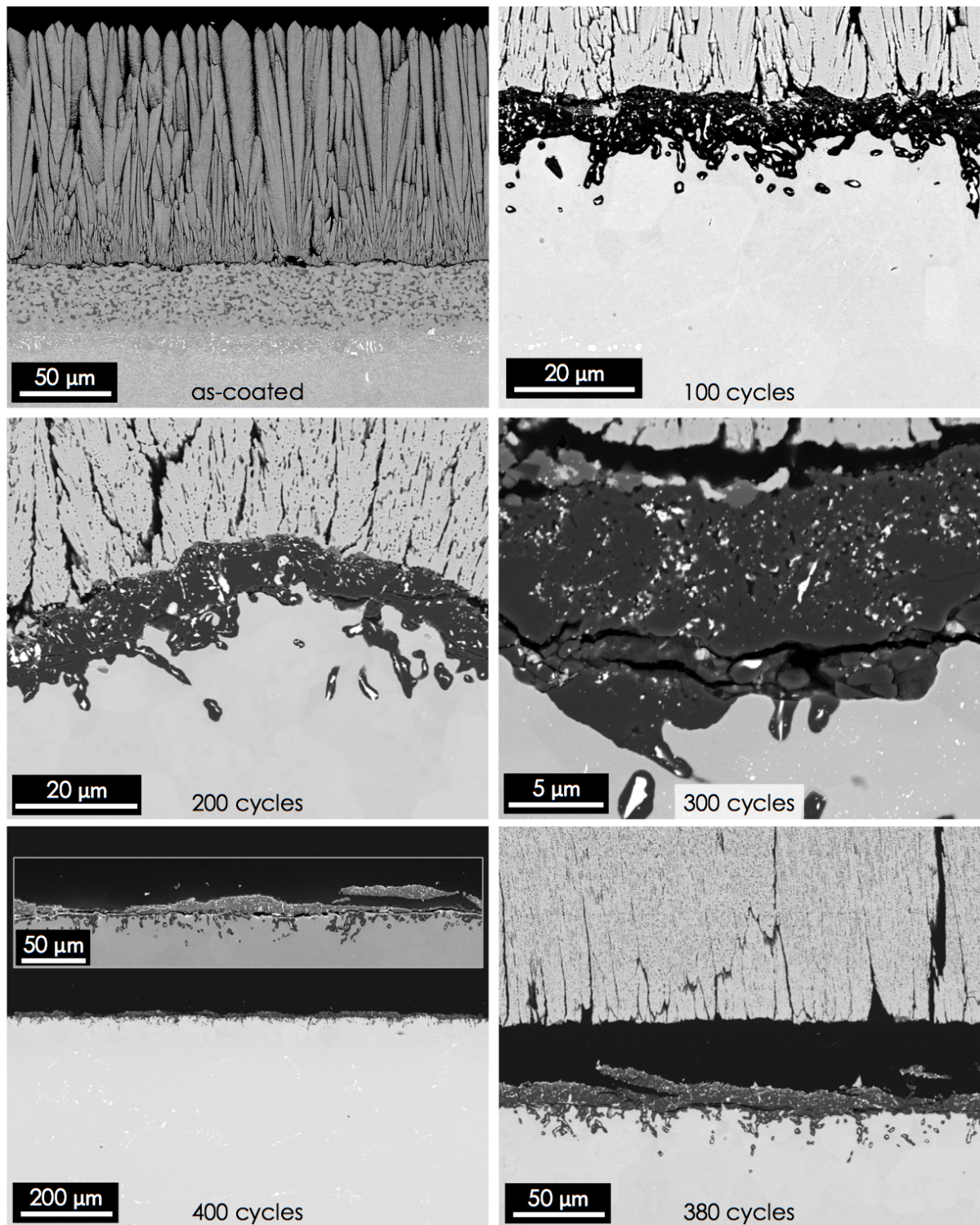


Figure 3.34: Cross sections of the DJ2 coating during furnace cycle testing of the TBC system at 1163 °C.

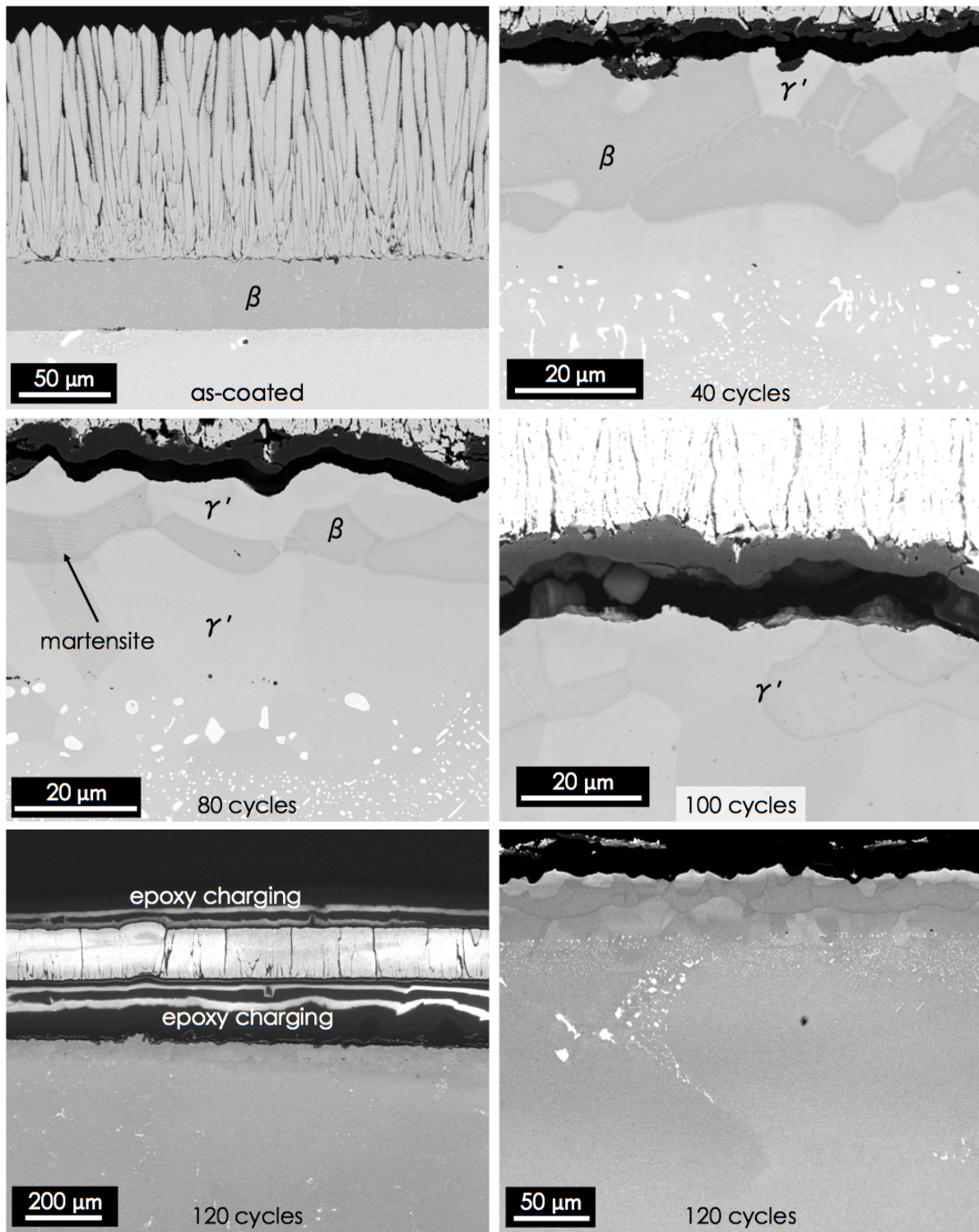


Figure 3.35: Cross sections of the DJb coating during furnace cycle testing of the TBC system at 1163 °C.

the darker contrast  $\beta$ -phase grains can be seen in the micrographs taken at 40 and 80 cycles. The  $\beta$  phase is no longer seen in this coating by 100 cycles.

The furnace cycling behavior of the industry-standard (Pt,Ni)Al coating demonstrates the typical response of a low-strength coating at high temperatures. As seen in Figure 3.36, the TGO grown on the the coating shows excellent continuity and low porosity, just as the TGO on the DJb coating. However, even by 60 cycles the formation of rumples can be seen at the top of the bond coat. Due to the topcoat constraint, the TBC cannot easily deform out of the plane (away from the substrate) and instead primarily deforms downward away from the topcoat. The topcoat has low compliance in this direction and cannot deform with the bond coat and TGO and instead fractures near the roots of the topcoat. These cracks near the TGO-topcoat interface begin linking up between 120 and 180 cycles at 1163 °C and by 200-240 cycles the topcoat buckles and spalls from the (Pt,Ni)Al coating. The images at 240 cycles, both taken from the same sample, clearly show the large rumpling deformations in the bond coat that cause topcoat delamination and failure of the TBC system. Even by 240 cycles the bond coat still contains a significant reservoir of Pt and Al and is maintaining a dense  $\text{Al}_2\text{O}_3$  scale. There is little evidence of spinel formation on top of the TGO after 240 cycles.

The invaginations produced in the (Pt,Ni)Al coating are very similar in appearance to the short cracks seen from the oxidation-assisted fatigue [26–28]. Specifically, the cracks caused by rumpling in a soft coating During stage I of the crack growth progression, while the cracks are still within the bond coat.

### **Cyclic oxidation testing at 1163 °C**

With an understanding of how the TBC systems failed, it is informative to evaluate the cyclic oxidation behavior of these systems to understand how the oxidation properties and bond coat deformation, or lack thereof, contribute to the demonstrated TBC life. The

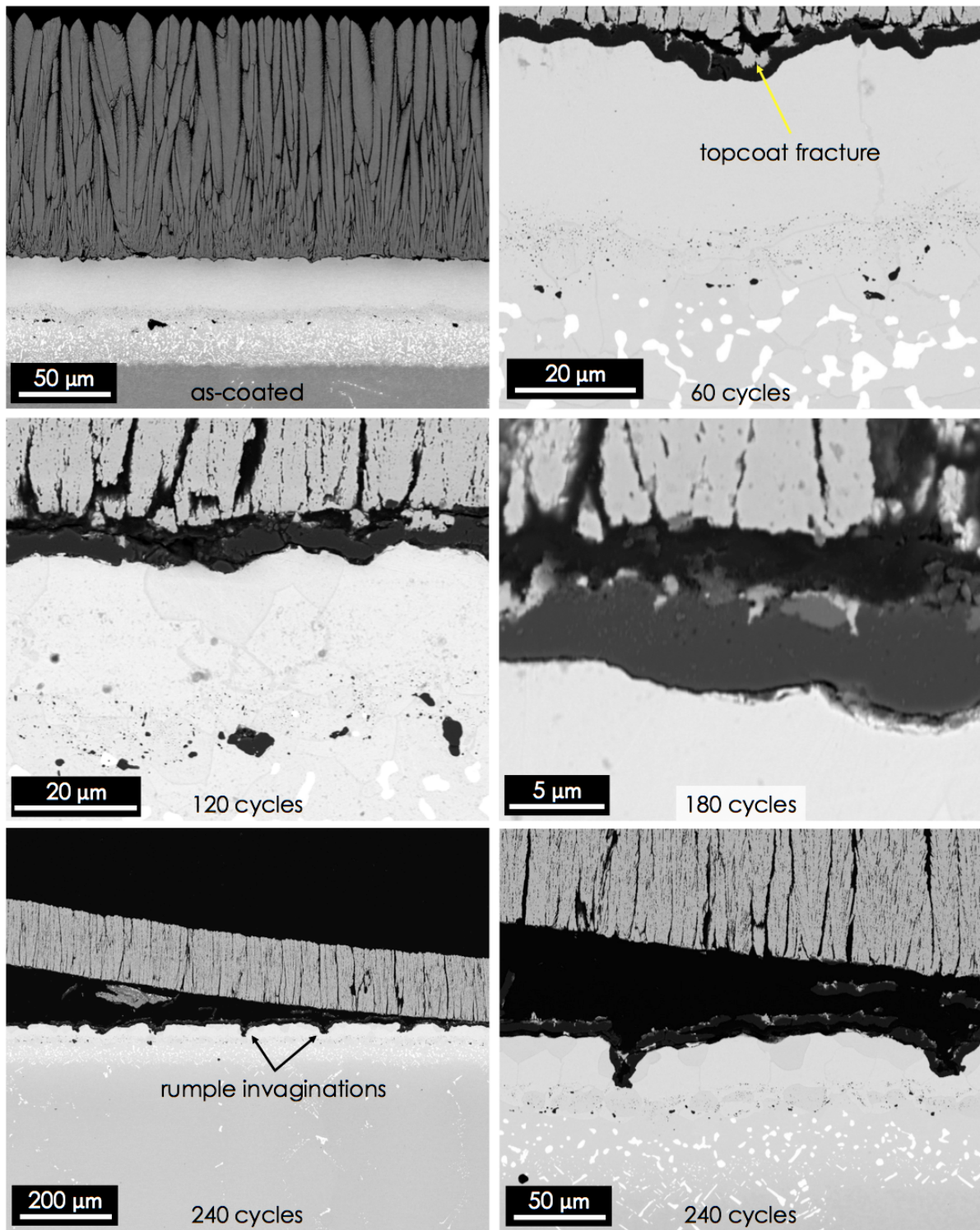


Figure 3.36: Cross sections of the (Pt,Ni)Al coating during furnace cycle testing of the TBC system at 1163 °C.

area-normalized mass change of the coatings during cyclic oxidation testing at 1163 °C is shown in Figure 3.37. This figure shows the disparate cyclic oxidation behavior of the experimental coatings to the industrial standard (Pt,Ni)Al. The initial mass gains of the experimental coatings were all significantly faster than the (Pt,Ni)Al coating. While the estimated lifetime, measured as the cycle of net mass loss, for the (Pt,Ni)Al coating is over 1000 cycles, all the experimental coatings had lifetimes lower than 500 cycles. The high-S DJb coating had the worst lifetime overall, with approximately 130 cycles followed by the low-S DJb coating with 270 cycles. The two  $\gamma'$  coatings, DJ1 and DJ2, had cyclic lifetimes that were about 460 and 340 cycles. The ranking of the coating oxidation performance would not change if the lifetime of the coatings is measured as the peak of the mass-cycle curve.

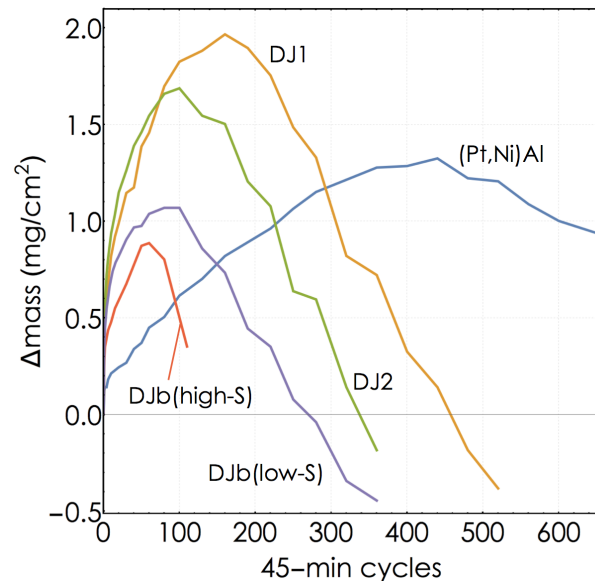


Figure 3.37: Mass change during cyclic oxidation at 1163 °C of the monolithic experimental coatings.

The rumpling behavior of these coatings was evaluated using the Fourier Transform algorithm explained in Section 3.3. The dominant rumpling wavelength as a function of cycles for the coatings is shown in Figure 3.38. Note that the magnitude is represented as

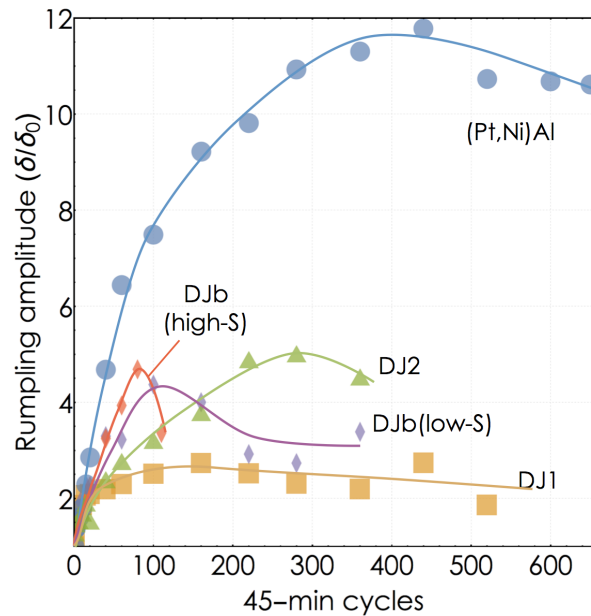


Figure 3.38: Amplitude of the dominant rumpling amplitude as a function of 45-min cycles at 1163 °C. The values are normalized by the amplitude of the dominant rumpling wavelength at 0 cycles.

$(\delta/\delta_0)$ , so the origin of the ordinate axis is at 1, which indicates no change in the rumpling amplitude. No background noise level has been subtracted from these measurements, as was done in Section 3.3; these measurements show the true increase in amplitude as a function of cycles/wavelength. This shows that the (Pt,Ni)Al coating experienced a maximum amplitude of about 11 times the initial value; the wavelength of this maximum was about 65  $\mu\text{m}$ . The rumpling amplitude tended to grow until about 400 cycles and then began to decay as oxide spalling became more prevalent, as described previously [103]. In stark contrast, the DJ1 coating had a maximum rumpling amplitude of only a bout 2.5 times the initial value. The wavelength of the peak rumpling amplitude had a large uncertainty and scatter due to the low amplitude, but tended to be in the range of 20-50  $\mu\text{m}$ , which strongly correlates with the size of the grains in the coating. Interestingly, the  $\beta$ -phase DJb coatings both experienced an increase in rumpling amplitude that was comparable to the (Pt,Ni)Al coating initially but decreased significantly once these coat-

ings transformed to the  $\gamma'$  and  $\gamma+\gamma'$  phases and oxide spallation became prevalent near the end of the coating lives.

The measured rumpling amplitude of DJ2 coating in Figure 3.38 requires a detailed investigation because there is no noise floor subtracted from radial averages when measuring the rumpling amplitude. Figure 3.39 shows radial averages from profilometry measurements and subsequent application of the FT algorithm for four of the coatings at various stages throughout cyclic oxidation testing. First, it is obvious by comparing the profiles of all the experimental coatings to the (Pt,Ni)Al benchmark, that the (Pt,Ni)Al coating is experiencing drastically more rumpling. In these profiles, this is manifested by the large amplitude increase in the radial average with a peak around 65  $\mu\text{m}$  wavelength. The amplitude of this peak grows monotonically until about 280 cycles and then levels off. While the amplitude of the other wavelengths are also increasing, they are doing so at a slower rate. Equal amplitude increase at all wavelengths is due to a surface that is has a random increase in roughness of the surface due to oxidation, not any specific mechanical stabilization of a dominant rumpling phenomenon. In contrast to the behavior of the (Pt,Ni)Al coating, the DJ2 coating exhibits a general increase in amplitude of the entire 20-120  $\mu\text{m}$  spectrum with flat profiles. This indicates explains why the peak amplitude of the DJ2 coating in Figure 3.38 increases so drastically compared to the other  $\gamma'$  coatings. The drastic increase in surface roughness at all wavelengths due to oxidation and spalling of both large and small pieces of TGO causes all wavelengths of the surface profile to increase in wavelength. The DJ1 and DJb coatings also exhibit some of this global increase in wavelength, but the DJb coating shows the development of broad peaks around 100-160 cycles.

For reference, a plot of the RMS surface roughness is in Figure 3.40 and indicates that the prevalent growth of oxide nodules in the TGO from the experimental coatings creates a surface roughness that is comparable to the increase in surface roughness of the

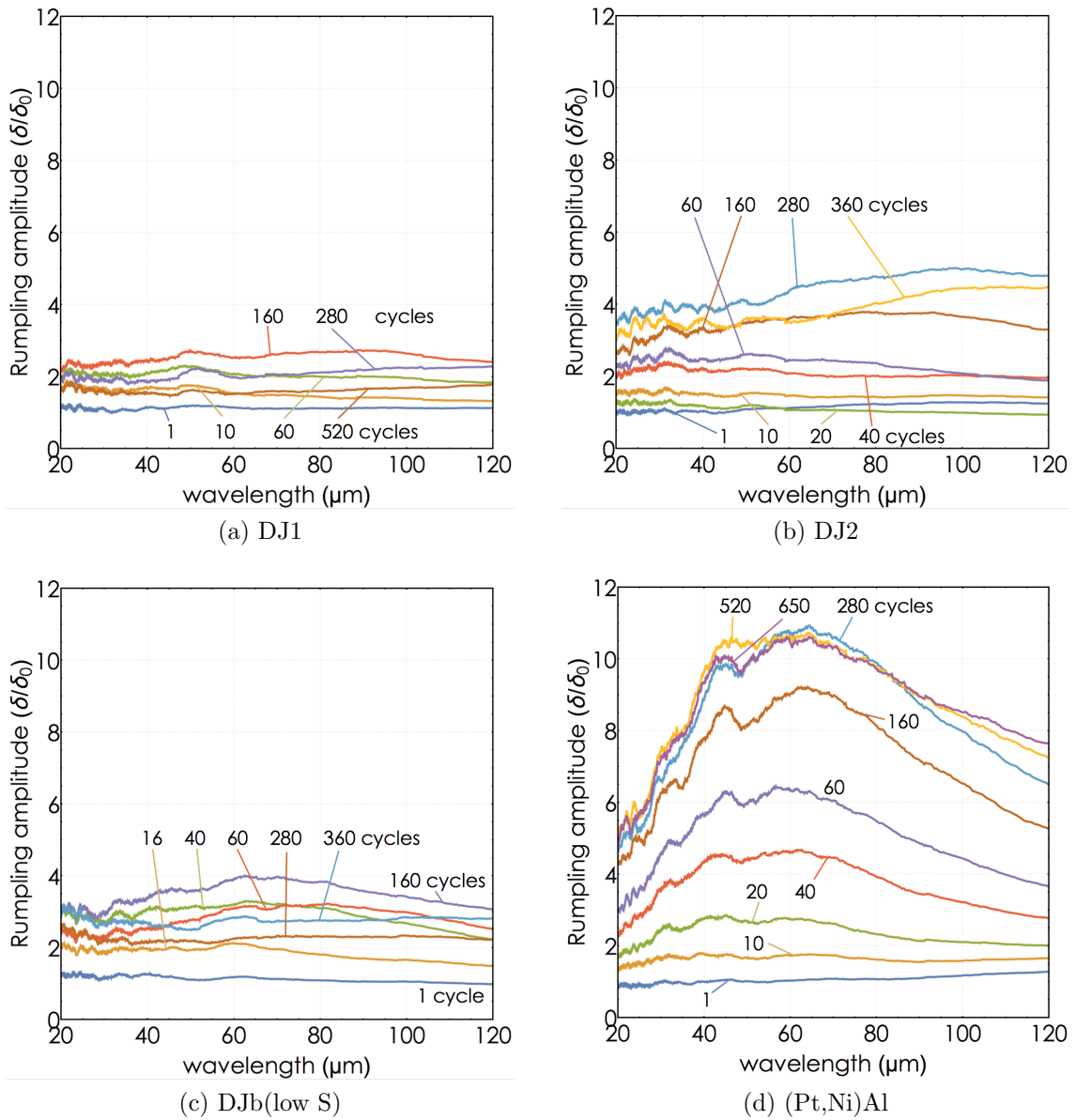


Figure 3.39: Radial averages of the FT algorithm applied to the surface topology scans of the DJ1, DJ2, DJb, and (Pt,Ni)Al coatings at various cycles throughout the cyclic oxidation test at 1163 °C.

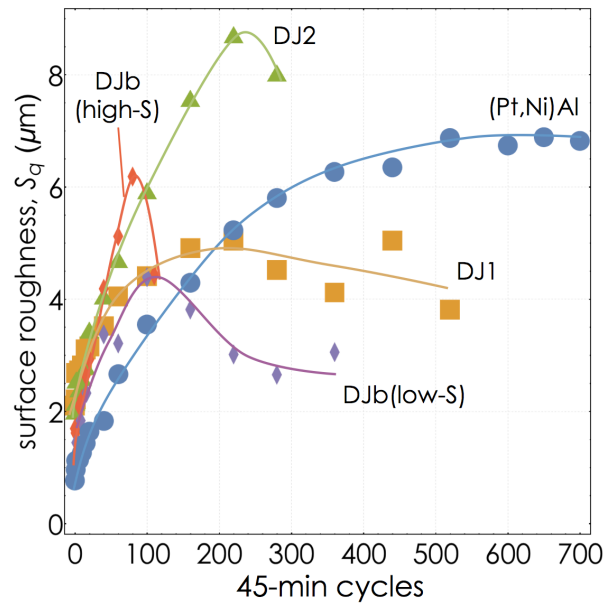


Figure 3.40: RMS surface roughness of the coatings as a function of 45-min cycles at 1163 °C.

(Pt,Ni)Al coating caused by rumpling. The initial roughness of all the coatings after grit blasting was in the range of 1-2  $\mu\text{m}$ . The DJ2 coating, which exhibited faster mass gain and faster oxide spalling compared to the DJ1 composition, had the largest increase in surface roughness maximum at about 9  $\mu\text{m}$ . The roughness of the  $\gamma'$  coatings did tend to decrease once TGO spalling became prevalent. This is because the thick oxide scales contained many inhomogeneities that are all removed from the surface when a section of TGO spalls.

A plot showing the integrated exposure of the bond coat surface, correlating to the area of full-thickness TGO that spalls from the coating during cyclic oxidation, is in Figure 3.41. Both of the DJb coatings again had the fastest rate of TGO spalling. However, the two  $\gamma'$  coatings were much more comparable to the (Pt,Ni)Al coating at this temperature, compared to the same measurement conducted during oxidation at 1204 °C (Figure 3.27). As shown in the previous section, this measurement does not

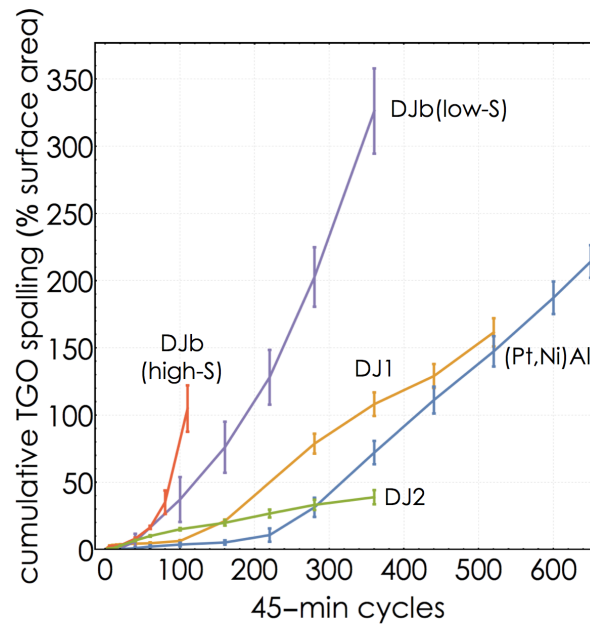


Figure 3.41: Accumulated failure of the TGO-bond coat interface as a function of 45-min cycles at 1163 °C. The TGO regrows and can spall from the same place more than once, resulting in values that exceed 100%.

account for oxide failure that occurs within the TGO and does not expose the bond coat surface.

Figure 3.42 shows the cross sections of the coating taken at the end of cyclic oxidation testing. These cross sections of the DJ2 coating show evidence of TGO fracture within the scale such as occurred during the furnace cycle test of the TBC system. This explains why the integrated TGO spalling value rate for the DJ2 coating (Figure 3.41) is much lower than the mass change would suggest (Figure 3.37). The DJ1 coating had a fairly thick and continuous spinel layer on top of the  $\text{Al}_2\text{O}_3$  by the end of the oxidation life. This is accompanied by a thick  $\gamma$  layer at the top of the bond coat, right below the TGO. Similar behavior is seen in the DJ2 coating, although evidence of TGO fracture exists because the spinel layer is not continuous and the oxide appears thinner in some locations. The DJb(low-S) coating transformed to  $\gamma+\gamma'$  by 360 cycles and exhibited a thin but persistent layer of spinel oxide on top of the TGO. In contrast, the DJb(high-S)

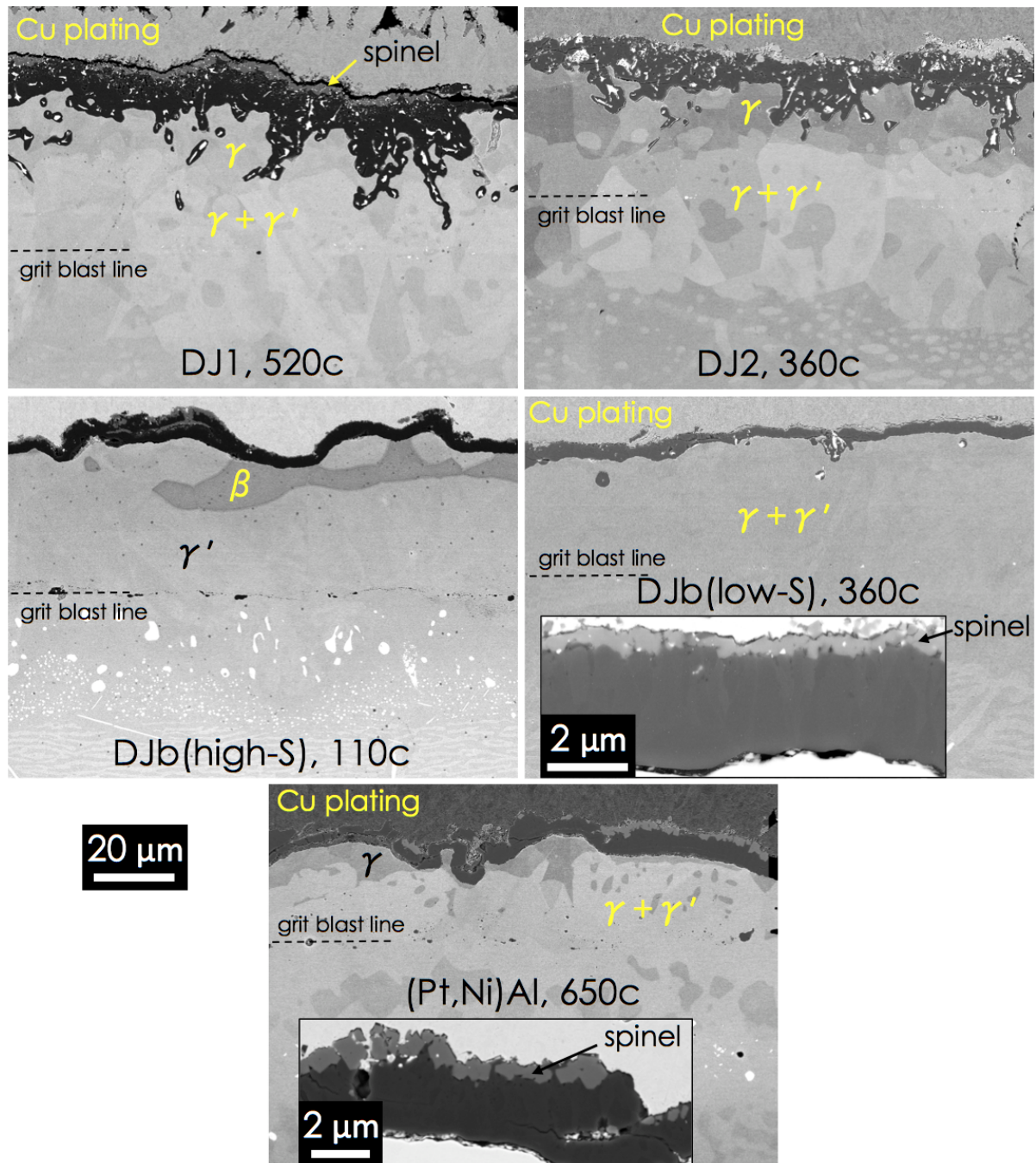


Figure 3.42: Cross sections of the cyclic oxidation specimens after testing at 1163 °C. The number of thermal cycles that each sample experienced is listed next to the sample name. All large micrographs are at the same magnification and the 20  $\mu\text{m}$  scale bar applies to all except the two insets showing detailed views of the thermally grown oxides on two  $\beta$  coatings.

coating, which still maintained some of the  $\beta$  phase, and therefore was in the  $\beta+\gamma'$  phase region, did not show a continuous spinel layer at the top of the TGO. Interestingly, the (Pt,Ni)Al coating, which generally has excellent oxidation properties, is beginning to develop a spinel layer at the top of its TGO as well. This is correlated with the transformation of the coating to  $\gamma+\gamma'$  due to the loss of Al. However, the bulk of the oxide scale on this coating still appears to be primarily  $\text{Al}_2\text{O}_3$  and is thin and relatively passivating.

### 3.5.3 Chemical degradation of DJ1 coating

A comparison of the cyclic oxidation and TBC furnace cycling behavior of the DJ1 coating suggests that the failure of the TBC system was ultimately due to the formation of spinel oxides on top of the TGO. These oxides are detrimental to TBC life because they have negligible fracture toughness and can lead to brittle fracture at the topcoat-TGO interface [10]. This allows the spinel layer to dissolve the bottom of the YSZ and destroy the bond between the topcoat and TGO. Figure 3.43 shows more detail of the spinel evolution. There are only isolated pockets of spinel oxide on top of the TGO at 25% of the TBC life. These pockets begin to grow and link up midway through the coating life; by the end of life the spinel has formed a continuous layer between the topcoat and the  $\text{Al}_2\text{O}_3$ . This spinel layer causes TGO-topcoat separation and is also susceptible to fracture as shown in the bottom right image of Figure 3.43.

Electron dispersive X-Ray spectroscopy (EDS) measurements of the DJ1 coating midway through life demonstrate the composition of the spinel layer and the cause of its formation. Figure 3.44 shows the Ni, Co, Hf, Ta, and Cr signals from an EDS map that were taken after 320 cycles at 1163 °C. Co and Cr segregate to the  $\gamma$  phase while Ta and Hf segregate to the  $\gamma'$  phase. Formation of the  $\gamma$  phase near the TGO is driven primarily

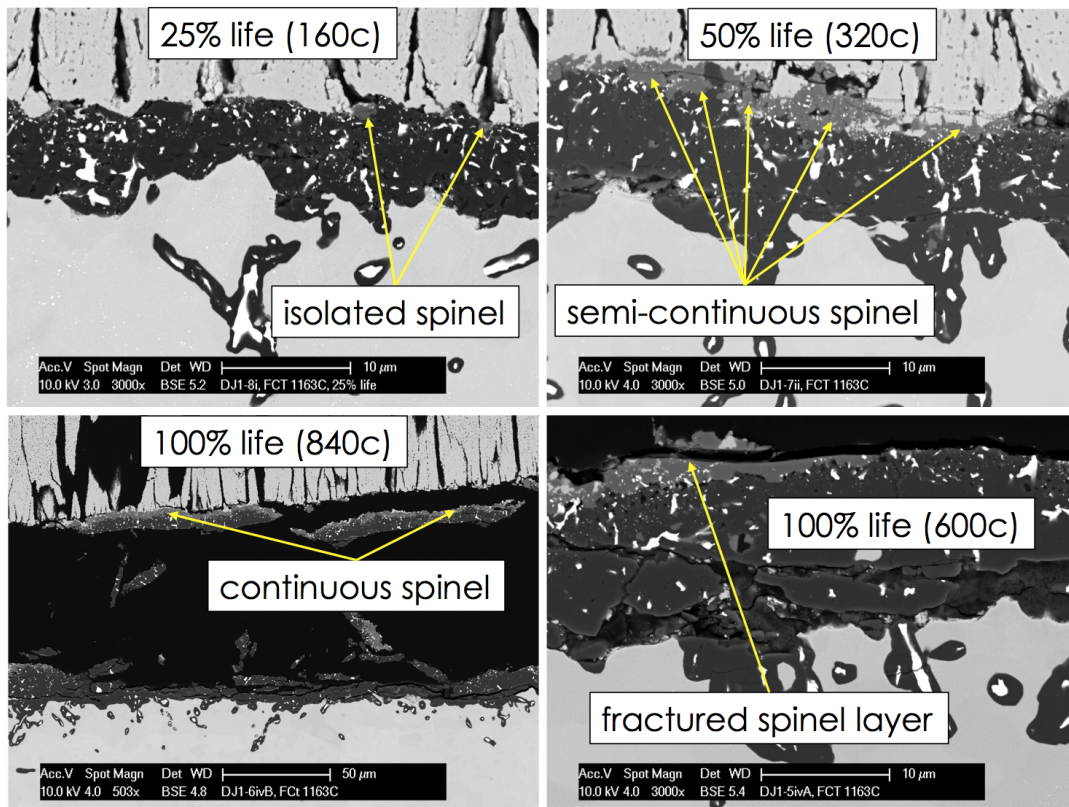


Figure 3.43: Evolution of the TGO on the DJ1 coating shows isolated pockets of spinel that appear on the top of the  $\text{Al}_2\text{O}_3$  layer at 25% of the coating life. The spinel layer is semi-continuous by 50% of the coating life. By the end of life the spinel layer is thick and continuous; a combination of dissolution of the YSZ and fracture in the spinel layer causes detachment of the ceramic topcoat and failure of the TBC system.

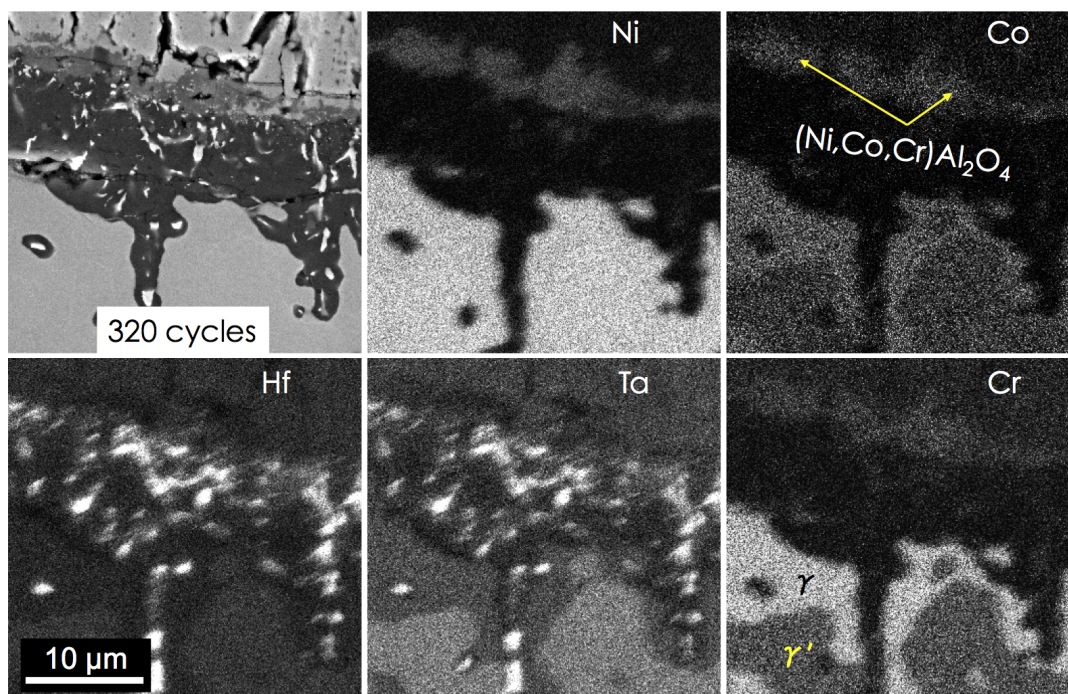


Figure 3.44: EDS measurements of the DJ1 coating after 320 cycles at 1163 °C, approximately 50% of the TBC life of the coating.

diffusion of Cr from the substrate, rather than by Ni diffusion. The  $\gamma'$  phase of this coating contains more nickel than the  $\gamma$  phase. Non standardized EDS measurements indicated that the composition of  $\gamma$  below the TGO contained 10.5 Al, 11.5 Cr, 3 Ta, 7 Co (in at%) whereas the  $\gamma'$  phase below had a composition that was approximately 16.5 Al, 3 Cr, 6 Ta, 4 Co (at%). As shown in Figure 3.43, the growth of the spinel correlates with presence of the Cr-enriched  $\gamma$  phase below the TGO. This spinel is a mixed spinel of the form  $(\text{Ni,Co,Cr})\text{Al}_2\text{O}_4$ , as seen by the presence of these species in the oxide phase above the  $\text{Al}_2\text{O}_3$ .

### 3.5.4 Discussion

Table 3.4 shows a summary of the cycles to failure of the experimental coatings in both the furnace cycle test with the topcoat and in the cyclic oxidation tests. This table

also indicates the primary failure location of the the TBC system as occurring at either the topcoat-TGO or TGO-bond coat interfaces or within the TGO itself as for the DJ2 coating. The TBC life is the most important measure for bond coat assessment because it evaluates the ability of the bond coat to hold the TBC system together; it is useful to compare this lifetime to the cyclic oxidation lifetime to understand the limiting behavior of the TBC. The discrepancy in TBC and cyclic oxidation lifetime of the (Pt,Ni)Al coating suggests that the oxidation properties are much better than needed at 1163 °C because the oxidation lifetime is about 5-fold longer than the TBC lifetime. On the other hand, the  $\gamma'$  coatings, which have been designed as a balance between oxidation and strength, show TBC and oxidation lifetimes that are self similar and longer than the (Pt,Ni)Al coating. Ultimately, this indicates a change in failure mechanism from thermo-mechanical degradation in the (Pt,Ni)Al coating to thermo-chemical degradation in the  $\gamma'$  coatings.

Table 3.4: Results of TBC furnace cycle and cyclic oxidation testing at 1163 °C with 45-min cycles. TBC life is the average number of cycles until  $\geq 20\%$  topcoat detachment for two samples and the sample standard deviation. Oxid. life is the actual or estimated number of cycles for net mass loss of oxidation samples. TBC failure loc. is the primary interface of failure resulting in TBC detachment. BC=bond coat, TBC=topcoat, TGO=thermally grown oxide.

coating	TBC life (cycles)	oxid. life (cycles)	TBC failure loc.
DJ1	700 $\pm$ 141	660	TBC-TGO
DJ2	390 $\pm$ 14	340	within TGO
DJb(low-S)	–	270	–
DJb(high-S)	120 $\pm$ 0	130	TGO-BC
(Pt,Ni)Al	210 $\pm$ 42	1070	TBC-TGO

The degradation of the topcoat bond strength via the formation of the spinel has been previously suggested by others [9, 10]. The growth of spinel oxide in binary systems is associated with Al depletion in traditional NiAl bond coats. However, for the  $\gamma'$  DJ1

bond coat, the growth of spinel was associated with the enrichment of Cr and depletion of Al to form a  $\gamma$  layer below the TGO. Diffusion in this direction will decrease the Al activity and increase the Cr and Ni activities. In this system, chemistry changes associated with formation of the  $\gamma$ -phase are associated with the critical activity levels that thermodynamically enable the the growth of  $(\text{Ni,Co,Cr})\text{Al}_2\text{O}_4$  [9]. The DJ1 system is similar to model NiAl systems studied elsewhere in that there is internal oxidation of  $\text{Al}_2\text{O}_3$  or the formation of stringers below the TGO scale, followed by the growth of spinel on top of the TGO [9, 120]. Both of these effects are characteristic of a decreasing Al activity with increase oxidation/diffusion. Because no NiO was detected or seen during these oxidation experiments, it is unlikely that the  $\text{NiAl}_2\text{O}_4$  growth is the result of a solid state reaction between NiO and  $\text{Al}_2\text{O}_3$ [121]. The delayed growth of spinel oxide on top of  $\text{Al}_2\text{O}_3$ -forming alloys with low Al content has been reported before [122].

### Modeling TBC failure with $\gamma'$ bond coats

Notwithstanding these complexities with regard to oxidation, it is of interest to understand and predict when a TBC system with a  $\gamma'$  bond coat will fail as compared to a  $\beta$ -phase coating. Jackson et al have developed an approach to evaluate the competition between the energy release rate for TBC or TGO delamination and the toughness of the topcoat and the TGO-bond coat interface [58]. In this treatment, the energy release rate for TGO delamination upon cooling scales with the steady state energy release rate for crack advance, Equation 1.1, which is a function of the TGO residual stress at room temperature as well as the TGO thickness.

$$G_0 = \frac{\sigma^2 h}{2E} \quad (1.1 \text{ revisited})$$

This driving force increases with the growth of the TGO, which can be expressed using parabolic kinetics (Equation 3.5). This energy release rate,  $\mathcal{G}_{BC-TGO}$ , opposes the bond coat-TGO interfacial toughness  $\Gamma_{BC-TGO}$ . The interfacial toughness  $\Gamma_{BC-TGO}$  decreases with time-at-temperature due to segregation of S impurities to the interface and ultimately the depletion of Al from the bond coat.

In addition to failure at the bond coat-TGO interface, there is also a driving force for fracture and delamination of the topcoat,  $\mathcal{G}_{topcoat}$ , that is due to the formation of cracks in the topcoat during service and imposed out-of-plane stresses during thermal cycling. Jackson et al suggest that rumpling is the primary means of increasing this driving force due to the development of strong in-plane stresses that can drive topcoat fracture in mode-II [58]. However,  $\mathcal{G}_{topcoat}$  also increases due to sintering and stiffening of the topcoat at service temperatures [10, 114]. Preexisting roughness and flaws in the bond coat also create out-of-plane stresses to drive topcoat fracture. The topcoat is expected to fail when the fracture energy release rate  $\mathcal{G}_{topcoat}$  exceeds the topcoat mode-II toughness,  $\Gamma_{topcoat}$ .

For the case of a  $\beta$ -phase coating the situation is relatively simple: rumpling and TBC sintering progressively increase  $\mathcal{G}_{topcoat}$  and the growth of the TGO progressively increases  $\mathcal{G}_{BC-TGO}$ . The toughness of the topcoat  $\Gamma_{topcoat}$  probably does not change rapidly during service until the bond coat is depleted of Al and spinel begins growing on top of the  $\text{Al}_2\text{O}_3$  and interacts with the topcoat. However, the TGO-bond coat interface toughness  $\Gamma_{BC-TGO}$  will undergo an initial rapid decay followed by a more moderate decrease due to sulfur and impurity segregation [123–125]. Failure of the TBC system occurs when either of these fracture driving forces exceeds the respective intrinsic material toughness. That is, when  $\mathcal{G}_{topcoat} \geq \Gamma_{topcoat}$  or  $\mathcal{G}_{BC-TGO} \geq \Gamma_{BC-TGO}$  the TBC system will fail near the bottom of the topcoat or at the TGO-bond coat interface as schematically shown in Figure 3.45. In this example, the rumpling of the bond coat at 1163 °C causes rapid

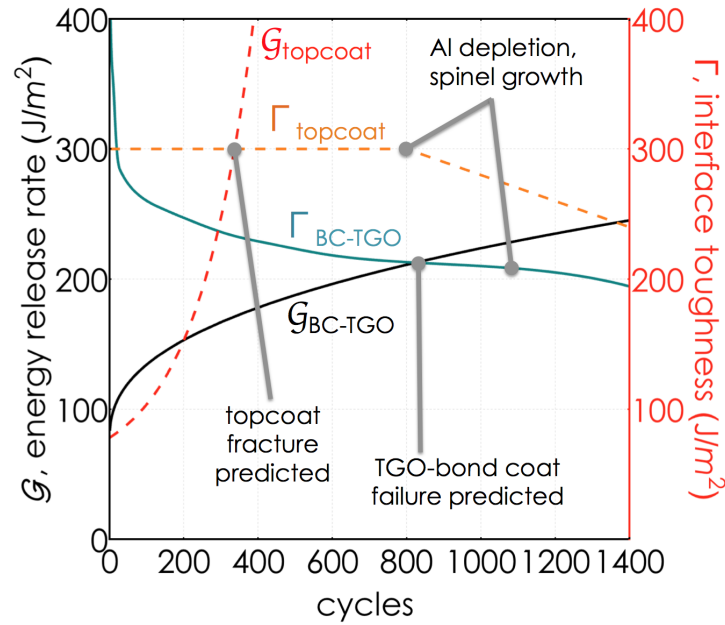


Figure 3.45: Prediction of competing failure mechanism in a TBC system with a (Pt,Ni)Al bond coat. TGO-bond coat separation occurs when the  $G_{BC-TGO} \geq \Gamma_{BC-TGO}$  and TBC fracture and spalling occurs when  $G_{topcoat} \geq \Gamma_{topcoat}$ . The faster mechanism determines the life of the TBC system.

increase in the driving force for topcoat fracture. Bond coat rumpling would proceed at a more moderate rate if the whole system were tested at lower temperatures where the bond coat has higher strength. Then, the driving force for topcoat fracture increases less precipitously and TBC system failure may occur instead at the TGO-bond coat interface at a later time. This suggests that there is a temperature dependence to the expected failure mode and coating lifetime in an ideal system.

Accurate prediction of TBC failure requires a thorough knowledge of the respective fracture driving forces and toughness value evolution with thermal cycling, temperature, and service. One can expect that the bond coat-TGO interface toughness  $\Gamma_{BC-TGO}$  will rapidly degrade once the bond coat is depleted in Al and begins to grow NiO and  $NiAl_2O_4$ . Further, it is expected that the topcoat toughness  $\Gamma_{topcoat}$  will also degrade once the spinel begins to grow on top of the TGO and react with YSZ although the functional

form of these degradations is either unknown or not in the public domain. The driving force for TGO spalling is relatively well understood, as mentioned previously. The strain energy release rate scales primarily with the TGO thickness and is therefore a function of both time and temperature as in Equation 3.5. The parabolic rate constants have been well-characterized for the NiAl system [126]. Fitting Grabke's oxidation data to an Arrhenius function gives a temperature-dependent parabolic rate constant for  $\alpha$ -Al<sub>2</sub>O<sub>3</sub>  $k_p(T) = k'_p \exp(-Q/RT)$  where  $k'_p = 59.23 \text{ g}^2/(\text{cm}^4 \text{ s})$  is the pre-exponential coefficient and  $Q = 381 \text{ kJ/mol}$  is the apparent activation energy for TGO growth on NiAl. This is converted to a relationship for the TGO thickness growth rate as:

$$h(t, T) = \frac{\bar{V}}{\bar{m}} \sqrt{k_p(T)t} \quad (3.10)$$

where  $\bar{V} = 25.62 \text{ cm}^3/\text{mol}$  is the molar volume of the Al<sub>2</sub>O<sub>3</sub> TGO,  $\bar{m} = 101.96 \text{ g/mol}$  is the molar mass of the TGO, and  $t$  is the oxidation time in seconds. This functional form of  $h$  can be substituted into Equation 1.1 to approximate how the TGO spalling driving force changes with time and temperature:

$$\mathcal{G}_{BC-TGO} \propto \frac{h(t, T)\sigma^2}{2\bar{E}} \quad (3.11)$$

The energy release rate for topcoat fracture increases from a combination of bond coat rumpling, which is a function of temperature and time, and topcoat sintering. In the absence of ample experimental data to understand how the energy release rate varies, one can assume the form suggested by Jackson et al [58] and Evans et al [10]:  $\mathcal{G}_{topcoat} = A \exp(Bt)$ . Here, it is assumed that:  $B = (10^{-3} \text{ s}^{-1}) \left(\frac{T}{900^\circ \text{C}}\right)^7$  for a  $\beta$ -phase coating. This describes the rumpling and sintering rates as increasing exponentially with temperature above 900 °C.

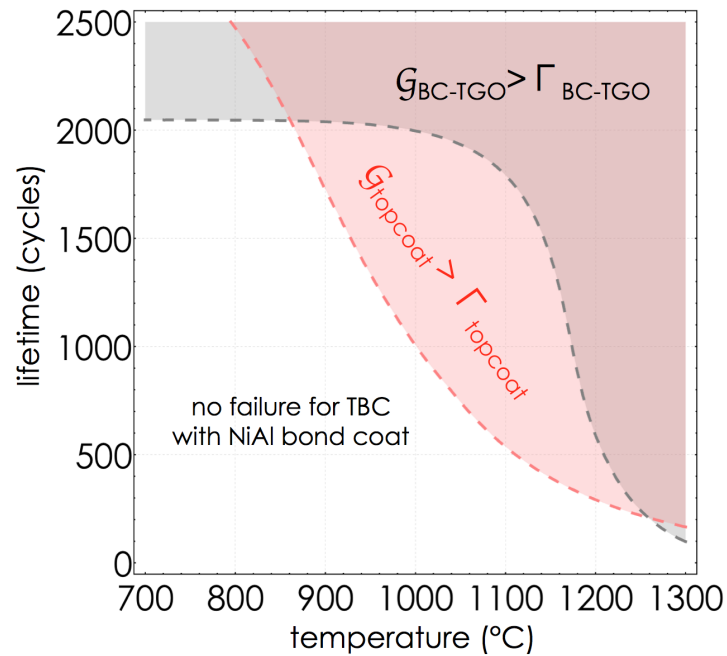


Figure 3.46: Schematic diagram showing cycling-temperature relationship for competing TBC system failure mechanisms –TGO spalling versus topcoat fracture –when using a (Pt,Ni)Al bond coat. Plot assumes 1 h cycles at testing temperature. In this example, rumpling is mostly nonexistent below 860 °C and the TBC ultimately fails due to loss of Al and a degradation of the TGO-bond coat interface toughness  $\Gamma_{BC-TGO}$ . Between 860-1250 °C the rumpling rate of the bond coat dominates the failure of the TBC. Above 1250 °C, the oxidation rate of the TGO leads to rapid increase in TGO thickness and a large TGO spalling driving force,  $G_{BC-TGO}$ .

Combining all of these effects, the two systems of equations shown above can be solved for the time  $t$  and temperature  $T$  expected to cause TBC system failure. A schematic example of this failure competition for material parameters representative of a (Pt,Ni)Al coating is shown in Figure 3.46. This plot shows the solutions to both systems of equations to determine TBC failure with 1 h thermal cycles. The pink highlighted region represents the combination of cycles (time) and temperature that are expected to cause failure due to fracture of the topcoat near the TGO interface. This occurs due to rumpling and topcoat sintering, which increase the driving force for topcoat fracture, and due to spinel growth on top of the  $\text{Al}_2\text{O}_3$  TGO forming a low-toughness layer below the topcoat. For this calculation, the decrease in topcoat toughness was modeled to occur linearly and decrease the YSZ mode-II toughness from  $300 \text{ J/m}^2$  at 800 cycles down to  $0 \text{ J/m}^2$  at 3800 cycles as a schematic representation of the YSZ- $\text{NiAl}_2\text{O}_4$  interaction because pure  $\text{NiAl}_2\text{O}_4$  has a very low fracture energy that is negligible compared to pristine YSZ [117, 118]. The gray highlighted region represents where the TBC would fail due to TGO spalling. The interface toughness is modeled to continually decrease similarly to that used in [58], except that the toughness decreases rapidly after 1500 cycles and reaches  $0 \text{ J/m}^2$  at about 2300 cycles to represent the effect of bond coat Al depletion, growth of  $\text{NiAl}_2\text{O}_4/\text{NiO}$ , and the resulting breakaway oxidation. The lowest number of cycles for a given temperature that satisfies either of these criteria (in the shaded regions) will cause TBC system failure. Clearly, the rumpling rate of the bond coat limits TBC lifetime for the majority of the temperatures of interest (900-1100 °C). The oxidation and TGO spallation is limiting TBC lifetime only at low and very high temperatures for this system.

For stronger coatings, such as the  $\gamma'$  phase, the rumpling rate will be diminished. This is described by decreasing, but not eliminating, the the power-law dependence of  $\mathcal{G}_{topcoat}$  because rumpling will no longer increase with temperature but the topcoat sintering

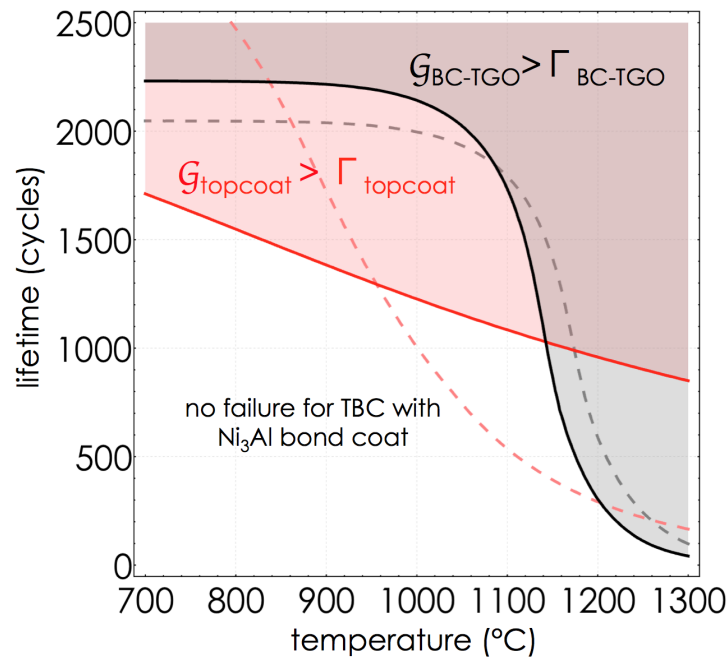


Figure 3.47: Schematic diagram showing the cycling-temperature relationship for competing TBC system failure mechanisms - TGO spalling versus topcoat fracture - when using a  $\gamma'$  bond coat. In this example, rumpling is nonexistent at all temperatures and only topcoat sintering impacts  $G_{topcoat}$ . Below about 1150 °C, the TBC ultimately fails due to a combination of decreasing TBC toughness due to reaction with the spinel layer growing above the TGO and sintering of the topcoat. At higher temperatures, the TGO growth rate is much faster and leads to coating failure if when the strain energy release rate exceeds the interface toughness. The dashed lines denote the failure zones for a (Pt,Ni)Al coating shown in Figure 3.46.

rate still remains unaffected. The oxidation rate on these coatings is also faster, and is described by increasing the parabolic rate constant. Furthermore, the presence of mechanical interlocking between  $\text{HfO}_2$  stringers and the bond coat and the presence of Hf at the interface can increase the interface toughness [101, 127]. To the same effect, the presence of Hf decreases the TGO growth stress and therefore decreases the driving force for TGO spalling [108, 128]. The poorer oxidation properties of this coating is predicted to have a plethora of effects on the behavior of the coating. First, the growth rate of  $\text{NiAl}_2\text{O}_4$  is predicted to start decaying the topcoat fracture energy (toughness) starting from the first cycle instead of after 800; the same discount rate ( $0.1 \text{ (J/m}^2\text{)}/\text{cycle}$ ) is used. Second, the presence of Hf leads to the growth of  $\text{HfO}_2$  stringers underneath the  $\text{Al}_2\text{O}_3$  layer is predicted to increase the TGO-bond coat interface toughness by forming a tortuous path for cracks at the interface [101]. This was modeled as a constant 15% increase of the initial interface toughness value to account for the increased surface area and possible mechanical interlocking. Finally, the oxidation properties of a  $\gamma'$  coating are different because the oxidation rate of the TGO is much higher; this was modeled by increasing the parabolic rate constant fivefold at all temperatures, which is similar to the effect between the DJb and DJ1 coatings from these experiments. Abatement of rumpling as a result of improved mechanical strength was modeled by decreasing the power-law relationship of the topcoat fracture driving force to so that  $B = (10^{-3}\text{s}^{-1})(\frac{T}{900^\circ\text{C}})^2$ . (A power of 7 was used for the rumpling (Pt,Ni)Al coating.)

A comparison TBC failure map generated using representative parameters for  $\gamma'$  coatings is in Figure 3.47. The shaded regions represent the same criteria as in Figure 3.46, and the dashed lines indicating the failure transitions for the (Pt,Ni)Al-based TBC are shown for comparison. Of interest, is that the total lifetime of the TBC system is predicted to improve in the range 950-1200 °C. It must be re-emphasized that this is a schematic representation to demonstrate what affects are anticipated; extensive exper-

imental measurements would be needed to quantitatively determine what temperature range and magnitude of TBC lifetime improvements are expected. However, the results of the present experiments corroborate the insight drawn from this model. The maximum improvement of cycle lifetimes occurs at about 1150 °C, where the  $\gamma'$  coating is predicted to have a lifetime of about 1000 cycles whereas rumpling ends the life of the (Pt,Ni)Al at about 400 cycles –a 2.5-fold improvement! This is in close agreement with the experimental results, which showed more than a three-fold improvement for the  $\gamma'$  layer (700 cycles versus 210 cycles at 1163 °C). Above 1200 °C, the oxidation rate of the  $\gamma'$  coating is fast and failure due to the thick TGO spalling dominates the TBC lifetime. It is noteworthy that a comparison of the solid black line with the dashed gray line indicates that the oxidation lifetime of the  $\gamma'$  coating is about 800 cycles shorter than that of the (Pt,Ni)Al coating at about 1150 °C; this is in accordance with the present experiments. Below about 950 °C, however, the lifetime of the topcoat is limited by the growth of spinel at the topcoat-TGO interface and the sintering of the topcoat, which indicates that the total TBC lifetime is predicted to be shorter than the (Pt,Ni)Al coating. This trade-off in behavior is important to consider when designing a TBC system. Depending on the exact time-temperature relationships of the pertinent properties, one type of coating is expected to outperform another.

The simplifications and assumptions in the previous model must be considered when drawing fundamental insight. First, the rate of bond coat-TGO interface toughness degradation was modeled as being independent of temperature for simplicity, although there is some evidence that it is a weak function of temperature [127]. Second, the Al-depletion of the bond coat and growth of spinel and/or decay of the topcoat fracture toughness was also not temperature-dependent. Third, it was assumed that only  $\alpha$ -Al<sub>2</sub>O<sub>3</sub> grows as the TGO at all temperatures. It is likely that metastable transition aluminas will dominate TGO growth at low temperatures depending on the coating composition and

pre-oxidation pretreatment choices. These oxides generally have a faster growth rate than would be calculated by extrapolation of corundum data collected by Grabke [126]. Last, the phenomenological description of spinel growth having a linear impact on the TBC fracture toughness requires experimental verification. Regardless, this type of analysis can be useful when designing BC systems for maximum lifetime in service, permitting semiquantitative assessments of where the trade-offs between rumpling and oxidation exist and can be used to proper advantage. This model also helps to explain the reason that the DJ1 and DJ2 coatings were able to outperform the (Pt,Ni)Al coating in the elevated temperature TBC lifetime experiments, namely that the  $\gamma'$  coatings are able to slow down the driving force for topcoat delamination by inhibiting rumpling while still maintaining adequate oxidation properties.

### 3.6 Chapter summary

A direct comparison of cyclic oxidation and furnace cycled TBC system performance has been made between a series of  $\gamma'$  and  $\beta$  bond coats. It has been shown that the TBC lifetime of the  $\gamma'$  bond coats is 2-3x longer than a benchmark  $\beta$ -phase (Pt,Ni)Al coating at 1163 °C. The  $\gamma'$  coatings have a longer TBC system lifetime even though they have a shorter oxidation lifetime at this temperature. This is due to a transition from thermo-mechanical degradation of the TBC system in the (Pt,Ni)Al coating to thermochemical degradation in the  $\gamma'$  system. The  $\gamma'$  TBC system has a longer lifetime at this elevated temperature because it inhibits rumpling. A semi-quantitative model has been proposed to explain the difference in performance between the two coatings. Best estimates of material properties suggest that a  $\gamma'$  bond coat will have superior TBC system lifetime to a (Pt,Ni)Al coating in the 950-1200 °C temperature range. The next chapter will

discuss the behavior of these high-strength  $\gamma'$ -phase bond coats when used in a bilayer  $\gamma'+\beta$  architected bond coat.

# Chapter 4

## Bilayer $\gamma' + \beta$ Bond Coats

The previous chapter demonstrated the performance of the monolayer  $\gamma'$  bond coats in cyclic oxidation and TBC system furnace cycle testing. It was shown that the both of the  $\gamma'$  coatings, DJ1 and DJ2, provided longer TBC lifetimes at 1163 °C than the (Pt,Ni)Al coating despite less optimal oxidation behavior. The  $\gamma'$  coatings increased TBC system life due to their higher strength, which enabled them to resist rumpling deformation during thermal cycling. After high temperature cycling, the  $\gamma'$  coatings transformed to the  $\gamma$  phase and formed spinel-type oxides on top of the TGO, which weakened the TGO-topcoat bond and ultimately resulted in topcoat spallation. It is, therefore, expected that the lifetime of  $\gamma'$ -based TBC systems can be improved further by improving the oxidation properties.

A comparison of the oxidation behavior of the DJ1/DJ2 and DJb coatings (see Figure 3.3) shows that the TGO grown on the  $\beta$ -phase DJb coating is significantly more dense and thinner than the TGO grown on the  $\gamma'$ -phase DJ1 and DJ2 coatings. The DJ1 coating would be more practical as a bond coat if the  $\gamma'$  coating would grow an oxide scale more similar to the  $\beta$ -phase coatings. To this end, a series of thermodynamically compatible  $\gamma' + \beta$  bilayer coatings were designed. These coatings were then fabricated by

depositing 45  $\mu\text{m}$  of a  $\gamma'$  layer followed by another 5  $\mu\text{m}$  of the DJb  $\beta$  layer. The thin  $\beta$  phase permits establishment of a thin and dense  $\text{Al}_2\text{O}_3$  TGO before transforming to the  $\gamma'$  phase. Thus the benefit of the slow-growing  $\text{Al}_2\text{O}_3$  scale can be combined with a rumple resistant under-layer. In theory, this combination will delay the onset of the  $\gamma'\rightarrow\gamma$  and associated growth of spinel oxides that decay the topcoat toughness and bond with the TGO. In some sense, once a better-performing (high-strength) bond coat system has been identified for high-temperature use, it is a matter of TGO engineering to further improve the TBC system. This topic will be discussed further in the following chapter. The ideal TGO would possess low growth stresses, be slow growing, passivating, and non-reactive with the topcoat. The TGO strain energy release rate (Equation 1.1) suggests that decreasing the modulus or increasing the thermal expansion coefficient of the TGO would also be beneficial in terms of decreasing the driving force for TGO spalling, but it not well known how these modifications would impact the other properties of the TGO.

This chapter will discuss the performance of the  $\gamma'+\beta$  bilayer bond coats in isothermal oxidation tests, cyclic oxidation tests without the ceramic topcoat, and their performance as part of TBC systems. They will be compared to both their monolayer counterparts and the (Pt,Ni)Al benchmark standard. It is found that the bilayer architecture exhibits a synergistic improvement in both the cyclic oxidation and TBC system life over either of the individual monolayered coatings. Furthermore, the last part of the chapter will cover the effects of high- and low-S  $\beta$  layers in these systems. Comparisons and conclusions will be drawn from cyclic oxidation testing at 1204 and 1163  $^\circ\text{C}$  as well as TBC testing. It will be demonstrated that the improvements gained with the bilayer system can be easily lost due to contamination in the 5  $\mu\text{m}$  layer.

## 4.1 Experimental sample preparation

Bilayer overlay bond coats with thick (45  $\mu\text{m}$ ), high-strength  $\gamma'$  layers (DJ1) topped by thin  $\beta$  layers (5  $\mu\text{m}$ ) were deposited onto (001) oriented single crystal René N5 disk substrates ( $\varnothing = 25.4$  mm,  $h = 3.2$  mm) using ion plasma deposition as discussed previously (Chapter 2). Separate  $\beta$  layers consisting of a high-S/low-Hf composition (DJb(high-S)) and a low-S/high-Hf composition (DJb(low-S)) were used to evaluate the impact of sulfur segregation and gettering near the surface of the bond coat. Measured compositions of the coatings tested are listed in Table 2.3. The high-S  $\beta$  composition had 15 wt.ppm S and 0.01 at% Hf while the low-S  $\beta$  composition had about 4 wt.ppm S and 0.04 at% Hf.

Micrographs of the coatings in the as-heat treated condition are in Figure 4.1. All coatings exhibited an interdiffusion zone (IDZ) with the substrate. Oxidation was carried out in a bottom-loading Rapid Temp furnace (CM Furnaces) in Santa Barbara, CA. The thermal cycle consisted of a nominal 15-min ramp from 93  $^{\circ}\text{C}$  to test temperature (1163  $^{\circ}\text{C}$ ), a 45-min hold, followed by 12 min of forced air cooling to below 93  $^{\circ}\text{C}$ . Samples were periodically removed for mass, X-ray diffraction (XRD), surface topology (3D profile), and oxide coverage analyses as discussed previously. Surface topology was analyzed with a Veeco white light interferometer (WYKO NT1100) using the vertical scanning interferometry (VSI) mode with a sub-micron lateral resolution and approximately nanometer vertical resolution. A standard (Pt,Ni)Al coating fabricated by GE Aviation in Evendale, OH by electroplating Pt followed by vapor phase aluminization of the disk was used as a benchmark.

### 4.1.1 Furnace cycling with a YSZ topcoat

Because the chemistry and properties of the bond coat exert a strong influence on the failure mechanisms of the entire system, including the ceramic topcoat, samples with

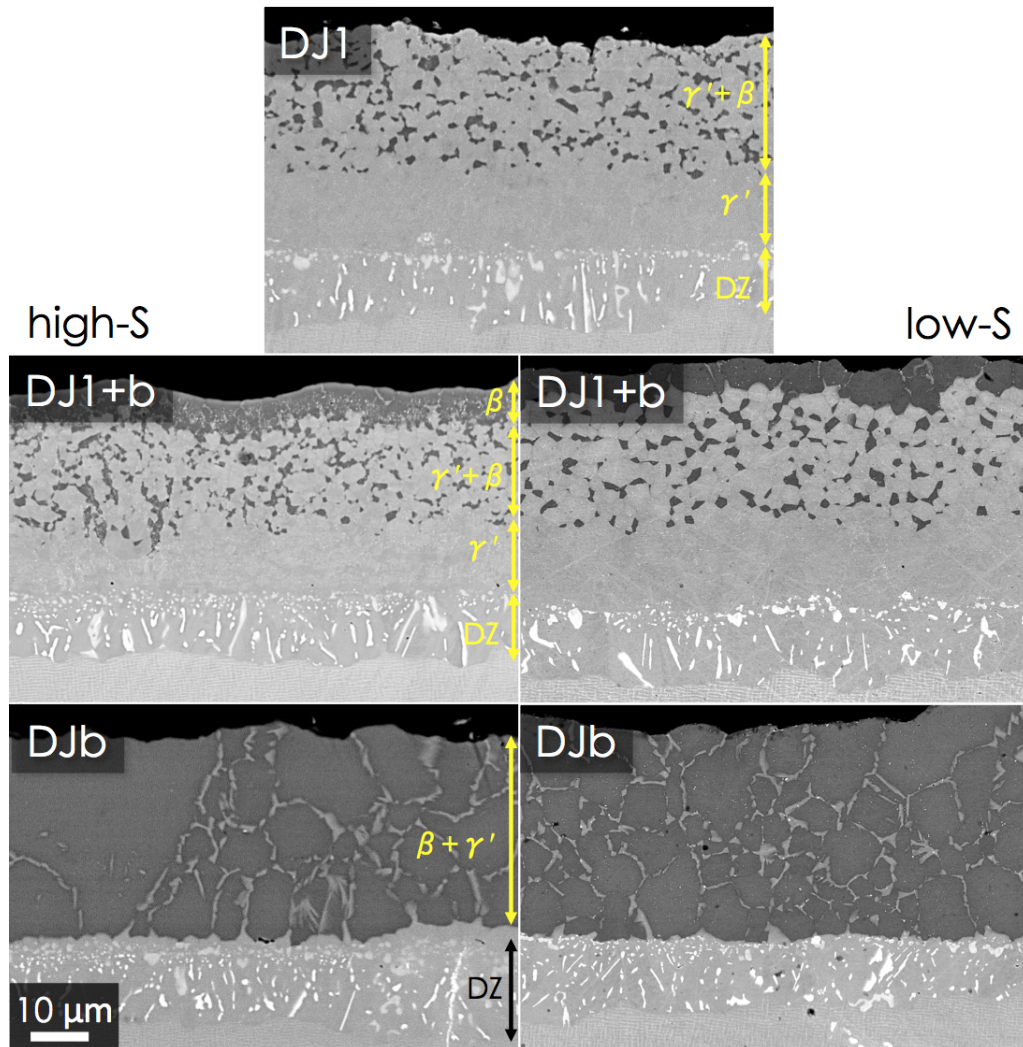


Figure 4.1: Cross sections of the  $\gamma'$  and  $\gamma'+\beta$  bilayer experimental coatings after a 4-hour vacuum heat treatment at 1080 °C. 10  $\mu\text{m}$  scale bar applies to all images.

130  $\mu\text{m}$  of 7wt% yttria stabilized zirconia (7YSZ) deposited by electron beam physical vapor deposition (EB-PVD) were fabricated for testing [58]. Samples were coated on one side, heat treated along with the other oxidation specimens, and then coated by Praxair Surface Technologies in Indianapolis, IN. Two each DJ1, DJ1+DJb(high-S), DJb(high-S), and (Pt,Ni)Al samples were furnace cycled under the same conditions as described above. The end-of-life for each sample was determined by the cycle at which  $\geq 20\%$  of the topcoat became detached (spalled or delaminated) from the sample. Low-angle incident light and image analysis methods were used to quantitatively determine percent area detached. A separate TBC test was conducted with two DJ1 and three DJ1+DJb(low-S) coated substrates. The EB-PVD topcoats for these samples were deposited in a separate coating run from the rest of the specimens discussed in Chapter 3. For this reason, the TBC lifetimes of these samples will be relative only to one another due to variability in the industrial top-coating process producing differing TBC microstructures, as discussed in Section 3.5.

## 4.2 Isothermal oxidation of bilayer bond coats

The bilayer coatings were subjected to the same series of isothermal oxidation tests described in Section 3.1. The measured oxide thicknesses at the specified conditions are in Figure 4.2 and the temperature-dependent parabolic fit parameters are listed in Table 4.1. In general, the addition of the  $\beta$ -phase top-layer did not dramatically change the long-time oxidation rates of the coatings, at least within the experimental measurement error. More measurements or thermo-gravimetric analysis would be needed to make a more accurate determination of any significant changes in oxidation rates between the monolayer and bilayer coatings.

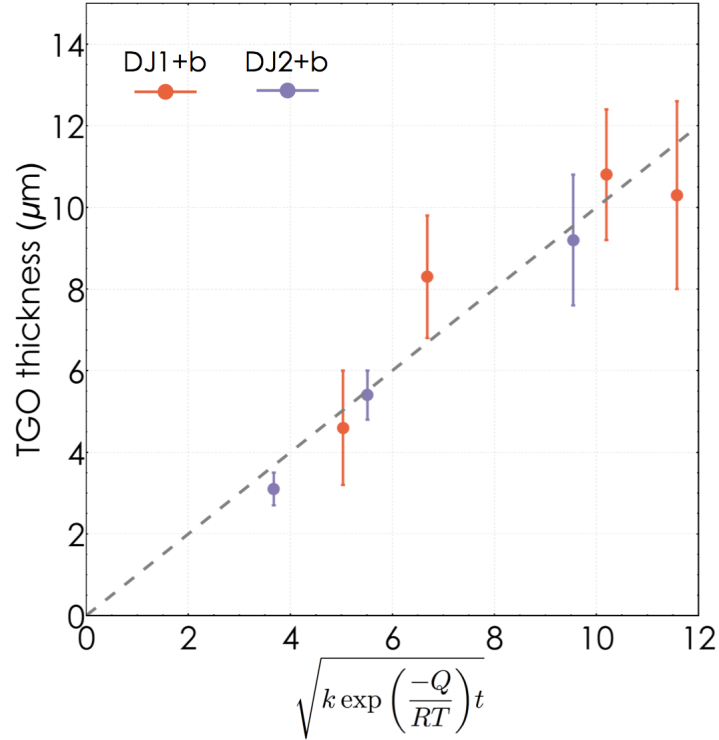


Figure 4.2: TGO thickness as a function of normalized oxidation time and temperature from four experiments: 1093 °C (250 h), 1163 °C (250 h), 1204 °C (50 h), and 1204 °C (150 h) for the two bilayer coatings tested with 45  $\mu\text{m}$  of DJ1/DJ2 + 5  $\mu\text{m}$  DJb(high-S). Error bars represent the standard deviation of all the measurements of the TGO thickness made from each sample. The data were fit simultaneously to Equation 3.5 and the results are in Table 4.1.

Table 4.1: Fitting parameters for the temperature-dependent parabolic oxidation rate Equation 3.5 for the two bilayer experimental coatings.

	$k$ ( $\text{cm}^2/\text{s}$ )	$Q$ ( $\text{kJ}/\text{mol}$ )
DJ1+DJb	1.1	329
DJ2+DJb	0.56	325

A metallographic cross section of the DJ1+DJb coating after 250 h isothermal oxidation at 1163 °C is in Figure 4.3. This coating developed a thick  $\gamma$  layer at the top of the bond coat, below the TGO. The transformation from  $\gamma' \rightarrow \gamma$  is likely aided by the high chromium content that was in the DJb layer, a concentration about two-fold higher than in the  $\gamma'$  coating. Of note in this micrograph is that there is no  $\text{NiAl}_2\text{O}_4$  spinel present at the top of the TGO, indicating that the presence of the  $\beta$  layer has inhibited the growth of this layer. However, the TGO still contains similar porosity to that grown on the monolithic DJ1 coating. Although the isothermal oxidation behavior of the bilayer coatings are very similar to the monolayer coatings, the next section will demonstrate that the cyclic oxidation properties of the  $\gamma'$  coatings are drastically enhanced by the addition of 5  $\mu\text{m}$  of  $\beta$ -phase on the top.

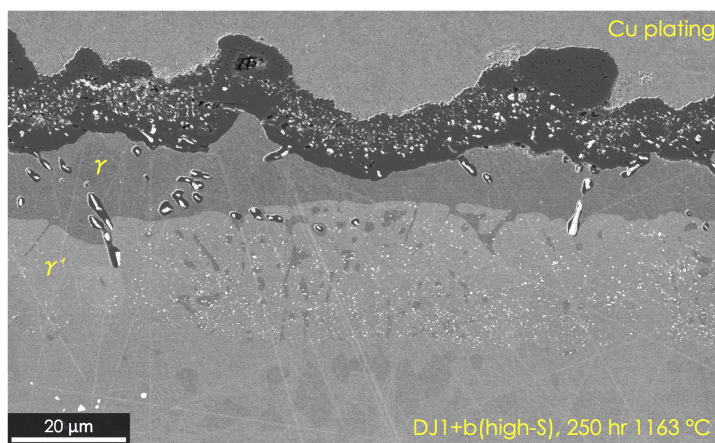


Figure 4.3: Cross section of the DJ1+DJb(high-S) bilayer coating after 250 h isothermal oxidation at 1163 °C. While the oxide thickness is identical to the DJ1 monolithic coating, the addition of the bilayer has inhibited the growth of spinel oxide on top of the TGO (compare to Figure 3.3).

### 4.3 Cyclic oxidation of bilayer coatings at 1163 °C

The two bilayer coatings, DJ1+DJb(low-S) and DJ2+DJb(low-S), were fabricated as discussed in Chapter 2 and put through the same cyclic oxidation testing at 1163 °C to

evaluate the oxidation, rumpling, and oxide adhesion properties of the bilayer architectures.

### 4.3.1 Results

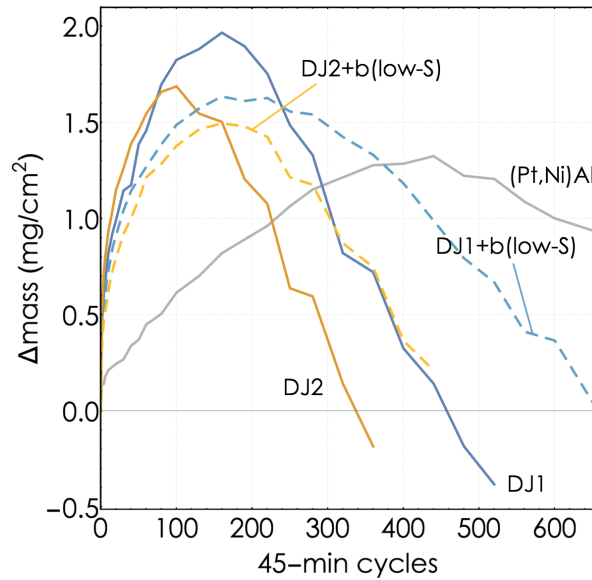


Figure 4.4: Surface area-normalized mass change as a function of 45-min oxidation cycles at 1163 °C for bilayer and select monolithic coatings. DJ1+b(low-S) is a bilayer with 45  $\mu\text{m}$  DJ1 and 5  $\mu\text{m}$  DJb(low-S) and similarly for DJ2+b(low-S).

Figure 4.4 shows the comparison of the area-normalized mass change of the bilayers in comparison with their  $\gamma'$  monolithic counterparts and the (Pt,Ni)Al coating for reference. In both cases, the bilayer architecture increased the cyclic oxidation lifetime by more than 40% compared to the monolithic  $\gamma'$  coating. The  $\beta$  layers served to decrease the overall rate of mass gain at the beginning of the test and also limited the maximum mass gain of the samples. This indicates that the  $\beta$  top-layer is promoting the growth of denser thermally grown oxide scales, but that these scales are spalling from the samples at a smaller average thickness compared to the monolithic  $\gamma'$  coatings. However, the TGO

spalling rate is slower on the bilayer coatings, as indicated by the shallower slope in the mass-loss portion of the curves.

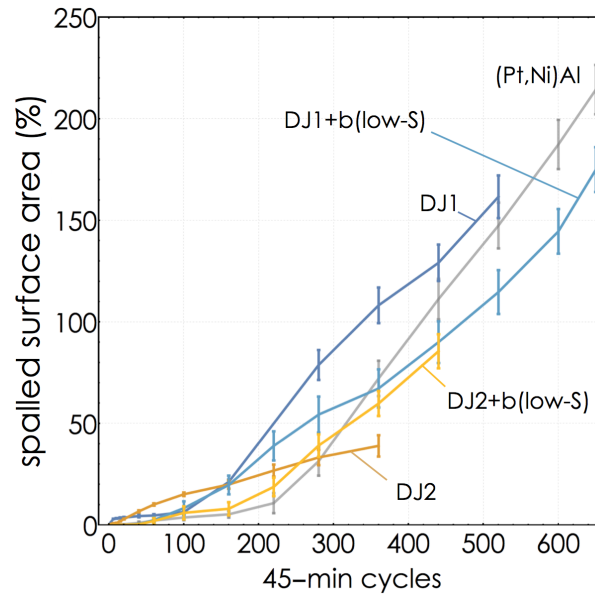


Figure 4.5: Cumulative percent of exposed bond coat surface as a function of 45-min oxidation cycles at 1163 °C for bilayer and select monolithic coatings. As discussed in the Chapter 3, rate of exposed bond coat is low in the DJ2 coating because the TGO was fracturing and spalling from within the scale and not exposing the bond coat.

A comparison of the cumulative TGO spalling measured with backscattered electron images is in Figure 4.5. This comparison shows the integrated percent of the surface area that is exposed each cycle due to full-thickness TGO spalling from the bond coat. The addition of the  $\beta$  top-layer to the DJ1 coating decreases the rate of exposed bond coat surface after about 150 cycles, in corroboration of a slower TGO spalling rate discussed in the previous paragraph. The bilayer DJ2+DJb coating had an initially lower spalling rate than both the DJ2 and DJ1+DJb coatings. However, comparison is difficult because the TGO-spalling rate was not accurately measured in the monolithic DJ2 coating due to significant intra-scale fracture and spalling once the DJ2 coating thickness became substantial (discussed in Section 3.4.2). The rate of TGO loss from the DJ2+DJb bilayer was obviously decreased based on the mass change measurements in Figure 4.4. In

general, it appears that the addition of a thermodynamically compatible  $\beta$ -phase top-layer improves the oxidation performance of the two  $\gamma'$ -phase coatings.

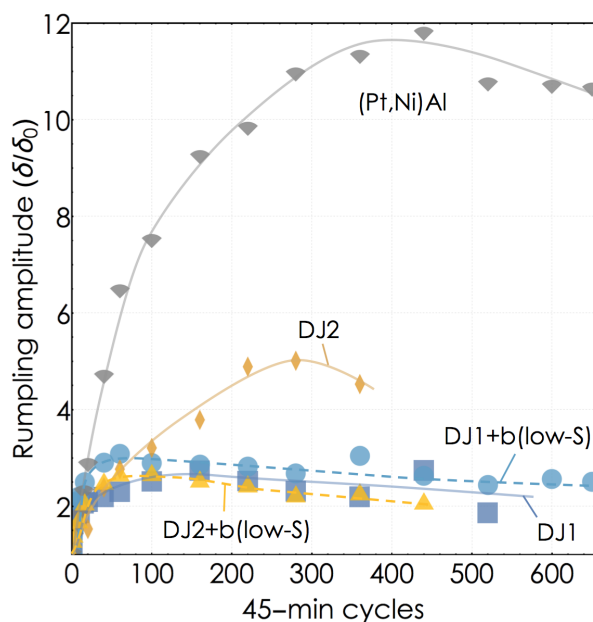


Figure 4.6: Amplitude of the maximum amplitude periodic surface features as a function of 45-min oxidation cycles at 1163 °C for bilayer and select monolithic coatings. The  $\gamma'$  and  $\gamma'+\beta$  coatings did not exhibit a dominant rumpling wavelength as the (Pt,Ni)Al coating did.

Having demonstrated that the oxidation performance of a  $\gamma'$ -phase coating can be improved with the addition of a thin  $\beta$ -phase layer, it is also essential to determine the impact on the rumpling rates of the coatings. Figures 4.6 and 4.7 show the change in peak rumpling wavelength amplitude and the root-mean-square surface roughness of the coatings during thermal cycling at 1163 °C. The rumpling measurements in Figure 4.6 indicate that the DJ1+DJb coating had a slight increase in the peak undulation amplitude during the first 100 cycles, but then had the same behavior as the monolithic DJ1 coating. Both rumpling and  $S_q$  measurements of the DJ2+DJb bilayer demonstrate that the improved oxidation properties dampen the precipitous roughness increase that was observed in the monolithic DJ2 coating. In short, the thin  $\beta$ -phase top-layers had no

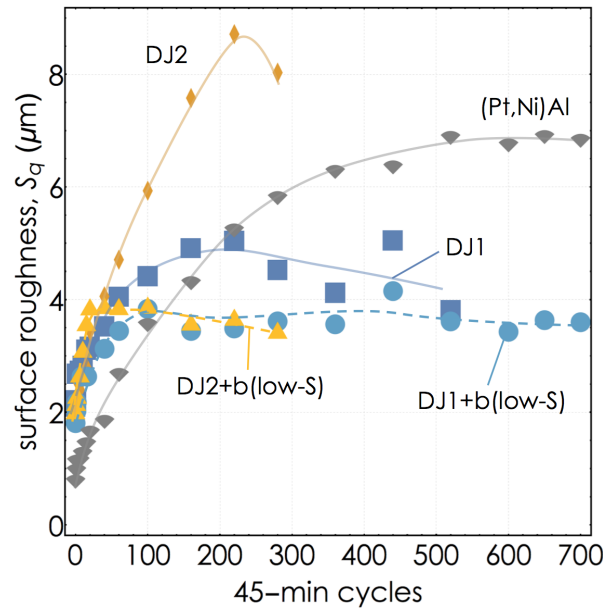


Figure 4.7: Root-mean-square (RMS) surface roughness,  $S_q$  as a function of 45-min oxidation cycles at 1163 °C for bilayer and select monolithic coatings.

adverse effects to the rumpling behavior of the  $\gamma'$  coatings, despite the addition of a thin layer that was shown to be susceptible to rumpling.

Metallographic cross sections from the DJ1+DJb bilayer samples cycled for 220 and 650 cycles at 1163 °C are in Figure 4.8. The peak in the mass-change plot (Figure 4.4) for the DJ1+DJb coating occurred at about 220 cycles. No signs of rumpling are present in either of the low-magnifications micrographs. An Al-depleted and Cr/Co-enriched  $\gamma$  layer formed beneath the TGO within the first 200 cycles of testing and the thickness of this layer continually increased with time, having about 10  $\mu\text{m}$  thickness (20% of the coating thickness) when the coating began to experience net mass loss. The top of the TGO shows the presence of Ni-Co-Cr spinel oxides similar to those seen on the monolithic DJ1 coating during cyclic oxidation. The thickness of the spinel layer is thicker at 220 cycles than it is at 250 cycles, due to spalling and regrowth of the TGO between this time. Figure 4.5 indicates that less than 40% of the scale would have spalled from the bond coat by 220 cycles, but on average, the entire scale would have spalled off almost

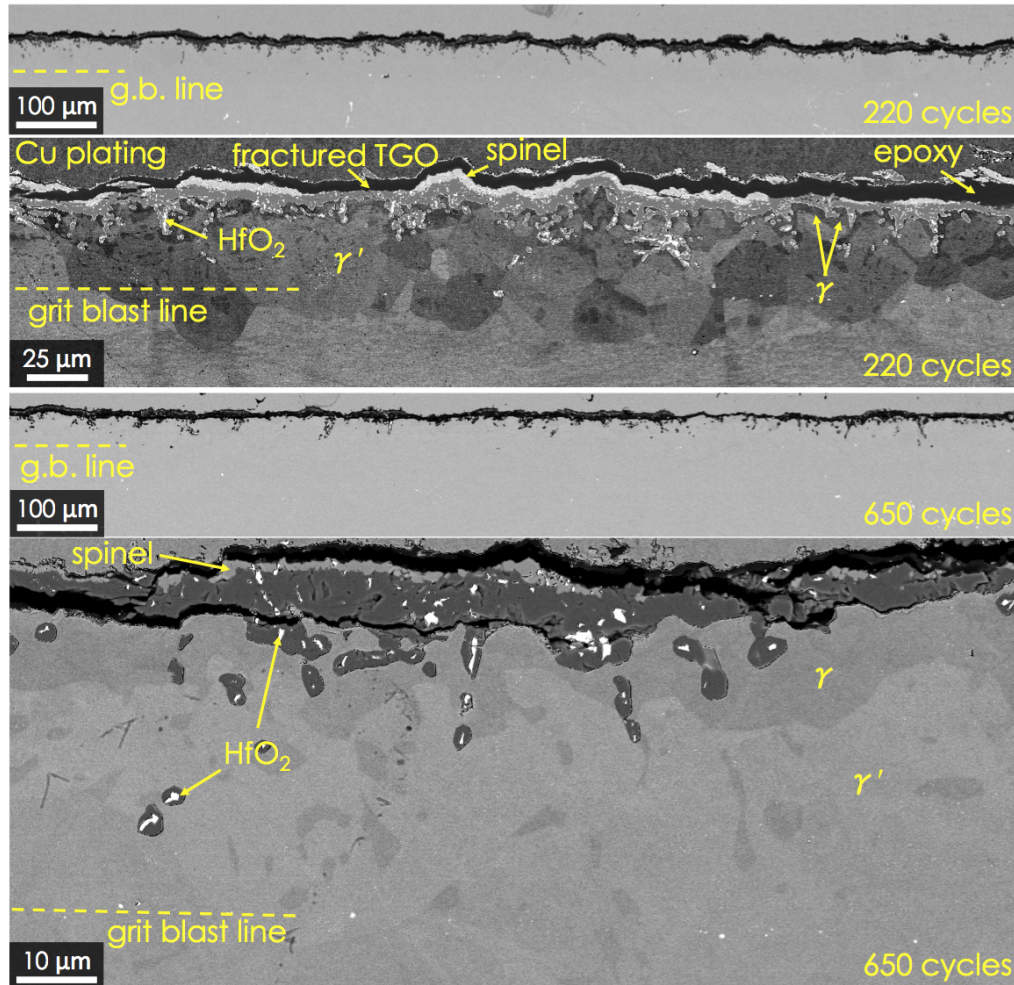


Figure 4.8: Cross sections of the DJ1+DJb(low-S) coating after the listed number of cycles at 1163 °C.

twice by 650 thermal cycles. This suggests that spinel growth occurs continuously once the  $\gamma$  layer develops. The bottom micrograph in Figure 4.8 shows a predominately  $\text{Al}_2\text{O}_3$  TGO that is more dense than the TGO grown on the monolithic DJ1 bond coat.

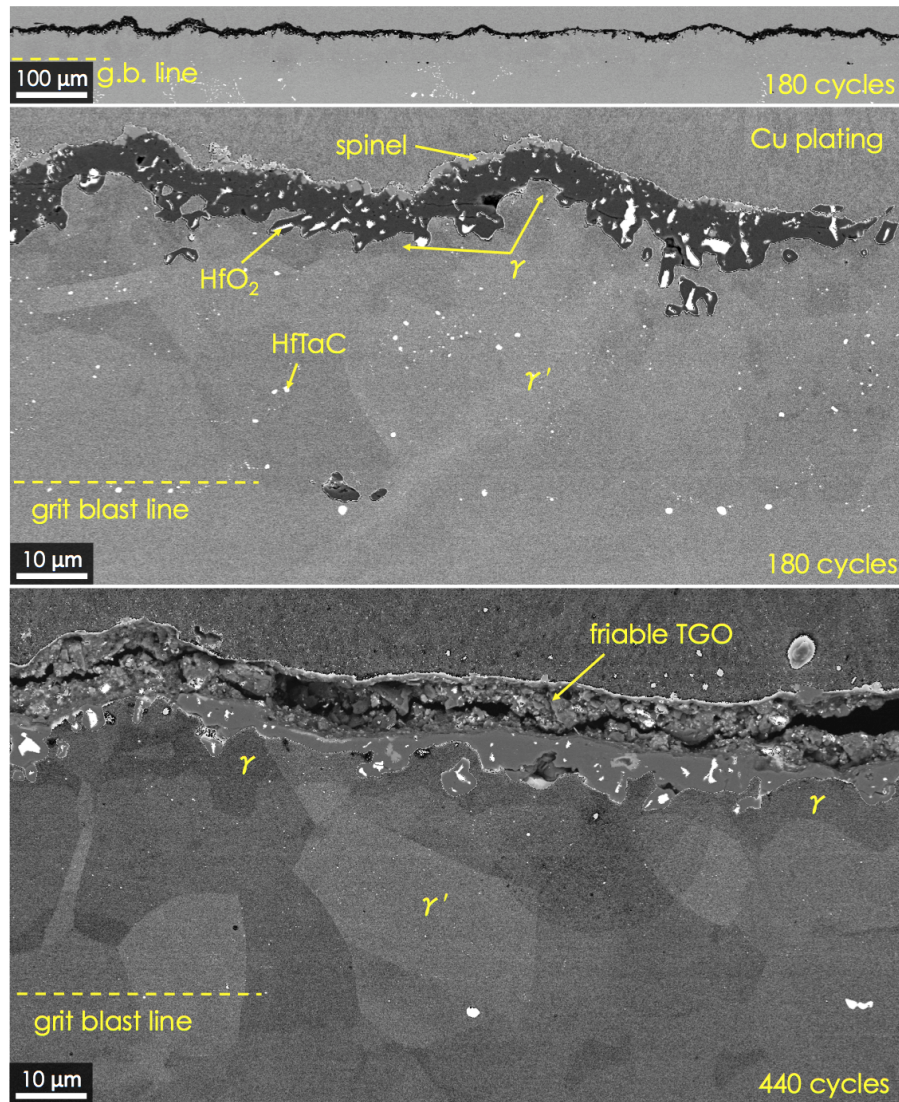


Figure 4.9: Cross sections of the DJ2+DJb(low-S) coating after the listed number of cycles at 1163 °C.

Cross section micrographs of the DJ2+DJb bilayer coating during cyclic oxidation testing are in Figure 4.9. Similar to DJ1+DJb, the DJ2+DJb bilayer contained a thin  $\gamma$ -phase layer near the TGO at the peak of the mass-change that grew thicker as the coating

was cycled longer. However, the TGO that regrew on the DJ2+DJb coating was much more friable than the original scale, as seen in the bottom micrograph where the TGO has severely fragmented during specimen polishing. It is interesting to note, however, that the presence of the Si and Ti in the DJ2 coating decreased internal oxidation in the bilayer compared to the DJ1+DJb coating; this is true even after 440 cycles when almost the entire oxide scale has been regrown on both of the coatings. Again, the oxide scales on the DJ2+DJb bilayer coatings appear more dense compared to the porous oxides grown on the monolithic DJ2 coating after a few hundred thermal cycles. The oxide scale on this bilayer coating is also significantly more homogeneous than that on the monolithic DJ2 coating (Figure 3.42).

### 4.3.2 Discussion

It has been shown that the cyclic oxidation properties of both the DJ1 and DJ2 coating are improved with the addition of a thin  $\beta$ -phase DJb layer. This improvement takes the form of a decreased initial oxidation rate and slower rate of TGO spalling, resulting in an improvement in cyclic oxidation lifetime at 1163 °C of more than 40%. This is accomplished by promoting the growth of a denser  $\text{Al}_2\text{O}_3$  scale on the bond coats. While it has already been established that the  $\beta$  phase alone can offer these advantages [75], it is also plausible that the Cr-enrichment near the surface from the DJb layer provides additional long-term benefit [78]. The DJb layer has approximately 4 at% Cr compared to 2.5 at% Cr in the DJ1 and DJ2 layers. If the Cr composition in the  $\gamma'$  layer was slightly below that required for the ideal formation and maintenance of a purely  $\alpha$ - $\text{Al}_2\text{O}_3$  scale, then the extra Cr from the DJb layer may be sufficient to promote selective oxidation of Al. Evidence of this effect is in the decreased internal oxidation in the DJ2+DJb coating, which has significantly fewer and shorter pegs than the DJ2 coating by itself even after

many thermal cycles. Isothermal oxidation experiments demonstrated that the presence of the thin  $\beta$  layer also serves to at least delay the presence of the spinel oxide growing on top of the TGO. Together these indicate that the  $\gamma'+\beta$  bilayer architecture should have oxidation behavior that is more advantageous for a TBC system, as will be seen in the next section.

## 4.4 $\gamma' + \beta$ bilayers in TBC systems

Furnace cycle tests of the  $\gamma'+\beta$  bilayer TBC systems, using DJ1+DJb(low-S), were conducted using the same conditions as explained previously. The bilayer architecture was benchmarked only against the monolayer DJ1 coating using ceramic topcoats that were deposited in their own coating run, separate from the rest of the samples discussed previously. Two DJ1 and three DJ1+DJb bond coated samples were furnace cycled until failure. Figure 4.10 shows the cycle lifetimes of the five specimens. The bilayer architecture resulted in an average lifetime increase of about 15%. This increase correlates to the cyclic oxidation lifetime differences using the peak in the mass-change curves as the definition of lifetime, suggesting that major  $\text{NiAl}_2\text{O}_4$  growth occurs after the samples begin prevalent TGO spalling. Relating the bilayer TBC lifetime to the (Pt,Ni)Al coatings, it is estimated that the  $\gamma'+\beta$  bond coat gives a TBC life that is about 375% the (Pt,Ni)Al value.

The microstructure of the as-coated YSZ layer was more dense than the other TBC coatings discussed previously, so the lifetime of these TBC systems is expected to be lower overall. However, the difference in lifetime between the two bond coatings in this test is indicative of relative bond coat performance. The as-coated microstructures of the bilayer bond coat and topcoat are in Figure 4.11 along with the end-of-life cross section. The increased lifetime of the bilayer architecture was achieved by delaying the onset of

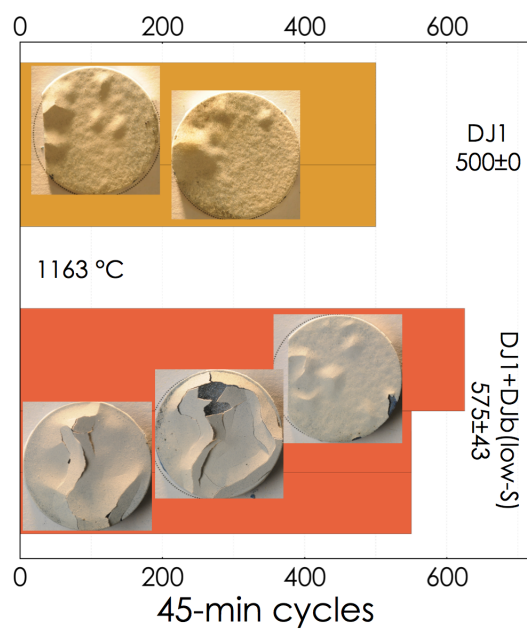


Figure 4.10: Cycle lifetime of experimental coatings during 45 min furnace cycling at 1163 °C. End-of-life is measured as  $\geq 20\%$  topcoat detachment. Reported values shows the mean and standard deviation between the samples. This test consisted of TBCs with DJ1 and DJ1+b(low-S) bond coats; the topcoats were deposited at a different time than those in Figure 3.32 and are not directly comparable. Insets shows plan view macroscopic images of the TBCs at failure.

the spinel oxide growth on top of the TGO, as discussed in the previous section. The growth of this layer leads to the failure of the TBC system because it has a low fracture toughness and weakens the topcoat-TGO bond. Overall, the addition of the  $\beta$  top-layer had a small increase in the total TBC system lifetime because the topcoat spalling was limited by spinel growth instead of TGO spalling. While an increase in the TBC system lifetime is obtained with the addition of the  $\beta$  layer, it will be shown in the next section that this improvement can be completely negated if the top-layer has a high concentration of sulfur; the bilayer architectures are very sensitive to impurity concentrations.

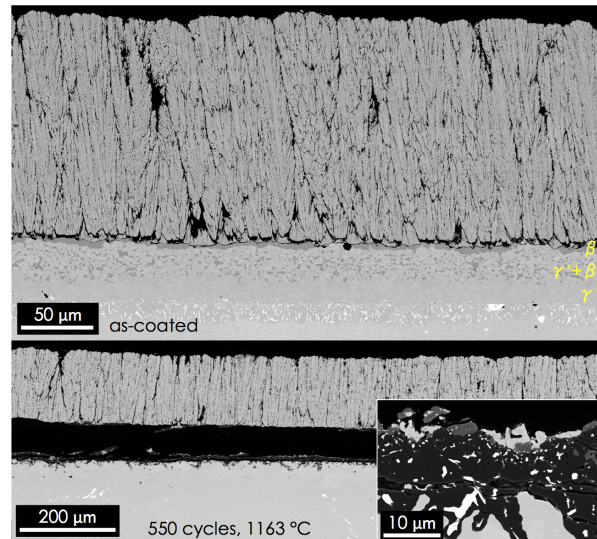


Figure 4.11: Metallographic cross sections of the DJ1+DJb bilayer bond coated TBC systems during furnace cycle testing at 1163 °C. The bilayer TBC systems had an average lifetime of 573 cycles and ultimately failed at the topcoat-TGO interface. The lower inset shows detail of the thermally grown oxide with fractured spinel and YSZ attached to the top of the Al<sub>2</sub>O<sub>3</sub> layer.

## 4.5 Sulfur and Hf effects in monolayer and bilayer architected bond coats

The previous section demonstrated the beneficial effects of adding a thin  $\beta$ -phase layer to a high-strength  $\gamma'$  bond coat. The  $\beta$  layer possessed a significant Cr content to improve the oxidation performance via selective oxidation of  $\text{Al}_2\text{O}_3$  at service temperatures [77, 78]. Unfortunately, Cr, which is a key element of both bond coats and the underlying substrates, is a common source of sulfur impurities. The impact of impurities on bond coat oxidation and thermal barrier coating life remains a critical uncertainty for TBC design and lifing [58, 77, 129]. It is well-established that high levels of S within a superalloy or  $\beta$ -phase bond coat will decrease the TBC life and that this effect can be mitigated to some extent by the addition of reactive elements such as Y and Hf [88, 91, 92, 123, 130]. However, the role of S and reactive elements is less understood in  $\gamma'$  bond coats or more complex multi-layered architectures. Therefore, an investigation of S contamination in the bond coat on the oxidation properties and TBC lifetimes during furnace cycling has been undertaken on single layer and bilayer bond coats.

In this research, bilayer coatings have been investigated as means of combining the high-strength and rumple-resistance of the  $\gamma'$  phase with the excellent oxidation performance of the  $\beta$ -phase. The design principle consists of deposition of a thin and thermodynamically compatible  $\beta$ -layer on top of the coating for formation of a dense and slow-growing  $\text{Al}_2\text{O}_3$  scale before transforming to the  $\gamma'$  phase due to Al loss. The  $\gamma'$  phase is then able to maintain the growth of the TGO while providing the strength to resist rumpling deformation that would otherwise cause TBC failure. The impurity and alloying element solubilities can vary significantly between the  $\gamma'$  and  $\beta$ -phases. Therefore,

---

<sup>1</sup>A substantial portion of the material in this section is reproduced from reference [90] *Sulfur and minor element effects in the oxidation of bilayer  $\gamma' + \beta$  bond coats for thermal barrier coatings on René N5* by Jorgensen, Suzuki, Lipkin, and Pollock accepted for inclusion in the Superalloys 2016 proceedings

an improved understanding of the synergistic effects of chemistry on failure mechanisms motivates this study.

### 4.5.1 Cyclic oxidation results

Cross sections of the experimental coatings after cyclic oxidation (no ceramic topcoat) are shown in Figure 4.12 and a magnified view of the TGO layer is in Figure 4.13. Figure 4.13 shows that the top  $\approx 40\%$  of the TGO layer on the DJ1 and DJ1+DJb(high-S) coatings have a high degree of porosity and small dispersed  $\text{HfO}_2$  particles. The bottom 60% of the TGO is more dense with larger  $\text{HfO}_2$  particles. Samples that were interrupted and cross sectioned at half their oxidation lifetime exhibited a TGO that also had a porous top portion but a much thinner dense layer below. This indicates that the TGO growth is dominated by anion transport through the scale for the majority of life; further short-time oxidation experiments would be needed to determine what portion of life the equiaxed, outward-growth scale dominates. Both of the monolithic  $\beta$  coatings (high and low-S) and the DJ1+DJb(low-S) coating exhibited a TGO that is considerably denser throughout its thickness.

$\text{HfO}_2$  and  $\text{Al}_2\text{O}_3$  stringers grow into the bond coats of the DJ1 samples during oxidation (see Figure 4.13); they are formed due to the high oxygen affinity of Hf. Comparing the  $\beta$  and  $\gamma'$  coatings in Figure 4.12, the monolithic  $\beta$  coatings inhibited the formation of  $\text{HfO}_2$  stringers to a high degree. In addition, the DJ1+DJb(low-S) coating had significantly shorter and smaller stringers at the end of the cyclic life than the high-S-bilayer.

#### Mass change

The coated samples were thermally cycled until they experienced net mass loss or until the coatings were losing mass at a predictable rate due to breakaway oxidation. A

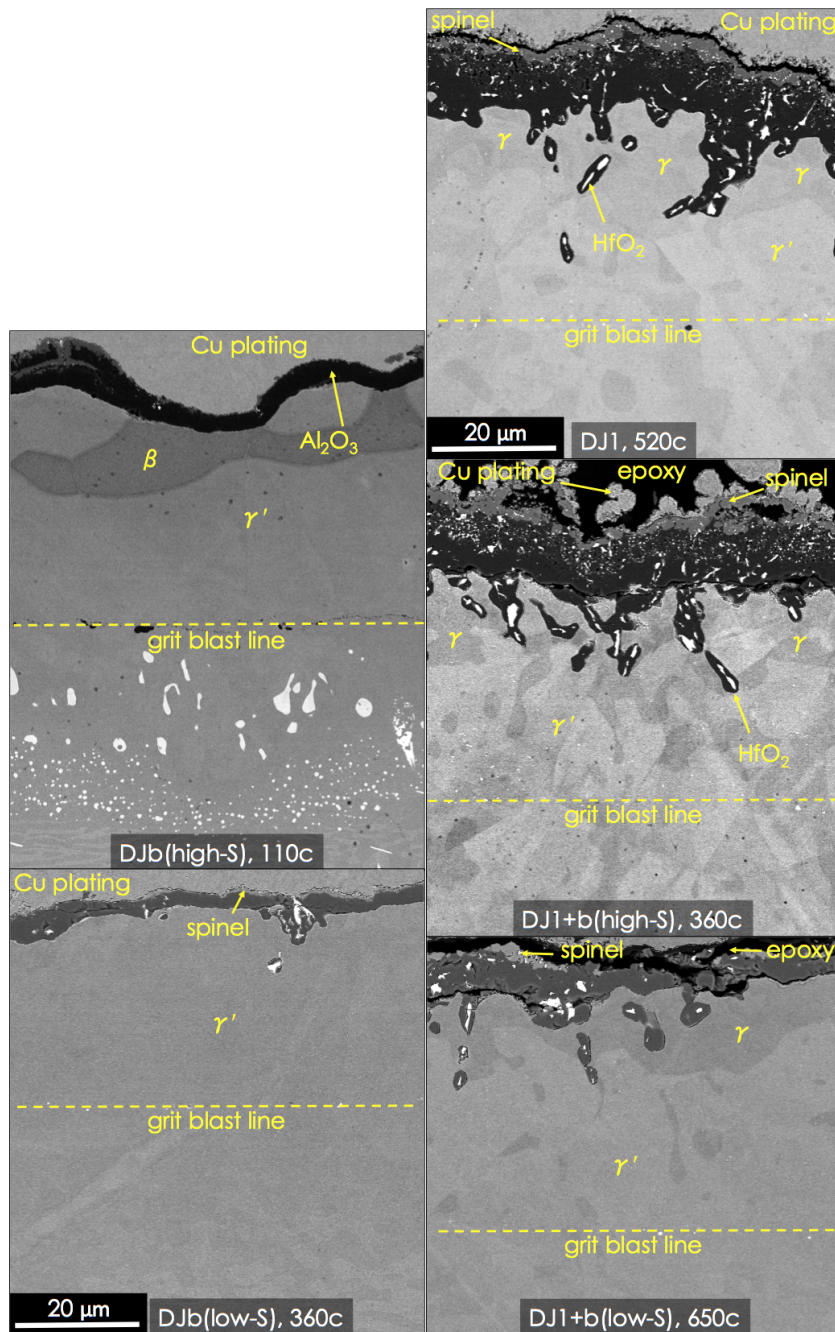


Figure 4.12: Cross sections of the experimental coatings at the end of 45-minute cyclic oxidation testing at 1163 °C. Number of cycles is indicated at the bottom of each image (e.g. 110c). Images are taken from a composite of two backscatter electron SEM images to enhance contrast of both TGO and bond coat. 20 μm scale bar applies to all images.

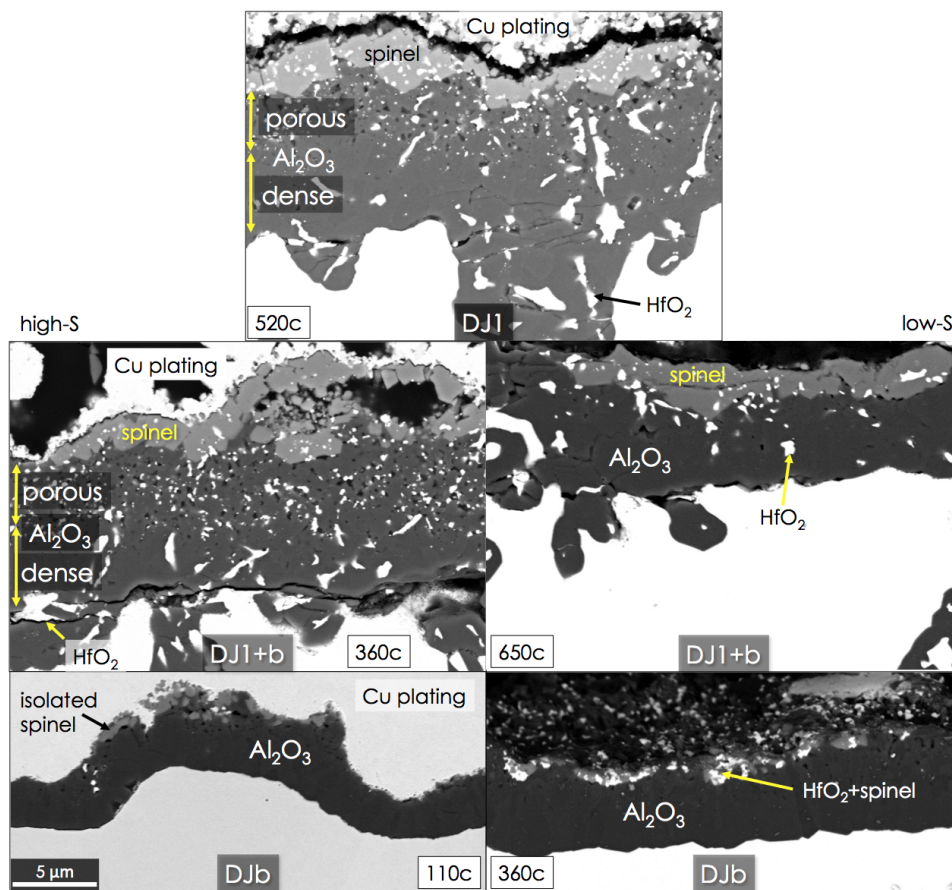


Figure 4.13: Enlarged views of the thermally grown oxides after cyclic oxidation testing at 1163 °C. 5 μm scale bar applies to all images.

plot of the change in mass for the six samples is shown in Figure 4.14. A second test to 50% life of each sample demonstrated good repeatability. If coating lifetime is measured as the cycle number at which net mass loss occurs, then the rank of the coatings from highest to lowest lifetime is: DJ1+DJb(low-S) > DJ1 > DJ1+DJb(high-S) > DJb(low-S) > DJb(high-S). This criterion for life is commonly used because it sufficiently amplifies differences in cyclic oxidation behavior to allow a clear ranking of coating performance. It also represents the point in time at which the coating begins to degrade and disappear rapidly. (Another common measure of coating lifetime is the crest of the mass change vs. cycle plot; this alternate definition does not change the performance ranking in the present experiments.) By this measure, all combinations of coatings with a  $\gamma'$  layer outperformed the  $\beta$ -only coatings. It should be noted that the (Pt,Ni)Al estimated end-of-life was 1070 cycles, meaning that all experimental coatings had oxidation lifetimes that were less than approximately 60% of the benchmark lifetime. In short, the bilayer samples had slower mass gain and slower mass loss than their monolayer counterparts.

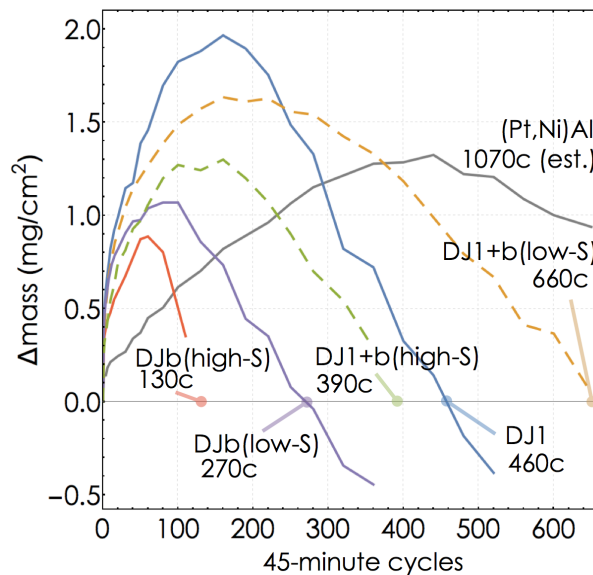


Figure 4.14: Change in mass of the five experimental coatings during cyclic oxidation testing at 1163 °C. Lines are labeled by coating designation and the end-of-life measurement or estimate as measured by net mass loss at location indicated.

## Oxide spalling

A plot showing the cumulative amount of TGO that spalled from the samples as a function of cycles is in Figure 4.15; values exceed 100% because the scale is continuously regrown, allowing spalling from the same area multiple times. This type of information can be more useful for bond coat evaluation than a mass change plot such as Figure 4.14 because an accumulation of TGO-bond coat interface failures can lead to Al depletion and TBC buckling and spalling if a critical adjacent area of TBC becomes detached from the substrate. In terms of preventing TGO spalling, the DJ1+DJb(low-S) coating outperformed all others. The coating with the next slowest rate of TGO spalling was the monolithic DJ1 coating. The coating with the least optimal performance was the DJb(high-S) sample. Although it had an initially lower rate of TGO spalling than the DJ1+DJb(high-S) sample, by 110 cycles the rate of TGO spalling from the DJb(high-S) coating was significantly greater than the other coatings. If this sample had been cycled longer, it is likely that the DJb(high-S) coating would have exhibited massive TGO loss as the TGO thickness increased. The test was interrupted at 110 cycles to investigate the coating microstructure just prior to failure in the TBC furnace cycle test and to preserve some of the primary-growth TGO.

## Rumpling

The change in the rumpling amplitude as a function of cycles is shown in Figure 4.16. Briefly, the bilayer systems had essentially the same rumpling behavior as their monolayer  $\gamma'$ -phase counterparts. Both of the monolithic  $\beta$ -phase coatings exhibited significant rumpling for the first one hundred cycles, which was at a rate intermediate to the DJ1 and benchmark (Pt,Ni)Al coating. These coatings were continuously being converted from  $\beta$  to  $\gamma'$ -phase throughout the test. The amplitude of rumpling decreased signifi-

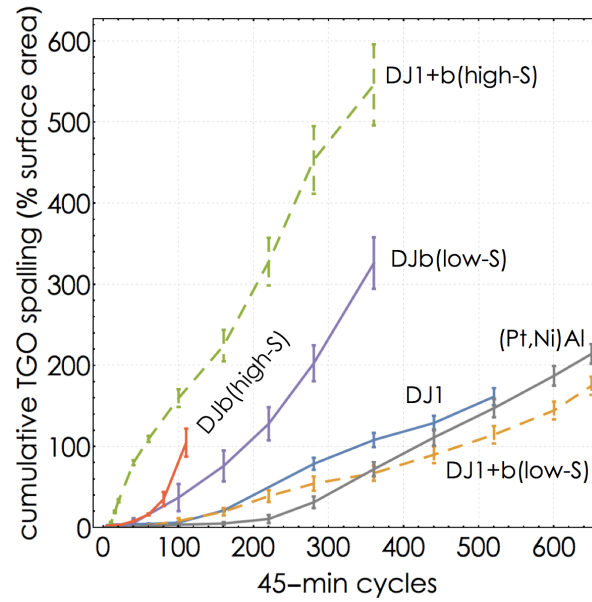


Figure 4.15: Cumulative loss of TGO via spalling as a function of cycles. Values exceed 100% because the scale is continuously regrown, allowing spalling from the same area multiple times.

cantly in these coatings as breakaway oxidation decreased the rumple peak heights at 100-200 cycles (note difference in rumpling amplitude of the 100 and 360 cycle images for the coatings in Figure 4.12). This phenomenon has been seen in other  $\beta$  coatings as well [103]. Comparing the DJ1+DJb(high-S) and DJ1+DJb(low-S) coatings, the S and Hf concentrations have little effect on the rumpling behavior of the bond coat. However, the addition of the low-S  $\beta$  top-layer to the DJ1 bond coat helps to maintain the developed surface roughness by resisting spalling whereas the monolithic DJ1 coating shows a decrease in rumpling amplitude in the last half of life. The decrease in rumpling amplitude on the monolithic DJ1 coating was due to preferential spallation of the TGO from the peaks of rumples during breakaway oxidation. This corroborates the evidence from Figures 4.14 and 4.15 that the DJb(low-S) top-layer improves TGO adherence.

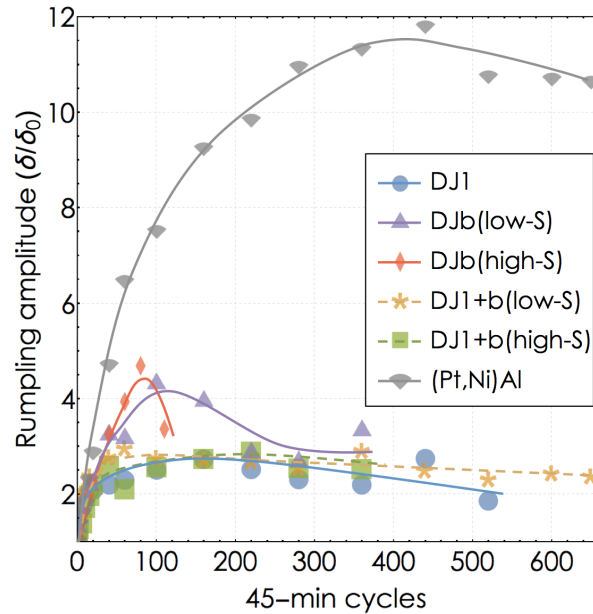


Figure 4.16: Amplitude of the primary rumpling wavelength of each sample as a function of cycles during a cyclic oxidation test at 1163 °C. Lines are drawn to guide the eye.

### Phase analysis

For all experimental coatings, the disappearance of the  $\beta$ -phase and the appearance of spinel  $\text{NiAl}_2\text{O}_4$  occurred simultaneously. This was confirmed via XRD analysis using a Pananalytical Empyrean with HighScore Plus to perform profile fits and refinements of the data [131]. Table 4.2 summarizes the cycles at which the disappearance of the  $\beta$ -phase and the presence of  $\text{NiAl}_2\text{O}_4$  was identified. The height of the XRD peaks used to identify the  $\beta$ -phase was continuously decreasing in amplitude throughout the test for all coatings. By the end of 110 cycles, the DJb(high-S) coating still contained  $\beta$ -phase as confirmed via SEM (Figure 4.12).

Table 4.2: Cycle number at which  $\beta$ -phase was no longer detected in the bond coat during cyclic oxidation tests (no topcoat) at 1163 °C. Same cycle at which spinel  $\text{NiAl}_2\text{O}_4$  was detected. Results of XRD analysis.

DJ1	DJb(high-S)	DJb(low-S)	DJ1+DJb(high-S)	DJ1+DJb(low-S)
1	> 110	220	15	40

### Furnace cycling with YSZ topcoat

The furnace cycling tests with thermal barrier coated samples showed complementary results to that of the cyclic oxidation tests without the topcoat. The results of the FCT and accompanying cyclic oxidation test are listed in Table 4.3 and show that the addition of a DJb(high-S) top-layer is detrimental to the overall performance of the DJ1 coating. The failure location for the DJ1+DJb(high-S) bilayer coating was evenly split between the TGO-topcoat and the TGO-bond coat interfaces. This indicates that the presence of a high S concentration near the surface was detrimental to TGO adhesion and therefore to maintaining topcoat attachment. TBC tests of DJ1+DJb(low-S) samples indicated an increase in TBC life of about 15% over the monolithic DJ1 coating, corresponding to roughly the same number of cycles that the  $\beta$ -phase layer delayed the onset of spinel growth (see Table 4.2). It should be emphasized that the oxidation lifetimes, defined as net mass loss, are very similar to the TBC spall lifetime of the experimental  $\gamma'$  coatings, whereas the (Pt,Ni)Al TBC lifetime is about five times shorter than its oxidation lifetime, indicating a disparate TBC failure mechanism. The (Pt,Ni)Al coating had excellent oxidation life, but the mechanical deformation (rumpling) of the bond coat led to premature topcoat delamination and the coating was not able to utilize all of its oxidation life. In contrast, the DJ1 coating did not rumple and its TBC lifetime was determined by the limit of its oxidation life. While the cyclic oxidation lifetime of the DJ1 coating was about 50% that of the (Pt,Ni)Al, the DJ1 TBC lifetime was over 300% the (Pt,Ni)Al value.

During interrupted TBC tests at 25, 50, and 75% life, it was noted that the amount of spinel oxide growth on top of the  $\text{Al}_2\text{O}_3$  scale continuously increased throughout the life of the monolithic DJ1 coating. Further, no spinel oxide or  $\text{HfO}_2$  pegs formed in the

bilayer coatings while the  $\beta$  layer was still present. After the disappearance of the  $\beta$  top-layer, the  $\text{HfO}_2$  pegs gradually formed below the TGO (Figure 4.17).

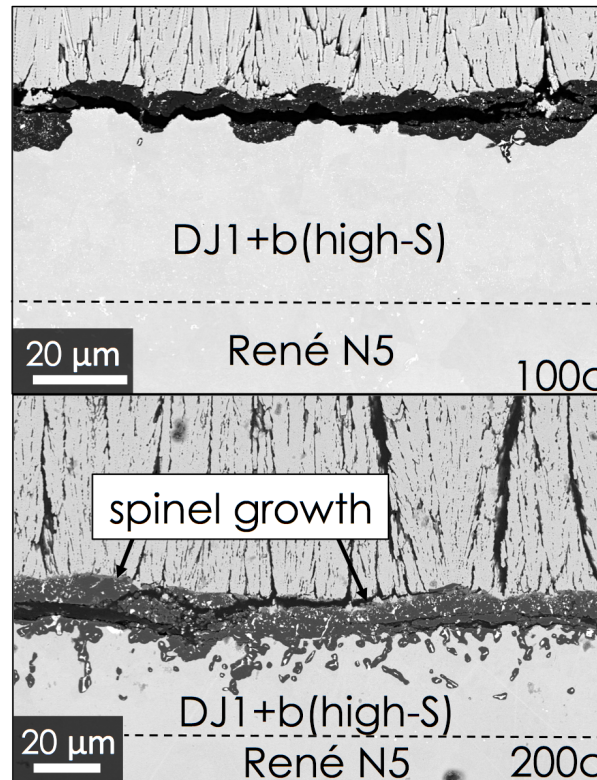


Figure 4.17: Cross sections of the DJ1+DJb(high-S) coating showing the progressive growth and formation of  $\text{HfO}_2$  pegs and spinel oxides on top of the  $\text{Al}_2\text{O}_3$  with further cycling after the disappearance of the  $\beta$  top-layer. Top images is after 100 cycles at 1163 °C and the bottom images is after 200 cycles.

## 4.5.2 Discussion

### $\gamma'$ + $\beta$ bilayer coatings

Bond coats for TBCs have two primary purposes: (1) they must serve as an Al reservoir from which to grow a dense and slow-growing  $\text{Al}_2\text{O}_3$  TGO and (2) they must serve as a compatibility layer between the metallic superalloy substrate and the ceramic topcoat. A major advantage of an  $\text{Al}_2\text{O}_3$  scale is its thermodynamic compatibility with 7YSZ, the

Table 4.3: Results of FCT and cyclic oxidation testing at 1163 °C with 45-min cycles with. TBC life is the average number of cycles until  $\geq 20\%$  topcoat detachment for two samples and the sample standard deviation. Oxid. life is the actual or estimated number of cycles for net mass loss of oxidation samples. TBC failure loc. is the primary interface of failure resulting in topcoat detachment. The DJ1+DJb(low-S) TBC lifetime is an estimate because it was compared to the DJ1 bond coat using topcoats made in a separate coating run. BC=bond coat, TBC=thermal barrier coating, TGO=thermally grown oxide.

coating	TBC life	oxid. life	TBC failure loc.
DJ1	700 $\pm$ 141	460	TBC-TGO
DJb(high-S)	120 $\pm$ 0	130	TGO-BC
DJ1+DJb(high-S)	360 $\pm$ 57	390	both
DJ1+DJb(low-S)	780 $\pm$ 22	660	TBC-TGO
(Pt,Ni)Al	210 $\pm$ 42	1070	TBC-TGO

topcoat material of choice, allowing for a strong mechanical bond between the TGO and topcoat. Further,  $\text{Al}_2\text{O}_3$  is passivating and corrosion resistant at service temperatures. Therefore, the ideal bond coat sustains a TGO to enable topcoat adhesion and oxidation protection while also resisting deformation to maintain compatibility between the topcoat and superalloy. The weak link in these two requirements ultimately determines the life of the TBC system. If the coating plastically deforms easily, the TBC, which has low out-of-plane compliance, will detach from the bond coat and spall off. However, if the coating has poor oxidation properties, the oxides in the TGO form a weak bond with the bond coat or TBC topcoat, resulting in the topcoat spalling off.

The DJ1 bond coat provides substantial improvement over the benchmark (Pt,Ni)Al with regard to maintaining TBC adhesion at high temperatures (Table 4.3). This is accomplished by mitigating the primary failure mode, rumpling (Figure 4.16), while forming a TGO that is primarily  $\text{Al}_2\text{O}_3$  accompanied with adequate adhesion with the topcoat. Ultimately, the growth of spinel  $\text{NiAl}_2\text{O}_4$  degrades the topcoat-TGO interface and leads to topcoat spalling. The transport mechanisms of Ni and Co through the TGO and the spinel growth rate on top of the  $\text{Al}_2\text{O}_3$  remain the subject of future investigation.

More so, the  $\gamma'+\beta$  bilayer system should provide significant additional benefit to TBC life because the  $\beta$  layer sets up a more dense and passivating  $\text{Al}_2\text{O}_3$  scale during the beginning of oxidation (Figure 4.17). This “higher quality” TGO likely slows the outward diffusion of cations from the bond coat and delays the formation and growth of a spinel layer above the  $\text{Al}_2\text{O}_3$  scale while simultaneously decreasing the overall oxidation rate. The rest of the bond coat consists of the high-strength  $\gamma'$ -phase and resists the rumpling deformation seen in (Pt,Ni)Al and MCrAlY coatings. The bilayer system has been shown to improve the microstructure of the TGO (Figure 4.13) and the cyclic oxidation performance of the coating (Figures 4.14 and 4.15), which allows the bilayer to improve TBC life considerably.

### Controlling sulfur in bilayer coatings

It is important to understand the impact of sulfur in the thin  $\beta$  layer because a small increase in sulfur (10 wt.ppm) has been shown in this investigation to drastically limit the oxidation performance of the bilayer by almost 2-fold (cyclic oxidation lifetime of 660 cycles for low-S and 390 cycles for high-S). Comparing the two monolithic  $\beta$  coatings provides insight into the decrement in oxidation lifetime. TGO spalling is controlled by the competition between the delamination driving force and the TGO-bond coat interface toughness; spalling occurs when the driving force is greater than the interface toughness. The delamination driving force scales as  $G_0 = \varepsilon^2 h \bar{E} / 2$ , where  $\varepsilon$  is the TGO strain after cooling,  $h$  is the TGO thickness, and  $\bar{E}$  is the biaxial modulus of the TGO [21]. The TGO strain,  $\varepsilon$ , is controlled by the thermal expansion mismatch between the TGO and substrate and is similar for both coatings. The elastic modulus,  $\bar{E}$ , is also expected to be similar for both high- and low-S variants. Therefore, the primary difference in spalling behavior between the high- and low-S  $\beta$  coatings is due to a difference in the interface toughness rather than the delamination driving force. The change in interface

toughness is directly related to the S concentration change [91, 132]. The monolithic  $\beta$ -phase coatings showed a 2-fold increase in cyclic oxidation lifetime by decreasing the S and increasing the Hf concentrations (270 cycles for low-S and 130 cycles for high-S). The bilayer coatings exhibit similar behavior, but with longer lifetimes. The increased lifetime of the bilayer coatings, relative to the monolayer  $\beta$  coatings with the same sulfur content, is explained by a decrease in TGO stiffness from increased porosity, as seen in Figure 4.13 and discussed in Section 3.1. A more compliant TGO has a lower initial delamination driving force,  $G_0$ . Therefore, the oxide grows to a larger thickness,  $h$ , before the driving force exceeds the interface toughness and spalling occurs.

As suggested by Pint [133], it may be the reactive element to sulfur ratio that is controlling performance more than the absolute sulfur concentration in  $\gamma+\gamma'$  alloys. In Pint's study, reactive element/S ratios  $\gg 1$  were shown to give good cyclic oxidation performance at 1100 °C. In the alloys of the present study, the only reactive element is Hf and the Hf/S atomic ratio for the DJ1, DJb(low-S), and DJb(high-S) alloys is approximately 2000, 1000, and 10. The DJb(high-S) coating should have significantly debited performance based on this measure, in agreement with the present experiments.

This same reasoning is also valid in the bilayer systems. In the DJ1+DJb(high-S) system, the TGO-bond coat interface toughness is low when the initial high-quality and dense TGO grows. This leads to rapid spalling of the TGO early on (note greater TGO spalling rate for DJ1+DJb(high-S) than all other coatings in Figure 4.15). Reactive element gettering theory does not satisfactorily explain the difference in performance in the bilayer coatings [78, 89, 133–135]. Since the top layer of the bilayer coatings is only 5  $\mu\text{m}$  thick, reactive element theory suggests that the ample supply of reactive elements in the rest of the coating should be available to diffuse to the oxide interface, react with S, and improve TGO adhesion. Even if immobile, the Hf should be available to getter S once the thin high-S top-layer has been consumed through oxidation, resulting

in improved oxidation performance after a certain delay. However, this is not observed in the present experiments. Instead, the DJ1+DJb(high-S) sample exhibits continuously poorer oxidation performance than both the DJ1+DJb(low-S) and DJ1 samples as shown by the earlier/faster mass loss in Figure 4.14 and the continuously faster rate of TGO spalling in Figure 4.15.

The present experiments suggest that the reactive elements in the base DJ1 layer of the bilayer coatings are not available for sulfur gettering at the surface during cyclic oxidation. It is unlikely that Hf is diffusing away from the surface and into the superalloy because the substrate, René N5, contains a higher concentration of Hf than the DJ1 coating used in these experiments. Instead, the Hf could be tied up in HfC or internal HfO<sub>2</sub> pegs and unavailable for sulfur gettering after the initial annealing vacuum heat treatment. In this view, the Hf selectively oxidizes below the inward-growing TGO front, as illustrated in Figure 4.18. Internal formation of HfO<sub>2</sub> pegs prevents the Hf from reaching the surface of the bond coat, where S has segregated.

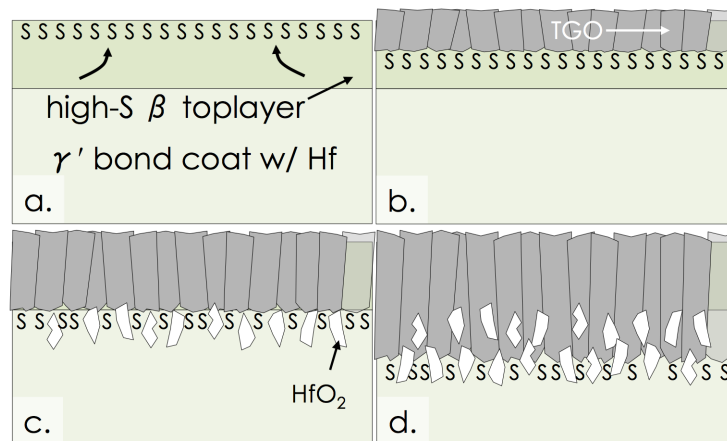


Figure 4.18: Schematic showing the segregation of sulfur in a bilayer bond coat with a high-S  $\beta$ -phase top-layer. a) S segregates to the surface during heat treatment and weakens the TGO-bond coat adhesion. b) S maintains localization at the interface by migrating inward with TGO growth during thermal cycling. c) Once the  $\beta$ -layer is consumed, Hf selectively oxidizes ahead of the TGO growth front and the majority of the S, which is at the TGO-bond coat interface. d). The S continues to migrate inward with the TGO growth front because Hf is unavailable to form HfS<sub>2</sub>.

## 4.6 TBC system failure in bilayer systems

The analysis developed in the previous chapter for determining the TBC life can be extended to incorporate the effects of the  $\gamma'+\beta$  bilayer bond coat systems discussed here. First, the most substantial effect of adding 5  $\mu\text{m}$  of  $\beta$ -phase on top of the  $\gamma'$  coating is the delay in the detection of spinel growth on top of the TGO. Furthermore, the oxide scale appears to be denser and more slowly growing based on the mass change measurements during cyclic oxidation. These effects are accounted for by modifying the previous model in the following ways: First, the growth rate of  $\text{NiAl}_2\text{O}_4$  is predicted to start decaying the topcoat fracture toughness after 300 cycles, but at the same rate as the monolayer  $\gamma'$  coating, 0.1 (J/m<sup>3</sup>)/cycle. Second, the degradation of the TGO-bond coat interface toughness due to breakaway oxidation was set to decrease rapidly after about 1800 cycles for the bilayer instead of 1500 cycles in the  $\gamma'$  coating. Other effects such as increasing the TGO modulus to account for decreased porosity are predicted to have second order effects and are not included here for clarity.

From Figure 4.19, delaying spinel growth on top of the TGO, and hence delaying the presence of the low-toughness layer above the TGO, is predicted to delay topcoat failure by about 10% at high temperatures. This proportion increases with decreasing temperature as topcoat sintering slows down. The  $\gamma'$  coating life is limited by oxidation (TGO spalling) at lower temperatures and this increases with the  $\beta$  layer addition, but the TBC system is still limited by the degradation of the TBC through spinel growth, as discussed in the previous chapter. This semi-quantitative model indicates that the  $\gamma'+\beta$  bilayer system should improve the lifetime of all  $\gamma'$  coatings at temperatures below about 1150 °C as substantiated in the present experiments.

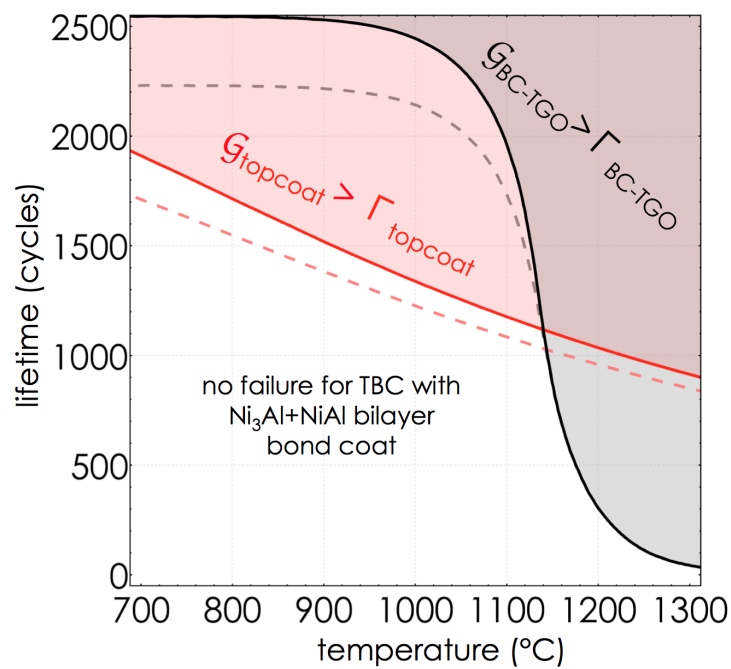


Figure 4.19: Schematic diagram showing the cycling-temperature relationship for competing TBC system failure mechanisms - TGO spalling versus topcoat fracture - when using a  $\gamma'+\beta$  bilayer bond coat. The dashed lines denote the failure zones for the monolayer  $\gamma'$  coating shown in Figure 3.47 and indicate the the bilayer should provide around a 10% benefit to TBC system life at temperatures below 1150 °C.

## 4.7 Chapter summary

The present studies compared the oxidation behavior of monolithic  $\gamma'$ -phase bond coats to bilayer architected  $\gamma' + \beta$  coatings. It was shown that the addition of 5  $\mu\text{m}$  of a thermodynamically compatible  $\beta$  layer improves the cyclic oxidation lifetime of two similar  $\gamma'$  coatings by about 40% at 1163 °C. This was achieved by delaying the  $\gamma' \rightarrow \gamma$  transition in the bond coat and the subsequent growth of spinel oxide without inhibiting the rumpling behavior of the bond coat. Further, an improvement in cyclic oxidation properties allowed the  $\gamma' + \beta$  bilayer architecture to increase the TBC furnace cycle lifetime by about 15% over the monolithic DJ1 coating. However, if the  $\beta$  layer contains high levels of S, it was found to decrease the TBC system life by about half, emphasizing the importance of understanding the effect of S in these bilayer bond coatings.

These studies also compare the 1163 °C cyclic oxidation behavior of a high-S/low-Hf  $\beta$  coating, low-S/high-Hf  $\beta$  coating, a  $\gamma'$  monolithic coating (DJ1), and two  $\gamma' + \beta$  bilayer coatings using the high/low S, low/high Hf  $\beta$  top-layers. The rank of cyclic oxidation lifetime in decreasing order is: DJ1+DJb(low-S) > DJ1 > DJ1+DJb(high-S) > DJb(low-S) > DJb(high-S).

Measurements of the amount of TGO that spalled from the coatings indicated that ranking of the TGO spall resistance in decreasing order is: DJ1+DJb(low-S) > DJ1 > DJb(low-S) > DJ1+DJb(high-S) > DJb(high-S). High amounts of sulfur in a bilayer coating are particularly catastrophic to the amount of scale loss. While the addition of a DJb(low-S)-layer on top of DJ1 was shown to decrease the overall TGO spallation rate, the addition of a DJb(high-S)-layer dramatically increased the TGO spallation rate. It is hypothesized that this is due to the unavailability of Hf in a  $\gamma'$  coating as the Hf selectively oxidizes before it can react with S at the TGO-bond coat interface. Further experiments measuring the surface concentration of free S during oxidation of  $\beta$  and  $\gamma'$

coatings are needed to verify this hypothesis. However, from these experiments it can be concluded that S is detrimental to the cyclic oxidation behavior of both  $\beta$ -phase and bilayer  $\gamma'+\beta$  bond coats. A large amount of Hf in the bulk of a  $\gamma'$  coating or substrate is unlikely to significantly improve the oxidation properties of a bilayer coating that has a high concentration of S at the surface. It is preferable to locate the high concentration of Hf near the surface of the coating. This can be accomplished by grading the Hf concentration in an overlay coating or by creating multi-layered bond coats with ion plasma deposition wherein the Hf is concentrated near the surface of the bond coat.

The results of this investigation have several significant implications for the development of future bond coatings. Table 4.3 shows that the DJ1 bond coat had a TBC lifetime that was more than threefold longer than the (Pt,Ni)Al coating even though the DJ1 coating had significantly shorter oxidation life. This demonstrates that the balance between oxidation properties and strength must necessarily be shifted towards achieving high-strength, rumple-resistant bond coats as airfoils are pushed to higher temperatures and longer lifetimes. The rumple-resistant DJ1 coating ultimately failed due to the formation of spinel oxides at the TGO-TBC interface. Delaying the growth of spinel oxides should, therefore, be a means of extending the TBC lifetime of high-strength  $\gamma'$  coatings. It has been shown in these experiments that the growth of spinel  $\text{NiAl}_2\text{O}_4$  can be delayed with the addition of a low-S/high-Hf  $\beta$  top-layer, resulting in an extension in TBC life by about 15%. Controlling S in the  $\beta$  top-layer is essential for this benefit. Other possibilities such as Pt alloying in the  $\beta$  and/or  $\gamma'$  layers or optimizing the reactive element doping levels are also future avenues to further push the high-temperature TBC life of these high-strength coatings.

## Chapter 5

# Interface Toughness Measurement Using Dynamic fs Laser Ablation

The importance of TGO-bond coat interface toughness increases as stronger bond coats are used and engines are pushed to higher temperatures, where the driving force for TGO spallation will increase. A larger TGO thickness,  $h$ , results in a higher driving force (Equation 1.1) for TGO delamination during cooling, as shown in Figure 1.4 [13]. When bond coats are designed to inhibit rumpling while maintaining adequate oxidation properties, it is likely that TGO spalling becomes a life-limiting failure mechanism for TBC systems due to this increased driving force with TGO growth. Again, TGO delamination is likely when  $\mathcal{G}_0 \geq \Gamma_{BC-TGO}$ . Therefore, engineering and design of coatings with high interface toughness will become an important consideration along with the rest of bond coat properties.

---

<sup>1</sup>A considerable amount of the material in this chapter is reproduced from the manuscript by Jorgensen, Pollock, and Belgey entitled *Dynamic response of thin films on substrates subjected to femtosecond laser pulses* Acta Materialia **84** 2015 [136], published by Elsevier and reproduced here with kind permission.

Engineering progress in BC systems requires a concurrent improvement in the oxidation properties, creep strength, and TGO/BC interface toughness of these systems. At present, there are well-established methods to measure the creep rate and high temperature yield strength of these alloys through microtensile tests [137] as well as the oxidation properties through isothermal and cyclic oxidation tests. Evaluating all three of these properties at once in a TBC furnace cycle test, while essential for BC development, tends to obfuscate the individual contributions of each attribute leading to failure. Clearly, a means of measuring the interfacial toughness by itself is important. Engineers need to understand how this property changes with chemical composition of the BC or superalloy [138], crystalline phase of the BC, segregation of impurities such as sulfur [91, 139], and cyclic life of the specimen [139, 140].

There exists over 200 tests designed to measure the interfacial toughness between films and substrates [141–143]. This suggests that measuring the interfacial toughness between a film and substrate is specific to the application and material. Brittle oxides grown on metals are some of the most difficult systems to assess due to very high interfacial toughness values [144], high residual compression in the film, and complications arising from plastic deformation in the substrate during typical interface fracture tests [145, 146]. Further, due to the inherently inhomogeneous nature of thermally grown oxides, a large scale fracture test will fail to capture the local interface variability across a sample. A straight-forward test with the characteristics described above is needed in order to understand the relationship between interface strength and the many parameters affecting it.

## 5.1 Impulse-based dynamic mechanics

A new method of probing the interfacial toughness of a transparent thin film on a metallic substrate has been developed. In short, the method herein utilizes a femtosecond laser to de-adhere circular regions of the interface where the size of the de-adhered region is controlled by the power and focal size of the incident pulse. The laser passes through the transparent film and ablates a thin layer of the substrate. The ablated material is accelerated out of plane and impacts the overlying film, transferring some of its momentum. As will be explained, this gives the de-adhered film an initial out-of-plane velocity and excites dynamic buckling modes. As the film moves out of plane, the driving force for interface crack growth increases until the film reaches an apex. There is a dynamic competition between the driving force for crack advance outward along the film-substrate interface or the crack kinking into the brittle film, which results in film failure and spalling from the substrate. The behavior of the system after the incident laser pulse gives information about the intrinsic material properties: interface toughness between the film and the substrate and the fracture toughness and flaw distributions in the film.

Femtosecond lasers are useful tools for the introduction of interface flaws due to the nature of the laser-metal interaction. The near-IR laser radiation is strongly absorbed by metals resulting in a short penetration depth and the ultra-short duration of the pulse allows rapid energy absorption and decay within the metal. For bare substrates, it is well established that femtosecond laser pulses effectively eject material from the surface [147, 148] with ablation depths and lateral dimensions that can be precisely controlled [149–151]. Laser-induced breakdown spectroscopy (LIBS) experiments have established that ejected material in the transient state is liquid-like in character without a detectable plasma plume in the low-fluence ablation regime [152]. Further, detailed

studies of heat effects of fs laser pulses on bulk substrates do not show significant microstructural changes, indicating that substrate heating is negligible [147, 150]. For a transparent film on a substrate, the laser pulse passes through the film and excites the substrate in the ablation region, releasing material at the film/substrate interface and generating pressures that lead to upward motion of the film over the region that has been irradiated. This process is shown schematically in Figure 5.1. The pressures generated in the cavity formed between the film and substrate are difficult to predict owing to the (largely unknown but undoubtedly) complex equation of state associated with phase changes of the nanoscopic layer of substrate material excited by the laser [151, 153, 154].

### 5.1.1 Impulse-based dynamic mechanics model

A seemingly overlooked aspect of the problem is the typical discrepancy in time-scales relating to the excitation of ablated material and the dynamic motion of the film. Measurements and simulations of excited material reveal that the ablated material returns to a low-energy state in a period on order of tens of nanoseconds [151, 154–156]. Conversely, the timescale of film motion is governed by the inertia and stiffness of the film, which often produces natural frequencies of the film with a much longer period (e.g. hundreds of nanoseconds, as will be elucidated). The relevant time scales for the fs laser-material interactions (absorption, pressure, heating, ablation) are shown in Figure 5.2. As a result, strong laser-metal interactions can occur in the near-surface region while the region physically changed by the incident pulse is small, on the order of nanometers deep. Furthermore, any localized heating of the substrate or film is dissipated before the film reacts. Thus, femtosecond or shorter-pulsed lasers are ideal for probing the interface properties of multi-material systems because one can insert interfacial flaws without changing the properties of the surrounding interface.

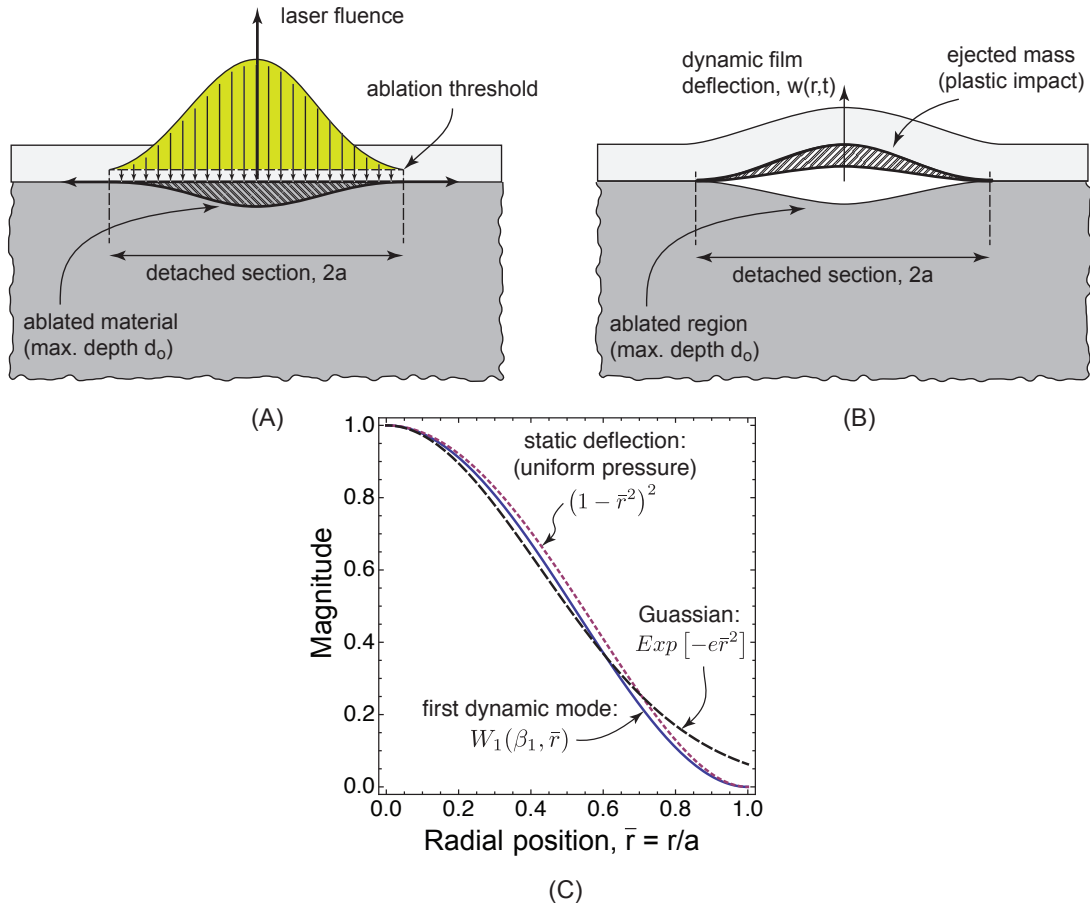


Figure 5.1: (A) Schematic illustration of the laser fluence distribution that passes through the film to excite material at the film/substrate interface, (B) schematic illustration of the film deformation that is triggered by impact of ablated material (assuming plastic impact), and (C) a comparison of the quasi-static deflection profile for uniform pressure, a Gaussian distribution (i.e. the laser energy) and the first vibration mode.

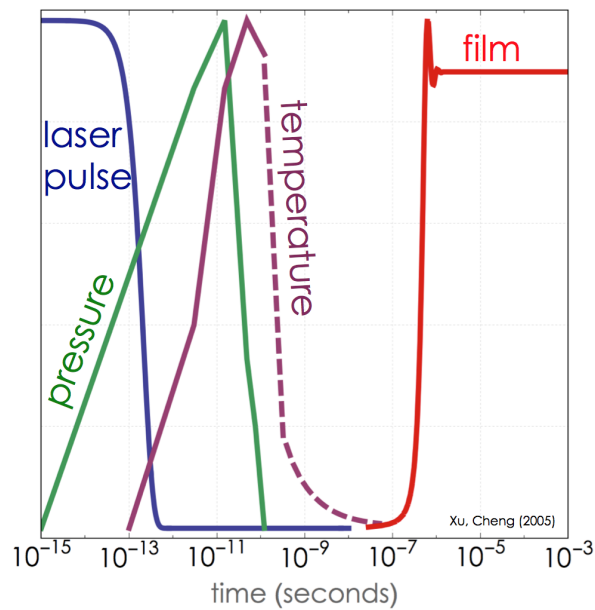


Figure 5.2: Normalized plot of the time scales for the fs laser-substrate interaction with a thin film. Abscissa uses a logarithmic scale and the ordinate axes is normalized separately for each interaction. Data are taken from molecular dynamics simulations by Cheng and Xu [156]. The timescale of the fs laser interactions are orders of magnitude shorter than the movement of the natural frequency of the thin film, which has a half period in the range of hundreds of nanoseconds.

Here, scenarios are considered wherein the motion of film (induced by the laser) is controlled by the impulse transmitted to the film from the ablated material and is therefore insensitive to the details of the pressure-volume-time relationship of the excited material. That is, in the limit that the generated pressure pulse duration is much shorter than the inertial timescale of the film, the film response is dictated solely by the velocity imparted to the film through momentum transfer from the material ejected from the substrate. The model presented here is shown to produce predictions that are in quantitative agreement with previous experimental observations of the velocity of the mass ejected from the substrate in bare substrate experiments [157], the velocity of an oxide film [158], and film fracture studies conducted for this work.

It should be noted that the present model requires that several key assumptions hold. The foremost assumption is that the film is largely transparent to the laser pulse in the low-fluence ablation regime of the substrate and is therefore relatively unaffected by irradiation. Direct observations of low-fluence fs laser experiments demonstrate that bulk systems return to ambient temperatures faster than crystallization can occur [159, 160] with electron cooling rates on the order of  $10^{13}$  °C/s [161–163], meaning that any thermal expansion of the film or substrate is negligible for the timescales of interest. Further, this means that the fraction of pulse energy imparted to the substrate is known such that previous studies of ablation velocities and energy absorption [153, 164–167] provide accurate estimates of the response of the substrate material just beneath the film. The conceptual picture underlying the model is that energy absorbed by the substrate under the film is translated to kinetic energy in the ablated material, which then impacts the film, transferring energy and momentum over a time-scale that is much smaller than that needed to change the position of the film. The result is that the film is subjected to an initial velocity distribution that entirely defines the subsequent motion of the film. A second assumption is that the Gaussian distribution of laser energy leads to dynamic

response in the film that is dominated by its first vibration mode; this is motivated by the quantitative similarity between the Gaussian profile of the laser energy, the first mode shape of the film, and the quasi-static deflection profile arising from uniform pressure (See Figure 5.1C). This is simply for convenience: one could work out the response of the film using modal decomposition without invoking this assumption.

Finally, the model presented in this work assumes that residual stresses in the film are negligible, and that there is no coupling between in-plane and out-of-plane deformations (i.e. displacements and rotations are “small”). For many systems, these effects can be important (e.g. [168]): however, this section identifies several key dimensionless parameters and relationships that are unaffected by these effects, as will be elucidated. A later section discusses additional analyses that include residual stress and large deflection with essentially no conceptual changes to the considerations detailed here.

### Dynamic response of the film subject to pressure pulse of short duration

This section describes the response of a circular film, clamped at its edges and subjected to a pressure pulse  $p(r, t)$ . For small deflections and no residual stress, the dynamic equation describing the transverse deflection of the film is given by:

$$\frac{\bar{E}h^3}{12} \left( w''''(r, t) + 2\frac{w'''(r, t)}{r} - \frac{w''(r, t)}{r^2} + \frac{w'(r, t)}{r^3} \right) + \rho h \ddot{w}(r, t) = p(r, t) \quad (5.1)$$

where  $\bar{E} = E/(1 - \nu^2)$  is the plane strain modulus of the film (with  $\nu$  being the Poisson’s ratio of the film and  $E$  being the Young’s modulus),  $h$  is the film thickness,  $w$  is the transverse (out-of-plane) displacement,  $\rho$  is the film density,  $p(r, t)$  is the pressure distribution applied to the film, and primes denote differentiation with respect to the radial coordinate. For a circular film with radius  $a$ , the imposed boundary conditions are  $w(a, t) = w'(a, t) = 0$  and  $w'(0, t) = 0$ , along with the condition that  $w(0, t)$  is finite.

For any pressure loading, the response can be written in terms of the modal superposition given by:

$$w(r, t) = \sum_n^{\infty} z_n(t) W_n(r) \quad (5.2)$$

where  $z_n(t)$  represents the time-dependent contribution of mode  $n$  and  $W_n(r)$  defines the mode shape for the  $n^{\text{th}}$  mode. The mode shapes for the present boundary conditions are given by:

$$W_n(\beta_n, \bar{r}) = \frac{I_1(\beta_n) J_0(\beta_n \bar{r}) + J_1(\beta_n) I_0(\beta_n \bar{r})}{I_1(\beta_n) + J_1(\beta_n)}, \quad (5.3)$$

where  $\bar{r} = r/a$ ,  $J_{0,1}$  are the Bessel functions of the first kind and  $I_{0,1}$  are the modified Bessel functions of the first kind. The constants  $\beta_n$  are defined by the roots of the characteristic equation:

$$I_1(\beta) J_0(\beta) + J_1(\beta) I_0(\beta) = 0, \quad (5.4)$$

and in turn, they define the natural frequencies according to:

$$\omega_n = \beta_n^2 \sqrt{\frac{\bar{E} h^2}{12 \rho a^4}} \quad (5.5)$$

The amplitudes  $z_n(t)$  are determined by the solutions to:

$$\ddot{z}_n(t) + \omega_n^2 z_n(t) = f_n(t); \quad f_n(t) = \left( \frac{1}{\rho h} \right) \frac{\int_0^1 \bar{r} W_n(\bar{r}) p(\bar{r}, t) d\bar{r}}{\int_0^1 \bar{r} W_n(\bar{r})^2 d\bar{r}} \quad (5.6)$$

where  $f_n(t)$  is a generalized force that has units of acceleration. Note that this de-coupled set of single degree of freedom dynamic equations is a consequence of the fact that the

mode shapes are orthogonal over the domain of interest, such that:

$$\int_0^1 W_n(\bar{r})W_m(\bar{r})\bar{r}d\bar{r} = 0 \text{ for } m \neq n \quad (5.7)$$

In order to elucidate the fundamental scaling controlling the dynamic response of the film, we adopt a single term approximation using only the first mode. The approach is exact in the limit that the spatial distribution of pressure is identical to the first mode shape, and it can be expected to be highly accurate for pressure distributions of similar shape. For the first mode,  $\beta_1 = 3.19622$  and  $W_1(\bar{r}) = 0.053I_o(\beta_1\bar{r}) + 0.947J_o(\beta_1\bar{r})$ . In the single term approximation, the film deflects with the shape  $W_1(\bar{r})$ , with the peak deflection (at  $\bar{r} = 0$ ) determined by the time-dependent pre-factor  $z_1(t)$ . Here,  $w_o(t)$  denotes the peak center point deflection, i.e.  $w_o(t) = z_1(t) = w(0, t)$ .

Further, to demonstrate that the time-dependence of the pressure is immaterial for pulses of short duration, consider the case where the pressure distribution is assumed to be  $p(\bar{r}, t) = p_o (\sin \pi t/t_o) W_1(\bar{r})$  for  $t \leq t_o$  and  $p(\bar{r}, t) = 0$  for  $t > t_o$ . That is, it is assumed the pressure rises to a peak magnitude of  $p_o$  over  $t < t_o/2$  and falls to zero pressure at time  $t = t_o$ . In this case, the dynamic equation of motion and solution for  $0 < t \leq t_o$  are given by:

$$\ddot{w}_o + \omega_1^2 w_o = \frac{p_o}{\rho h} \sin(\pi t/t_o); \quad w_o(t) = \left( \frac{p_o t_o}{\rho h} \right) \frac{\omega_1 t_o \sin(\pi t/t_o) - \pi \sin(\omega_1 t)}{\omega_1^3 t_o^2 - \pi^2 \omega_1} \quad (5.8)$$

At the end of the pressure pulse  $t = t_o$ , the displacement and velocity of the center point of the film are:

$$w_o(t_o) = \frac{\pi p_o t_o}{\rho h (\pi^2 \omega_1 - t_o^2 \omega_1^3)} \sin \omega_1 t_o = \frac{p_o t_o^2}{\pi \rho h} (1 + O[(\omega_1 t_o)^2]) \quad (5.9)$$

$$\dot{w}_o(t_o) = \frac{\pi p_o t_o}{\rho h (\pi^2 - t_o^2 \omega_1^2)} (1 + \cos \omega_1 t_o) = \frac{2 p_o t_o}{\pi \rho h} \left( 1 + \frac{\omega_1 t_o}{\pi^2} + O[(\omega_1 t_o)^2] \right) \quad (5.10)$$

Thus, it is seen that when  $\omega_1 t_o \ll 1$ , the film experiences negligible motion during the pressure pulse, and acquires an initial velocity dictated by the peak pressure and the duration of the pulse.

However, conservation of momentum implies that the momentum of the film at the end of the pressure pulse ( $t = t_o$ ) is equal to the impulse delivered by the pressure pulse. That is, if we compute the momentum at  $t = t_o$  using velocity distribution given by the first mode shape,

$$M = \int_0^a 2\pi r \rho h \dot{w}(r, t_o) dr = 0.979 a^2 \rho h \dot{w}_o(t_o) \quad (5.11)$$

and equate this result to the impulse of the pressure pulse,

$$Im = \int_0^{t_o} \left( \int_0^a 2\pi r p(r, t) dr \right) dt = 0.623 a^2 p_o t_o, \quad (5.12)$$

the same velocity at  $\dot{w}_o(t_o)$  is obtained as using the pressure pulse (noting that  $2/\pi = 0.623/0.979$ ).

Thus, by re-defining zero time as the end of the pressure pulse, the initial velocity can be computed from the momentum acquired during the pressure pulse and while ignoring the details of the pressure-time excitation of the film. This is justifiable when the timescale of the pressure pulse is small in comparison to the natural period (inverse frequency) of the film. For oxide films with micron-scale thickness and spot sizes ( $a$ ) in the tens of microns, one computes  $1/\omega_1$  is on the order of hundreds of nanoseconds. However, estimates of shock pressures based on pump-probe shadowgraphic microscopy reveal that the pressures in the shock front created by ablated material decrease from several GPa to several tens of MPa in the first ten nanoseconds for fluences  $< 3 \text{ J/cm}^2$  [157]. Therefore, in the remainder of the analysis,  $\dot{w}_o$  is computed from energy/momentum considerations

of the laser pulse, and this is used as the initial condition that dictates the dynamic response of the film.

### Estimate of impulse delivered during laser pulse

Here, it is presumed that the laser pulse ejects a small mass from the substrate that impacts the film. The details of this process (*i.e.* the time/space details of the colliding masses) are unimportant, provided the collisions of all ejected particles with the film occur over a time scale that is small compared to the inertial time scale of the film (*i.e.* in the above, that  $\omega_1 t_o \ll 1$ ). Let it be assumed that the laser pulse imparts a total energy of  $\pi a^2 \phi_{avg}$  to the substrate, and that the total energy of the ejected particles is  $f \pi a^2 \phi_{avg}$ , such that  $f$  represents the fraction of laser energy that is converted to kinetic energy in the ejected mass and  $\phi_{avg}$  is the average fluence of the laser pulse.

Let  $d(r)$  be the spatial distribution of the depth of ejected particles, and  $v^{(1)}(r)$  be the spatial distribution of the velocity of the ejected particles prior to any collision. The momentum of the system prior to impact is simply that of the particles, and is given by:

$$M^{(1)} = \int_0^a 2\pi \rho_s d(r) [v^{(1)}(r)] r dr \quad (5.13)$$

where  $\rho_s$  is the density of the substrate. After impact, the momentum of the system involves contributions from both the reflected particles and the film motion:

$$M^{(2)} = \int_0^a 2\pi \rho_s d(r) [v^{(2)}(r)] r dr + \int_0^a 2\pi \rho h \dot{w}(r) r dr \quad (5.14)$$

where  $v_o^{(2)}(r)$  is the velocity distribution of the ejected particles after impact, and  $\dot{w}(r)$  is the velocity of the film at the end of the impact. For purely elastic impact, the kinetic

energy before and after impact is conserved, such that:

$$\int_0^a \pi \rho_s d(r) [v^{(1)}(r)]^2 r dr = \int_0^a \pi \rho_s d(r) [v^{(2)}(r)]^2 r dr + \int_0^a \pi \rho h [\dot{w}(r)]^2 r dr \quad (5.15)$$

Note that there is no potential (strain) energy in the film after impact, because the assumption of a short impact duration implies the film does not deform during the impact.

Assumptions regarding the spatial distribution of particles ejected from the substrate, the velocity distribution before impact, and the velocity distribution after impact must now be made. These distributions are ultimately controlled by the distribution of the fluence in the laser pulse, *e.g.* a Gaussian distribution. For simplicity, it is assumed that both distributions (the depth of ejected material and the resulting velocity) have the same spatial distribution, and further, that it is given by the first mode shape of the film  $W_1(\bar{r})$ . That is, the assumed spatial distribution of ejected mass and ejection velocity is maximum in the center and zero at the edges where it has zero slope, as shown in Figure 5.1C. This approximation is reasonable given the qualitative similarity between a Gaussian distribution and the first mode shape (see Figure 5.1c).

Thus, the distributions of the depth of ejected mass, the velocity of the ejected mass, and the film deflection are given by:

$$d(r) = d_o W_1(r); \quad v(r) = v_o W_1(r); \quad w(r) = w_o(t) W_1(r) \quad (5.16)$$

where  $d_o$ ,  $v_o$ , and  $w_o$  represent the maximum ejected depth, maximum ejected velocity, and maximum film deflection. This implies that the momentum equations given above

become:

$$M^{(1)} = 0.57\rho_s a^2 d_o v_o^{(1)} = M^{(2)} = 0.57\rho_s d_o a^2 v_o^{(2)} + 0.98\rho h a^2 \dot{w}_o \quad (5.17)$$

For elastic impacts, the energy is conserved such that the ejected particles will rebound with finite kinetic energy. The energy balance expressions are given by:

$$f\pi a^2 \phi_{avg} = 0.2\rho_s d_o a^2 [v_o^{(1)}]^2 \quad (5.18)$$

$$0.2\rho_s d_o [v_o^{(1)}]^2 = 0.2\rho_s d_o [v_o^{(2)}]^2 + 0.29\rho h [\dot{w}_o]^2 \quad (5.19)$$

where Eq. 5.18 represents the translation of laser energy to kinetic energy, and Eq. 5.19 represents conservation of momentum before and after impact. (Note again that the film acquires no potential energy during the impact event, as it does not move over this small timescale.) Equations 5.17-5.19 involve three unknowns: the initial velocity of the ejected mass prior to impact, and the velocities of the ejected mass and film after impact. The solution yields:

$$v_o^{(1)} = 2.24 \sqrt{\frac{f\pi\phi_{avg}}{\rho_s d_o}}; \quad \dot{w}_o = 5.30 \sqrt{\frac{f\pi\phi_{avg}}{\rho_s d_o}} \left( \frac{1}{1 + 2.04 \frac{\rho h}{\rho_s d_o}} \right) \quad (5.20)$$

For purely plastic impacts, the energy of the system is not conserved and instead a simple momentum balance before and after impact is used. Plastic impact implies the velocity of the ejected material after impact is equal to that of the film after impact, such that Eq. 5.19 is replaced by:

$$0.57\rho_s d_o a^2 v_o^{(1)} = (0.57\rho_s d_o a^2 + 0.98\rho h a^2) \dot{w}_o \quad (5.21)$$

Solving for the initial ejected velocity  $v_o^{(1)}$  and the initial film velocity  $\dot{w}_o$  yields:

$$v_o^{(1)} = 2.24 \sqrt{\frac{f\pi\phi_{avg}}{\rho_s d_o}}; \quad \dot{w}_o = 2.24 \sqrt{\frac{f\pi\phi_{avg}}{\rho_s d_o}} \left( \frac{1}{1 + 1.72 \frac{\rho h}{\rho_s d_o}} \right) \quad (5.22)$$

One observes that the initial film velocity is approximately one-half the result for an elastic impact. Comparisons between these predictions and direct observations from experiments are presented in subsection 5.1.3.

### 5.1.2 Film failure and interface debonding

The results detailed above can be used to evaluate two different failure scenarios: (i) the film cracks at the outer edge of the laser pulse, leading to spalling of the film above the exposed area, and (ii) the film debonds at the outer edge of the exposed area. Evidence of these two failure scenarios is shown in Figure 5.3 for a silicon dioxide film grown on a silicon substrate; in Figure 5.3a, the final deformed shape of the film as measured *via* interferometry is shown for a laser pulse of relatively low fluence ( $\phi_{avg} \approx 230 \text{mJ/cm}^2$ ). At low fluences, the film remains intact and comes to rest in a slightly deformed state due to ejected material attached to the backside of the film, residual stresses in the oxide, or both. (A micrograph of the surface is essentially featureless due to the small displaced amplitude of the buckle.) At moderate fluences ( $400 < \phi_{avg} < 450 \text{mJ/cm}^2$ ), one observes the formation of cracks around the outer edge of the exposed region, as shown in Figure 5.3B. At higher fluence ( $\phi_{avg} > 550 \text{mJ/cm}^2$ ), the entire film cracks along the periphery of the exposed region, spalling a circular section of film (Figure 5.3C).

Here, the conditions that lead to either type of failure are outlined; a discussion of which failure mode is anticipated is in the next section. The dynamic response of the film is  $w(\bar{r}, t) = (\dot{w}_o/\omega_1)W(\bar{r}) \sin \omega_1 t$ , which results from an initial velocity distribution given by:  $\dot{w}(\bar{r}, 0) = \dot{w}_o W_1(\bar{r})$  (where  $t = 0$  references the end of the impact event). The

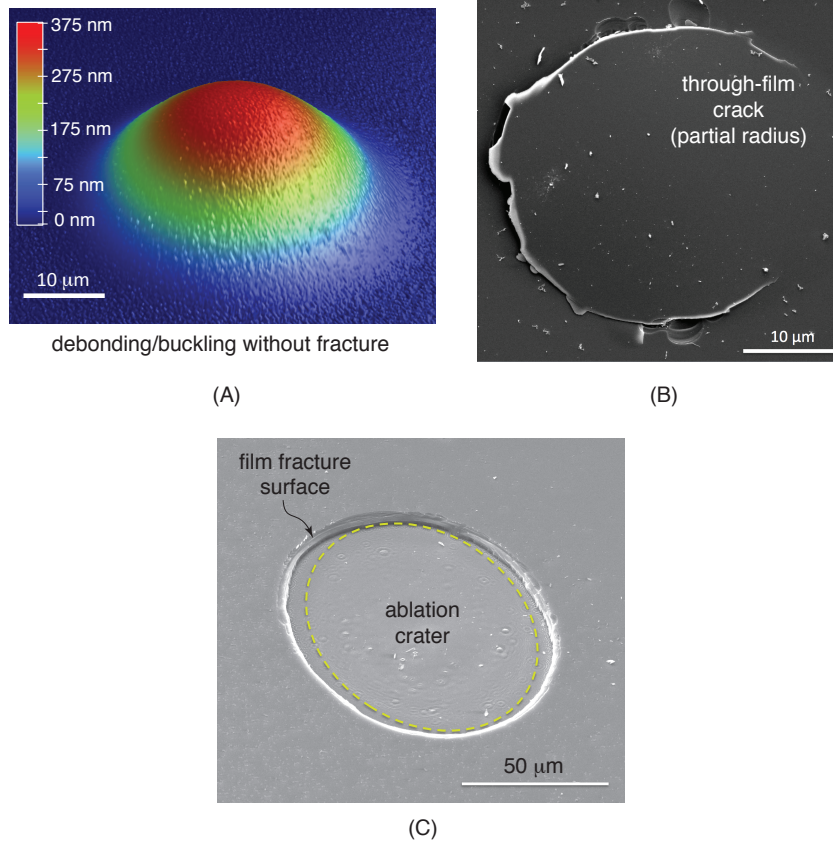


Figure 5.3: Film responses at (a) low fluence - debonding and no fracture in a 1.3  $\mu\text{m}$   $\text{SiO}_2$  film on Si with a 400 mm focal length lens, (b) moderate fluence - partial fracture in a 1.3  $\mu\text{m}$   $\text{SiO}_2$  film on Si with a  $f=200$  mm lens, (c) higher fluence - complete spalling in a 3  $\mu\text{m}$   $\text{SiO}_2$  film on Si with a  $f=400$  mm lens. In this case, it is difficult to confirm the existence of a small amount of interface debonding that may have occurred before film fracture. All tests were conducted within the low-fluence ablation regime of silicon ( $< 4 \text{ J/cm}^2$  [169]).

bending strains in the film are given by:

$$\epsilon_\theta = \frac{hw'(\bar{r}, t)}{2r}; \quad w'(\bar{r}, t) = \frac{\dot{w}_o}{\omega_1 a} W_1'(\bar{r}) \sin \omega_1 t \quad (5.23)$$

$$\epsilon_r = \frac{hw''(\bar{r}, t)}{2}; \quad w''(\bar{r}, t) = \frac{\dot{w}_o}{\omega_1 a^2} W_1''(\bar{r}) \sin \omega_1 t \quad (5.24)$$

where the primes denote differentiation with respect to  $\bar{r}$ . Using the first mode shape, the peak strains (with respect to time) in the film are given by:

$$\epsilon_r(0, t) = \epsilon_\theta(0, t) = 2.28 \frac{h\dot{w}_o}{\omega_1 a^2} \sin \omega_1 t = 0.77 \dot{w}_o \sqrt{\frac{\rho}{E}} \sin \omega_1 t \quad (5.25)$$

$$\epsilon_r(a) = 3.09 \frac{h\dot{w}_o}{\omega_1 a^2} \sin \omega_1 t = 1.05 \dot{w}_o \sqrt{\frac{\rho}{E}} \sin \omega_1 t \quad (5.26)$$

with monotonic variations from the center to the outer edge. (Note  $\epsilon_\theta(a) = 0$ .) Thus, the radial strains are maximum at the outer edge of the film, while the hoop strains are maximum in the center of the film. The film will fail when the induced bending stress at the outer edge ( $r = a$ , or  $\bar{r} = 1$ ) is larger than the intrinsic strength of the material. It should be noted that while circumferential cracking is the most common failure mode in these experiments, many lower-fluence experiments involve radial cracks emanating from the center. This is not surprising in light of the facts that the hoop stress in the film is only slightly lower than the radial stress and that the failure location is strongly influenced by the spatial distribution of film flaws.

If it is assumed that the presence of small flaws of size  $c$  in the film, the critical strain that produces film failure may be solved according to elastic fracture mechanics. Assuming an edge flaw in the film much smaller than its thickness and loading in pure

bending, fracture will be avoided provided that:

$$\dot{w}_o^f < \sqrt{\frac{\Gamma_f}{4\rho c}} \quad (5.27)$$

where  $\Gamma_f$  is the toughness of the film.

Interface debonding at the outer edge of the film can be predicted using the dynamic energy release rate [170–172]. For a penny shaped crack of radius  $a$ , centered at the origin in an isotropic medium, the full axisymmetric result for the dynamic J-integral is given by:

$$J = \frac{1}{a} \left[ \int_{\Gamma_o} (W n_r - T_r u' - T_z w') r d\ell - \int_{A_o} \left( W - T_\theta \frac{u}{r} \right) dA + \int_{A_o} \rho (\ddot{u} \cdot u' + \ddot{w} \cdot w') r dA \right]$$

where  $\Gamma_o$  defines a contour surrounding the crack tip, and  $A_o$  is the area inside the contour. In the above definition,  $u$  and  $w$  are the radial and vertical displacements as a function of position, respectively. For axisymmetric plates subjected to small deflections, the vertical displacement  $w$  is uniform through the thickness of the plate, while bending implies  $u' = -zw'' = \epsilon_r$ , and  $u = -zw' = r\epsilon_\theta$ . Hence, the  $J$ -integral for the axisymmetric plate problem becomes:

$$J = \frac{1}{a} \left[ \int_{\Gamma_o} (W n_r - T_r z w'') r d\ell - \int_{A_o} \left( W - T_\theta \frac{z w'}{r} \right) dA + \int_{A_o} \rho (z^2 \ddot{w}' \cdot w'' + \ddot{w} \cdot w') dA \right] \quad (5.28)$$

Taking a contour that runs through the film along the symmetry axis, along the top surface and back through the film at a radial location far past the crack tip, the first term (i.e. the path integral) is zero, leaving just the remaining two terms (i.e. area

integrals). Using the first mode shape, one computes:

$$J = 1.59 \frac{\bar{E}h^5}{a^4} [\bar{w}_o(t)]^2 \quad (5.29)$$

Note that the deflection of the center  $\bar{w}_o(t)$  for the impulse problem is given by  $\bar{w}_o(t) = (\dot{w}_o/\omega_1) \sin \omega_1 t$  (where  $\dot{w}_o$  is the initial velocity at the center, as defined earlier). Using the definition of the first natural frequency given earlier, this implies:

$$J(t) = 0.18 \rho h \dot{w}_o^2 \sin^2 \omega_1 t \quad (5.30)$$

Interface debonding can be expected when  $J \geq \Gamma_i$ , where  $\Gamma_i$  is the interface toughness. Here, an ideally brittle interface with no mode-mixity effects is assumed; this is discussed further in the next subsection. Thus, debonding is avoided provided that:

$$\dot{w}_o^d < \sqrt{\frac{5.47\Gamma_i}{\rho h}} \quad (5.31)$$

### 5.1.3 Discussion

The model prediction for the velocity of the material ejected by the laser pulse (*i.e.*  $v_o^{(1)}$ ) can be compared to direct measurements obtained using pump-probe shadowgraph microscopy on a nickel alloy *without* an oxide film [157, 173]. These measurements track the location of the shock front as a function of time, which enables calculation of the material velocity leaving the surface. Using Taylor-Sedov models to back-calculate the energy of the shock-wave, one can then compute the kinetic conversion factor  $f$ . Experiments on the nickel based superalloy CMSX-4 suggest that the initial velocity is approximately 10 – 12 km/s for a pulse in the low-fluence ablation regime of 2.7 J/cm<sup>2</sup>. (This velocity range was estimated based on visual inspection of Figure 3a in [157].) The

ablation depth for this fluence was directly measured *via* AFM to be  $d_o \sim 50$  nm and the extracted kinetic conversion factor was  $f = 0.123$  [157]. Using Eq. 5.22 above, one computes  $v_o^{(1)} = 11.0$  km/s for this case, which is a strong endorsement of the model.

Similar experimental observations made on silicon substrates coated with thin films of silicon dioxide enable direct comparisons of the film velocity after the pulse,  $\dot{w}_o$ . The film velocity after the pulse is shown in Figure 5.4 for this system with a laser fluence of  $1.3$  J/cm<sup>2</sup>, using the data from McDonald *et al* [158] and kinetic conversion factors in the range of  $0.01 < f < 0.1$ . The observed ablation depth at this fluence is approximately 80 nm [173]. The agreement between predicted velocity (Eq. 5.22) and measured velocity is excellent if one assumes plastic impact and  $f = 0.02$ . Plastic impacts, where amorphous silicon adheres to the back side of the buckled oxide, have been directly observed experimentally as shown in Figure 5.5.

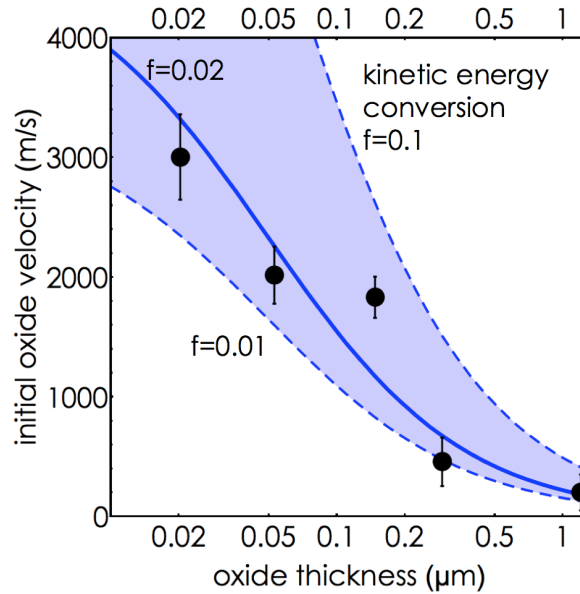


Figure 5.4: A comparison of predicted and measured initial velocities involving silicon dioxide films on silicon substrates [158], using the ablation properties cited in [173]

In the high-fluence ablation regime, in which the incident pulse induces a significant plasma plume [152, 167] ( $\phi_{avg} \gtrsim 10$  J/cm<sup>2</sup> for nickel based superalloys) the model appears

to under-predict the observed initial velocity. It should be emphasized again that plasma plume-pulse interactions at high fluences and the thermal diffusion of electrons has been neglected: future work accounting for these effects may improve the agreement between theory and experiment in this regime. In addition, profiles of the ablated surface at high-fluence deviate from the Gaussian shape and exhibit ‘pile-up’ at the outer edges of the ablation crater [150, 157, 174], presumably from more extensive melting, re-deposition of ablated material, or both. This implies that the model is overestimating the total mass of material that is ejected from the surface and hence underestimating the velocity at which it is leaves. The agreement between predicted and measured velocities at high fluences is much better if the maximum ablation depth  $d_o$  is adjusted by estimating the volume of ejected material to account for the pile-up region [174].

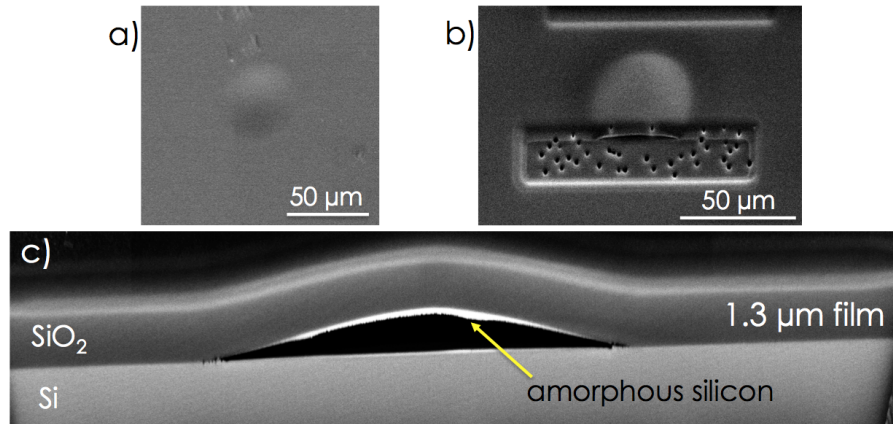


Figure 5.5: FIB cross section of a buckle created with a single fs laser pulse in a 1.3  $\mu\text{m}$   $\text{SiO}_2$  film grown at 1200  $^\circ\text{C}$  on a (001) single crystal Si substrate. a) Secondary electron image of the buckled film before cross section. b) Plan view of the buckle and cross FIB-etched area during machining. c) Tilted cross section showing the Si substrate,  $\text{SiO}_2$  film, and the amorphous silicon that was ablated from the substrate during fs laser irradiation and plastically impacted the underside of the film.

An important application of the present model is the specification of laser pulses that introduce a well-defined interface flaw while avoiding failure, which can be used for subsequent studies of film delamination. For a given laser pulse, one can determine

whether cracking or debonding occurs by comparing the initial film velocity with the critical values associated with each failure mode. There are four possible scenarios:

- (i) neither failure mechanism is possible: this happens when the kinetic energy density imparted to the film,  $\rho\dot{w}_o^2$ , is less than **both**  $5.47\Gamma_i/h$  and  $\Gamma_f/(4c)$ .
- (ii) film fracture is possible but debonding is not: this happens when  $\rho\dot{w}_o^2$  is greater than  $\Gamma_f/(4c)$  but less than  $5.47\Gamma_i/h$ .
- (iii) debonding is possible but film fracture is not: this happens when  $\rho\dot{w}_o^2$  is greater than  $5.47\Gamma_i/h$  but less than  $\Gamma_f/(4c)$ .
- (iv) both debonding and film fracture are possible: this happens when  $\rho\dot{w}_o^2$  is greater than **both**  $5.47\Gamma_i/h$  and  $\Gamma_f/(4c)$ .

These four conditions are shown graphically in Figure 5.6, which provides a universal map indicating relevant failure modes as a function of system properties. In this figure, data points corresponding to laser pulses applied to a silicon/silicon dioxide system are overlaid: the values associated with these data points correspond to multiple levels of laser fluence, spot size and two values of oxide thickness (1.3 and 3.0  $\mu\text{m}$ ). The relationship between laser fluence and ablation crater depth  $d_o$  is taken from the work of Coyne et al [169]. The critical flaw size  $c$  is assumed to be 15 and 45 nm, respectively. The film toughness and interface toughness are assumed to be 1 J/m<sup>2</sup>. The error bars correspond to  $\pm 50\%$  changes in toughness and flaw size.

In Figure 5.6, agreement between the experiment and predictions is ensured by the choice of the defect size in the film. While direct observations of flaw sizes would be ideal (thus removing any fitting parameter), it is difficult to envision how such observations would be made, given the high quality of oxide films grown on silicon. Moreover, one would need an accurate idea of the flaw size distribution *and* spatial distribution of

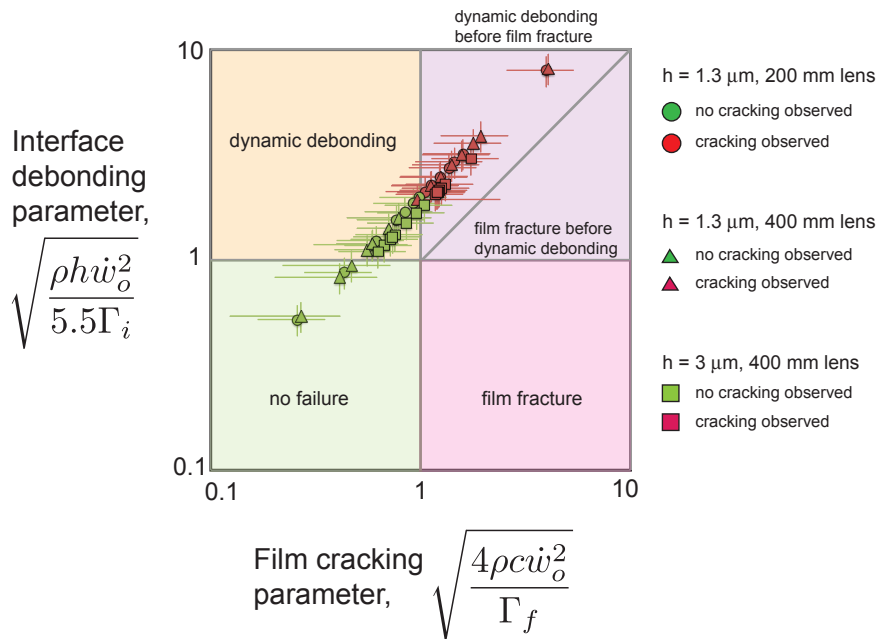


Figure 5.6: Regime map indicating whether film debonding or film fracture will be triggered by the laser pulse; the initial velocity of the film  $\dot{w}_o$  is related to the pulse characteristics as shown above the figure. The line delineating between debonding and fracture regimes is described by equating the film debonding and film fracture parameters. Experimental data are from a series of experiments conducted with 1.3 and 3  $\mu\text{m}$  thermally grown  $\text{SiO}_2$  films on Si substrates with 200 and 400 mm focal length lenses.

flaws in the area exposed to the laser pulse. Clearly, the model implies flaw sizes that are reasonable (not negligible but also not a significant fraction of the film thickness). Thus, the model combined with high throughput laser pulses distributed across a surface presents an opportunity to rapidly assess the flaw size distribution in oxides.

The data in Figure 5.6 were collected from a number of experiments with different SiO<sub>2</sub> films thermally grown on single crystal Si substrates. The experimental setup is discussed and illustrated in detail in Section 5.2.1. An example of one series of experiments, conducted with a 1.3 μm SiO<sub>2</sub> film grown on a Si substrate, is in Figure 5.7. This optical micrograph shows some of the fs laser irradiated spots from the series of tests. Repeat experiments with the same laser fluence (energy/area) were conducted moving horizontally along the rows and the laser parameters were changed for each row. The spots in the left three columns all resulted in film fracture around the perimeter of the irradiated area while the right columns have all formed stable silica buckles.

These experiments can be used to measure the SiO<sub>2</sub>-Si separation threshold by fitting the diameter of film separation/fracture to the fluence of the Gaussian pulse at the indicated radius. The results of these measurements are in Figure 5.8 and indicate that the separation threshold is about 170 mJ/cm<sup>2</sup>, which is in close agreement with the ablation threshold of Si (200 mJ/cm<sup>2</sup> [169]). This series of experiments was conducted with a 1.3 μm SiO<sub>2</sub> film grown on a (001) Si substrate and used two different planoconvex lenses. The 400 mm focal length lens spreads out the laser pulse energy more than the f=200 mm lens and so has a larger detachment radius for a given pulse energy. The experiments were conducted with a 1 kHz pulse repetition rate and a 150 fs pulse length.

To further illustrate the agreement of the model and the Si/SiO<sub>2</sub> experiments, Figure 5.9 plots the observations of cracking as a function of laser fluence and film thickness. The theoretical prediction for the critical fluence to cause cracking and debonding is also shown, using the same properties described above. For the 1.3 μm thick oxides,

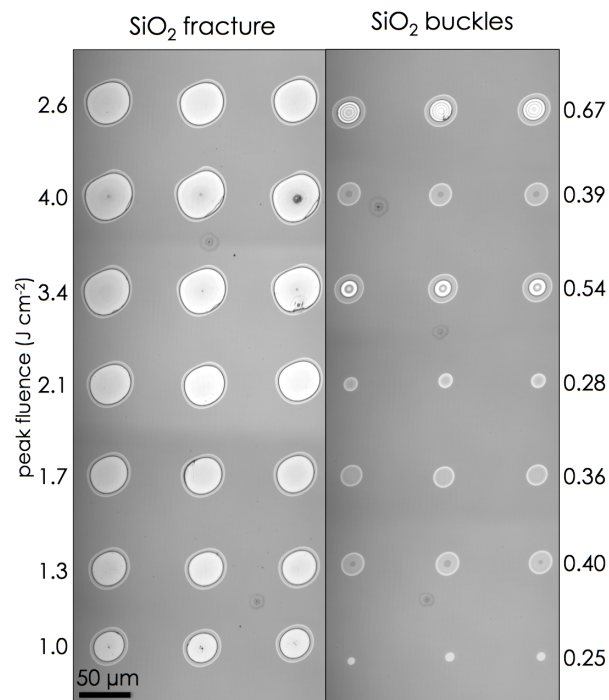


Figure 5.7: Optical micrograph showing the plan view of a  $\text{SiO}_2$  film that was thermally grown on a Si substrate. Horizontal rows are repeats of the same laser parameters; the uniform behavior of the film reveals the uniformity of both the  $\text{SiO}_2$  film and the  $\text{SiO}_2$ -Si interface. The laser-irradiated spots in the left three columns all resulted in fracturing of the film whereas the film remained intact for the parameters in the right three columns. Test was conducted with a  $f=400$  mm planoconvex lens.

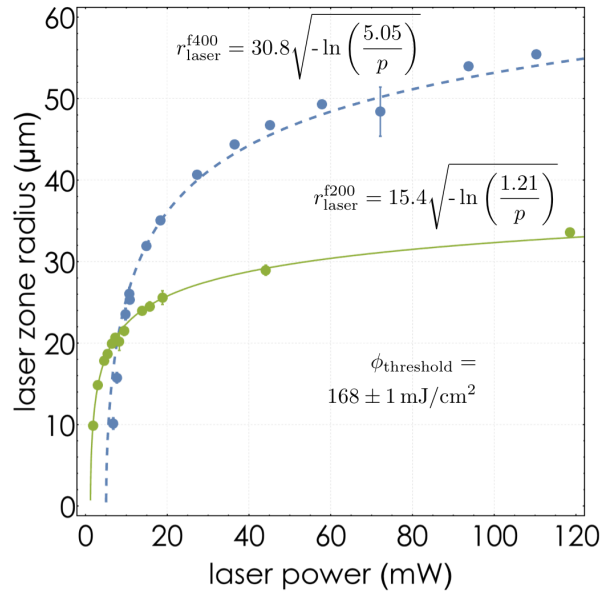


Figure 5.8: Test was conducted with a  $f=400$  and  $f=200$  mm planoconvex lenses.

experiments were conducted using two optical lenses with different focal lengths, resulting in distinct laser spot sizes: one of them is slightly displaced to  $1.35 \mu\text{m}$  thickness such that one can distinguish between these two different experiments. The agreement is quite good, again due to the chosen flaw size.

In Figures 5.6 and 5.9, one observes that some of the experiments were conducted with laser pulses where debonding is predicted. Determining whether or not debonding occurs is quite challenging, as the films remain essentially flat. Large exposed areas can lead to buckling with small deformed amplitudes, but even then it is difficult to identify the extent of debonding. Generally, for the experiments on the Si/SiO<sub>2</sub> system shown in Figures 5.4-5.9, obvious evidence of debonding does not occur significantly outside the exposed area. (By contrast, for nickel alloy/Al<sub>2</sub>O<sub>3</sub> systems, with much larger residual stresses in the film, there are obvious indications of significant debonding beyond the exposed area; this will be reported later.) Hence, comparison of experiments in Figure 5.6 with the debonding axis is meaningless because evidence of debonding was not obtained.

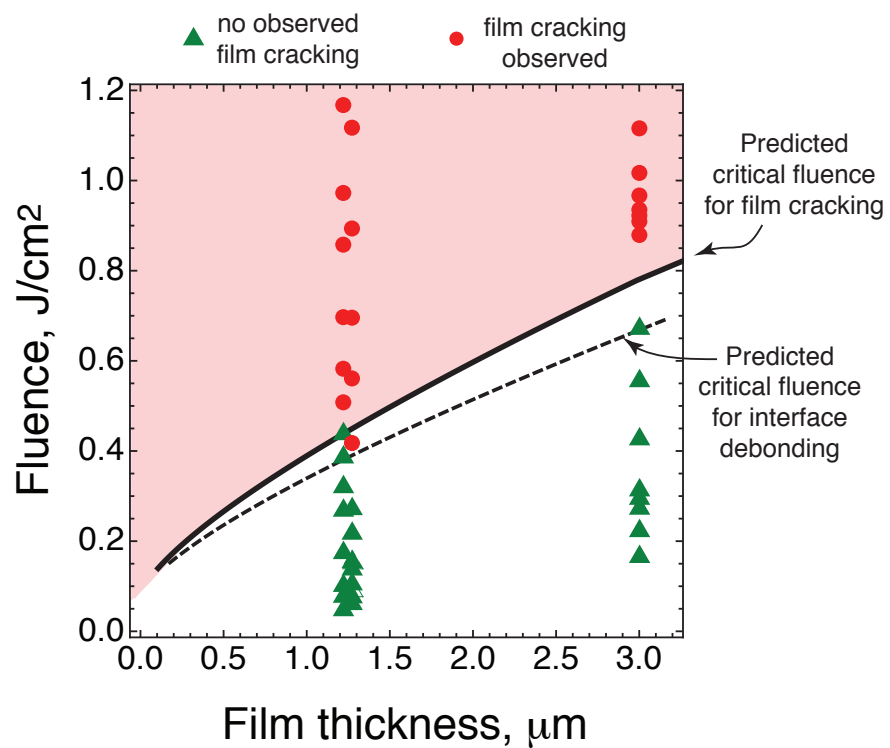


Figure 5.9: Failure map indicating the critical average fluence required to trigger debonding and film fracture for the case of silicon dioxide on a silicon substrate. Experimental data are the same as in Figure 5.6.

Additional experiments and simulations are required to address the validity of the model with regard to debonding. It is worth emphasizing that the model indicates whether or not dynamic debonding initiates, but does not address the extent of delamination. It seems reasonable to believe that if the pulse excites the film to just above the threshold for debonding, the extent of debonding will be rather small. The peak driving force for debonding is obtained near the peak deflection, such that the driving force decreases a short time after the peak as the film returns to its initial position. Simply put, there may not be a large enough period of time where the energy release rate is higher than the critical value needed to advance the interface crack. Further, the model does not address whether or not the film fractures *after* dynamic debonding has occurred. Debonding may not dramatically lower the dynamic stresses in the film; cracking after debonding is a real possibility when one considers that the critical flaw in the film may lie just outside the exposed area. (Presumably, if fracture occurs prior to debonding, the driving force for delamination will drop precipitously as cracking alleviates strain energy in the film.)

While the above considerations rule out conclusive statements regarding debonding in the present experiments, it is interesting to consider the underlying scaling in Figure 5.6. The “no failure” region extends to the experimental boundary between fractured and intact films if one assumes an interface toughness of  $\Gamma_i = 3\text{J/m}^2$  (*i.e.* a value three times larger than used to plot the data points). Such values of interface toughness may be appropriate when one considers that interface debonding is mixed-mode. The point to this observation is that plausible values of interface toughness put the critical condition for cracking and debonding in close proximity, at least for films with relatively small internal defects.

The presented model also suggests which failure mode occurs first in time, which may provide additional insight with regards to interpreting future experiments. The time at

which each failure condition is reached can be computed using the above results, which yields the time-to-fracture ( $\omega_1 t_*^f = \sin^{-1} \dot{w}_o^f / \dot{w}_o$ ) and the time-to-debonding ( $\omega_1 t_*^d = \sin^{-1} \dot{w}_o^d / \dot{w}_o$ .) These results indicate that the failure mode is indicated by the smaller of the values of  $\dot{w}_o^f / \dot{w}_o$  and  $\dot{w}_o^d / \dot{w}_o$ . The time to reach both failure modes is equal when the ratio given by:

$$\frac{\dot{w}_o^d}{\dot{w}_o^f} \approx 22 \frac{\Gamma_{ic}}{\Gamma_{fh}} \quad (5.32)$$

is equal to unity, which defines a straight line in Figure 4 that delineates between “film fracture first” and “dynamic debonding first”. That is, for systems with  $\dot{w}_o^d / \dot{w}_o^f < 1$  debonding will occur first (provided the debond parameter is above the threshold), while for  $\dot{w}_o^d / \dot{w}_o^f > 1$ , film fracture will occur first (again, provided the fracture parameter is above the threshold).

Although the placement of the observations in the failure map requires an estimate for the flaw size, the model clearly captures the essential scaling of the problem. The agreement of the model and the observations of cracking suggest that residual stress may induce off-setting effects (at least for low values of compressive stress): compressive stresses will make the film more compliant for large deformations, but also will decrease the total mechanical strain in the film at the edge of the debonding region. Ongoing modeling and simulations are addressing the role of residual stress, which may play a key role in other systems, notably oxides grown on nickel-based superalloys.

Finally, it should be noted again that the above treatment does not address the role of mode-mixity in delamination [175], which is known to have a large effect in the static response of ductile systems. Unfortunately, the model neglects a key factor in mode-mixity: the role of axial displacements in the film and their dynamic (temporal) behavior. More sophisticated modeling and simulations will be needed to address this

aspect of the problem; once conducted, an effective mixed-mode phase angle for dynamic debonding might be identified, as has been done for quasi-static systems prone to buckling (i.e. a phase angle of  $-70^\circ$  [176]). One would then use the toughness at the ‘equivalent’ phase angle in the above models.

#### 5.1.4 Conclusions

Femtosecond laser pulses are fundamentally disparate from ns lasers in that they ablate material at a film/substrate interface and generate a complex time-history of internal pressure with negligible heating and damage. In the low-fluence ablation regime, the ejectile is liquid-like without significant plasma generation. This process can ultimately lead to film cracking or debonding. For many films, the pressure burst occurs over timescales that are much shorter than the characteristic timescale of film motion (as determined by the film’s bending stiffness and inertia). This implies that the film motion can be accurately predicted using the impulse delivered by the pressure pulse, obviating the need to resolve its complicated space-time relationships.

The impulse delivered to the the film can be computed from conservation of linear momentum (for plastic impacts of the ablated material) and conservation of energy (for elastic impacts), provided one has an estimate of the mass of material that is released from the substrate and its initial velocity. The initial velocity of ablated material is well approximated by equating the laser pulse energy to the kinetic energy of the mass leaving the surface using a conversion factor that can be determined experimentally. Calculations of the impulse delivered to the film using this model and direct observations of system properties lead to accurate predictions of the initial velocity of the film, as verified by direct observations of film velocity.

A conventional dynamic film model for the film motion after the impulse yields the displacement and stress distributions in the film as a function of space and time, which can be used to predict film fracture from pre-existing flaws or film debonding using a dynamic form of the J-integral. A comparison of cracking observations in the Si/SiO<sub>2</sub> system and the model indicates that the model will be useful in the design of laser pulse experiments that produce well-defined interface flaws while avoiding film failures. Furthermore, the model indicates that information about the interface toughness and film toughness can be learned based on the behavior that the system exhibits after laser irradiation. Applications of this model and justification for its use with systems having moderate residual stress will be the subject of the next section.

## 5.2 Interface toughness of Al<sub>2</sub>O<sub>3</sub>–FeCrAl(Y)

Sulfur and reactive elements have a significant effect on the interface toughness and cyclic oxidation behavior of Al<sub>2</sub>O<sub>3</sub>-metal interfaces, as discussed in Section 4.5. Sulfur or other impurity segregation to the Al<sub>2</sub>O<sub>3</sub>-substrate interface can weaken the adhesive strength of the oxide scale and increase the rate TGO spalling [123, 124, 132]. Therefore, a means of measuring the interface strength quickly and in a straightforward means is of interest. FeCrAl and FeCrAlY systems are common model systems for NiCoCrAlY bond coats because they have similar coefficients of thermal expansion and also form a pure Al<sub>2</sub>O<sub>3</sub> scale. It is known that Y added to FeCrAl acts as a S gettering agent and improves TGO retention during cyclic oxidation [133–135]. A comparison of the interface toughness assessment of these two system conducted with a fs laser demonstrates the different behaviors found for residually compressed films having significantly differing interface toughnesses.

### 5.2.1 Laser testing procedure

A femtosecond laser is used to create controlled sizes of interface flaws and to give the detached film an initial out-of-plane velocity as described in the previous section. The subsequent behavior of the film-substrate interface crack gives information about the interfacial toughness of the system. A Clark MXR CPA-Series (Nd:YAG-pumped Ti:Sapphire) laser is used to create controlled interface flaws between the substrate and transparent film. Emission is linearly polarized with a wavelength centered around 778 nm with a nominal pulse length of 150 fs. Laser power and thereby pulse fluence is attenuated with a rotating half-wave plate in combination with a polarized beam splitter and neutral density filters (see Figure 5.10). Photographs of the optical setup are shown in Figures 5.11 and 5.12. Plano-convex objective lenses with a 400 or 200 mm focal length were used to control the incident spot size. The profile of the beam is roughly Gaussian at focus as can be seen in the inset of Figure 5.10. Controlling the laser power (and thereby the pulse energy) for a given lens allows control of the energy density (fluence) and spot size, which impacts the initial velocity of the detached film. A custom-coded LabView program is used to take microscope images before and after the laser pulses. The program moves the stage in front of the microscope, focuses and captures an image of the scale, moves the sample to the focal point of the chosen laser path, irradiates the spot with a single pulse, and then moves the sample back to the microscope for a post-pulse image.

### 5.2.2 FeCrAl(Y) oxidation

Polycrystalline specimens of commercially available Kanthal AF, a good  $\alpha$ -alumina former, with a nominal composition (in at%) Fe-(20.4-23.3)Cr-10.1Al-(0-1.3)Si-(0-0.4)Mn-(0-0.3)C and FeCrAlY were used as substrates. Rectangular specimens with 2.2

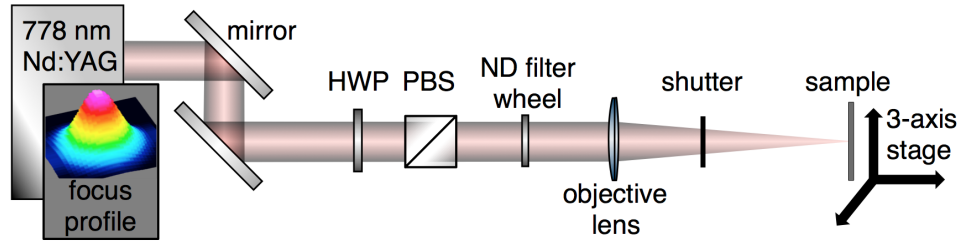


Figure 5.10: Schematic showing the optical setup used for ultra-fast single pulse buckling experiments. The labeled elements (from left to right) are a half-wave plate (HWP), polarized beam splitter (PBS), neutral density (ND) filter wheel (OD = 0.1 to 4), plano-convex objective lens, shutter, and the sample mounted to a three-axis stage. The ND filters are used to coarsely control the pulse fluence. The HWP is used to rotate the polarization of the beam as it enters the PBS, which only passes the vertically polarized component, thereby finely attenuating the pulse fluence incident onto sample.

*inset:* Image showing the Gaussian shape of the laser profile at focus with an  $f=400$  mm lens. Focus was measured using a DataRay<sup>TM</sup> WinCam D optical beam profiler to have an effective  $1/e^2$  focus radius of  $45.5 \mu\text{m}$  and an ellipticity of 0.85.

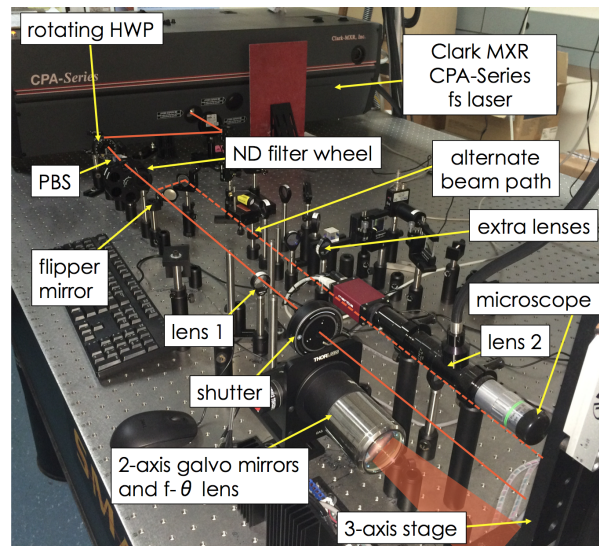


Figure 5.11: Photograph showing the optical setup used for ultra-fast single pulse buckling experiments. Alternate optical path is used so that two lenses can be mounted and used on the same sample at once. A mechanical flipper mirror is used to switch the beam line between the two beam legs. The 2-axis galvanometric mirrors equipped with the F-Theta scan lens is used for micromachining and occasional surface preparation of samples. A second flipper mirror is used to direct the laser beam into the galvanometric mirror path. PBS- polarized beam splitter, ND - neutral density, HWP - half wave plate.

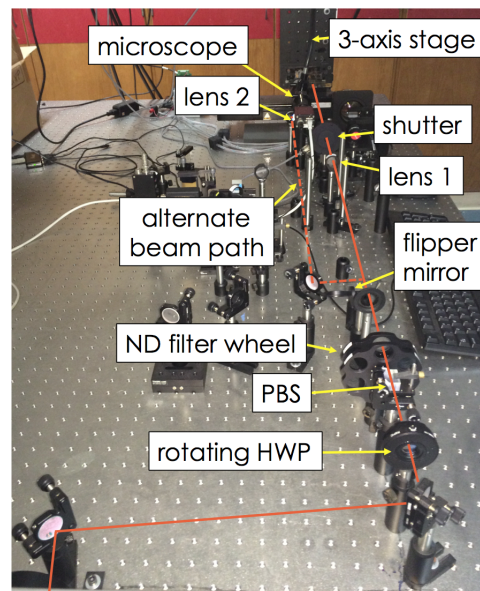


Figure 5.12: Photograph showing the optical setup used for ultra-fast single pulse buckling experiments. Alternate optical path is used so that two lenses can be mounted and used on the same sample at once. A mechanical flipper mirror is used to switch the beam line between the two beam legs. PBS- polarized beam splitter, ND - neutral density, HWP - half wave plate.

Table 5.1: Physical constants used in the  $\alpha$ -Al<sub>2</sub>O<sub>3</sub>-FeCrAl model system.

	$\alpha$ (ppm/°C)	$\nu$	E (GPa)	$\rho$ (kg/m <sup>3</sup> )	$\Gamma_1^c$ (J/m <sup>2</sup> )
$\alpha$ -Al <sub>2</sub> O <sub>3</sub>	8.2	0.27	375	3980	20 [180]
FeCrAl	15	0.3	182	7150	

mm thickness were ground on both sides with SiC paper (1200-grit) and then polished to a final finish with 1- $\mu$ m diamond suspension. Specimens were ultrasonically cleaned in acetone and isopropyl alcohol and dried with clean air before oxidation.

Oxidation was performed for 30 hours at 1200 °C in a two-zone horizontal tube furnace with standing ambient air. The heating and cooling rates were approximately 200 °C/min and -10 °C/min. The mass of the specimens was measured before and after oxidation in order to determine 4.9  $\mu$ m as the nominal thickness of the thermally grown oxide (TGO) on FeCrAl and 3.5  $\mu$ m on FeCrAlY, in agreement with previous observations that the addition of Y creates a denser and more slow-growing Al<sub>2</sub>O<sub>3</sub> scale on MCrAl alloys. A polycrystalline  $\alpha$ -alumina film of these thicknesses remains more than 97% transparent at the incident laser wavelength [177].

The biaxial stress of the TGO was measured via a piezospectroscopic technique [22, 178, 179], as described in Section 5.2.3, to be  $\sigma_0 = -3.7 \pm 0.5$  GPa on FeCrAl and  $\sigma_0 = -3.4 \pm 0.3$  GPa on FeCrAlY at room temperature. This value is based on the average and standard deviation peak shift of five measurements and is in good agreement to the calculated value using the CTE mismatch,  $\sigma_0 = E\Delta\alpha\Delta T = -4.1$  GPa, using the values in Table 5.1. Flaws of controlled size were introduced in the TGO-FeCrAl substrate interface as described in Section 5.2.1.

### 5.2.3 Al<sub>2</sub>O<sub>3</sub> stress measurements via piezospectroscopy

The biaxial residual stress in the oxide scale was measured using a photo-stimulated luminescence spectroscopic (PSLS) technique using an Horiba Jobin Yvon LabRAM HTS Raman spectrometer with a 633 nm incident wavelength. The stress was determined using a piezospectroscopic principle wherein the location was identified for the ruby R2 peak, resulting from Cr<sup>3+</sup> impurities in the Al<sub>2</sub>O<sub>3</sub> scale. The peak shift was compared to a stress-free polycrystalline alumina sample to determine the stress state of the film using Equation 5.33 where  $\Pi_{ii} = 7.61 \text{ cm}^{-1}/\text{GPa}$  [22, 178, 179, 181].

$$\overline{\Delta\nu} = \frac{1}{3}\Pi_{ii}\sigma_{jj} \quad (5.33)$$

The R2 peak was used because the peak frequency shift-stress relationship was found to be more linear than that of the R1 peak [181].

### 5.2.4 Results

Broad plan view micrographs of the fs laser irradiation experiments conducted on FeCrAl and FeCrAlY are in Figures 5.13 and 5.14. The rows are labeled with the laser pulse peak fluence used for the indicated row; the same laser parameters were repeated across each row with spacing of 300  $\mu\text{m}$  between pulses. The variation in behavior moving across individual rows indicates the vast disparity in local TGO and interface properties throughout both of the systems. Broadly speaking, a comparison of the two different tests indicates that the TGO-substrate interface toughness, as expected, is much greater in the FeCrAlY system than for FeCrAl. Irradiated spots in the FeCrAlY system tend to form buckles with peak fluences  $1.2 \leq \phi_{peak} \leq 2.8 \text{ J/cm}^2$  and fracture the TGO film around the perimeter at fluences  $\phi_{peak} \geq 3.1 \text{ J/cm}^2$ . In contrast, there tends to be

extensive interface separation for all fluences  $\phi_{peak} \geq 2.2 \text{ J/cm}^2$  in the FeCrAl system, indicating that the interface cracks extended along the interface before kinking into the film and causing spalling of the film.

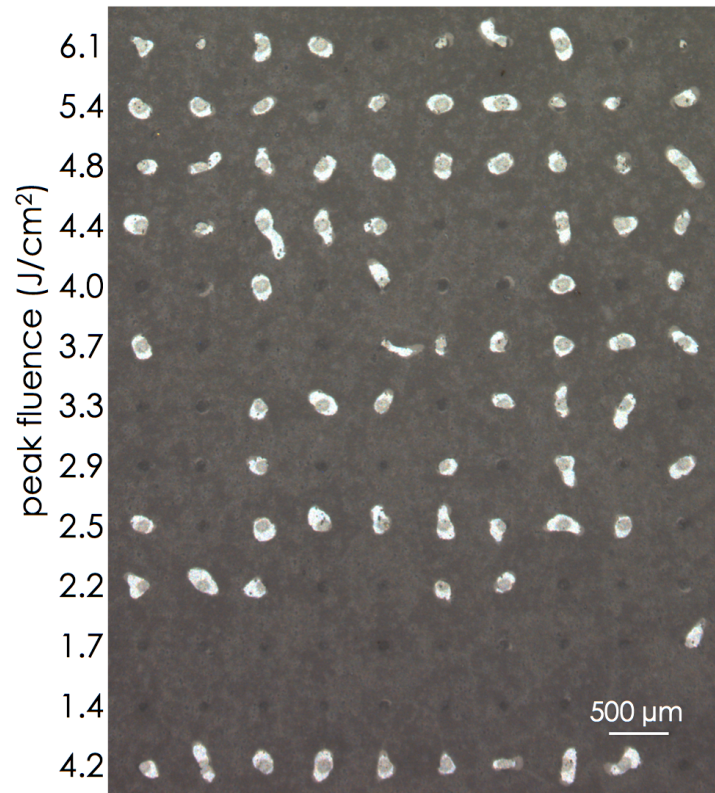


Figure 5.13: Light optical micrograph of a fs laser test conducted on a FeCrAl substrate with a  $4.9 \mu\text{m}$   $\text{Al}_2\text{O}_3$  TGO that was grown at  $1200 \text{ }^\circ\text{C}$  in air. Test spots were evaluated with a 150 fs laser using a  $f = 400 \text{ mm}$  focal length plano-convex lens. Peak fluence calculated from the Gaussian focus profile is listed to the left of each row. TGO is under  $-3.7 \text{ GPa}$  of biaxial compressive stress. The bright spots show areas where the TGO has spalled from the substrate and the FeCrAl below is exposed.

Higher magnification images showing details of some examples from the FeCrAl and FeCrAlY fs laser experiments are in Figures 5.15 and 5.16. The morphology of the TGO grain imprints in the base alloy can be seen where the oxide scale has been ex-foliated. There is a clear delineation between the laser-affected alloy and the virgin alloy surface, as shown in Figure 5.15. Detail images of the TGOs in cross section are in Figure 5.17,

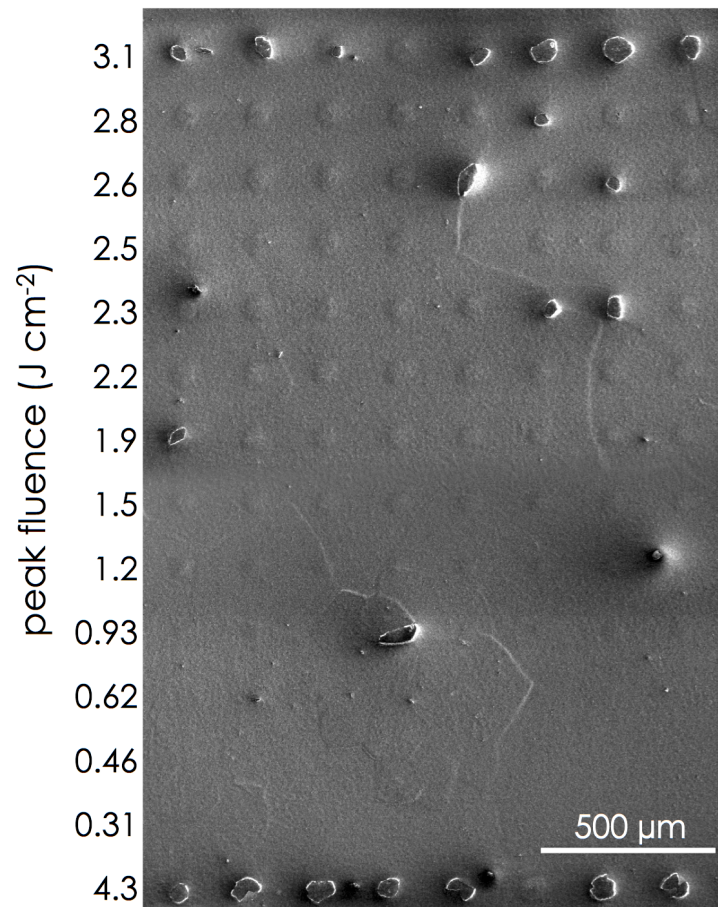


Figure 5.14: Secondary electron micrograph of a fs laser test conducted on a FeCrAlY substrate with a  $3.5 \mu\text{m}$   $\text{Al}_2\text{O}_3$  TGO that was grown at  $1200^\circ\text{C}$  in air. Test spots were evaluated with a 150 fs laser using a  $f = 400$  mm focal length plano-convex lens. Peak fluence calculated from the Gaussian focus profile is listed to the left of each row. TGO is under  $-3.4$  GPa of biaxial compressive stress. Charging of buckles in the TGO scale, due to low electrical conductivity where the TGO is not attached to the substrate, are seen in rows with peak fluence  $\phi_{peak} \geq 1.2 \text{ J/cm}^2$ .

showing the difference in growth morphology with and without yttrium. The addition of Y to MCrAl alloys promotes inward growth of the TGO by inhibiting cation diffusion through the scale. This results in a thinner oxide with a columnar microstructure.

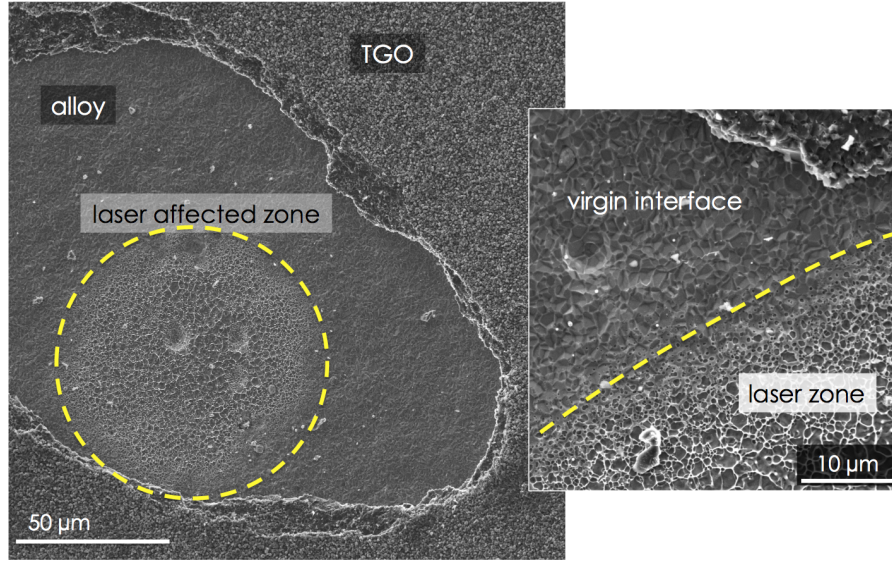


Figure 5.15: Secondary electron micrograph showing detail of a single fs laser-irradiated spot for the  $\text{Al}_2\text{O}_3\text{-FeCrAl}$  system. The delineation between the laser-affected (ablated) substrate and the unaffected alloy is clearly visible in the inset on the right. The image on the left shows a clear laser-affected zone, surrounded by the exposed alloy interface and the fractured TGO around the perimeter. The TGO exhibits dual inward and outward growth behavior due to lack of yttrium; both layers of the scale are visible. Detail of the TGO is in Figure 5.17.

An ablation calibration experiment on a bare alloy surface with the same initial finish ( $1\ \mu\text{m}$ ) indicated that the ablation radius with an  $f = 400\ \text{mm}$  lens is represented as

$$r_{laser}(\mu\text{m}) = 30.7694 \sqrt{-\ln\left(\frac{2.34526\ \text{mW}}{p_0}\right)} \quad (5.34)$$

where  $p_0$  is the average power of laser beam in milliwatts. This leads to TGO-FeCrAl detachment threshold that is about  $78 \pm 5\ \text{mJ}/\text{cm}^2$ . This is relatively close to the behavior seen in the fs laser ablation of NiAl using similar conditions [182]. Borrowing this

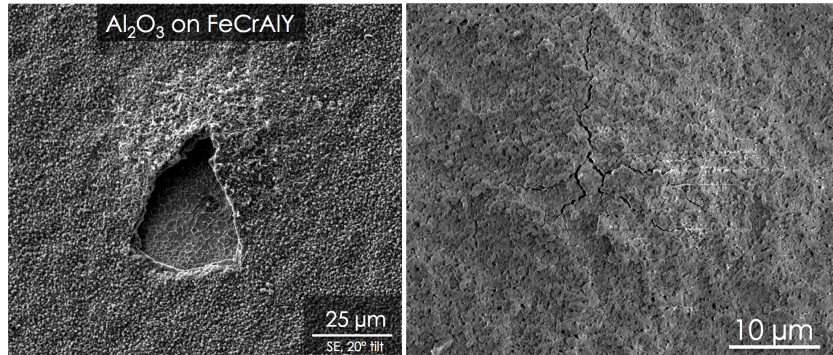


Figure 5.16: Secondary electron micrograph showing detail of a single fs laser-irradiated spot for the Al<sub>2</sub>O<sub>3</sub>-FeCrAlY system. The right image shows a buckle that formed and then partially fractured, allowing the inside of the cavity to be seen. The right image shows an example of radial cracks emanating from the center of a TGO buckle. Detail of the TGO is in Figure 5.17.

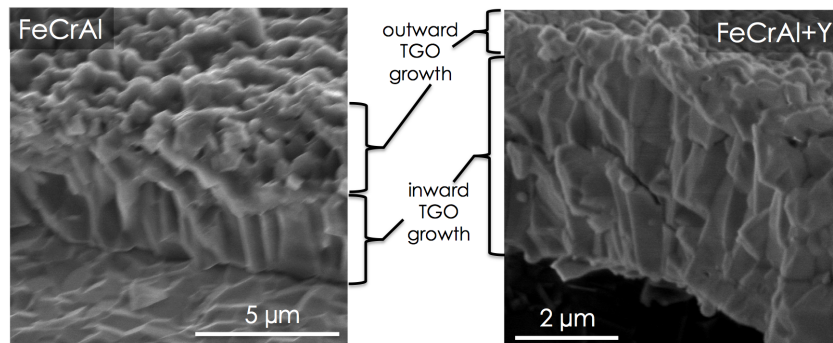


Figure 5.17: Detail micrographs of the thermally grown oxides from the FeCrAl and FeCrAlY systems. The addition of Y to the alloy promotes inward growth of the oxide scale and results in a columnar microstructure whereas the FeCrAl has a significant portion of the TGO with an equiaxed microstructure.

description of the ablation depth and size as a function of laser power, one can calculate the initial velocity of the overlying film using the impulse mechanics developed in the previous sections (Equation 5.22). A comparison of the film initial velocities as a function of peak laser fluence (equivalently laser average power) is shown in Figure 5.18. This calculation uses the ablation-fluence relationships derived for NiAl in [182], but with the material parameters (density, moduli, etc.) for the  $\text{Al}_2\text{O}_3$ -FeCrAl systems. The difference between the initial velocities in the systems arises from the thickness of the TGO films; the FeCrAlY substrate has a thinner film, which has a lower mass. A transfer of an equivalent amount of momentum from the fs laser ablation interaction of the substrate gives the thinner film a higher initial velocity.

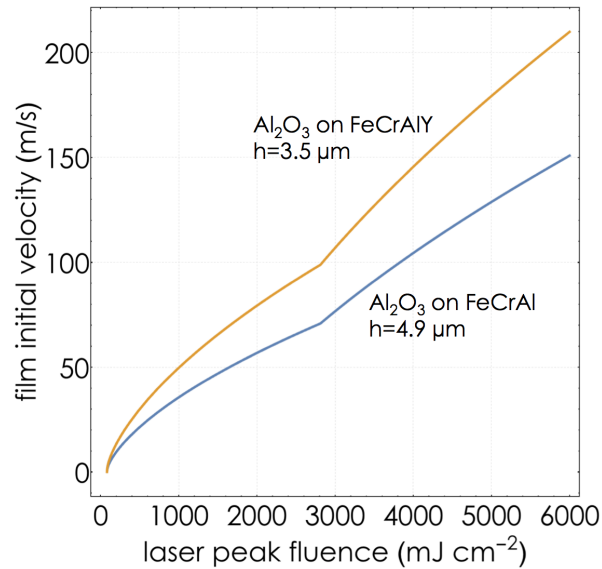


Figure 5.18: Calculation of the initial velocity of a circularly detached thin  $\text{Al}_2\text{O}_3$  film that is grown on a FeCrAl or FeCrAlY substrate and irradiated by a fs laser. Calculation assumes the laser ablation parameters (ablation depth and radius as a function of fluence) for NiAl, which appear to be similar to FeCrAl.

### 5.2.5 Discussion

Closely examining the behavior of the  $\text{Al}_2\text{O}_3$ -FeCrAl system, it is clear that the transition from TGO failure and no TGO failure occurs at a peak fluence around  $\phi_{peak} = 2.2 \text{ J/cm}^2$ , where about half of the irradiated spots showed interface delamination while half did not (Figure 5.13). Using Equations 5.22 and 5.31 to calculate the initial film velocity ( $\dot{w}_o = 60 \text{ m/s}$ ) and then the interface toughness required for a transition between interface delamination and no crack advance at this fluence gives a value of  $\Gamma_{int} = 13 \pm 2 \text{ J/m}^3$ , where the uncertainty is derived from the experimental fluence range from which the transition may have occurred (1.7-2.2  $\text{J/cm}^2$ ). This is a reasonable value and within the range that would be expected for a weak, impurity-rich interface [124, 125, 129, 144]. The fracture behavior of the interface crack kinking into the film to cause film spalling is highly sensitive to the local topology of the interface and the flaw distribution in the film.

The behavior of the FeCrAlY system, with the stronger TGO-substrate interface, indicates that there was never any clearly visible interface delamination. It is possible that a small amount of delamination occurred but it did not lead to TGO failure at lower laser fluence values. Further examination using FIB cross sections of the individual buckles would be required to determine if this is the case. Attempts to measure the radii of the buckles using piezospectroscopy had insufficient resolution to determine if interface cracks advanced an amount less than about  $5 \mu\text{m}$  from the initial laser-separated region. Nevertheless, the fact that there is no obvious interface delamination and that there is a transition from stable buckling to immediate film fracture allows the lower bound of the interface toughness to be determined. The transition between stable buckling without film failure to immediate film fracture occurs around a fluence of  $\phi_{peak} = 3.2 \text{ J/cm}^2$ . This value gives an initial film velocity  $\dot{w}_o = 115 \text{ m/s}$ , and a minimum interface toughness

of  $\Gamma_{int} \geq 34 \text{ J/cm}^2$ . However, it is also important to consider the competition with film fracture for this system because interface delamination cannot occur if the TGO fractures earlier in time. Assuming that the critical flaw size in the TGO is 5% of the film thickness and that the fracture energy of the TGO is  $20 \text{ J/cm}^3$ , the critical velocity for film fracture is  $\dot{w}_o^f \geq 85 \text{ m/s}$ . This means that  $\dot{w}_o^d/\dot{w}_o^f > 1$  and that it would be expected that film fracture will always occur first for such a high interface toughness. Therefore, the reported minimum interface toughness must be discounted using the transition at  $\dot{w}_o^d = \dot{w}_o^f$ . This calculation gives a maximum measurable interface toughness for this system of  $\Gamma_{int} \geq 18.3 \text{ J/cm}^2$ . The TGO will always fracture before the interface has the chance to delaminate if the interface toughness is greater than this value, providing a lower bound for the FeCrAlY system.

It is important to consider the effect of residual stress in these systems with high CTE mismatches. The previous analysis was made with the assumption that the impulse effects dominate the behavior of the competing interface and film kinking failure mechanisms. This analysis has been justified by discrete element modeling (DEM) performed by J. Will Pro [183]. In these simulations, he evaluated the effects of changes in residual stress, interface toughness, and film toughness in a plane-strain version of the buckling model. It was found that the residual stress of the film had little effect on the transition from interface delamination to film fracture for moderate (and realistic) film toughness values,  $\Gamma_{film} \leq 30 \text{ J/m}^2$ . Because the toughness of an alumina film is considerably lower than this value, in the range of  $20 \text{ J/m}^2$  [180], there is a good indication that this system is laser impulse-dominated for tests of interest. An analytical model describing the dynamic competition between interface and film fracture is work in progress.

A limitation of the developed models is that they assume planar interfaces and films. This is an accurate assumption for thermally grown  $\text{SiO}_2$  films on Si substrates, but it less accurate for thermally grown  $\text{Al}_2\text{O}_3$  films on FeCrAlY or superalloy substrates due to the

alumina grain impressions on the metal during growth. Further, if the substrate has been grit blasted or has a rough surface before oxidation, it is likely that the average roughness of the interface exceeds the film thickness, meaning that beam theory is no longer valid. A third example where roughened films occur is when a bond coated superalloy system is being assessed. If the bond coat is susceptible to rumpling (as explained in the previous chapters), the periodic undulations in the bond coat and TGO can exceed the thickness of the TGO and again limit the applicability of this described mechanics. The same is true for wrinkling thermally grown oxides, such as was demonstrated with the DJb(high-S) coating during isothermal oxidation at 1204 °C (see Figure 3.4).

From this dissertation, an obvious interface toughness comparison would be between the TGOs grown on the DJb(low-S) and DJb(high-S) bond coats. To this end, 1 sample each of bond coated and heat treated René N5 were carefully polished with a 1  $\mu\text{m}$  grit diamond suspension to a mirror finish. The samples were then oxidized at 1150 °C for 20 h with 200 °C/min heating and cooling rates. Unfortunately, rumpling and wrinkling of the DJb(high-S) system gives undulation amplitudes in the range of 8  $\mu\text{m}$ , as shown in Figure 5.19. The oxide thickness in these systems is approximately 3  $\mu\text{m}$ , so an undulation amplitude of such a large magnitude precludes the measurement of the TGO-bond coat interface toughness because beam theory is no longer satisfied. The non-planar orientations of the film act as significant stress concentrators and flaws during the film motion. In fact, there is immediate film fracture with no evidence of interface delamination on the DJb(high-S) sample during a fs laser test.

The limitation to the fs laser test was demonstrated above to be only useful in measuring the interface toughness by a transition in behavior for interfaces with very low toughness. This inherent limitation means that this system is likely useful at screening systems for anomalously low interface toughness values. However, once an analytical model has been validated, it would allow a thorough examination of more material prop-

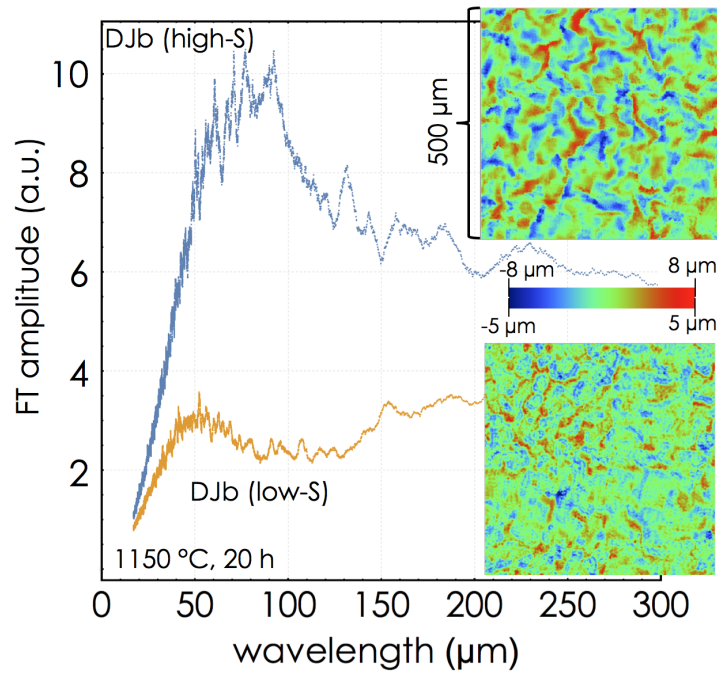


Figure 5.19: The FT algorithm (see Section 3.3) applied to  $2 \times 2$  mm optical profilometer datasets collected after 20 h oxidation at  $1150$  °C. The high-S sample experienced significant wrinkling and rumpling with a dominant wavelength of about  $70\text{--}90$   $\mu\text{m}$ . The large amplitude of this deformation relative to the oxide scale thickness ( $3$   $\mu\text{m}$ ) precluded accurate assessment of the TGO-bond coat interface using the fs laser-based procedure developed in this chapter. Insets show  $500$   $\mu\text{m}$  square sections of the surface profiles where the Z-scaling is indicated for the two samples. The DJb(low-S) sample did not experience such significant wrinkling or rumpling and therefore has a flatter surface profile.

erty space (aspect ratios, elastic modulus, interface toughness, film toughness, initial velocity) to determine if there are combinations of laser and material parameters that would allow the successful measurements for systems with very high interface toughness.

### 5.3 Chapter summary

New developments in bond coat design are allowing TBC systems to be pushed to higher temperatures. Higher strength bond coats can maintain compatibility for a top-coat for a longer time, which results in thicker TGOs due to increased growth time. Therefore, the driving force for TGO delamination is expected to increase for future TBC systems, meaning that the substrate-TGO interface toughness will become an important design parameter for engineers. A novel fs laser-based method to assess the toughness of this interface has been developed and described. This method uses a fs laser to ablate a small amount of the substrate and impart the ceramic film with an initial velocity through a momentum impulse. The subsequent competing behaviors of interface crack advance and crack kinking to cause film fracture are described with a dynamic mechanics model. This model can be used to understand the parameters leading to interface or film failure and ultimately to bound or measure the toughness of the film-substrate interface. The mechanics model has been validated with a series of experiments with the low residual stress  $\text{SiO}_2\text{-Si}$  system. Further, the utility of the fs laser test has been demonstrated by the difference in behavior of the FeCrAl and FeCrAl- $\text{Al}_2\text{O}_3$  systems, where the FeCrAl system has much lower interface toughness. Further developments to explore a wider range of material properties can be used in subsequent research to understand the combination of laser and material parameters allowing accurate assessment of very-tough interfaces. This will require the validation of an analytical model to

incorporate film residual stress because the discrete element model simulations are too time-intensive to thoroughly explore all parameters of interest.

## Chapter 6

# Conclusions and Future Outlook

This dissertation has focused on the design and characterization of  $\text{Ni}_3\text{Al}$  bond coats that can extend the high-temperature lifetime of TBC systems. These coatings resist rumpling due to their higher strength imparted by the  $L1_2$  crystal structure compared to the B2 structure of the industry standard (Pt,Ni)Al coatings. The improved strength of the  $\gamma'$  coatings is accompanied by a debit in oxidation performance due to a lower concentration of Al in the coating.  $\text{Ni}_3\text{Al}$  coatings strike a new balance between mechanical strength and oxidation performance, ultimately leading to an increased TBC system life at elevated temperatures where poor mechanical properties are the life-limiting factor for (Pt,Ni)Al coatings. More than a threefold improvement in TBC system life has been demonstrated for the  $\gamma'$ -phase DJ1 coating over the  $\beta$ -phase (Pt,Ni)Al benchmark in furnace cycle tests conducted at 1163 °C. Ratcheting creep deformation of the (Pt,Ni)Al bond coat during thermal cycling leads to topcoat spalling because the ceramic has low out-of-plane compliance and cannot deform with the bond coat. On the other hand, the  $\gamma'$  coating inhibits this rumpling deformation and therefore maintains contact with the ceramic topcoat for a more thermal cycles. The eventual failure of the DJ1 coating was due

spinel  $\text{NiAl}_2\text{O}_4$  growing on top of the thermally grown oxide that was associated with the formation of a  $\gamma$  layer at the bond coat surface due to Al-depletion and Cr-enrichment.

A comparison of cyclic oxidation tests without the ceramic topcoat and furnace cycling tests of the whole TBC system indicated that the TBC lifetime of the  $\gamma'$  bond coats, measured as the number of cycles until more than 20% of the topcoat became detached, was closely correlated to their oxidation lifetime, measured as the number of cycles until net mass loss occurred. In contrast, the cyclic oxidation lifetime the (Pt,Ni)Al coating was about 5-fold longer than the TBC system life. This indicates that the improved strength of the experimental  $\gamma'$  coatings allows them to utilize all of their oxidation potential in a TBC system. It also reveals that best means of improving  $\gamma'$ -based TBC system life is to improve the oxidation properties of the  $\gamma'$  bond coat.

Non destructive characterization tools to detect rumpling during cyclic oxidation testing of coatings that grow nonuniform oxide scales were developed. A combination of two-dimensional optical profilometry measurements with Fourier transform filtering technique were used to isolate the large-scale deformation of the bond coat from the shorter wavelength effects of surface inhomogeneities. This technique was benchmarked with synthetic datasets and shown to outperform the traditional surface descriptors used to characterize rumpling in  $\text{Al}_2\text{O}_3$ -forming systems. The Fourier transform algorithm was employed to demonstrate that the experimental  $\gamma'$  bond coats do not rumple at 1163 °C, whereas the (Pt,Ni)Al coatings exhibit significant amplitude increases during cyclic oxidation testing. This technique was also used to identify the primary rumpling wavelength of a  $\beta$  coating, which compared favorably with mechanics models. Furthermore, an examination and comparison of the Balint and Hutchinson mechanics model with the Tolpygo and Clarke rumpling experiments demonstrates that rumpling behavior of bond coats is much more dependent on the TGO growth stresses and normal traction than previously thought. The biaxial stress transients from the martensitic transformation and bond

coat-substrate CTE mismatch have a less significant effect on the rumpling behavior of coatings. Rather, it has been shown in isothermal oxidation tests at 1204 °C of the high-S DJb coating exhibits rumpling at shorter times and then the TGO deformation is dominated by shorter-wavelength wrinkling once the TGO can no longer deform the bond coat due to the  $\beta \rightarrow \gamma'$  phase transition at longer times.

Bilayer  $\gamma' + \beta$  bond coats were presented as means of further improving the oxidation properties of  $\gamma'$  bond coats. The thin  $\beta$ -phase layer has excellent oxidation properties and promotes the growth of a denser and slower-growing  $\text{Al}_2\text{O}_3$  scale. The  $\beta$ -phase is quickly converted to the  $\gamma'$ -phase through Al loss and combination  $\gamma' + \beta$  coating provides rumpling resistance that is comparable to the monolithic  $\gamma'$ -phase coating, but with a 40% improvement in cyclic oxidation life measured by net mass loss or a 15-25% improvement measured by the peak in the mass gain curves. However, the  $\gamma' + \beta$  architecture provides an additional 15% improvement in TBC system life over the monolithic  $\gamma'$  bond coat. This is accomplished by delaying the onset of spinel oxide growth on top of the TGO by about 20 thermal cycle. Even though the the TGO spalling rate was decreased in the bilayer coatings, the growth of the  $\text{NiAl}_2\text{O}_4$  layer weakened the topcoat-TGO bond and lead to topcoat detachment. Bilayer architected overlay bond coats can be manufactured using industrial methods such as cathodic arc coating, and are therefore a viable solution for improved TBC life at elevated temperatures.

The importance of properly balancing reactive elements and impurities, such as sulfur, must be stressed in these bilayer architected coatings. Reactive elements have been shown to be less available to getter impurities during oxidation of the  $\gamma'$  phase because they are susceptible to internal oxidation before they can reach the bond coat surface and react with segregated impurities. While a  $\gamma' + \beta$  bond coat exhibits a slight increase in TBC system life when the S levels are properly controlled in the  $\beta$  top-layer, the lifetime can decrease by about half with too much S contamination, as demonstrated in the

experiments with DJ1+DJb bond coats. Although S contamination is always undesirable, it is important to note that the high-S  $\gamma'+\beta$  bilayer bond coat still exhibits a TBC system lifetime that is almost twofold longer than the (Pt,Ni)Al benchmark. The sensitivity of these systems to the TGO-bond coat interface toughness increases the importance of understanding how this material property varies with common service conditions and alloying. It is essential to be able to assess and screen for interface toughness while designing next-generation bond coats for TBC systems.

To this end, a fs laser technique has been developed and deployed to assess the interface toughness of these difficult-to-measure ceramic film-metallic substrate systems. The fs laser ablation interaction with the substrate incorporates little heat or damage into the system while simultaneously creating a controlled film detachment and accelerating the film out-of-plane. The subsequent behavior of interface cracks as the dynamic buckle moves away from the substrate are used to infer the toughness of the interface and the properties of the oxide film. Crack extension along the interface indicates a weak interface toughness, while crack kinking into the film, which results in film spallation, occurs in systems with a higher-toughness interface. Dynamic mechanics models have been validated with SiO<sub>2</sub>-Si systems having high uniformity. These models were extended to model bond coat systems, Al<sub>2</sub>O<sub>3</sub>-FeCrAl and Al<sub>2</sub>O<sub>3</sub>-FeCrAlY, to demonstrate that the interface cracks extend along interfaces having low toughness but kink into the film when the interface has high toughness. This indicates that this technique can be used to screen for low interface toughness bond coat systems during development.

In all, this dissertation has developed a suite of tools and a process whereby the performance and properties of bond coats can be anticipated and assessed quickly. Thermodynamic models are used to develop bond coat compositions that are in close equilibrium with the substrate and can provide adequate oxidation behavior. They are also used to design bilayer architectures that are chemically compatible with one another during

service. Once candidate bond coat samples have been made, they can be assessed in cyclic oxidation tests and their rumpling and TGO spalling behavior can be characterized and associated with the mass change of the coatings. Furthermore, the TGO-bond coat interface toughness can be assessed using a fs laser technique to identify systems with suboptimal or adequate toughness values. The interplay between oxide growth/loss and bond coat deformation during a cyclic oxidation test without the topcoat can be used to determine the likely failure mechanism of the full TBC system, which requires a more costly and time-consuming furnace cycle testing. Proper data collection and analysis of a large series of these tests would allow one to predict the TBC system behavior before testing it, allowing a dramatic improvement in the speed and quality of bond coat design as engineers create TBC systems for more efficient and higher-temperature gas turbine engines. The remainder of this chapter discusses future avenues for testing and improvement applicable to  $\gamma'$  bond coats.

## 6.1 Sustained peak low cycle fatigue testing

Another failure mechanism observed during thermomechanical cycling of coated parts is surface crack initiation and growth through oxidation-assisted fatigue. Large through-thickness thermal gradients develop on internally cooled turbine blades during takeoff and landing cycles that put the outer surface into a state of compression at high temperature. Creep relaxation during the compressive hold results in a tensile stress upon release of the compressive strain, which opens surface cracks promoting crack face oxidization. The oxidized crack tips push into the coating and substrate upon the next compression cycle, as has been shown in sustained peak low-cycle fatigue (SPLCF) experiments [25, 26]. Crack growth in this scenario is dependent on the superalloy and coating properties [26]. Modeling of the SPLCF cycle indicates that increasing the creep strength of the bond coat

will decrease the crack extension rate [27] even after the crack has penetrated completely into the substrate [28].

To determine if a high-strength bond coat can improve both the TBC system life and the fatigue properties, a series of fatigue bars have been IPD coated with the rumpling-resistant  $\gamma'$  DJ1 composition in order to investigate their performance at 1093 °C in comparison to (Pt,Ni)Al coatings and uncoated specimens in SPLCF experiments.

The SPLCF test is conducted with strain-controlled loading. A SPLCF strain cycle consists of a ramp from 0 to -0.35% strain in 1.5 s, a 2 min hold, and a ramp back to 0 strain in 1.5 seconds [26]. This is an important test to consider during bond coat development because the mechanical fatigue properties of a coating are also important during service; fatigue-related failures can be catastrophic in turbine engines. Ensuring that a high-strength coating is, at the very least, not detrimental to fatigue properties is a requirement before commercial adaptation.

## 6.2 Hot corrosion and water vapor testing

One important aspect that has been neglected during the characterization of the experimental  $\gamma'$  coatings discussed in this dissertation is hot corrosion properties and oxidation in a humid environment. Gas turbine engine environments are corrosive due to fuel impurities and injected contaminants and contain water vapor from the combustion reaction. It is possible that the corrosion properties of these specific  $\gamma'$  coatings are not ideal due to the low concentration of Cr, an element that has been demonstrated to improve corrosion resistance [184, 185]. Further testing of the oxidation and corrosion rates of these coatings in atmospheres with water vapor or with sulfides would be needed to assess if the more porous oxide scales provide an adequate level of protection against attack. It is expected that the bilayer coatings will have better corrosion properties

because they form a more dense TGO scale that would be more resistant to sulfide attack. Furthermore, it might be possible to further enhance the corrosion and oxidation properties of the bilayer architectures by using a thin Pt or Pd-doped top-layer, elements that have also been shown to improve hot corrosion resistance [186]. Specifically tailoring the  $\beta$  top-layers may be a practical means of adapting a high-strength bond coat to a variety of anticipated environments.

### 6.3 High-strength coatings enabling advanced TBCs

A major advantage of these rumpling-resistant  $\gamma'$  bond coats is that they decrease the driving force for TBC fracture near the bond coat-topcoat interface because there are lower out-of-plane stresses due to the lack of bond coat deformation. A lower driving force for topcoat fracture may enable the use of ceramics with lower fracture toughness, but also have better CMAS resistance or lower thermal conductivity, to be used. Introducing these options gives more flexibility to TBC system engineers and designers. Once bond coats that can sustain higher temperatures for prolonged period are commonplace, CMAS infiltration and chemical attack will become a much more important failure mechanism. The flexibility to use lower-toughness topcoat compositions that react with and stop CMAS infiltration will become important.

### 6.4 Alloying for improved oxidation of $\gamma'$ phase

As demonstrated in this dissertation, a fruitful avenue for  $\gamma'$  bond coat development is to optimize the oxidation properties of this system. It is well known that Pt, Pd, and Cr tend to improve the high-temperature oxidation of Ni-based alloys. Small additions ( $< 5\text{at}\%$ ) of these elements by themselves or in combination may have a drastic

improvement on the oxidation behavior of this phase. In  $\beta$  bond coats, the addition of Pt prevents S segregation to the TGO-bond coat interface, which improves the interface toughness [124]. Further, Pt additions also lower the Al activity near the surface of the bond coat, which causes diffusion of Al from within the coating and the substrate to the surface against the concentration gradient, helping to maintain selective oxidation of Al. If Pt or Pd had similar effects in  $\gamma'$  coatings as in  $\beta$  coatings, it is likely that small additions of these elements could significantly enhance the oxidation properties of the bond coat. It will be important to ensure that the stability of the  $\gamma'$  phase is not compromised, but some combination is likely possible. Gleeson has already patented a series of Pt-containing  $\gamma+\gamma'$  bond coats [97–99], suggesting that this avenue has promise. Combinatorial investigations using IPD coating methods can be used to quickly screen the optimal combination of Pt-Pd-Cr for oxidation properties of the  $\gamma'$  coatings.

In this same vein, optimization of the diffusion/aging path of  $\gamma'$  coatings can be performed to maximize the amount of time the bond coat maintains the  $\gamma'$  phase and delays the formation of a  $\gamma$  layer near the surface. Delaying the onset of the  $\gamma$  layer has been shown to delay the growth of spinel  $\text{NiAl}_2\text{O}_4$ , so it is expected that proper alloying to stabilize the  $\gamma'$  phase throughout the evolution of the coating will maximize TBC life. Such a significant amount of Cr diffusion from the substrate was not anticipated when the coatings were designed. Because Cr is a strong  $\gamma$ -former, it may be helpful to add additional elements to stabilize the  $\gamma'$  phase to counteract the effect of Cr enrichment from the substrate as the coating ages.

## 6.5 Tailor-made bond coats for TBC systems

A plethora of tools have been developed to enable fast bond coat design: thermodynamic databases to predict phase equilibria and diffusion [187], combinatorial studies

using IPD methods to quickly deposit coatings with systematic chemical variations [18], nondestructive characterization of bond coats to measure rumpling [103], and a fs laser test to evaluate TGO-bond coat interface toughness. The use of these tools in conjunction puts engineers in a position to quickly design bond coats that are tailored to meet the specific demands of their environment based on variables such as differing substrates or locations and temperature profiles in the engine. Interdiffusion with the substrate can be accurately modeled, but the oxidation behavior of coatings is still difficult to predict a priori. More development and understanding between the kinetics and thermodynamics involved is required to create models that can accurately predict the effect of arbitrary chemistry changes on oxidation behavior.

These types of advances will be important as gas turbine engines are pushed to their limits. It will no longer be possible to design a superalloy, a bond coat, and a topcoat separately, assemble them all together, and achieve increased temperature capabilities. Instead, the entire system will need to be designed in conjunction to maximize the system life while pushing temperature limits. This is especially true as the wall thickness of high pressure turbine blades becomes thinner. Bond coats are becoming a greater proportion of the total wall thickness, and so their properties are becoming more important. It may become necessary that all superalloy substrates need a suite of tailored bond coats that are designed for strength, diffusion compatibility, and local oxidation/corrosion environments to achieve maximum enhancement of component and engine lifetimes. Considering the whole system together by designing high-strength coatings to complement the substrate and ceramic overlayers will ultimately lead to the maximum turbine engine efficiency of which metal components are capable. This will help to reduce green house gas emission and help to minimize humans impact on the environment in turn.

# Appendix A

## FT Algorithm for Rumpling Quantification

### A.1 2D mean surface roughness $S_a$

The 2D equation used to calculate the mean surface roughness of the coatings is:

$$S_a = \frac{1}{MN} \sum_{k=0}^{M-1} \sum_{i=0}^{N-1} |z(x_k, y_i)| \quad (\text{A.1})$$

$z(x_k, y_i)$  is the height of each pixel,  $M$  is the number of pixels in the  $k$  direction, and  $N$  is the number of pixels in the  $i$  direction.

### A.2 2D root-mean-square surface roughness $S_q$

The 2D equation used to calculate the RMS surface roughness of the coatings is:

$$S_q = \sqrt{\frac{1}{MN} \sum_{k=0}^{M-1} \sum_{i=0}^{N-1} z(x_k, y_i)^2} \quad (\text{A.2})$$

$z(x_k, y_i)$  is the height of each pixel,  $M$  is the number of pixels in the  $k$  direction, and  $N$  is the number of pixels in the  $i$  direction.

### A.3 2D surface tortuosity

The 2D equation used to calculate the surface tortuosity of the coatings is:

$$\begin{aligned} \frac{A}{A_0} &= \frac{1}{4A_0} \sum_{k=0}^{M-1} \sum_{i=0}^{N-1} \\ &\quad \sqrt{\delta^2 + (z(x_k, y_i) - z(x_k, y_{i+1}))^2} \\ &\quad + \sqrt{\delta^2 + (z(x_{k+1}, y_i) - z(x_{k+1}, y_{i+1}))^2} \\ &\quad + \sqrt{\delta^2 + (z(x_k, y_i) - z(x_{k+1}, y_i))^2} \\ &\quad + \sqrt{\delta^2 + (z(x_k, y_{i+1}) - z(x_{k+1}, y_{i+1}))^2} \end{aligned} \tag{A.3}$$

where  $\delta$  is the lateral sampling distance,  $z(x_k, y_i)$  is the height of a pixel,  $M$  is the number of pixels in the  $k$  direction,  $N$  is the number of pixels in the  $i$  direction, and  $A_0$  is the area of the scan ( $A_0 = M \times N \times \delta^2$ ).

### A.4 Mathematica code

# Functions

**radialAvgPSDpadZero** - takes an ordinary matrix, calculates the FT, creates a DC-centered matrix and then calculates the radial average normalized so that the amplitude in k-space is the amplitude in real space.

turns PSD into a square by padding short dimensions with 0s and calculates radial average of the top half of the spectrum. It uses a pre-calculated list of indexed points to save time.

```
radialAvgPSDpadZero[matrix_] :=
Module[{matrixTemp, dimDiff, fp2D, xx, yy, pts, rho, theta,
  positions, i, fp2Dflat, avgValues, coordList, kNyquist, radii,
  indices, avgComplexValues, ft, indexList, radiiList},

(*initialize a matrix to do some work on*)
matrixTemp = matrix;

(*images size. n = height, m = width*)
{nOrig, mOrig} = Dimensions[matrixTemp];

(*ensure that the matrix has an even dimension,
accomplished by padding on a necessary side*)
If[OddQ[nOrig], matrixTemp = ArrayPad[matrixTemp,
  {{(*T*)0, (*B*)1}, {(*L*)0, (*R*)0}}];];
If[OddQ[mOrig], matrixTemp = ArrayPad[matrixTemp, {{0, 0}, {1, 0}}];];
{n, m} = Dimensions[matrixTemp];
dimDiff = Abs[n - m];

PutAppend[" dims = " <> ToString[Dimensions[matrixTemp]] <>
  ". Squaring and padding the matrix...", "log.log"];

(*make the matrix square by padding the short sides with 0s*)
If[n ≥ m,
  (*true n > m, more rows than columns (or square matrix)*)
  If[EvenQ[dimDiff], (*even difference in dimensions,
    pad columns to match the number of rows*)
    matrixTemp = ArrayPad[matrixTemp, {{(*T*)0, 0(*B*)},
      {(*L*)dimDiff/2, (*R*)dimDiff/2}}];];
  ];,

(*false, n < m, more columns than rows*)
If[EvenQ[dimDiff], (*even difference in dimensions,
  pad rows to match the number of columns*)
  matrixTemp = ArrayPad[matrixTemp,
    {{(*T*)dimDiff/2, dimDiff/2(*B*)}, {(*L*)0, (*R*)0}}];];
];
```

```

];
(*update dims*)
{n, m} = Dimensions[matrixTemp];
dimMax = Max[n, m]; (*max dimension of matrix*)

If[n ≠ m,
  PutAppend[" ERROR, failed to square the matrix properly, dims = "<>
    ToString[Dimensions[matrixTemp]], "log.log"],
  PutAppend[" squared properly...dims are "<>
    ToString[Dimensions[matrixTemp]], "log.log"];];

(*pad the file based on the resolution selected*)
Switch[resolution,

  "low" (*3500x3500 padding*),
  (*Pad the entire matrix with a
    lot of zeros to increase resolution in k-space*)
  PutAppend[" low res, 3500 pixels used.", "log.log"];
  If[dimMax < 3500,
    matrixTemp = ArrayPad[matrixTemp, (3500 - dimMax) / 2];
    (*update dims*)
    {n, m} = Dimensions[matrixTemp];
    dimMax = Max[n, m];
    (*max dimension of matrix, they should be the same at this point*)
    If[n ≠ m,
      PutAppend[" ERROR, failed to pad the matrix properly...dims are"<>
        ToString[Dimensions[matrixTemp]], "log.log"];,
      PutAppend[" padded properly...dims are "<>
        ToString[Dimensions[matrixTemp]], "log.log"];];
  ] (*dimMax < 3500*);,

  "medium" (*6000x6000 padding*),
  PutAppend[" medium res, 6000 pixels used.", "log.log"];
  If[dimMax < 6000,
    (*true*)
    matrixTemp = ArrayPad[matrixTemp, (6000 - dimMax) / 2];
    (*update dims*)
    {n, m} = Dimensions[matrixTemp];
    dimMax = Max[n, m];
    (*max dimension of matrix, they should be the same at this point*)
    If[n ≠ m,
      PutAppend[" ERROR, failed to pad the matrix properly...dims are"<>
        ToString[Dimensions[matrixTemp]], "log.log"];,
      PutAppend[" padded properly...dims are "<>
        ToString[Dimensions[matrixTemp]], "log.log"];];
  ] (*dimMax < 6000*);,

  "high" (*10k x 10k padding*),
  PutAppend[" high res, 10k pixels used.", "log.log"];
  If[dimMax < 10 000,

```

```

matrixTemp = ArrayPad[matrixTemp, (10 000 - dimMax) / 2];
(*update dims*)
{n, m} = Dimensions[matrixTemp];
dimMax = Max[n, m];
(*max dimension of matrix, they should be the same at this point*)
If[n ≠ m,
  PutAppend[" ERROR, failed to pad the matrix properly...dims are" <>
    ToString[Dimensions[matrixTemp]], "log.log"];,
  PutAppend[" padded properly...dims are " <>
    ToString[Dimensions[matrixTemp]], "log.log"];];
] (*dimMax < 10k*);,

"custom" (*custom padding size,
need to have precalculated the index and radii files*),
PutAppend[" custom res, 2000 pixels used.", "log.log"];
If[dimMax < 2000,
  matrixTemp = ArrayPad[matrixTemp, (2000 - dimMax) / 2];
  (*update dims*)
  {n, m} = Dimensions[matrixTemp];
  dimMax = Max[n, m];
  (*max dimension of matrix, they should be the same at this point*)
  If[n ≠ m,
    PutAppend[" ERROR, failed to pad the matrix properly...dims are" <>
      ToString[Dimensions[matrixTemp]], "log.log"];,
    PutAppend[" padded properly...dims are " <>
      ToString[Dimensions[matrixTemp]], "log.log"];];
] (*dimMax < 2000*);,

_ (*no definition of resolution*),
PutAppend[" resolution not defined as
'low/medium/high'. Using max dim of image.", "log.log"];
];

(*calculate the FT and DC-center it*)
PutAppend[" calculating FT of the matrix...", "log.log"];
ft = shiftFT[Fourier[matrixTemp, FourierParameters → {1, 1}]];

(*Nyquist frequency - we really only need to calculate the average up
to the fN because anything of higher resolution is meaningless*)
fNyquist = 1 / (2 * latRes);
kNyquist = dimMax / 2;
(*this is the number of pixels
from the center that it sensible to average*)

(*Import index list based on resolution*)
PutAppend[" indexing matrix...", "log.log"];
Switch[resolution,

```

```

"low" (*3500x3500 padding*),
(*Pad the entire matrix with a
  lot of zeros to increase resolution in k-space*)
PutAppend[" low res, 3500 pixels used.", "log.log"];
If[dimMax ≤ 3500,
  (*Import index list for a 3500x3500 file*)
  SetDirectory[NotebookDirectory[]];
  indices = Rationalize[Import["indices3500.mat"]];
  indexList = Import["radiiList3500.mat"];
  (*pad the normalized spectrum so that it fits the 3500x template*)
  ft = ArrayPad[ft, (3500 - dimMax) / 2];
];,

"medium" (*6000x6000 padding*),
PutAppend[" medium res, 6000 pixels used.", "log.log"];
If[dimMax ≤ 6000,
  (*Import index list for file*)
  SetDirectory[NotebookDirectory[]];
  indices = Rationalize[Import["indices6000.mat"]];
  indexList = Import["radiiList6000.mat"];
  (*pad the normalized spectrum so that it fits the template*)
  ft = ArrayPad[ft, (6000 - dimMax) / 2];
];,

"high" (*10k x 10k padding*),
PutAppend[" high res, 10k pixels used.", "log.log"];
If[dimMax ≤ 10 000,
  (*Import index list for file*)
  SetDirectory[NotebookDirectory[]];
  indices = Rationalize[Import["indices10k.mat"]];
  indexList = Import["radiiList10k.mat"];
  (*pad the normalized spectrum so that it fits the template*)
  ft = ArrayPad[ft, (10 000 - dimMax) / 2];
];,

"custom" (*custom padding -
  NEEDS TO BE ADJUSTED FOR EACH DIMENSION*),
PutAppend[" custom res, 2000 pixels used.", "log.log"];
If[dimMax ≤ 2000,
  (*Import index list for file*)
  SetDirectory[NotebookDirectory[]];
  indices = Rationalize[Import["indices2000b.mat"]];
  indexList = Import["radiiList2000b.mat"];
  (*pad the normalized spectrum so that it fits the template*)
  ft = ArrayPad[ft, (2000 - dimMax) / 2];
];,

_(*no definition of resolution*),

```

```

PutAppend[" matrix indexing with custom file...", "log.log"];
{n, m} = Dimensions[matrixTemp];
dimMax = Max[n, m];

(*need to custom calculate this is there is no resoution definition*)
(*This isn't quite right now that the index list can be some arbitrary
size depending on the rounding used in the radial average*)
If[FileExistsQ["indicesLastCalc.mat"],
  (*file is there, check if it is the right size*)
  indices = Rationalize[Import["indicesLastCalc.mat"]];
  If[Length[Flatten[indices, 2]] == dimMax^2,
    (*correct size file, use it. Nothing else to do*)
    indexList = Import["radiiListLastCalc.mat"];
    PutAppend[
      " found previous index file of proper size.", "log.log"];,

    (*not the right size, so recalculate it*)
    PutAppend[
      " previous index file is wrong size, recalculating...", "log.log"];
    (*calculate a custom index list for the specific matrix size*)
    coordList = Table[{i, j},
      {j, -dimMax/2, dimMax/2, 1}, {i, -dimMax/2, dimMax/2, 1}];
    (*calculate the radius at which each point is from
    the center of the image, round to nearest pixel*)
    radii = Map[Sqrt[#[[All, 1]]^2 + #[[All, 2]]^2] &, coordList];
    (*remove the last column and bottom row so that the dims are even*)
    radii = Drop[radii, {dimMax + 1}, {dimMax + 1}];
    (*create a list of all the unique radii*)
    indexList = Sort[DeleteDuplicates[Flatten[radii, Infinity]]];
    (* (X,Y) positions in the matrix that are at an indexed radius*)
    indices =
      Parallelize[Table[Position[radii, index], {index, indexList}]];
    SetDirectory[NotebookDirectory[]];
    Export["indicesLastCalc.mat", indices];
    Export["radiiListLastCalc.mat", indexList];
  ];,

  (*file does not exist, must calculate it*)
  PutAppend[" calculating index file...", "log.log"];
  (*calculate a custom index list for the specific matrix size*)
  coordList = Table[{i, j},
    {j, -dimMax/2, dimMax/2, 1}, {i, -dimMax/2, dimMax/2, 1}];
  (*calculate the radius at which each point is from the
  center of the image, round to nearest pixel*)
  radii = Map[Sqrt[#[[All, 1]]^2 + #[[All, 2]]^2] &, coordList];
  (*remove the last column and bottom row so that the dims are even*)
  radii = Drop[radii, {dimMax + 1}, {dimMax + 1}];
  (*create a list of all the unique radii*)
  indexList = Sort[DeleteDuplicates[Flatten[radii, Infinity]]];
  (* (X,Y) positions in the matrix that are at an indexed radius*)
  indices =

```

```

    Parallelize[Table[Position[radii, index], {index, indexList}]];
    SetDirectory[NotebookDirectory[]];
    Export["indicesLastCalc.mat", indices];
    Export["radiiListLastCalc.mat", indexList];
  ]>(*end If FileExists*);
]>(*end Switch resolution*);

(*Calculating the radial average of the FT...*)
PutAppend[" averaging values at indexed radii...", "log.log"];
avgValues =
  Map[Mean[Abs[Extract[ft, #]]] &, indices[[1 ;; Length[indices] - 5]]];

(*(*normalization*)
avgValues=(*Abs[avgComplexValues]*2/(dimMax/latRes)^2;*)
  avgValues/dimMax;*)

PutAppend[" done.", "log.log"];

Return[{avgValues, indexList[[1, 1 ;; -6, 1]], ft}];];

```

Code to pre-calculate radial average index matrix "indicesXXXXXX.mat"

```

Module[{dimMax, coordList, radii, indices, indexList},
  dimMax = 2 * 10^3;
  coordList =
    Table[{i, j}, {j, -dimMax/2, dimMax/2, 1}, {i, -dimMax/2, dimMax/2, 1}];
  (*calculate the radius at which each point is from
  the center of the image, round to nearest pixel*)
  radii = Map[Sqrt[#[[All, 1]]^2 + #[[All, 2]]^2] &, coordList];
  (*remove the last column and bottom row so that the dims are even*)
  radii = Drop[radii, {dimMax + 1}, {dimMax + 1}];
  (*create a list of all the unique radii*)
  indexList = Sort[DeleteDuplicates[Flatten[radii, Infinity]]];
  (* (X,Y) positions in the matrix that are at an indexed radius*)
  indices = Parallelize[Table[Position[radii, index], {index, indexList}]];
  SetDirectory[NotebookDirectory[]];
  Export["indices2000.mat", indices];
  Export["radiiList2000.mat", indexList];
];

```

## Matrix/Array processing functions

**kSpaceAbscissa** - creates a frequency abscissa ( $\mu\text{m}^{-1}$ ) based on the presently stored lateral resolution (latRes in nanometers)

```

kSpaceAbscissa[array_] := Module[{abscissa},
  abscissa =
    Table[i / (2 * Length[array] * (latRes * 10-3)), {i, 0, Length[array] - 1}];
  Return[abscissa];
];

(*Uses an imported index-list that has non-
integer values for the pixel-radii used for averaging,
needs to have the dimMax of the square matrix precalculated*)
kSpaceAbscissa2[indexList_] := Module[{indexListReal},
  indexListReal = indexList / (dimMax * latRes * 10-3);
  Return[Flatten[indexListReal]];
];

```

I am using 2N here because my radial averaging scheme cuts down the length of the array to half the original length (because it is a radial average). However, the true resolution is set by the dimensions of the matrix that is being FT'd. Sort of semantics, but the function is now written to create the abscissa to the actual radial average of the FT'd data rather than an input of the original data.

The Nyquist-Shannon Theorem (Sampling Theorem) states that any continuous baseband signal may be identically reconstructed if the signal is bandwidth limited and the sampling frequency is  $\geq 2x$  the bandwidth of the signal (highest frequency). So, if  $\Delta x$  is the distance between successive measurements (lateral resolution), then the highest frequency resolution that is sensible is  $1/(2\Delta x) = \text{Nyquist frequency}$ .

**shiftFT: takes a 2D Fourier transf. matrix & shifts the DC to the center**

```

(*function to shift an FT matrix so that it is DC-centered*)
shiftFT[matrix_] := Module[{t1, t2, t3, t4, j1, j2},

  (*Take, is in the form [Matrix, Rows, Columns] from a
  matrix. It is set up to handle odd-dimensioned matrices,
  although this should not be utilized because it doesn't
  really make sense. Better to make sure you have an even-
  dimensioned matrix in the first place*)
  (*grabbing all the separate quadrants*)
  t1 = Take[matrix, -Ceiling[(1/2) * Dimensions[matrix][[
    1]]], Floor[(1/2) * Dimensions[matrix][[2]]]];

  t2 = Take[matrix, Floor[(1/2) * Dimensions[matrix][[
    1]]], Floor[(1/2) * Dimensions[matrix][[2]]]];

  t3 = Take[matrix, Floor[(1/2) * Dimensions[matrix][[
    1]]], -Ceiling[(1/2) * Dimensions[matrix][[2]]]];

  t4 = Take[matrix, -Ceiling[(1/2) * Dimensions[matrix][[
    1]]], -Ceiling[(1/2) * Dimensions[matrix][[2]]]];

  (*splicing the quadrants together*)
  j1 = Join[t1, t2];
  j2 = Join[t4, t3];

  Return[Transpose[Join[Transpose[j2], Transpose[j1]]]];
];

```

## Misc matrix functions

```

(*takes an arbitrary matrix and rescales on a 0-
 1 range. Leaves 0 values alone,
 good for B&W images*)
scale0to1[matrix_] := Module[{min, max, range, newMatrix, infMatrix},
  min = Min[matrix];
  max = Max[matrix];
  range = max - min;
  infMatrix = (ReplaceAll[matrix, 0 → Infinity] - min) / range;
  (*this takes care of all the invalid points*)
  newMatrix = ReplaceAll[infMatrix, {Infinity → 0, Indeterminate → 0}];
  Return[{newMatrix, range}]];

(*arbitrary matrix and rescales it on a 0-1 scale, with log scaling*)
scale0to1Log[matrix_] := Module[{min, max, newMatrix, infMatrix, range},
  min = Min[matrix];
  max = Max[matrix];
  range = max - min;
  infMatrix = Log[(ReplaceAll[matrix, 0 → Infinity] - min)] / Log[range];
  (*this takes care of all the invalid points*)
  newMatrix = ReplaceAll[infMatrix, {Infinity → 0, Indeterminate → 0}];
  Return[{newMatrix, range}]];

imageFT[matrix_] := Module[{picRange, pic},
  (*proper normalization of image*)
  picRange = Max[Log[Abs[matrix]]] - Min[Log[Abs[matrix]]];
  pic = Image[(Log[Abs[matrix]] - Min[Log[Abs[matrix]]]) / picRange];
  Return[pic];
]

```

An interesting resource on FTs:

<http://www.av8n.com/physics/fourier-refined.htm#sec-hetero>

## Rq of a matrix

$$Rq = \sqrt{\frac{1}{MN} \sum^M \sum^N z^2(x_i, y_j)}$$

(\*RMS roughness in whatever units are put into it.\*)

```

rq[matrix_] :=
  Sqrt[(1 / (Dimensions[matrix][[1]] * Dimensions[matrix][[2]]))
    Total[Total[matrix^2]]];

```

## squarePad - pads an array with zeros to be square, also makes the square even-dimensional

```

squarePad[array_] := Module[{matrixTemp, dimDiff, n, m},
  matrixTemp = array;
  {n, m} = Dimensions[matrixTemp];
  If[OddQ[n], matrixTemp =
    ArrayPad[matrixTemp, {{(*T*)0, (*B*)1}, {(L*)0, (R*)0}}];];
  If[OddQ[m], matrixTemp = ArrayPad[matrixTemp, {{0, 0}, {1, 0}}];];

  {n, m} = Dimensions[matrixTemp];
  dimDiff = Abs[n - m];

  (*make the matrix square by padding the short sides with 0s*)
  If[n ≥ m,
    (*true n > m, more rows than columns (or square matrix)*)
    If[EvenQ[dimDiff], (*even difference in dimensions,
      pad columns to match the number of rows*)
      matrixTemp = ArrayPad[matrixTemp, {{(*T*)0, 0(*B*)},
        {(L*)dimDiff/2, (R*)dimDiff/2}}];];
    ];,
    (*false, n < m, more columns than rows*)
    If[EvenQ[dimDiff], (*even difference in dimensions,
      pad rows to match the number of columns*)
      matrixTemp = ArrayPad[matrixTemp,
        {{(*T*)dimDiff/2, dimDiff/2(*B*)}, {(L*)0, (R*)0}}];];
    ];
  ];
  Return[matrixTemp];
];

```

## arrayToDepthMatrix

```
(*converts a 1D array .asc file with a 12-
line preamble into a depth matrix where only the Z-values are stored,
converts all the "Bad" points into Infinity
This is used for datafiles from the WYKO NT1100 at UCSB *)
arrayToDepthMatrix[array_] := Module[{a, b, xDim, yDim, zRes},
  (*turn array into a matrix*)
  xDim = array[[2]][[2]];
  yDim = array[[3]][[2]];
  zRes = array[[
    First[Flatten[Position[array[[All, 1]], "Wavelength"]], -1]] / 1000;
  (*z-res resolution in microns*) (*array[[9]][[4]];*)
  a = Table[array[[ (12 + i) + (j * yDim) ]][[3]], {i, 1, yDim}, {j, 0, xDim - 1}];
  (*replace all the "Bad" data points with Infinity*)
  b = ReplaceAll[a, "Bad" → Infinity];
  b = ReplaceAll[b, "" → Infinity];
  (*returns the depth matrix in micrometers*)
  Return[b * zRes];
```

# Import profilometer files

## PNG w/ text file (from Alicona at GE)

The files from the Alicona GE profilometer were stored as .png depth images with a best-fit slope correction applied. Each file has an accompanying .txt file (with the same name) explaining the depth range, height resolution, and pixel sizes, etc.

This is the file directory of the 120-cycle test (2000°F) data files.

```
SetDirectory[
  "/Users/Davey/Dropbox/UCSB/Research/γ' Coating Study/Gamma' coatings
  work at GE/Images and Profilometry/Exported
  Data in png format/120 cycle test 2000F"];

files = FileNames[];
```

```

pic = Import[files[[1]];
text = Import[files[[2]]];

(*open up a text stream*)
stext = OpenRead[files[[2]]];
(*gray scale resolution*)
SetStreamPosition[stext, 0];
(*break up the text stream into groupings of words*)

(*upper bound is #8, lower bound is #11,
vertical resolution is #14, zero level is #19,
horizontal and vertical sampling resolutions are #24 & 27*)
words = ReadList[stext, Word];
extractNumber[pos_] :=
  ToExpression[
    StringTake[words[[pos]], StringPosition[words[[pos]], "m"][[1, 1]] - 2]];

upBound = extractNumber[8] (*microns*);
lowBound = extractNumber[11] (*microns*);
zRes = extractNumber[14] (*nanometers / gray value*);
zero = extractNumber[19] (*microns*);
latRes = extractNumber[24] (*nanometers/pixel*)

```

Turning an image into a 3D dataset, FT and DC-centered FT

```

data = ImageData[pic];
ListPlot3D[data[[4 ;; 100, 4 ;; 150]]]
ft = Fourier[data, FourierParameters -> {1, 1}];
Image[Log[Abs[ft]]];
Image[Log[Abs[shiftFT[ft]]]];

picRange = Max[Log[Abs[sft]]] - Min[Log[Abs[sft]]];
Image[(Log[Abs[shiftFT[ft]]] - Min[Log[Abs[sft]])] / picRange]

```

Calculating the radial average of the power series of the data, export plot to desktop folder

```

Export["/Users/Davey/Desktop/Power Series/PS_" <> files[[1]],
  ListLinePlot[Transpose[{abscissa, Log[powerseries]}],
    PlotRange -> {{0, 700}, {4, 20}}, Frame -> True, AspectRatio -> 1,
    FrameTicks -> {{Automatic, Automatic}, {Automatic, Automatic}},
    GridLines -> Automatic, GridLinesStyle -> Directive[LightGray, Dashed],
    FrameLabel -> {{(*L*) "Log power (a.u.)", (*R*) ""},
      {(*B*) "frequency ( $\mu\text{m}^{-1}$ ", (*T*) "\nPower series" files[[1]]}},
    BaseStyle -> {FontFamily -> "Helvetica", FontSize -> 18}, ImageSize -> 450]];

```

## Calculate power series of a .png image

```

DeleteCases[{{1, 2, 3}, {4, 5, 6}}, _?NumberQ[Max[{{1, 2, 3}, {4, 5, 6}}]]]

```

```

SetDirectory[NotebookDirectory[]];
pic = Import["DJ2-3_1c_10x_Orestore_XYZpixel.asc_Data.png"];
data = ImageData[pic];
ListPlot3D[data[[4 ;; 100, 4 ;; 150]]] (*small example of the data*);
ft = Fourier[data, FourierParameters -> {1, 1}];
Dimensions[ft];
Abs[ft[[1 ;; 10, 1 ;; 10]]];
Image[Abs[ft[[1 ;; 50, 1 ;; 50]]] / Max[Delete[Abs[ft], {1, 1}]]];
Image[Abs[ft] / Max[Delete[Abs[ft[[1 ;; 50, 1 ;; 50]], {1, 1}]]];
Image[Log[Abs[shiftFT[ft]]]];

picRangeLog = Max[Log[Abs[ft]]] - Min[Log[Abs[ft]]];
picRange = Max[Abs[ft]] - Min[Abs[ft]];
Image[(Log[Abs[shiftFT[ft]]] - Min[Log[Abs[sft]]]) / picRange]

```

Calculating the radial average of the power series of the data, export plot to desktop folder

```

(*Export["/Users/Davey/Desktop/Power Series/PS_"<>files[[1]],
ListLinePlot[Transpose[{abscissa, Log[powerseries]}],
PlotRange -> {{0, 700}, {4, 20}}, Frame -> True, AspectRatio -> 1,
FrameTicks -> {{Automatic, Automatic}, {Automatic, Automatic}},
GridLines -> Automatic, GridLinesStyle -> Directive[LightGray, Dashed],
FrameLabel -> {{(*L*) "Log power (a.u.)", (*R*) ""},
{(*B*) "frequency ( $\mu\text{m}^{-1}$ ", (*T*) "\nPower series"files[[1]]}},
BaseStyle -> {FontFamily -> "Helvetica", FontSize -> 18}, ImageSize -> 450]];*)

```

## Turn a matlab file (.mat) into an image (.png)

```

file = Import[
"/Users/Davey/Dropbox/UCSB/Research/ $\gamma$ ' Coating Study/Pt5_100cycles
(from Wes's combi expts).mat"][[1]];

```

Turning the .mat file into a 3D dataset, FT and DC-centered FT

Checks the lateral resolution

```

rowEndPosition = 0;
res = beta[[1, rowEndPosition + 1]];
For[i = 1, i <= 5, i++,
rowEndPosition =
Position[beta[[1, All]], beta[[1, rowEndPosition + 1]][[-1, 1]];
res = Abs[beta[[1, rowEndPosition]] - beta[[1, rowEndPosition + 1]]];
Print[res]
];

```

```

(*converts a (mm,mm,μm) triplet to (μm, μm, μm) *)
beta = {file[[All, 1]] * 10^3, file[[All, 2]] * 10^3, file[[All, 3]]};
latRes = beta[[1, rowEndPosition + 1]] (*μm/pixel*);
picRange = Max[beta[[3, All]]] - Min[beta[[3, All]]];

img = ListDensityPlot[Transpose[beta[[All, All]]],
  ColorFunction → GrayLevel, BoxRatios → 1, Frame → False,
  MaxPlotPoints → (*Dimensions[beta][[2]]*) 10 000, PlotLegends → False,
  Axes → False, ImagePadding → None, PlotRangePadding → None];
Export["/Users/Davey/Desktop/Test1.png", img];

```

Takes png image and calculates the FT and powerseries, exports images and data

```

pic = Import["/Users/Davey/Desktop/Test1.png"];
data = ImageData[pic][[All, All, 1]];
ListPlot3D[data[[4 ;; 150, 4 ;; 250]]]
ft = Fourier[data, FourierParameters → {1, 1}];
Image[Log[Abs[ft]]];
Image[Log[Abs[shiftFT[ft]]]];

picRange = Max[Log[Abs[ft]]] - Min[Log[Abs[ft]]];
Image[(Log[Abs[shiftFT[ft]]] - Min[Log[Abs[ft]]]) / picRange]

```

```

powerseries = radialAvgPSDpadZero[data];
(*calculate the abscissa for the power series*)
abscissa = kSpaceAbscissa[powerseries];

```

Calculating the radial average of the power series of the data, export plot to desktop folder

```

powerseries = radialAvgPSDcropMapMirror[data];

picRange = Max[Log[Abs[ft]]] - Min[Log[Abs[ft]]];
Export["/Users/Davey/Desktop/" <> "Test1" <> "_FT.png",
  Image[(Log[Abs[ft]] - Min[Log[Abs[ft]]]) / picRange]];

Export["/Users/Davey/Desktop/PS_" <> "Test1.png",
  ListLinePlot[Transpose[{abscissa, Delete[Log[powerseries], -1]}],
    PlotRange → {{0, 700}, {4, 20}}, Frame → True, AspectRatio → 1,
    FrameTicks → {{Automatic, Automatic}, {Automatic, Automatic}},
    GridLines → Automatic, GridLinesStyle → Directive[LightGray, Dashed],
    FrameLabel → {{(*L*) "Log power (a.u.)", (*R*) ""},
      {(*B*) "frequency (μm-1)", (*T*) "\nPower series" <> "Test1"}},
    BaseStyle → {FontFamily → "Helvetica", FontSize → 18}, ImageSize → 450]];

```

## Turn an ASCII file into a .png file (.asc)

These ASCII files should be exported from the Veeco Vision in either XYZ real or XYZ pixel format.

At 10x, the pixels are 967 nm on each side. Z-scale is in  $\mu\text{m}$ .

at 20x, the pixels are 478 nm on each side. Z-scale is in  $\mu\text{m}$ .

```

SetDirectory[NotebookDirectory[]];
fileList = FileNames[];
fileList // TableForm

(*list filename here*)
filename = fileList[[4]];

(*notebook and file must be in the same directory,
imports file and creates a matrix of the XYZ-pairs*)
SetDirectory[NotebookDirectory[]];
file = Import[filename];
latRes = file[[13, 2]] - file[[14, 2]];
data = arrayToDepthMatrix[file];

img = Image[scale0to1[data]];
Export[ToString[filename] <> "_Data.png", img];

(*do this for the second file*)
filename = "DJ2-3_0c_10x_0restore_XYZpixel.asc";

file = Import[filename];
data = arrayToDepthMatrix[file];
img = Image[scale0to1[data]];
Export[ToString[filename] <> "_Data.png", img];

```

Automating this for all the .asc files in the directory.

```

SetDirectory[NotebookDirectory[]];
fileList = FileNames[];
Clear[i];

For[i = 1, i ≤ Length[fileList], i++,
  filename = fileList[[i]];
  If[FileExtension[filename] == ".asc",
    Print[filename];
    file = Import[filename];
    latRes = Abs[file[[13, 2]] - file[[14, 2]]];
    data = arrayToDepthMatrix[file];
    {matrix, range} = scale0to1[data];
    (*spits out the new 0-1 matrix and the old range value*)
    Export[ToString[filename] <>
      "_DataRange-" <> ToString[range] <> ".nm.png", Image[matrix]];
  ];
];

```

## ASCII to depth matrix

These ASCII files should be exported from the Veeco Vision in either XYZ real or XYZ pixel format.

At 10x, the pixels are 967 nm on each side. Z-scale is converted from "waves" to  $\mu\text{m}$ .

at 20x, the pixels are 478 nm on each side. Z-scale is converted from "waves" to  $\mu\text{m}$ .

```

directory = NotebookDirectory[];
fileList = FileNames[];

fileName = fileList[[1]]
(*notebook and file must be in the same directory,
imports file and creates a matrix of the XYZ-pairs*)
SetDirectory[directory];
file = Import[fileName];
latRes = file[[13, 2]] - file[[14, 2]];
(*latRes=
file[[First[Flatten[Position[file[[All,1]], "Pixel_size"]], -1]]*1000*)
data = arrayToDepthMatrix[file];

```

## FT algorithm on batch of files

Written to calculate the power spectrum of files that are ASCII files saved with a minimal header from the WYKO profilometer.

Data that I want to save and store from each file

- DC-centered power spectrum (log scale), png format
- Power series plot
- FT radial average .mat file
- FT matrix .mat file
- CSV file with all power spectra and abscissa's saved

Batch analysis - analyzes all the ASCII files in the notebook directory

```

(*preamble, stays the same for all files*)
ClearAll[ifile];
SetDirectory[NotebookDirectory[]];
PutAppend["-----Start time = " <>DateString[], "log.log"];

files = FileNames[];
totalfiles = Length[files];
resolution = "custom" (*low, medium, high, custom are the options*);

masterfile = {};

(*-----start of the large data compilation code-----*)
For[ifile = 1, ifile <= (* 5*)totalfiles, ifile++,
filename = files[[ifile]];

```

```

If[FileExtension[filename] == "asc",
Module[{fileBase, abscissa, powerseries,
  avgComplexValues, ft2, picRange, a, b, pixelRadii, file, data},

PutAppend[" " <> ToString[filename], "log.log"];
PutAppend[" " <> DateString[], "log.log"];
fileBase = StringTake[filename, {1, -5}];

(*Import the file*)
If[FileExistsQ[filename],
  file = Import[filename];,
  PutAppend[" ERROR: file not found.", "log.log"];
  Continue;];

(*pull out the lateral and Z-resolution from array*)
zRes(*microns*) = file[[
  First[Flatten[Position[file[[All, 1]], "Wavelength"]], -1]]/1000;
latRes(*nanometers*) = Abs[file[[13, 2]] - file[[14, 2]]] * 1000^2;

(*need to take the Infinity values out of the matrix for the FT,
maybe make this a SparseArray?*)
data = ReplaceAll[arrayToDepthMatrix[file], Infinity -> 0];

(*-----Calculate the radially-
averaged power series as fast as possible*)
{powerseries, pixelRadii, ft2} = radialAvgPSDpadZero[data];
(*calculate the abscissa for the power series*)
abscissa = kSpaceAbscissa2[pixelRadii];

PutAppend[" exporting data...", "log.log"];

(*-----Export the DC-
centered power spectrum image for future reference*)
picRange = Max[Log[Abs[ft2] + 10^-9]] - Min[Log[Abs[ft2] + 10^-9]];
Export[fileBase <> "_FT.png", ImageCrop[
  Image[(Log[Abs[ft2] + 10^-9] - Min[Log[Abs[ft2] + 10^-9]])/picRange],
  500]];

(*-----Export the PSD plot*)
Export[fileBase <> "_PS.png",
ListLinePlot[Transpose[{abscissa, Take[Log[(Abs[powerseries] + 10^-9)/
  (dimMax/latRes)^2], Length[abscissa]]}],
  PlotRange -> {{0, 0.05}, All}, Frame -> True, AspectRatio -> 1,
  PlotStyle -> {Normal},
  FrameTicks -> {{Automatic, Automatic}, {Automatic, Automatic}},
  GridLines -> Automatic,
  GridLinesStyle -> Directive[LightGray, Dashed], FrameLabel ->
  {{{(*L*) "Log power (a.u.)", (*R*) ""}, {(*B*) "frequency ( $\mu\text{m}^{-1}$ ",
  (*T*) "FT radial average \n" <> ToString[fileBase]}}}, BaseStyle ->
  {FontFamily -> "Century Gothic", FontSize -> 18}, ImageSize -> 600]];

```

```

(*-----Build up the large .csv file of all the PSDs*)
a = Join[{fileBase <> "_PSD", "points", "sq. mm area", "nm, z-resolution",
  "nm, lateral resolution"}, Take[powerseries, Length[abscissa]]];
b = Join[{"frequency (1/um)", nOrig*mOrig,
  n*m*latRes^2/10^(6*2), zRes, latRes}, abscissa];
AppendTo[masterfile, b];
AppendTo[masterfile, a];];
(*export temporary data sets so that the data are always saved -
breaks it up into 10 files to speed export*)
Export["PSD_data_Temp_.csv", Transpose[PadRight[masterfile,
  {Length[masterfile], Max[Length/@masterfile]}, 0]]];
'
(*File is not an .asc*)
PutAppend[" skipping " <> ToString[filename], "log.log"];
](*end If extension = asc *)

];(*end For iFile*)
(*cleaning up the master file so that it can be exported properly*)
masterfile =
  PadRight[masterfile, {Length[masterfile], Max[Length/@masterfile]}, 0];

Export["PSD_data_All.csv", Transpose[masterfile]];

PutAppend["-----Finish time = " <> DateString[], "log.log"];

Export["All PSD data.csv", Transpose[masterfile]];

```

# Tortuosity measurement

## Example of a single measurement

We can define the tortuosity to be: (borrowed from Tolpygo and Clarke, Acta Mat 2005)

$$L = \int_0^{x=\text{width}} \sqrt{1 - (f')^2}$$

However, since I have 2D data instead of 1D data, I'll use a 2D description:

$$L = \int_0^{x=\text{width}} \int_0^{y=\text{height}} \sqrt{1 - (\nabla f)^2}$$

Here,  $\nabla$  can be defined as the Sobel gradient filter convolution with the original matrix. It can easily be shown that in the limit of an infinitely large matrix this is the exact analogue to the 1D case (the border values in the matrix are what prevents it from being exact).

```

testdata =
  ImageData[Import["/Users/Davey/Documents/UCSB/γ' Coating Study/Fourier

```

```

Transform Profile analysis/L12 coatings after
1204C COT/120 cycle test 2000F/BC5X-2 00c.png]]];

zRes = 214.4 (*nanometers*);
latRes = 878.569 (*nanometers*);

(*-----Fourier filtering to add a bit of smoothing*)
(*crop off the edges just to ensure
that there aren't any missint data points*)
testdata = testdata[[10 ;; -10, 10 ;; -10]];
{height, width} = Dimensions[testdata];

(*pad the data to be square*)
dataSq = squarePad[testdata];
length = Dimensions[dataSq][[1]];

(*ft the data*)
ft = Fourier[dataSq, FourierParameters -> {1, 1}];
fts = shiftFT[ft];

(*masking function in k-space -
throws out all frequencies higher than 1/25 micron*)
cutoff = (1 / 25 (*micron*)) * length * latRes / 1000
(* radius in pixels to cut off the FT for filtering,
Vladimir did 10 μm averaging = 0.1 1/μm,*);
(*using graphics objects and converting to a matrix is very fast*)
circRadius = Ceiling[cutoff];
mask = Graphics[
  {Black, Rectangle[{-length / 2, -length / 2}, {length / 2, length / 2}],
  White, Disk[{0, 0}, circRadius]}, ImageSize -> {length, length},
  ImagePadding -> None, PlotRangePadding -> None];
maskMat = Rationalize[ImageData[mask][[All, All, 1]]];

(*multiply the mask by the FT'd image*)
ftm = fts * maskMat;

(*inverse FT the image*)
dataFilt = InverseFourier[shiftFT[ftm], FourierParameters -> {1, 1}];

(*crop back to the original dimensions,
only take the Real data because the original data was Real*)
dataFiltC =
  Re[dataFilt[[Round[length / 2 - height / 2] + 1 ;; Round[length / 2 + height / 2],
  Round[length / 2 - width / 2] + 1 ;; Round[length / 2 - width / 2] + width]]];

(*-----done with filtering, back to Tortuosity calculation*)
testdata = zRes * dataFiltC;

(*gradient of the profile*)
(*grad=GradientFilter[testdata,1,Method->"Sobel"];*)
(*total area of the surface*)

```

```

(*surfArea=Total[Total[Sqrt[1+grad^2]]]*latRes^2 (*in nanometers*);*)

(*this is the standard definition of the 2D surface area as used in the
  Sdr (Surface area ratio) calculations, slow to calculate though*)
surfArea = Total[Total[Table[(1/4) * (Sqrt[latRes^2 +
  (zRes * (testdata[[i, j]] - testdata[[i, j + 1]]) )^2] + Sqrt[latRes^2 +
  (zRes * (testdata[[i + 1, j]] - testdata[[i + 1, j + 1]]) )^2)] *
  (Sqrt[latRes^2 + (zRes * (testdata[[i, j]] - testdata[[i + 1, j]]) )^2] +
  Sqrt[latRes^2 + (zRes * (testdata[[i, j + 1]] - testdata[[i + 1, j + 1]]) )^2]
  2)], {i, 1, height - 1}, {j, 1, width - 1}]]];
(*RMS value of the surface slope = Sdq*)
avgSlope = Sqrt[(1/((height - 1) * (width - 1))) * Total[
  Total[Table[(zRes * (testdata[[i, j]] - testdata[[i + 1, j]]) / latRes)^2 +
  (zRes * (testdata[[i, j]] - testdata[[i, j + 1]]) / latRes)^2,
  {i, 1, height - 1}, {j, 1, width - 1}]]]]];

(*surface area in mm*)
surfAreaMM = surfArea (1/10^18 (*to m^2*)) * (1000^2 (*to mm^2*));
(*{height,width} = Dimensions[ImageData[pic]];*)
(*area of the scan*)
a0 = latRes^2 * (height - 1) * (width - 1) (*nm*);
(*tortuosity*)
tortuosity = surfArea / a0;

(*spitting out some useful values*)
surfArea;
surfAreaMM
a0;
tortuosity

```

## All the samples, collecting all the data together

```

(*preamble, stays the same for all files*)
ClearAll[ifile];
SetDirectory[NotebookDirectory[]];

PutAppend["-----Start time = " <>DateString[], "log.log"];
files = FileNames[];
totalfiles = Length[files];
resolution = "high" (*low, medium, high are the options*);

(*upper bound is #8, lower bound is #11,
  vertical resolution is #14, zero level is #19,
  horizontal and vertical sampling resolutions are #24 & 27*)
extractNumber[pos_] :=
  ToExpression[
    StringTake[words[[pos]], StringPosition[words[[pos]], "m"][[1, 1]] - 2]];

masterfile =

```

```

{"filename", "points", "sq. mm plan view area", "sq. mm surface area",
 "nm, z-res", "nm, lat Res", "avg slope", "Tortuosity"}};

(*-----start of the large data compilation code-----*)
For[ifile = 1, ifile ≤ totalfiles, ifile++,
 filename = files[[ifile]];

If[FileExtension[filename] == "png",
 Module[
 {fileBase, pic, textFile, stext, abscissa, powerseries, avgComplexValues,
 ft2, picRange, a, b, pixelRadii, grad, surfArea, surfAreaMM, a0,
 height, width, tortuosity, testdata, ft, fts, cutoff, mask, maskMat,
 ftm, dataFilt, dataFiltC, avgSlope, length, dataSq, circRadius},

 PutAppend["" <> ToString[filename], "log.log"];
 fileBase = StringTake[filename, {1, -5}];

 (*chooses the proper files*)
 pic = Import[filename];
 textFile = fileBase <> ".txt";

 (*pull out the lateral and Z-
 resolution from the associated text file*)
 If[FileExistsQ[fileBase <> ".txt"],

 (*open up a text stream for the info file*)
 stext = OpenRead[textFile];
 words = ReadList[stext, Word];
 SetStreamPosition[stext, 0];
 (*break up the text stream into groupings of words*)

 zRes = extractNumber[14] (*nanometers / gray value*);
 latRes = extractNumber[24] (*nanometers/pixel*);
 PutAppend[
 " (zRes,latRes) = " <> ToString[{zRes, latRes}], "log.log",
 (*false, file does not exist*)
 PutAppend[
 " ERROR: cannot find resolution file. zRes=latRes=1", "log.log"];
 zRes = 1;
 latRes = 1;
 ]; (*end If*)

 (*-----Fourier filtering to add a bit of smoothing*)
 (*crop off the edges just to
 ensure that there aren't any missint data points*)
 testdata = ImageData[pic] [[10 ;; -10, 10 ;; -10]];
 {height, width} = Dimensions[testdata];

 (*pad the data to be square*)
 dataSq = squarePad[testdata];

```

```

length = Dimensions[dataSq][[1]];

(*ft the data*)
ft = Fourier[dataSq, FourierParameters -> {1, 1}];
fts = shiftFT[ft];

(*masking function in k-space -
throws out all frequencies higher than 1/25 micron*)
cutoff = (1 / 25(*micron*)) * length * latRes / 1000
(* radius in pixels to cut off the FT for filtering,
Vladimir did 10 μm averaging = 0.1 1/μm,*);
(*using graphics objects and converting to a matrix is very fast*)
circRadius = Ceiling[cutoff];
mask = Graphics[
  {Black, Rectangle[{-length / 2, -length / 2}, {length / 2, length / 2}],
  White, Disk[{0, 0}, circRadius]}, ImageSize -> {length, length},
  ImagePadding -> None, PlotRangePadding -> None];
maskMat = Rationalize[ImageData[mask][[All, All, 1]]];

(*multiply the mask by the FT'd image*)
ftm = fts * maskMat;

(*inverse FT the image*)
dataFilt = InverseFourier[shiftFT[ftm], FourierParameters -> {1, 1}];

(*crop back to the original dimensions,
only take the Real data because the original data was Real*)
dataFiltC = Re[dataFilt[[Round[length / 2 - height / 2] + 1 ;;
  Round[length / 2 + height / 2], Round[length / 2 - width / 2] + 1
  ;; Round[length / 2 - width / 2] + width]]];

(*-----done with filtering, back to Tortuosity calculation*)
testdata = zRes * dataFiltC;

surfArea =
  Total[Total[Table[(1 / 4) * (Sqrt[latRes^2 + (zRes * (testdata[[i, j]] -
    testdata[[i, j + 1]])^2) + Sqrt[latRes^2 +
      (zRes * (testdata[[i + 1, j]] - testdata[[i + 1, j + 1]])^2)] *
    (Sqrt[latRes^2 + (zRes * (testdata[[i, j]] - testdata[[
      i + 1, j]])^2) + Sqrt[latRes^2 +
        (zRes * (testdata[[i, j + 1]] - testdata[[i + 1, j + 1]])^2)],
    {i, 1, height - 1}, {j, 1, width - 1}]]];
(*RMS value of the surface slope = Sdq*)
avgSlope = Sqrt[(1 / ((height - 1) * (width - 1))) * Total[
  Total[Table[(zRes * (testdata[[i, j]] - testdata[[i + 1, j]]) / latRes)^2
    + (zRes * (testdata[[i, j]] - testdata[[i, j + 1]]) / latRes)^2,
    {i, 1, height - 1}, {j, 1, width - 1}]]]]];

```

```

(*surface area in mm*)
surfAreaMM = surfArea (1/10^18 (*to m^2*)) * (1000^2 (*to mm^2*));
(*{height,width} = Dimensions[ImageData[pic]];*)
(*area of the scan*)
a0 = latRes^2 * (height - 1) * (width - 1) (*nm*);
(*tortuosity*)
tortuosity = surfArea / a0;

PutAppend[" tortuosity = " <> ToString[tortuosity], "log.log"];

(*-----Build up the large .csv file of all the PSDs*)
a = {fileBase, height * width, height * width * latRes^2 / 10^(6 * 2),
     surfAreaMM, zRes, latRes, avgSlope, tortuosity};
AppendTo[masterfile, a];
]; (*Module*)

PutAppend[" skipping " <> ToString[filename], "log.log"];
] (*If extension = png *)

]; (*For iFile*)

Export["All Tortuosity data.csv", Transpose[masterfile]];

PutAppend["-----Finish time = " <> DateString[], "log.log"];

```

## Appendix B

# Balint and Hutchinson Rumpiling Model

### B.1 Mathematica code for B&H model

# Vladimir Tolpygo's standard thermal cycle

## ■ Superalloy properties

### René N5 - Measured by GE

```
(*Pollock, Hemker, Lipkin, MRS Bulletin 2012,
RN5 CTE data, {C, CTE}*)geN5Data =
  Transpose[{{23.6272, 75.2149, 153.876, 229.970, 313.814, 377.013, 458.268,
    543.393, 605.311, 669.813, 742.049, 809.148, 855.599,
    905.926, 967.897, 1007.91, 1073.78, 1130.34, 1171.43} + 273,
  {11.9211, 12.0591, 12.2218, 12.4351, 12.7241, 12.9124, 13.1509,
    13.4019, 13.6282, 13.8797, 14.1310, 14.4709, 14.6975, 14.9619,
    15.4284, 15.6930, 16.2985, 16.8469, 17.4195} * 10^-6}];
αSUB := Interpolation[geN5Data, T];
Show[Plot[αSUB, {T, 273 + 25, 1150 + 273},
  PlotRange → All, AxesOrigin → {273, 11 * 10^-6}],
  ListPlot[geN5Data], Plot[αBCcool, {T, 300, 1400}]]];
```

## ■ Bond Coat properties

### Bond coat biaxial stress from CTE mismatch

```
σBCdotHeat :=
  eModBC / (1 - νBC) * (-εOBCdot / 2 * (Abs[σBC] / σOBC)^(nBC - 1) * (σBC / σOBC) *
    Exp[-Tref / T] + (αSUB - αBCheat) * (Tdot));

σBCdotCool :=
  eModBC / (1 - νBC) * (-εOBCdot / 2 * (Abs[σBC] / σOBC)^(nBC - 1) * (σBC / σOBC) *
    Exp[-Tref / T] + (αSUB - αBCcool) * (Tdot));
```

## Bond coat properties from Hemker's papers

```

(*elastic properties*)
eModBC := (118 - 0.024 * (T - 273)) * 10^3; (*MPa,
from Pan and Hemker 2003, converted equation to handle Kelvin*)
vBC := 0.27;
nBC = 4; (*stress exponent of BC, from Pan 2003*)
Tref := 15000; (*reference temp in K, from Balint/Hutch 2005*)
σ0BC := 25 * 10^0; (*MPa, yield stress of PtAl coating at 1150°C*)
ε0BCdot := 0.2 (*1/s, reference* creep rate for Power law creep of BC*)

(*martensite transformation temperatures (low end)*)
TtranHeat := 600 + 273; (*K, start of the heating transformation*)
TtranCool := 450 + 273; (*K, end of the cooling transformation*)

(*CTEs of the bond coat, accounts for martensite*)
αBCheat := Piecewise[{{14.6 * 10^-6, T < TtranHeat}, {86 * 10^-6,
TtranHeat ≤ T ≤ TtranHeat + 100}, {12.4 * 10^-6, T > TtranHeat + 100}}];

αBCcool := Piecewise[{{14.6 * 10^-6, T < TtranCool}, {86 * 10^-6,
TtranCool ≤ T ≤ TtranCool + 100}, {12.4 * 10^-6, T > TtranCool + 100}}];

```

## Bond coat deformation

Initially, the  $a_{BC} = 0.72$  and  $b_{BC} = 0.15$ .  $a_{BC}$  is the weight of the biaxial stress resulting from BC-superalloy CTE mismatch and  $b_{BC}$  is the weight of the normal traction from the TGO.

```

(*undulation growth rate - eq'n 9 from B&H 2005*)
δdot2 := L * ε0BCdot * Exp[-Tref / T] * (pTrac / σ0BC) *
(aBC * (Abs[σBC] / σ0BC)^(nBC - 1) + bBC * Abs[pTrac / σ0BC]^(nBC - 1));

(*coefficients from FE simulations,
valid for 1 < nBC < 5. From Balint and Hutch 2003*)
bBC := (1.152 - 0.6117 * nBC + 0.1551 * nBC^2 - 0.02081 * nBC^3 + 0.001170 * nBC^4);

(*A.29 from B&H 2003, equibiaxial stress state*)
aBC := (6 * nBC / (π * (3 + nBC))) *
Cos[(1 / 2) * (ArcTan[Sqrt[3 * (nBC - 1) * (nBC + 3)] / (3 - nBC)] + mBC * π)];

(*assuming equibiaxial stress state*)
mBC := If[nBC > 2, 1, 0];

bBC
aBC // N

```

## ■ TGO properties and governing equation

```

(*elastic properties*)
eBarTGO := eModTGO / (1 - νTGO^2);
eModTGO := 375 * 10^3; (*MPa*)
νTGO := 0.2;
αTGO := 8.5 * 10^-6;

(*TGO growth properties*)
εTGOgrowdot := If[T == 1150 + 273, hTGOdot / d, 0];
hTGOdot := kp / (2 hTGO);
kp := ((3 (*μm end*) * 10^0)^2 - (0.5 (*μm start*) * 10^0)^2) / 360 000
(*seconds in 100h*); (*m2/s, parabolic growth constant of TGO*)
d := (3 (*μm*) * 10^0 - 0.5 (*μm*) * 10^0) / (5 (*% growth strain*) * 10^-2);

(*governing equations*)
(*δN - cumulative deflection at last occurrence
of yield or elastic unloading (end of Nth cycle)
Δδe - current cycle elastic deflection
Δδp - current cycle plastic deflection*)

QTGO := -Abs[σTGO] * hTGO * π^2 / L^2 * (Sign[σTGO] + (Lstar / L)^2);
Lstar := hTGO * Sqrt[π^2 * eBarTGO / (12 * Abs[σTGO])];
PTGO := -Sign[σTGO] * (Abs[σTGO] * hTGO * π^2) / L^2;
σTGOR := 300 * 10^0; (*MPa, yield stress of TGO*)

(* (eq'n 5 from B&H 2003*)
pTracEqn:=QTGO*(Δδe+δN[[-1]]+Δδp)+PTGO*δ0;*)

(*eq'n 13 from B&H 2005, probaby wrong?*)
pTracEqn2 := QTGO * Δδe + PTGO (δ0 + δN[[-1]] + Δδp);

(*TGO stress rate - eq'n 8 from B&H 2005*)
σTGOdot2 := (*Sign[σTGO]*)
(eBarTGO * (π^2 * (δ0 + δ) * δdot2 / L^2 - εTGOgrowdot) +
eModTGO / (1 - νTGO) * (αSUB - αTGO) * Tdot);
(*total increment in the TGO displacement*)
δ := δN[[-1]] + Δδe + Δδp;

```

## ■ Calculation for changes in $L^*$

```

lList = {9, 11, 13, 15, 19, 24, 28, 33, 42, 51, 60, 80, 100} (*microns*);
SetDirectory[NotebookDirectory[]];
diagnose = False;
(*True gives a more detailed export of variables each cycle*)

Do[
(*cycles for each calculation*)

```

```

cycles = 100;

(*initial conditions for each calculation*)
hTGOSTart = 0.5 * 10^0; (*um, initial TGO thickness*)
hTGO = hTGOSTart;
δ0 = hTGOSTart / 10;
(*um, initial TGO out of plane displacement*)
Δδe = 0; (*starting with no elastic def' on current cycle*)
Δδp = 0;
(*starting with no plastic deformation on current cycle*)
δtotaln = {0};
(*list to store the total instantaneous out of plane displacement*)
δN = {0}; (*no initial deformation from previous cycles*)
clock = 0;
(*wavelength of the undulation as a function of the reference length*)

σOld = 0;
σTGOOld = -σTGOR;
σBCn = {σOld}; (*logger for BC stress*)
clockδN = {0}; (*clock to plot the deformation*)
clockAll = {0}; (*clock to plot all variables*)
hTGO = {0};
pTracn = {0};
εTGO = {0};
σTGORaten = {0};
σTGO = {σTGOOld}; (*log for TGO stress*)
tempn = {1150};
If[diagnose,
  δen = {0};
  δpn = {0};
  dδn = {0};
  δtotaln2 = {0};
  Ln = {1};
  Lstarn = {1};
  qtgon = {0};
  ptgon = {0};
  dσBCn = {0};
];

L = lList[[iRatio]];
(*originally this was written for L/Lstar ratios,
now it uses exact wavelengths*)
iCycle = 0; (*reset the cycle counter*)

Do[
  Check[
    PutAppend["L= " <> ToString[lList[[iRatio]]] <>
      ", c= " <> ToString[++iCycle], "CycleLog.log"];
    (*-----Cooling cycle-----*)

```

```

(*Vladimir's cycles had heating/cooling rates of 200 C/min*)
tStep := 0.56;
TStart := 1150 + 273;
TEnd := 25 + 273;
time := 5.6(*min*) * 60; (*convert to sec*)
Tdot = ((TEnd - TStart) / time); (*Kelvin/s*)
steps = time / tStep;
TOld = TStart;

Do[
  (*A - calculate traction and undulation displacement*)
  pTrac = ReplaceAll[pTracEqn2,  $\sigma_{TGO}$  ->  $\sigma_{TGOold}$ ];
   $d\delta$  =
    ReplaceAll[ $\delta\dot{2}$ , { $\sigma_{BC}$  ->  $\sigma_{Old}$ , T -> TOld,  $\sigma_{TGO}$  ->  $\sigma_{TGOold}$ }] * tStep;

  (*B - plastic or elastic displacement?*)
  If[Abs[ $\sigma_{TGOold}$ ] <  $\sigma_{TGOR}$  || TOld < (273 + 1150),
    (*elastic deformation*)  $d\Delta\delta_e = d\delta$ ;  $d\Delta\delta_p = 0$ ;;
    (*plastic*)  $d\Delta\delta_e = 0$ ;  $d\Delta\delta_p = d\delta$ ;
  ];

  (*C - increment in stresses*)
   $d\sigma_{BC}$  = ReplaceAll[ $\sigma_{BCdotCool}$ , {T -> (TOld),  $\sigma_{BC}$  ->  $\sigma_{Old}$ }] * tStep;
   $d\sigma_{TGO}$  = ReplaceAll[ $\sigma_{TGOdot2}$ ,
    { $\sigma_{TGO}$  ->  $\sigma_{TGOold}$ , T -> TOld,  $\sigma_{BC}$  ->  $\sigma_{Old}$ }] * tStep;

  (*D - oxide growth*)
   $dh_{TGO}$  =  $h_{TGOdot}$  * tStep;
   $d\epsilon_{TGOgrow}$  = ReplaceAll[ $\epsilon_{TGOgrowdot}$ , T -> TOld] * tStep;

  (*E - check for yielding or elastic unloading*)
  If[Abs[ $\sigma_{TGOold} + d\sigma_{TGO}$ ]  $\geq \sigma_{TGOR}$  && TOld == (1150 + 273),
    (*yielding occurs, load previous elastic displacements into  $\delta N$ *)
    AppendTo[ $\delta N$ ,  $\delta N[[-1]] + \Delta\delta_e$ ];
    AppendTo[clock $\delta N$ , clock];
     $\Delta\delta_e = 0$ ; (*reset elastic displacement term*)
  ];

  If[ $\Delta\delta_p \neq 0$  && Abs[ $\sigma_{TGOold} + d\sigma_{TGO}$ ] <  $\sigma_{TGOR}$ ,
    (*elastic unloading occurs,
    load previous plastic displacements into  $\delta N$ *)
    AppendTo[ $\delta N$ ,  $\delta N[[-1]] + \Delta\delta_p$ ];
    AppendTo[clock $\delta N$ , clock];
     $\Delta\delta_p = 0$ ; (*reset plastic disp term*)
     $\Delta\delta_e = 0$ ;
  ];

  (*F - update all quantities*)
   $\sigma_{Old}$  =  $\sigma_{Old} + d\sigma_{BC}$ ; (*BC stress*)
  (*TGO stress*)
  If[Abs[ $\sigma_{TGOold} + d\sigma_{TGO}$ ]  $\geq \sigma_{TGOR}$  && TOld == (1150 + 273),

```

```

     $\sigma_{TGOold} = -\sigma_{TGOR}(**Sign[\sigma_{TGOold}]*) ; ,$ 
     $\sigma_{TGOold} += d\sigma_{TGO}$ ;
];

(*TGO growth*)
If[TOld == (1150 + 273),
  hTGO += dhTGO;
]; (*only grow TGO at 1150C*)

(*undulation displacements*)
 $\Delta\delta e = \Delta\delta e + d\Delta\delta e$ ;
 $\Delta\delta p = \Delta\delta p + d\Delta\delta p$ ;
(*temperature*)
TOld += Tdot * tStep;

(*variable logs, etc*)
clock += tStep;
AppendTo[ $\sigma_{TGO}n$ ,  $\sigma_{TGOold}$ ];
AppendTo[ $\sigma_{BC}n$ ,  $\sigma_{Old}$ ];
AppendTo[hTGO, hTGO];
AppendTo[clockAll, clock];
AppendTo[ $\delta_{total}n$ ,  $\Delta\delta p + \Delta\delta e + \delta N[[-1]]$ ];
AppendTo[ $\epsilon_{TGO}$ , ( $\epsilon_{TGO}[-1] + d\epsilon_{TGO}grow$ )];
AppendTo[pTracn, pTrac];
AppendTo[tempn, TOld];
If[diagnose,
  AppendTo[d $\sigma_{BC}n$ , d $\sigma_{BC}$ ];
  AppendTo[ $\sigma_{TGO}raten$ , d $\sigma_{TGO}$ ];
  AppendTo[ $\delta pn$ ,  $\Delta\delta p$ ];
  AppendTo[ $\delta en$ ,  $\Delta\delta e$ ];
  AppendTo[d $\delta n$ , d $\delta$ ];
  AppendTo[ $\delta_{total}n2$ ,  $\delta N[[-1]]$ ];
  AppendTo[Lstarn, ReplaceAll[Lstar,  $\sigma_{TGO} \rightarrow \sigma_{TGOold}$ ]];
  AppendTo[Ln, L];
  AppendTo[qtgon, ReplaceAll[QTGO,  $\sigma_{TGO} \rightarrow \sigma_{TGOold}$ ]];
  AppendTo[ptgon, ReplaceAll[PTGO,  $\sigma_{TGO} \rightarrow \sigma_{TGOold}$ ]];
];

, {steps}];

(*-----Soak at low T-----*)
tStep := 0.5; (*seconds*)
TStart := 25 + 273;
TEnd := 25 + 273;
time := 0.1(*min*) * 60; (*convert to sec*)
Tdot = ((TEnd - TStart) / time); (*Kelvin/s*)
steps = time / tStep;

(* $\sigma_{Old} = \sigma_{Old}$ ;
 $\sigma_{TGOold} = -\sigma_{TGOR}$ ;*)
TOld = TStart;

```

```

Do[
  (*A - calculate traction and undulation displacement*)
  pTrac = ReplaceAll[pTracEqn2,  $\sigma$ TGO ->  $\sigma$ TGOOld];
  d $\delta$  =
    ReplaceAll[ $\delta$ dot2, { $\sigma$ BC ->  $\sigma$ Old, T -> TOld,  $\sigma$ TGO ->  $\sigma$ TGOOld}] * tStep;

  (*B - plastic or elastic displacement?*)
  If[Abs[ $\sigma$ TGOOld] <  $\sigma$ TGOR || TOld < (273 + 1150),
    d $\Delta\delta$ e = d $\delta$ ; d $\Delta\delta$ p = 0;,
    d $\Delta\delta$ e = 0; d $\Delta\delta$ p = d $\delta$ ;
  ];

  (*C, increment the stresses*)
  d $\sigma$ BC = ReplaceAll[ $\sigma$ BCdotCool, {T -> (TOld),  $\sigma$ BC ->  $\sigma$ Old}] * tStep;
  d $\sigma$ TGO = ReplaceAll[ $\sigma$ TGODot2,
    { $\sigma$ TGO ->  $\sigma$ TGOOld, T -> TOld,  $\sigma$ BC ->  $\sigma$ Old}] * tStep;

  (*D - oxide growth*)
  dhTGO = hTGOdot * tStep;
  deTGOgrow = ReplaceAll[eTGOgrowdot, T -> TOld] * tStep;

  (*E - check for yielding or elastic unloading*)
  If[Abs[ $\sigma$ TGOOld + d $\sigma$ TGO]  $\geq$   $\sigma$ TGOR && TOld == (1150 + 273),
    (*yielding occurs, load previous elastic displacements into  $\delta$ N*)
    AppendTo[ $\delta$ N,  $\delta$ N[[-1]] +  $\Delta\delta$ e];
    AppendTo[clock $\delta$ N, clock];
     $\Delta\delta$ e = 0; (*reset elastic displacement term*)
  ];

  If[ $\Delta\delta$ p  $\neq$  0 && Abs[ $\sigma$ TGOOld + d $\sigma$ TGO] <  $\sigma$ TGOR,
    (*elastic unloading occurs,
    load previous plastic displacements into  $\delta$ N*)
    AppendTo[ $\delta$ N,  $\delta$ N[[-1]] +  $\Delta\delta$ p];
    AppendTo[clock $\delta$ N, clock];
     $\Delta\delta$ p = 0;
     $\Delta\delta$ e = 0;
  ];

  (*F - update all quantities*)
   $\sigma$ Old += d $\sigma$ BC; (*BC stress*)
  (*TGO stress*)
  If[Abs[ $\sigma$ TGOOld + d $\sigma$ TGO]  $\geq$   $\sigma$ TGOR && TOld == (1150 + 273),
     $\sigma$ TGOOld = - $\sigma$ TGOR(**Sign[ $\sigma$ TGOOld]*);,
     $\sigma$ TGOOld += d $\sigma$ TGO;
  ];

  (*TGO growth*)
  If[TOld == (1150 + 273),
    hTGO += dhTGO;
  ]; (*only grow TGO at 1150C*)

```

```

    (*undulation displacements*)
    Δδe = Δδe + dΔδe;
    Δδp = Δδp + dΔδp;
    (*temperature*)
    Told += Tdot * tStep;
    (*variable logs, etc*)
    clock += tStep;
    AppendTo[σTGOon, σTGOold];
    AppendTo[σBCn, σOld];
    AppendTo[hTGOon, hTGO];
    AppendTo[clockAll, clock];
    AppendTo[δtotaln, Δδp + Δδe + δN[[-1]]];
    AppendTo[εTGO, (εTGO[[-1]] + dεTGOgrow)];
    AppendTo[pTracn, pTrac];
    AppendTo[tempn, Told];
    If[diagnose,
      AppendTo[dσBCn, dσBC];
      AppendTo[σTGOraten, dσTGO];
      AppendTo[δpn, Δδp];
      AppendTo[δen, Δδe];
      AppendTo[dδn, dδ];
      AppendTo[δtotaln2, δN[[-1]]];
      AppendTo[Lstarn, ReplaceAll[Lstar, σTGO → σTGOold]];
      AppendTo[Ln, L];
      AppendTo[qtgon, ReplaceAll[QTGO, σTGO → σTGOold]];
      AppendTo[ptgon, ReplaceAll[PTGO, σTGO → σTGOold]];
    ];
, {steps}];

    (*end of isothermal period,
    add the plastic displacement to the total displacement*)
    AppendTo[δN, δN[[-1]] + Δδp];
    Δδp = 0;
    AppendTo[clockδN, clock];

    (*-----Heating cycle-----*)
    tStep := 0.56; (*seconds*)
    TStart := 25 + 273;
    TEnd := 1150 + 273;
    time := 5.6(*min*) * 60; (*convert to sec*)
    Tdot = ((TEnd - TStart) / time); (*Kelvin/s*)
    steps = time / tStep;

    Told = TStart;

    Do[
      (*A - calculate traction and undulation displacement*)
      pTrac = ReplaceAll[pTracEqn2, σTGO -> σTGOold];
      dδ =
        ReplaceAll[δdot2, {σBC -> σOld, T -> Told, σTGO -> σTGOold}] * tStep;

```

```

(*B - plastic or elastic displacement?*)
If[Abs[σTGOold] < σTGOR || Told < (273 + 1150),
  dΔδe = dδ; dΔδp = 0(*elastic*);,
  dΔδe = 0; dΔδp = dδ(*plastic*);
];

(*C, increment the stresses*)
dσBC = ReplaceAll[σBCdotHeat, {T -> Told, σBC -> σOld}] * tStep;
dσTGO = ReplaceAll[σTGOdot2,
  {σTGO -> σTGOold, T -> Told, σBC -> σOld}] * tStep;

(*D - oxide growth*)
dhTGO = hTGOdot * tStep;
deTGOgrow = ReplaceAll[εTGOgrowdot, T -> Told] * tStep;

(*E - check for yielding or elastic unloading*)
If[Abs[σTGOold + dσTGO] ≥ σTGOR && Told == (1150 + 273),
  (*yielding occurs, load previous elastic displacements into δN*)
  AppendTo[δN, δN[[-1]] + Δδe];
  AppendTo[clockδN, clock];
  Δδe = 0;
];

If[Δδp ≠ 0 && Abs[σTGOold + dσTGO] < σTGOR,
  (*elastic unloading occurs,
  load previous plastic displacements into δN*)
  AppendTo[δN, δN[[-1]] + Δδp];
  AppendTo[clockδN, clock];
  Δδp = 0; (*reset plastic disp term*)
  Δδe = 0;
];

(*F - update all quantities*)
σOld += dσBC; (*BC stress*)
(*TGO stress*)
If[Abs[σTGOold + dσTGO] ≥ σTGOR && Told == (1150 + 273),
  σTGOold = -σTGOR(**Sign[σTGOold]*);,
  σTGOold += dσTGO;
];

(*TGO growth*)
If[Told == (1150 + 273),
  hTGO += dhTGO;
]; (*only grow TGO at 1150C*)

(*undulation displacements*)
Δδe = Δδe + dΔδe;
Δδp = Δδp + dΔδp;
(*temperature*)
Told += Tdot * tStep;

```

```

(*variable logs, etc*)
clock += tStep;
AppendTo[σTGOn, σTGOOld];
AppendTo[σBCn, σOld];
AppendTo[hTGOn, hTGO];
AppendTo[clockAll, clock];
AppendTo[δtotaln, Δδp + Δδe + δN[[-1]]];
AppendTo[εTGO, (εTGO[[-1]] + δεTGOgrow)];
AppendTo[pTracn, pTrac];
AppendTo[tempn, TOld];
If[diagnose,
  AppendTo[dσBCn, dσBC];
  AppendTo[σTGOraten, dσTGO];
  AppendTo[δpn, Δδp];
  AppendTo[δen, Δδe];
  AppendTo[dδn, dδ];
  AppendTo[δtotaln2, δN[[-1]]];
  AppendTo[Lstarn, ReplaceAll[Lstar, σTGO → σTGOOld]];
  AppendTo[Ln, L];
  AppendTo[qtgon, ReplaceAll[QTGO, σTGO → σTGOOld]];
  AppendTo[ptgon, ReplaceAll[PTGO, σTGO → σTGOOld]];
];

, {steps}];

(*-----High Temp Soak-----*)
TStart := 1150 + 273;
TEnd := 1150 + 273;
time := 60(*min*) * 60; (*convert to sec*)
Tdot = ((TEnd - TStart) / time); (*Kelvin/s*)
timeElap = 0;

TOld = TStart;

While[
  timeElap < time,
  tStep = If[timeElap < 10 || timeElap > (time - 10), 0.2, 10];

  (*Cut tStep in half if there is yielding soon to occur*)
  If[
    Abs[σTGOOld + 3 * dσTGO] ≥ σTGOR && TOld == (1150 + 273) && iCycle > 3,
    tStep = 5;];

  (*A - calculate traction and undulation displacement*)
  pTrac = ReplaceAll[pTracEqn2, σTGO -> σTGOOld];
  dδ =
    ReplaceAll[δdot2, {σBC -> σOld, T -> TOld, σTGO -> σTGOOld}] * tStep;

  (*B - plastic or elastic displacement?*)
  If[Abs[σTGOOld + dσTGO(*added this term*)] < σTGOR ||
    TOld < (273 + 1150),

```

```

dΔδe = dδ; dΔδp = 0;,
dΔδe = 0; dΔδp = dδ;];

(*C, increment the stresses*)
dσBC = ReplaceAll[σBCdotHeat, {T -> (TOld), σBC -> σOld}] * tStep;
dσTGO = ReplaceAll[σTGOdot2,
  {σTGO -> σTGOOld, T -> TOld, σBC -> σOld}] * tStep;

  (*D - oxide growth*)
  dhTGO = hTGOdot * tStep;
  deTGOgrow = ReplaceAll[εTGOgrowdot, T -> TOld] * tStep;

  (*E - check for yielding or elastic unloading*)
  If[Abs[σTGOOld + dσTGO] ≥ σTGOR && TOld == (1150 + 273),
    (*yielding occurs, load previous elastic displacements into δN*)
    AppendTo[δN, δN[[-1]] + Δδe];
    AppendTo[clockδN, clock];
    Δδe = 0;
  ];

  If[Δδp ≠ 0 && Abs[σTGOOld + dσTGO] < σTGOR,
    (*elastic unloading occurs,
    load previous plastic displacements into δN*)
    AppendTo[δN, δN[[-1]] + Δδp];
    AppendTo[clockδN, clock];
    Δδp = 0; (*reset plastic disp term*)
    Δδe = 0;
  ];

  (*F - update all quantities*)
  σOld += dσBC; (*BC stress*)
  (*TGO stress*)
  If[Abs[σTGOOld + dσTGO] ≥ σTGOR && TOld == (1150 + 273),
    σTGOOld = -σTGOR(**Sign[σTGOOld]*);,
    σTGOOld += dσTGO;
  ];

  (*TGO growth*)
  If[TOld == (1150 + 273),
    hTGO += dhTGO;
  ]; (*only grow TGO at 1150C*)

  (*undulation displacements*)
  Δδe = Δδe + dΔδe;
  Δδp = Δδp + dΔδp;
  (*temperature*)
  TOld += Tdot * tStep;
  (*variable logs, etc*)
  clock += tStep;
  AppendTo[σTGOon, σTGOOld];
  AppendTo[σBCn, σOld];
  AppendTo[hTGOon, hTGO];

```

```

AppendTo[clockAll, clock];
AppendTo[ $\delta$ totaln,  $\Delta\delta p + \Delta\delta e + \delta N[[-1]]$ ];
AppendTo[ $\epsilon$ TGO, ( $\epsilon$ TGO[[-1]] +  $d\epsilon$ TGOgrow)];
AppendTo[pTracn, pTrac];
AppendTo[tempn, TOld];
If[diagnose,
  AppendTo[d $\sigma$ BCn, d $\sigma$ BC];
  AppendTo[ $\sigma$ TGORaten, d $\sigma$ TGO];
  AppendTo[ $\delta$ pn,  $\Delta\delta p$ ];
  AppendTo[ $\delta$ en,  $\Delta\delta e$ ];
  AppendTo[d $\delta$ n, d $\delta$ ];
  AppendTo[ $\delta$ totaln2,  $\delta N[[-1]]$ ];
  AppendTo[Lstarn, ReplaceAll[Lstar,  $\sigma$ TGO  $\rightarrow$   $\sigma$ TGOold]];
  AppendTo[Ln, L];
  AppendTo[qtgon, ReplaceAll[QTGO,  $\sigma$ TGO  $\rightarrow$   $\sigma$ TGOold]];
  AppendTo[ptgon, ReplaceAll[PTGO,  $\sigma$ TGO  $\rightarrow$   $\sigma$ TGOold]];
];

timeElap += tStep;
]; (*end While*)

(*end of isothermal period,
add the plastic displacement to the total displacement*)
AppendTo[ $\delta$ N,  $\delta N[[-1]] + \Delta\delta p$ ];
 $\Delta\delta p = 0$ ;
AppendTo[clock $\delta$ N, clock];
AppendTo[ $\sigma$ TGOn,  $\sigma$ TGOold];
AppendTo[ $\sigma$ BCn,  $\sigma$ Old];
AppendTo[hTGOn, hTGO];
AppendTo[clockAll, clock];
AppendTo[ $\delta$ totaln,  $\Delta\delta p + \Delta\delta e + \delta N[[-1]]$ ];
AppendTo[ $\epsilon$ TGO, ( $\epsilon$ TGO[[-1]] +  $d\epsilon$ TGOgrow)];
AppendTo[pTracn, pTrac];
AppendTo[tempn, TOld];
If[diagnose,
  AppendTo[d $\sigma$ BCn, d $\sigma$ BC];
  AppendTo[ $\sigma$ TGORaten, d $\sigma$ TGO];
  AppendTo[ $\delta$ pn,  $\Delta\delta p$ ];
  AppendTo[ $\delta$ en,  $\Delta\delta e$ ];
  AppendTo[d $\delta$ n, d $\delta$ ];
  AppendTo[ $\delta$ totaln2,  $\delta N[[-1]]$ ];
  AppendTo[Lstarn, ReplaceAll[Lstar,  $\sigma$ TGO  $\rightarrow$   $\sigma$ TGOold]];
  AppendTo[Ln, L];
  AppendTo[qtgon, ReplaceAll[QTGO,  $\sigma$ TGO  $\rightarrow$   $\sigma$ TGOold]];
  AppendTo[ptgon, ReplaceAll[PTGO,  $\sigma$ TGO  $\rightarrow$   $\sigma$ TGOold]];
];
/
PutAppend["L= " <> ToString[lList[[iRatio]]] <>
  ",c= " <> ToString[iCycle] <> " ERROR, SKIP", "CycleLog.log"];
Break[(*skip cycle if there is an error*)] (*end Check*);

```

# Bibliography

- [1] I. E. Agency, *Key world energy statistics*. International Energy Agency, 2015.
- [2] S. Manabe and R. T. Wetherald, *On the distribution of climate change resulting from an increase in CO<sub>2</sub> content of the atmosphere*, *Journal of the Atmospheric Sciences* **37** (1980), no. 1 99–118.
- [3] M. Alvin, D. Zhu, K. Klotz, B. McMordie, B. Warnes, B. Gleeson, B. Kang, and J. Tannenbaum, *Development and assessment of coatings for future power generation turbines*, in *ASME Turbo Expo 2012: Turbine Technical Conference and Exposition*, pp. 163–173, American Society of Mechanical Engineers, 2012.
- [4] E. CENTER, *Life-cycle energy costs and greenhouse gas emissions for gas turbine power*, 2000.
- [5] J. H. Perepezko, *The hotter the engine, the better*, *Science* **326** (2009), no. 5956 1068–1069.
- [6] N. P. Padture, M. Gell, and E. H. Jordan, *Thermal barrier coatings for gas-turbine engine applications*, *Science* **296** (2002), no. 5566 280–284.
- [7] D. R. Clarke, M. Oechsner, and N. P. Padture, *Thermal-barrier coatings for more efficient gas-turbine engines*, *MRS bulletin* **37** (2012), no. 10 891–898.
- [8] R. Darolia, *Thermal barrier coatings technology: critical review, progress update, remaining challenges and prospects*, *International Materials Reviews* **58** (2013), no. 6 315–348.
- [9] M. Stiger, N. Yanar, M. Topping, F. Pettit, and G. Meier, *Thermal barrier coatings for the 21st century*, *Zeitschrift fur Metallkunde* **90** (1999), no. 12 1069–1078.
- [10] A. Evans, D. Mumm, J. Hutchinson, G. Meier, and F. Pettit, *Mechanisms controlling the durability of thermal barrier coatings*, *Progress in Materials Science* **46** (2001), no. 5 505–553.

- [11] D. Pan, M. Chen, P. Wright, and K. Hemker, *Evolution of a diffusion aluminide bond coat for thermal barrier coatings during thermal cycling*, *Acta Materialia* **51** (2003), no. 8 2205–2217.
- [12] V. Tolpygo and D. Clarke, *Temperature and cycle-time dependence of rumpling in platinum-modified diffusion aluminide coatings*, *Scripta materialia* **57** (2007), no. 7 563–566.
- [13] C. G. Levi, J. W. Hutchinson, M.-H. Vidal-Sétif, and C. A. Johnson, *Environmental degradation of thermal-barrier coatings by molten deposits*, *MRS bulletin* **37** (2012), no. 10 932–941.
- [14] K. M. Grant, S. Krämer, J. P. Löfvander, and C. G. Levi, *CMAS degradation of environmental barrier coatings*, *Surface and Coatings Technology* **202** (2007), no. 4 653–657.
- [15] S. Krämer, J. Yang, and C. G. Levi, *Infiltration-inhibiting reaction of gadolinium zirconate thermal barrier coatings with CMAS melts*, *Journal of the American Ceramic Society* **91** (2008), no. 2 576–583.
- [16] T. A. Schaedler, R. M. Leckie, S. Krämer, A. G. Evans, and C. G. Levi, *Toughening of nontransformable t'-YSZ by addition of titania*, *Journal of the American Ceramic Society* **90** (2007), no. 12 3896–3901.
- [17] M. Chen, R. Ott, T. Hufnagel, P. Wright, and K. Hemker, *Microstructural evolution of platinum modified nickel aluminide bond coat during thermal cycling*, *Surface and Coatings Technology* **163-164** (2003) 25–30.
- [18] T. Pollock, D. Lipkin, and K. Hemker, *Multifunctional coating interlayers for thermal-barrier systems*, *MRS Bulletin* **37** (2012), no. 10 923–931.
- [19] D. Balint, T. Xu, J. Hutchinson, and A. Evans, *Influence of bond coat thickness on the cyclic rumpling of thermally grown oxides*, *Acta Materialia* **54** (2006), no. 7 1815–1820.
- [20] T. Pollock and S. Tin, *Nickel-based superalloys for advanced turbine engines: chemistry, microstructure and properties*, *Journal of Propulsion and Power* **22** (2006), no. 2 361–374.
- [21] J. Hutchinson and Z. Suo, *Mixed mode cracking in layered materials*, *Advances in Applied Mechanics* **29** (1992), no. 63 191.
- [22] D. Lipkin and D. Clarke, *Measurement of the stress in oxide scales formed by oxidation of alumina-forming alloys*, *Oxidation of Metals* **45** (1996), no. 3-4 267–280.

- [23] K. Hemker and W. Nix, *High-temperature creep of the intermetallic alloy Ni<sub>3</sub>Al*, *Metallurgical Transactions A* **24** (1993), no. 2 335–341.
- [24] B. Veal and A. Paulikas, *Growth strains and creep in thermally grown alumina: Oxide growth mechanisms*, *Journal of Applied physics* **104** (2008), no. 9 093525.
- [25] T. Pollock, B. Laux, C. Brundidge, A. Suzuki, and M. He, *Oxide-assisted degradation of Ni-base single crystals during cyclic loading: the role of coatings*, *Journal of the American Ceramic Society* **94** (2011), no. s1 s136–s145.
- [26] A. Suzuki, M. Gigliotti, B. Hazel, D. Konitzer, and T. Pollock, *Crack progression during sustained-peak low-cycle fatigue in single-crystal Ni-base superalloy René N5*, *Metallurgical and Materials Transactions A* **41** (2010), no. 4 947–956.
- [27] M. He and A. Evans, *A model for oxidation-assisted low cycle fatigue of superalloys*, *Acta Materialia* **58** (2010), no. 2 583–591.
- [28] A. Evans, M. He, A. Suzuki, M. Gigliotti, B. Hazel, and T. Pollock, *A mechanism governing oxidation-assisted low-cycle fatigue of superalloys*, *Acta Materialia* **57** (2009), no. 10 2969–2983.
- [29] V. K. Tolpygo, *Development of internal cavities in platinum-aluminide coatings during cyclic oxidation*, *Surface and Coatings Technology* **202** (2007), no. 4 617–622.
- [30] D. Mumm, A. Evans, and I. Spitsberg, *Characterization of a cyclic displacement instability for a thermally grown oxide in a thermal barrier system*, *Acta Materialia* **49** (2001), no. 12 2329–2340.
- [31] D. Balint and J. Hutchinson, *An analytical model of rumpling in thermal barrier coatings*, *Journal of the Mechanics and Physics of Solids* **53** (2005), no. 4 949–973.
- [32] V. K. Tolpygo and D. Clarke, *On the rumpling mechanism in nickel-aluminide coatings: Part I: an experimental assessment*, *Acta Materialia* **52** (2004), no. 17 5115–5127.
- [33] D. Balint and J. Hutchinson, *Undulation instability of a compressed elastic film on a nonlinear creeping substrate*, *Acta Materialia* **51** (2003), no. 13 3965–3983.
- [34] A. Karlsson, J. Hutchinson, and A. Evans, *The displacement of the thermally grown oxide in thermal barrier systems upon temperature cycling*, *Materials Science and Engineering: A* **351** (2003), no. 1 244–257.
- [35] A. M. Karlsson, C. Levi, and A. Evans, *A model study of displacement instabilities during cyclic oxidation*, *Acta Materialia* **50** (2002), no. 6 1263–1273.

- [36] A. Karlsson and A. Evans, *A numerical model for the cyclic instability of thermally grown oxides in thermal barrier systems*, *Acta Materialia* **49** (2001), no. 10 1793–1804.
- [37] V. Tolpygo and D. Clarke, *Surface rumpling of a (Ni,Pt) Al bond coat induced by cyclic oxidation*, *Acta Materialia* **48** (2000), no. 13 3283–3293.
- [38] V. K. Tolpygo and D. Clarke, *On the rumpling mechanism in nickel-aluminide coatings: Part II: characterization of surface undulations and bond coat swelling*, *Acta Materialia* **52** (2004), no. 17 5129–5141.
- [39] V. K. Tolpygo and D. Clarke, *Rumpling induced by thermal cycling of an overlay coating: the effect of coating thickness*, *Acta Materialia* **52** (2004), no. 3 615–621.
- [40] V. Tolpygo, K. Murphy, and D. Clarke, *Effect of Hf, Y and C in the underlying superalloy on the rumpling of diffusion aluminide coatings*, *Acta Materialia* **56** (2008), no. 3 489–499.
- [41] R. Panat, S. Zhang, and K. J. Hsia, *Bond coat surface rumpling in thermal barrier coatings*, *Acta Materialia* **51** (2003), no. 1 239–249.
- [42] R. Panat and K. J. Hsia, *Experimental investigation of the bond-coat rumpling instability under isothermal and cyclic thermal histories in thermal barrier systems*, in *Proceedings of the Royal Society of London A: Mathematical, Physical and Engineering Sciences*, vol. 460, pp. 1957–1979, The Royal Society, 2004.
- [43] R. P. Panat, *On the rumpling instability in thermal barrier systems*. PhD thesis, University of Illinois at Urbana-Champaign, 2004.
- [44] R. Panat, K. J. Hsia, and D. G. Cahill, *Evolution of surface waviness in thin films via volume and surface diffusion*, *Journal of applied physics* **97** (2005), no. 1 013521.
- [45] R. Panat, K. J. Hsia, and J. Oldham, *Rumpling instability in thermal barrier systems under isothermal conditions in vacuum*, *Philosophical Magazine* **85** (2005), no. 1 45–64.
- [46] V. K. Tolpygo and D. R. Clarke, *Damage induced by thermal cycling of thermal barrier coatings*, *Elevated Temperature Coatings: Science & Technology IV* (2001) 94.
- [47] L. B. Freund and S. Suresh, *Thin Film Materials: Stress, Defect Formation, and Surface Evolution*. Cambridge University Press Cambridge, 2003.

- [48] M. Chen, M. Glynn, R. Ott, T. Hufnagel, and K. Hemker, *Characterization and modeling of a martensitic transformation in a platinum modified diffusion aluminide bond coat for thermal barrier coatings*, *Acta Materialia* **51** (2003), no. 14 4279–4294.
- [49] R. Noebe, R. Bowman, and M. Nathal, *Physical and mechanical properties of the B2 compound NiAl*, *International Materials Reviews* **38** (1993), no. 4 193–232.
- [50] B. Tryon, T. Pollock, M. Gigliotti, and K. Hemker, *Thermal expansion behavior of ruthenium aluminides*, *Scripta Materialia* **50** (2004), no. 6 845–848.
- [51] B. Tryon, *Multi-Layered Ruthenium-Containing Bond Coats for Thermal Barrier Coatings*. PhD thesis, The University of Michigan, 2005.
- [52] B. Tryon, Q. Feng, T. Pollock, R. Wellman, J. Nicholls, K. Murphy, J. Yang, and C. Levi, *Multilayered ruthenium-modified bond coats for thermal barrier coatings*, *Metallurgical and Materials Transactions A* **37** (2006), no. 11 3347–3358.
- [53] B. Tryon, F. Cao, K. Murphy, C. Levi, and T. Pollock, *Ruthenium-containing bond coats for thermal barrier coating systems*, *JoM* **58** (2006), no. 1 53–59.
- [54] B. Tryon, K. Murphy, J. Yang, C. Levi, and T. Pollock, *Hybrid intermetallic Ru/Pt-modified bond coatings for thermal barrier systems*, *Surface and Coatings Technology* **202** (2007), no. 2 349–361.
- [55] B. Tryon, D. Litton, B. Zimmerman, and R. Beers, *Multi-layer metallic coating for TBC systems*, July 30, 2013. US Patent 8,497,028.
- [56] R. R. Adharapurapu, J. Zhu, V. S. Dheeradhada, D. M. Lipkin, and T. M. Pollock, *A combinatorial investigation of palladium and platinum additions to  $\beta$ -NiAl overlay coatings*, *Acta Materialia* **77** (2014) 379–393.
- [57] R. Jackson, D. Lipkin, and T. Pollock, *The oxidation and rumpling behavior of overlay B2 bond coats containing Pt, Pd, Cr and Hf*, *Surface and Coatings Technology* **221** (2013) 13–21.
- [58] R. Jackson, D. Lipkin, and T. Pollock, *Thermal barrier coating adherence to Hf-modified B2 NiAl bond coatings*, *Acta Materialia* **80** (2014) 39–47.
- [59] M. A. Alvin, K. Klotz, B. McMordie, D. Zhu, B. Gleeson, and B. Warnes, *Extreme temperature coatings for future gas turbine engines*, *Journal of Engineering for Gas Turbines and Power* **136** (2014), no. 11 112102.
- [60] R. Yu and P. Y. Hou, *First-principles calculations of the effect of Pt on NiAl surface energy and the site preference of Pt*, *Applied physics letters* **91** (2007), no. 1 011907.

- [61] C. Rae and R. Reed, *The precipitation of topologically close-packed phases in rhenium-containing superalloys*, *Acta Materialia* **49** (2001), no. 19 4113–4125.
- [62] D. Das, B. Gleeson, K. Murphy, S. Ma, and T. Pollock, *Formation of secondary reaction zone in ruthenium bearing nickel based single crystal superalloys with diffusion aluminide coatings*, *Materials Science and Technology* **25** (2009), no. 2 300–308.
- [63] W. Walston, *Coating and surface technologies for turbine airfoils*, *Superalloys* (2004) 579–588.
- [64] K. Hemker, B. Mendis, and C. Eberl, *Characterizing the microstructure and mechanical behavior of a two-phase NiCoCrAlY bond coat for thermal barrier systems*, *Materials Science and Engineering: A* **483** (2008) 727–730.
- [65] D. J. Jorgensen, A. Suzuki, D. M. Lipkin, and T. M. Pollock, *Bond coatings with high rumpling resistance: Design and characterization*, *Surface and Coatings Technology* **300** (2016) 25–34.
- [66] A. M. Karlsson, J. Hutchinson, and A. Evans, *A fundamental model of cyclic instabilities in thermal barrier systems*, *Journal of the Mechanics and Physics of Solids* **50** (2002), no. 8 1565–1589.
- [67] K. Fujiwara and Z. Horita, *Measurement of intrinsic diffusion coefficients of Al and Ni in Ni<sub>3</sub>Al using Ni/NiAl diffusion couples*, *Acta materialia* **50** (2002), no. 6 1571–1579.
- [68] G. Hancock, *Diffusion of nickel in alloys based on the intermetallic compound Ni<sub>3</sub>Al ( $\gamma'$ )*, *Physica Status Solidi (a)* **7** (1971), no. 2 535–540.
- [69] G. Hancock and B. McDonnell, *Diffusion in the intermetallic compound NiAl*, *Physica Status Solidi (a)* **4** (1971), no. 1 143–150.
- [70] Q. Xu and A. Van der Ven, *First-principles investigation of migration barriers and point defect complexes in B2–NiAl*, *Intermetallics* **17** (2009), no. 5 319–329.
- [71] Q. Xu and A. Van der Ven, *Atomic transport in ordered compounds mediated by local disorder: Diffusion in B2–Ni<sub>x</sub>Al<sub>1-x</sub>*, *Physical Review B* **81** (2010), no. 6 064303.
- [72] M. Rudy and G. Sauthoff, *Creep behaviour of the ordered intermetallic (Fe,Ni)Al phase*, in *MRS Proceedings*, vol. 39, Cambridge Univ Press, 1984.
- [73] D. Shah and D. Duhl, *Evaluation of multicomponent nickel base L1<sub>2</sub> and other intermetallic alloys as high temperature structural materials*, in *MRS Proceedings*, vol. 81, Cambridge Univ Press, 1986.

- [74] U. R. Kattner, *The thermodynamic modeling of multicomponent phase equilibria*, *JOM* **49** (1997), no. 12 14–19.
- [75] F. Pettit, *Oxidation mechanisms for nickel-aluminum alloys at temperatures between 900° and 1300 °C*, *Transactions of the Metallurgical Society of AIME* **239** (1967) 1296–1305.
- [76] G. Wallwork and A. Hed, *Some limiting factors in the use of alloys at high temperatures*, *Oxidation of Metals* **3** (1971), no. 2 171–184.
- [77] B. Gleeson, N. Mu, and S. Hayashi, *Compositional factors affecting the establishment and maintenance of Al<sub>2</sub>O<sub>3</sub> scales on Ni–Al–Pt systems*, *Journal of Materials Science* **44** (2009), no. 7 1704–1710.
- [78] C. Giggins and F. Pettit, *Oxidation of Ni–Cr–Al alloys between 1000° and 1200°C*, *Journal of the Electrochemical Society* **118** (1971), no. 11 1782–1790.
- [79] *Thermo-Calc Software Database TCNI5 Ni-based Superalloys version 5*, 2013.
- [80] D. Tsipas, H. Lefakis, R. Rawlings, A. Staton-Bevan, and S. Tsipas, *Mechanical and oxidation properties of Ni<sub>3</sub>Al-based alloys*, *Materials and Manufacturing Processes* **16** (2001), no. 1 127–140.
- [81] R. D. Rawlings and A. E. Staton-Bevan, *The alloying behaviour and mechanical properties of polycrystalline Ni<sub>3</sub>Al ( $\gamma'$  phase) with ternary additions*, *Journal of Materials Science* **10** (1975) 505–514.
- [82] C. E. Lowell and G. J. Santoro, *The 1200 °C cyclic oxidation behavior of two nickel-aluminum alloys (Ni<sub>3</sub>Al and NiAl) with additions of chromium, silicon, and titanium*, Technical Note D-6838, NASA, 1972.
- [83] B. Hazel, J. Rigney, M. Gorman, B. Boutwell, and R. Darolia, *Development of improved bond coat for enhanced turbine durability*, *Superalloys* (2008) 753–760.
- [84] X. Zhang, S. Wang, F. Gesmundo, and Y. Niu, *The effect of Cr on the oxidation of Ni–10 at% Al in 1 atm O<sub>2</sub> at 900–1000 °C*, *Oxidation of Metals* **65** (2006), no. 3-4 151–165.
- [85] Y. Wu, Y. Niu, and W.-t. Wu, *Effect of silicon on oxidation of Ni-15Al alloy*, *Trans. Nonferrous Met. Soc. China* **15** (2005), no. 2.
- [86] P. Thornton, R. Davies, and T. Johnston, *The temperature dependence of the flow stress of the  $\gamma$  phase based upon Ni<sub>3</sub>Al*, *Metallurgical Transactions* **1** (1970), no. 1 207–218.

- [87] H. Grabke, M. Steinhorst, M. Brumm, and D. Wiemer, *Oxidation and intergranular disintegration of the aluminides NiAl and NbAl<sub>3</sub> and phases in the system Nb-Ni-Al*, *Oxidation of metals* **35** (1991), no. 3-4 199–222.
- [88] N. Bornstein, M. DeCrescente, and J. Smeggil, *The influence of sulfur on the oxidation of coatings*, *Materials Science and Engineering: A* **120** (1989) 175–178.
- [89] A. Funkenbusch, J. Smeggil, and N. Bornstein, *Reactive element-sulfur interaction and oxide scale adherence*, *Metallurgical Transactions A* **16** (1985), no. 6 1164–1166.
- [90] D. J. Jorgensen, A. Suzuki, D. M. Lipkin, and T. M. Pollock, *Sulfur and minor element effects in the oxidation of bilayer  $\gamma' + \beta$  bond coats for thermal barrier coatings on René N5*, *Superalloys* (2016).
- [91] J. Smialek, *Effect of sulfur removal on Al<sub>2</sub>O<sub>3</sub> scale adhesion*, *Metallurgical Transactions A* **22** (1991), no. 3 739–752.
- [92] J. Smialek, *Scale adhesion, sulfur content, and TBC failure on single crystal superalloys*, in *26th Annual Conference on Composites, Advanced Ceramics, Materials, and Structures: B: Ceramic Engineering and Science Proceedings, Volume 23, Issue 4*, pp. 485–495, Wiley Online Library, 2002.
- [93] V. Tolpygo and H. Grabke, *The effect of impurities on the alumina scale growth: an alternative view*, *Scripta materialia* **38** (1997), no. 1 123–129.
- [94] N. Birks, G. H. Meier, and F. S. Pettit, *Introduction to the high temperature oxidation of metals*. Cambridge University Press, 2006.
- [95] K. Phani and S. Niyogi, *Young's modulus of porous brittle solids*, *Journal of Materials Science* **22** (1987), no. 1 257–263.
- [96] J. Wang, H. Li, and R. Stevens, *Hafnia and hafnia-toughened ceramics*, *Journal of materials science* **27** (1992), no. 20 5397–5430.
- [97] B. M. Gleeson, D. J. Sordelet, and W. Wang, *High-temperature coatings with Pt metal modified  $\gamma$ -Ni+ $\gamma'$ -Ni<sub>3</sub>Al alloy compositions*, Sept. 25, 2007. US Patent 7,273,662.
- [98] B. Gleeson, D. Sordelet, and W. Wang, *High-temperature coatings with Pt metal modified  $\gamma$ -Ni+ $\gamma'$ -Ni<sub>3</sub>Al alloy compositions*, Dec. 18, 2012. US Patent 8,334,056.
- [99] B. Gleeson and D. Sordelet, *Pt metal modified  $\gamma$ -Ni+ $\gamma'$ -Ni<sub>3</sub>Al alloy compositions for high temperature degradation resistant structural alloys*, Sept. 2, 2014. US Patent 8,821,654.

- [100] H. Zhu, N. A. Fleck, A. C. Cocks, and A. Evans, *Numerical simulations of crack formation from pegs in thermal barrier systems with NiCoCrAlY bond coats*, *Materials Science and Engineering: A* **404** (2005), no. 1 26–32.
- [101] B. Pint, I. Wright, W. Lee, Y. Zhang, K. Pruessner, and K. Alexander, *Substrate and bond coat compositions: factors affecting alumina scale adhesion*, *Materials Science and Engineering: A* **245** (1998), no. 2 201–211.
- [102] R. W. Jackson, M. S. Titus, M. R. Begley, and T. M. Pollock, *Thermal expansion behavior of new Co-based alloys and implications for coatings*, *Surface and Coatings Technology* (2016).
- [103] D. J. Jorgensen, R. W. Jackson, and T. M. Pollock, *A robust technique to characterize rumpling in next-generation high-strength bond coats*, *Surface and Coatings Technology* **submitted** (2016).
- [104] V. Tolpygo, D. Clarke, and K. Murphy, *The effect of grit blasting on the oxidation behavior of a platinum-modified nickel-aluminide coating*, *Metallurgical and materials transactions A* **32** (2001), no. 6 1467–1478.
- [105] J. O. Smith, *Mathematics of the discrete Fourier transform (DFT): with audio applications*. Julius Smith, 2007.
- [106] D. J. Whitehouse, *Handbook of Surface Metrology*. Taylor & Francis, 1994.
- [107] M. J. Bannister and J. M. Barnes, *Solubility of  $TiO_2$  in  $ZrO_2$* , *Journal of the American Ceramic Society* **69** (1986), no. 11.
- [108] J. Haynes, B. Pint, W. Porter, and I. Wright, *Comparison of thermal expansion and oxidation behavior of various high-temperature coating materials and superalloys*, *Materials at High Temperatures* **21** (2004), no. 2 87–94.
- [109] T. Izumi, N. Mu, L. Zhang, and B. Gleeson, *Effects of targeted  $\gamma$ -Ni+ $\gamma$ - $Ni_3Al$ -based coating compositions on oxidation behavior*, *Surface and Coatings Technology* **202** (2007), no. 4 628–631.
- [110] Y. Zhang, D. Ballard, J. Stacy, B. A. Pint, and J. A. Haynes, *Synthesis and oxidation behavior of platinum-enriched  $\gamma$ + $\gamma$  bond coatings on Ni-based superalloys*, *Surface and Coatings Technology* **201** (2006), no. 7 3857–3861.
- [111] V. Deodeshmukh, N. Mu, B. Li, and B. Gleeson, *Hot corrosion and oxidation behavior of a novel Pt+ Hf-modified  $\gamma'$ - $Ni_3Al$ + $\gamma$ -Ni-based coating*, *Surface and Coatings Technology* **201** (2006), no. 7 3836–3840.

- [112] C. Leyens, U. Schulz, B. Pint, and I. Wright, *Influence of electron beam physical vapor deposited thermal barrier coating microstructure on thermal barrier coating system performance under cyclic oxidation conditions*, *Surface and Coatings Technology* **120** (1999) 68–76.
- [113] U. Schulz, K. Fritscher, C. Leyens, and M. Peters, *Influence of processing on microstructure and performance of electron beam physical vapor deposition (EB-PVD) thermal barrier coatings*, *Journal of engineering for gas turbines and power* **124** (2002), no. 2 229–234.
- [114] U. Schulz, B. Saruhan, K. Fritscher, and C. Leyens, *Review on advanced EB-PVD ceramic topcoats for TBC applications*, *International Journal of Applied Ceramic Technology* **1** (2004), no. 4 302–315.
- [115] C. Johnson, J. Ruud, R. Bruce, and D. Wortman, *Relationships between residual stress, microstructure and mechanical properties of electron beam–physical vapor deposition thermal barrier coatings*, *Surface and Coatings Technology* **108** (1998) 80–85.
- [116] U. Schulz, K. Fritscher, C. Leyens, M. Peters, and W. Kaysser, *Thermocyclic behavior of differently stabilized and structured EB-PVD thermal barrier coatings*, *Materialwissenschaft und Werkstofftechnik* **28** (1997), no. 8 370–376.
- [117] E. Üstündag, R. Subramanian, R. Dieckmann, and S. Sass, *In situ formation of metal-ceramic microstructures in the Ni-Al-O system by partial reduction reactions*, *Acta metallurgica et materialia* **43** (1995), no. 1 383–389.
- [118] E. Üstündag, P. Ret, Y. Shapiro, R. Subramanian, R. Dieckmann, and S. Sassa, *Ductile phase toughened ceramics by partial reduction reactions in the Ni-Al-O system: Mechanical properties and effect of dopants*, in *MRS Proceedings*, vol. 365, p. 125, Cambridge Univ Press, 1994.
- [119] A. U. Munawar, U. Schulz, and M. Shahid, *Microstructure and lifetime of EB-PVD TBCs with Hf-doped bond coat and Gd-zirconate ceramic top coat on CMSX-4 substrates*, *Surface and Coatings Technology* (2016).
- [120] D. F. Susan and A. R. Marder, *Oxidation of Ni–Al-base electrodeposited composite coatings II: oxidation kinetics and morphology at 1000 °C*, *Oxidation of Metals* **57** (2002), no. 1-2 159–180.
- [121] J. Armijo, *The kinetics and mechanism of solid-state spinel formation—a review and critique*, *Oxidation of metals* **1** (1969), no. 2 171–198.
- [122] X. Zhao, I. Shapiro, and P. Xiao, *Spinel formation in thermal barrier systems with a Pt-enriched  $\gamma$ -Ni +  $\gamma'$ -Ni<sub>3</sub>Al bond coat*, *Surface and Coatings Technology* **202** (2008), no. 13 2905–2916.

- [123] P. Hou, *Impurity effects on alumina scale growth*, *Journal of the American Ceramic Society* **86** (2003), no. 4 660–68.
- [124] P. Hou and K. McCarty, *Surface and interface segregation in  $\beta$ -NiAl with and without Pt addition*, *Scripta materialia* **54** (2006), no. 5 937–941.
- [125] P. Hou, *Segregation behavior at TGO/bondcoat interfaces*, *Journal of materials science* **44** (2009), no. 7 1711–1725.
- [126] H. Grabke, *Oxidation of NiAl and FeAl*, *Intermetallics* **7** (1999), no. 10 1153–1158.
- [127] A. G. Evans, D. R. Clarke, and C. G. Levi, *The influence of oxides on the performance of advanced gas turbines*, *Journal of the European Ceramic Society* **28** (2008), no. 7 1405–1419.
- [128] P. Tortorelli, K. More, E. Specht, B. Pint, and P. Zschack, *Growth stress–microstructure relationships for alumina scales*, *Materials at High Temperatures* **20** (2003), no. 3 303–310.
- [129] P.-Y. Théry, M. Poulain, M. Dupeux, and M. Braccini, *Spallation of two thermal barrier coating systems: experimental study of adhesion and energetic approach to lifetime during cyclic oxidation*, *Journal of Materials Science* **44** (2009), no. 7 1726–1733.
- [130] I. Lomaev, D. Novikov, S. Okatov, Y. N. Gornostyrev, A. Cetel, M. Maloney, R. Montero, and S. Burlatsky, *On the mechanism of sulfur fast diffusion in 3-D transition metals*, *Acta Materialia* **67** (2014) 95–101.
- [131] T. Degen, M. Sadki, E. Bron, U. König, and G. Nénert, *The HighScore suite*, *Powder Diffraction* **29** (2014), no. S2 S13–S18.
- [132] P. Y. Hou and K. Priimak, *Interfacial segregation, pore formation, and scale adhesion on NiAl alloys*, *Oxidation of Metals* **63** (2005), no. 1-2 113–130.
- [133] B. Pint, *Optimization of reactive-element additions to improve oxidation performance of alumina-forming alloys*, *Journal of the American Ceramic Society* **86** (2003), no. 4 686–95.
- [134] D. Whittle and J. Stringer, *Improvements in high temperature oxidation resistance by additions of reactive elements or oxide dispersions*, *Philosophical Transactions of the Royal Society of London A: Mathematical, Physical and Engineering Sciences* **295** (1980), no. 1413 309–329.
- [135] D. Moon, *Role of reactive elements in alloy protection*, *Materials Science and Technology* **5** (1989), no. 8 754–764.

- [136] D. J. Jorgensen, T. M. Pollock, and M. R. Begley, *Dynamic response of thin films on substrates subjected to femtosecond laser pulses*, *Acta Materialia* **84** (2015) 136–144.
- [137] A. Pandey, V. K. Tolpygo, and K. J. Hemker, *Thermomechanical behavior of developmental thermal barrier coating bond coats*, *JOM* **65** (2013), no. 4 542–549.
- [138] M. De Graef, B. J. Dalgleish, M. Turner, and A. G. Evans, *Interfaces between alumina and platinum: structure, bonding and fracture resistance*, *Acta metallurgica et materialia* **40** (1992) S333–S344.
- [139] A. Evans, J. Hutchinson, and Y. Wei, *Interface adhesion: effects of plasticity and segregation*, *Acta Materialia* **47** (1999), no. 15 4093–4113.
- [140] J. Wang and A. Evans, *Effects of strain cycling on buckling, cracking and spaling of a thermally grown alumina on nickel-based bond coat*, *Acta Materialia* **47** (1999), no. 2 699–710.
- [141] A. A. Volinsky, N. R. Moody, and W. W. Gerberich, *Interfacial toughness measurements for thin films on substrates*, *Acta Materialia* **50** (2002), no. 3 441–466.
- [142] Z. Chen, K. Zhou, X. Lu, and Y. C. Lam, *A review on the mechanical methods for evaluating coating adhesion*, *Acta Mechanica* (2013) 1–22.
- [143] J. Chen and S. Bull, *Approaches to investigate delamination and interfacial toughness in coated systems: an overview*, *Journal of Physics D: Applied Physics* **44** (2011), no. 3 034001.
- [144] A. G. Evans and B. J. Dalgleish, *The fracture resistance of metal-ceramic interfaces*, *Acta Metallurgica et Materialia* **40, Supplement** (1992), no. 0 S295 – S306.
- [145] M. Begley, D. Mumm, A. Evans, and J. Hutchinson, *Analysis of a wedge impression test for measuring the interface toughness between films/coatings and ductile substrates*, *Acta Materialia* **48** (2000), no. 12 3211 – 3220.
- [146] M. R. Begley, A. G. Evans, and J. W. Hutchinson, *Spherical impression of thin elastic films on elastic–plastic substrates*, *International journal of Solids and structures* **36** (1999), no. 18 2773–2788.
- [147] Q. Feng, Y. N. Picard, H. Liu, S. M. Yalisove, G. Mourou, and T. M. Pollock, *Femtosecond laser micromachining of a single-crystal superalloy*, *Scripta Materialia* **53** (2005), no. 5 511–516.

- [148] Q. Feng, Y. N. Picard, J. P. McDonald, P. A. V. Rompay, S. M. Yalisove, and T. M. Pollock, *Femtosecond laser machining of single-crystal superalloys through thermal barrier coatings*, *Materials Science and Engineering: A* **430** (2006), no. 1-2 203 – 207.
- [149] N. G. Semaltianos, W. Perrie, P. French, M. Sharp, G. Dearden, S. Logothetidis, and K. G. Watkins, *Femtosecond laser ablation characteristics of nickel-based superalloy C263*, *Applied Physics A* **94** (2009), no. 4 999–1009.
- [150] S. Ma, J. McDonald, B. Tryon, S. Yalisove, and T. Pollock, *Femtosecond laser ablation regimes in a single-crystal superalloy*, *Metallurgical and Materials Transactions A* **38** (2007), no. 13 2349–2357.
- [151] S. Rapp, M. Domke, M. Schmidt, and H. P. Huber, *Physical mechanisms during fs laser ablation of thin SiO<sub>2</sub> films*, *Physics Procedia* **41** (2013) 727–733.
- [152] K. Furusawa, K. Takahashi, H. Kumagai, K. Midorikawa, and M. Obara, *Ablation characteristics of Au, Ag, and Cu metals using a femtosecond Ti: sapphire laser*, *Applied Physics A* **69** (1999), no. 1 S359–S366.
- [153] J. Reif, *Laser-Surface Interactions for new Materials Production: Tailoring Structure and Properties*. Springer, 2010.
- [154] S. Rapp, J. Rosenberger, M. Domke, G. Heise, H. P. Huber, and M. Schmidt, *Ultrafast pump-probe microscopy reveals the mechanism of selective fs laser structuring of transparent thin films for maskless micropatterning*, *Applied Surface Science* **290** (2014) 368–372.
- [155] M. Domke, S. Rapp, M. Schmidt, and H. P. Huber, *Ultra-fast movies of thin-film laser ablation*, *Applied Physics A* **109** (2012), no. 2 409–420.
- [156] C. Cheng and X. Xu, *Mechanisms of decomposition of metal during femtosecond laser ablation*, *Physical Review B* **72** (2005), no. 16 165415.
- [157] J. P. McDonald, S. Ma, T. M. Pollock, S. M. Yalisove, and J. A. Nees, *Femtosecond pulsed laser ablation dynamics and ablation morphology of nickel based superalloy CMSX-4*, *Journal of Applied Physics* **103** (2008), no. 9 093111.
- [158] J. P. McDonald, J. A. Nees, and S. M. Yalisove, *Pump-probe imaging of femtosecond pulsed laser ablation of silicon with thermally grown oxide films*, *Journal of Applied Physics* **102** (2007), no. 6 063109.
- [159] J. Jia, M. Li, and C. Thompson, *Amorphization of silicon by femtosecond laser pulses*, *Applied physics letters* **84** (2004), no. 16 3205–3207.
- [160] T. Höche, D. Ruthe, and T. Petsch, *Low-fluence femtosecond-laser interaction with a Mo/Si multilayer stack*, *Applied Physics A* **79** (2004), no. 4-6 961–963.

- [161] Y. N. Picard and S. M. Yalisove, *Femtosecond laser heat affected zones profiled in Co/ Si multilayer thin films*, *Applied Physics Letters* **92** (2008), no. 1 014102.
- [162] J. Liu, R. Yen, H. Kurz, and N. Bloembergen, *Phase transformation on and charged particle emission from a silicon crystal surface, induced by picosecond laser pulses*, *Applied Physics Letters* **39** (1981), no. 9 755–757.
- [163] M. Thompson, J. Mayer, A. Cullis, H. Webber, N. Chew, J. Poate, and D. Jacobson, *Silicon melt, regrowth, and amorphization velocities during pulsed laser irradiation*, *Physical Review Letters* **50** (1983), no. 12 896.
- [164] B. J. Demaske, V. V. Zhakhovsky, N. A. Inogamov, and I. I. Oleynik, *Ablation and spallation of gold films irradiated by ultrashort laser pulses*, *Physical Review B* **82** (2010), no. 6 064113.
- [165] D. Perez and L. J. Lewis, *Molecular-dynamics study of ablation of solids under femtosecond laser pulses*, *Physical Review B* **67** (2003), no. 18 184102.
- [166] R. F. W. Herrmann, J. Gerlach, and E. E. B. Campbell, *Ultrashort pulse laser ablation of silicon: an MD simulation study*, *Applied Physics A: Materials Science & Processing* **66** (1998), no. 1 35–42.
- [167] J. P. McDonald, D. K. Das, J. A. Nees, T. M. Pollock, and S. M. Yalisove, *Approaching non-destructive surface chemical analysis of CMSX-4 superalloy with double-pulsed laser induced breakdown spectroscopy*, *Spectrochimica Acta Part B: Atomic Spectroscopy* **63** (2008), no. 5 561–565.
- [168] J. P. McDonald, M. Thouless, and S. M. Yalisove, *Mechanics analysis of femtosecond laser-induced blisters produced in thermally grown oxide on Si (100)*, *Journal of Materials Research* **25** (2010), no. 6 1087.
- [169] E. Coyne, J. P. Magee, P. Mannion, G. M. O’connor, and T. J. Glynn, *STEM (scanning transmission electron microscopy) analysis of femtosecond laser pulse induced damage to bulk silicon*, *Applied Physics A* **81** (2005), no. 2 371–378.
- [170] T. Nakamura, C. F. Shih, and L. B. Freund, *Computational methods based on an energy integral in dynamic fracture*, *International Journal of Fracture* **27** (1985), no. 3-4 229–243.
- [171] T. Nakamura, C. F. Shih, and L. B. Freund, *Elastic-plastic analysis of a dynamically loaded circumferentially notched round bar*, *Engineering Fracture Mechanics* **22** (1985), no. 3 437–452.
- [172] C. F. Shih, B. Moran, and T. Nakamura, *Energy release rate along a three-dimensional crack front in a thermally stressed body*, *International Journal of Fracture* **30** (1986), no. 2 79–102.

- [173] J. P. McDonald, *Near threshold femtosecond laser interactions with materials: Ablation thresholds, morphologies, and dynamics*. PhD thesis, University of Michigan, 2007.
- [174] J. H. Yoo, S. H. Jeong, X. L. Mao, R. Greif, and R. E. Russo, *Evidence for phase-explosion and generation of large particles during high power nanosecond laser ablation of silicon*, *Applied Physics Letters* **76** (2000), no. 6 783–785.
- [175] J. W. Hutchinson and Z. Suo, *Mixed mode cracking in layered materials*, *Advances in Applied Mechanics* **29** (1992), no. 63 191.
- [176] J. W. Hutchinson, M. D. Thouless, and E. G. Liniger, *Growth and configurational stability of circular, buckling-driven film delaminations*, *Acta Metallurgica et Materialia* **40** (1992), no. 2 295–308.
- [177] Y. O, J. Koo, K. Hong, J. Park, and D. Shin, *Effect of grain size on transmittance and mechanical strength of sintered alumina*, *Materials Science and Engineering: A* **374** (2004) 191–195.
- [178] Q. Ma and D. R. Clarke, *Stress measurement in single-crystal and polycrystalline ceramics using their optical fluorescence*, *Journal of the American Ceramic Society* **76** (1993), no. 6 1433–1440.
- [179] Q. Ma and D. R. Clarke, *Piezospectroscopic determination of residual stresses in polycrystalline alumina*, *Journal of the American Ceramic Society* **77** (1994), no. 2 298–302.
- [180] V. Tolpygo and D. Clarke, *Spalling failure of  $\alpha$ -alumina films grown by oxidation. II. decohesion nucleation and growth*, *Materials Science and Engineering: A* **A278** (2000) 151–161.
- [181] D. R. Clarke and D. J. Gardiner, *Recent advances in piezospectroscopy*, *International Journal of Materials Research* **98** (2007), no. 8 756–762.
- [182] D. J. Jorgensen, M. S. Titus, and T. M. Pollock, *Femtosecond laser ablation and nanoparticle formation in intermetallic NiAl*, *Applied Surface Science* **353** (2015) 700–707.
- [183] J. W. Pro, *Discrete element methods for modeling fracture in brittle coating systems and composites*. PhD thesis, University of California, Santa Barbara, June, 2016.
- [184] B. Gleeson, W. Cheung, W. Da Costa, and D. Young, *The hot-corrosion behavior of novel co-deposited chromium-modified aluminide coatings*, *Oxidation of metals* **38** (1992), no. 5-6 407–424.

- [185] G. Meier, W. Coons, and R. Perkins, *Corrosion of iron-, nickel-, and cobalt-base alloys in atmospheres containing carbon and oxygen*, *Oxidation of Metals* **17** (1982), no. 3-4 235–262.
- [186] B. Gleeson, W. Wang, S. Hayashi, and D. Sordelet, *Effects of platinum on the interdiffusion and oxidation behavior of Ni-Al-based alloys*, *Materials Science Forum* **461–464** (2004) 213–222.
- [187] J.-O. Andersson, T. Helander, L. Höglund, P. Shi, and B. Sundman, *Thermo-Calc and DICTRA, computational tools for materials science*, *Calphad* **26** (2002), no. 2 273–312.